

Improving Predictions with Reliable Extrapolation Schemes
and Better Understanding of Factorization

Dissertation

Presented in Partial Fulfillment of the Requirements for
the Degree Doctor of Philosophy in the
Graduate School of The Ohio State University

By

Sushant N. More, M.S.

Graduate Program in Physics

The Ohio State University

2016

Dissertation Committee:

Prof. Richard Furnstahl, Advisor

Prof. Robert Perry

Prof. Michael Lisa

Prof. John Beacom

© Copyright by

Sushant N. More

2016

Abstract

New insights into the inter-nucleon interactions, developments in many-body technology, and the surge in computational capabilities has led to phenomenal progress in low-energy nuclear physics in the past few years. Nonetheless, many calculations still lack a robust uncertainty quantification which is essential for making reliable predictions. In this work we investigate two distinct sources of uncertainty and develop ways to account for them.

Harmonic oscillator basis expansions are widely used in ab-initio nuclear structure calculations. Finite computational resources usually require that the basis be truncated before observables are fully converged, necessitating reliable extrapolation schemes. It has been demonstrated recently that errors introduced from basis truncation can be taken into account by focusing on the infrared and ultraviolet cutoffs induced by a truncated basis. We show that a finite oscillator basis effectively imposes a hard-wall boundary condition in coordinate space. We accurately determine the position of the hard-wall as a function of oscillator space parameters, derive infrared extrapolation formulas for the energy and other observables, and discuss the extension of this approach to higher angular momentum and to other localized bases. We exploit the duality of the harmonic oscillator to account for the errors introduced by a finite ultraviolet cutoff.

Nucleon knockout reactions have been widely used to study and understand nuclear properties. Such an analysis implicitly assumes that the effects of the probe can be separated from the physics of the target nucleus. This factorization between nuclear structure and reaction components depends on the renormalization scale and scheme, and has not been well understood. But it is potentially critical for interpreting experiments and for extracting process-independent nuclear properties. We use a class of unitary transformations called the similarity renormalization group (SRG) transformations to systematically study the scale dependence of factorization for the simplest knockout process of deuteron electrodisintegration. We find that the extent of scale dependence depends strongly on kinematics, but in a *systematic* way. We find a relatively weak scale dependence at the quasi-free kinematics that gets progressively stronger as one moves away from the quasi-free region. Based on examination of the relevant overlap matrix elements, we are able to qualitatively explain and even predict the nature of scale dependence based on the kinematics under consideration.

To the memory of my late grandparents, who valued integrity and education above
everything else.

Acknowledgments

It was an absolute pleasure to work with Prof. Richard Furnstahl. Even after four years of working closely with Dick, I am still in awe of the time and effort he invests in his students. His passion towards physics, dedication towards mentorship, and caring about the scientific community is exemplary. I certainly consider it a privilege to be his padawan and hope to have imbibed at least part of his scientific ethos.

I am also thankful to my committee members, in particular Robert Perry. Their constructive criticism and feedback has helped me develop professionally. I was fortunate to learn from a few exceptional teachers at Ohio State. I thank them for instilling in me a joy for learning advanced physics. I would like to express my gratitude towards Scott Bogner and Thomas Papenbrock; they have been a constant source of support, and I look up to them as mentors. I am grateful to Sabine Jeschonnek for helping with the deuteron disintegration theory. I have also benefited tremendously from the interactions with professors and peers in the wider nuclear physics community.

My time at Ohio State coincided with some of the best post-docs in the group—Heiko, Kai, and Sebastian. They were always ready to help and my PhD experience has been enriched immensely through interactions with them. I have worked closest with Sebastian; I admire his efficiency and his attention to details.

I was also lucky to overlap with excellent fellow graduate students in the group. It was fun growing up with my physics siblings—Kyle, Sarah, and Alex. Special mention

goes to Kyle for doing a great job of an elder sibling. It was a pleasure to share office space with Brian, Russell, and Khal. I thank them for being a jolly company and for putting up with my idiosyncrasies. The other physics graduate students that I would like to acknowledge are my gym buddies Hudson and Chuck and my former officemate Omar. I have enjoyed discussion with them over a full gamut of topics and have always turned to them for friendly advice when needed.

My friend Kaushik and I landed in the US together five years ago. We have had a good run as flatmates since then. From teaching me cooking to being my driving instructor, I am indebted to him for many things. One of the best things that happened to me at OSU was joining the student group Sankalpa. I thank Gayatri, Vinayak, and Keerthi for getting me started along that path. Friends formed through Sankalpa have been like a family to me and have helped me grow as a person. I thank Mithila, Dhruv, and Garima for being my safety net; Janani, Pooja, Shubhendu, and Keshav for intellectually engaging discussions; and Vipul, Nandan, Subhasree, Bakul, and Madhura for being a lot of fun.

I would like to take this opportunity to visit my roots and express gratitude towards my undergraduate teachers, friends, and relatives back in India. They trusted in me when I had little to show. I value the decade-long friendship of my pals Sheetal Kumar, Ajit, Shishir, Vivek, and Lakshmi Priya.

Finally, I must put on record the unremitting love of my doting yet disciplinarian parents and my headstrong but sweet younger sister. Their unwavering encouragement through thick and thin keeps me going and motivates me to scale new heights.

Vita

May 2011	Dual B.S. M.S., Indian Institute of Science Education and Research (IISER), Pune, India
December 2013	M.S., The Ohio State University, Columbus, Ohio

Publications

- Deuteron electrodisintegration with unitarily evolved potentials*
S. N. More, S. König, R. J. Furnstahl, and K. Hebeler, Phys. Rev. C **92**, 064002 (2015)
- Ultraviolet extrapolations in finite oscillator bases*
S. König, S. K. Bogner, R. J. Furnstahl, S. N. More, and T. Papenbrock, Phys. Rev. C **90**, 064007 (2014)
- Systematic expansion for infrared oscillator basis extrapolations*
R. J. Furnstahl, S. N. More, and T. Papenbrock, Phys. Rev. C **89**, 044301 (2014)
- Universal properties of infrared oscillator basis extrapolations*
S. N. More, R. J. Furnstahl, A. Ekström, G. Hagen, and T. Papenbrock, Phys. Rev. C **87**, 044326 (2013)
- Non-local linear stability of ion beam eroded surfaces*
S. N. More, R. Kree. Applied Surface Science 258 (2012) 4179-4185

Fields of Study

Major Field: Physics

Table of Contents

	Page
Abstract	ii
Dedication	iv
Acknowledgments	v
Vita	vii
List of Figures	x
List of Tables	xxii
1. Introduction	1
1.1 Overview of Nuclear Physics	1
1.2 Checkered past; promising future	3
1.3 Understanding the Force	7
1.3.1 Chiral EFT	9
1.4 Many-body methods	13
1.4.1 “It from the bit”—lattice theories	18
1.5 RG techniques	20
1.5.1 SRG	25
1.6 Path forward for LENP	30
1.7 Thesis organization	32
2. Extrapolation	34
2.1 Infrared story	38
2.1.1 Tale of tails	38
2.1.2 Cashing in on the hard wall correspondence	50
2.1.3 The proof is in the pudding	62

2.1.4	Higher angular momenta	82
2.1.5	Radii and phase shifts	90
2.2	Ultraviolet story	98
2.2.1	Duality and momentum-space boxes	99
2.2.2	Separable approximations	103
2.3	Moving forward and related developments	108
2.3.1	IR front	108
2.3.2	UV front	112
3.	Factorization	116
3.1	Motivation	116
3.2	Test ground: Deuteron disintegration	126
3.2.1	Formalism	126
3.2.2	Evolution setup	135
3.2.3	Numerical implementation	138
3.2.4	Results	140
3.2.5	Operator evolution and q -factorization	157
3.3	Summary and Outlook	165
4.	Epilogue	168
	Bibliography	172

Appendices

A.	t -matrix details	184
A.1	Solving the Lippmann-Schwinger equation	184
A.2	t -matrix checks	189
A.3	Using the LSE for the wave function interpolation	191
B.	Evolution details for deuteron disintegration	194
B.1	Expressions for the evolved matrix elements	194
B.2	Evolution of the final state	198
B.3	Evolution of the current	200

List of Figures

Figure	Page
1.1 Nuclear landscape. A total of 288 isotopes (black squares) are stable on the time scale of the solar system. As more protons or neutrons are added to these stable nuclei, we enter the regime of short-lived radioactive nuclei (green squares). ‘Drip lines’ mark the limit of nuclear existence, where the last nucleon is no longer bound. The uncertainties around drip lines (in red) were obtained by averaging the results of different theoretical models. Figure from [1].	2
1.2 AV18 [12], Reid93 [13], and Bonn [14] potentials for 1S_0 channel as functions of internucleonic distance. These potentials accurately describe neutron-proton scattering up to laboratory energies of 300 MeV. Regions I, II, and III correspond to long-range, intermediate-range, and short-range parts discussed in the text. Figure from [15].	5
1.3 Evolution of the inter-nucleon interaction picture over time. Figures from a talk by Witold Nazarewicz.	6
1.4 Summary of measurements of the QCD coupling α_s as a function of energy scale Q [16].	7
1.5 LENP version of Moore’s law and its violation. Y axis is the mass number of nuclei that can be calculated from ab-initio calculations. In past few years, it has been possible to push the ab-initio frontier to heavier nuclei. Figure from a talk by Gaute Hagen.	8
1.6 Hierarchy of degrees of freedom and associated energy scales in nuclear physics [20].	10
1.7 Diagrams for a chiral Lagrangian at each order. Solid lines are the nucleons and dashed lines pions. Figure from [24].	12

1.8	Convergence of energies as a function of the truncation parameter N_{\max} [27].	14
1.9	Matrix dimension grows factorially with the number of nucleons. Figure courtesy of Pieter Maris.	15
1.10	Lattice QCD vs. lattice EFT. Figures from a talk by Dean Lee.	19
1.11	The 1S_0 AV18 potential in momentum space. Figure from [44].	20
1.12	Physics interpretation often changes with resolution.	22
1.13	Low-pass filter on nuclear potential—illustration and effect on phase shifts.	23
1.14	Schematic illustration of two types of RG evolution. For given Λ_i or λ_i the matrix elements outside the corresponding lines are negligible. This decouples the high-momentum modes from the low-momentum ones. Figure from [44].	24
1.15	SRG evolution of the chiral N ³ LO potential [51] in the 3S_1 channel. Figure from [46].	26
1.16	3S_1 probability density in deuteron for the AV18 potential and the AV18 potential evolved to three SRG λ 's. Figure from [45].	26
1.17	Effect of RG evolution on (non-)observables.	28
1.18	SRG evolution greatly accelerates the convergence in many-body calculations. Figure from [45].	28
1.19	Nuclear matrix element for $0\nu\beta\beta$ for various nuclei calculated using different methods. The legends indicate the different methods used for calculations. Figure from a talk by Petr Vogel.	31
2.1	Ground state energy for ${}^6\text{He}$ as a function of N_{\max} and Ω . Figure taken from [60].	35

2.2	The estimate for exact ${}^6\text{He}$ ground state energy using Eq. 2.3. Extrapolated answer from the constrained fit and the experimental binding energy are indicated by horizontal lines. Figure from [61].	36
2.3	(a) The exact radial wave function (dashed) for a square well Eq. 2.6 with depth $V_0 = 4$ (and $\hbar = \mu = R = 1$) is compared to the wave function obtained from an HO basis truncated at $N_{\max} = 4$ with $\hbar\Omega = 6$ (solid). The spatial extent of the wave function obtained from the HO basis truncation is dictated by the square of HO wave function for the highest radial quantum number (dot-dashed). (b) The wave functions obtained from imposing a Dirichlet boundary condition (bc) at L_0 , L'_0 and L_2 are compared to the wave function in truncated HO basis.	40
2.4	Ground-state energies versus L_0 (top), L'_0 (middle), and L_2 (bottom) for a Gaussian potential well Eq. 2.8 with $V_0 = 5$ and $R = 1$. The crosses are the energies from HO basis truncation. The energies obtained by numerically solving the Schrödinger equation with a Dirichlet bc at L lie on the solid line. The horizontal dotted lines mark the exact energy $E_\infty = -1.27$	42
2.5	Ground-state energies versus L_0 (top), L'_0 (middle), and L_2 (bottom) for a square well potential well Eq. 2.6 with $V_0 = 4$ and $R = 1$. The crosses are the energies from HO basis truncation. The energies obtained by numerically solving the Schrödinger equation with a Dirichlet bc at L lie on the solid line. The horizontal dotted lines mark the exact energy $E_\infty = -1.51$	43
2.6	Ground-state energies versus L_0 (top), L'_0 (middle), and L_2 (bottom) for the Entem-Machleidt 500 MeV N ³ LO potential [66]. The horizontal dotted lines mark the exact energy $E_\infty = -2.2246$ MeV.	44
2.7	Eigenfunctions of p^2 in the truncated HO basis compared to those in a box of size L_2	49
2.8	The staircase function of the s states of the operator p^2 in a finite oscillator basis with $N = 32$ (black) compared to its semiclassical estimate (smooth red curve). $M(k)$ denotes the number of states of the operator p^2 with eigenvalues $p^2 \leq \hbar^2 k^2$	50

2.15 Energy versus L_2 for the first excited states of deep (a) Gaussian Eq. 2.8 and (b) quartic Eq. 2.9 potential wells for a wide range of N and $\hbar\Omega$ (circles) ($\hbar = \mu = R = 1$). The solid line is a fit to Eq. 2.46 with A , k_∞ and E_∞ as fit parameters while the dashed line is the prediction from Eqs. 2.45. The horizontal dotted lines are the exact energies for the first excited states; Gaussian well: $E_\infty = -1.2147$, quartic well: $E_\infty = -1.8236$	68
2.16 (a) Ground-state energy versus L_2 for model Gaussian potential. (b) Energy versus L for the square well. The energies for the square well are from solving the Schrödinger equation exactly with a Dirichlet bc on wave functions at $r = L$. The dashed line is the prediction from Eqs. 2.45. The depths of these model potentials are chosen so that the scaled energies (with $\hbar = \mu = R = 1$) are the same as the deuteron binding energy.	69
2.17 Bound-state energy for a square well of depth $V_0 = 4$ (lengths are in units of R and energies in units of $1/R^2$ with $\hbar^2/\mu = 1$) from solving the Schrödinger equation with a Dirichlet bc at $r = L$. The diamonds are exact results for each L while the horizontal dotted line is the energy for $L \rightarrow \infty$, $E_\infty = -1.5088$. The dashed, dot-dashed and solid lines are predictions for the energy using the systematic correction formula Eq. 2.58 at LO (first term only), L-NLO (first two terms), and full NLO (all terms), respectively. The dotted curve on top of the solid line and the dot-double-dashed lines are respectively the NLO and N2LO predictions for the square well from the Taylor expansion using Eqs. 2.77 and 2.79.	72
2.18 Error plots of the energy correction at each L for the square well of Fig. 2.17 ($V_0 = 4$) predicted at different orders by Eq. 2.58 and by the Taylor expansion method, each compared to the exact energy. Lines proportional to $Le^{-4k_\infty L}$ (dashes) and $L^2e^{-6k_\infty L}$ (with arbitrary normalization) are plotted for comparison to anticipated error slopes.	73
2.19 Bound-state energy for a square well of depth $V_0 = 1.83$ (units with $R = 1$), which simulates a deuteron, from solving the Schrödinger equation with a Dirichlet bc at $r = L$. The horizontal dotted line is the exact energy, $E_\infty = -0.1321$ and the other curves are as the same as in Fig. 2.17.	74

2.20 Comparison of the actual energy correction due to truncation to the energy correction predicted to different orders by Eq. 2.58 for a square well (Eq. 2.6) with $V_0 = 1.83$ and $R = 1$	75
2.21 Deuteron energy versus L_2 (see Eq. 2.113) for the chiral N ³ LO (500 MeV) potential of Ref. [66]. To eliminate the UV contamination we only plot results for $\hbar\Omega > 49$ MeV. The dashed, dot-dashed and solid lines are respectively the LO (first term in Eq. 2.58), L-NLO (first two terms in Eq. 2.58) and the full NLO (all the terms in Eq. 2.58) predictions for the energy correction. The horizontal dotted line is the deuteron energy.	76
2.22 Comparison of the actual energy correction due to HO basis truncation ($\hbar\Omega$ restricted to be greater than 49 MeV to eliminate UV contamination) for the deuteron to the energy correction predicted to different orders from Eq. 2.58. For the parameter w_2 in Eq. 2.58 we use the value reported in [76].	77
2.23 Deuteron energy versus L_2 for the potential of Ref. [66] evolved by the SRG to four different resolutions (specified by λ). To eliminate the UV contamination we only keep points for which $\hbar\Omega > 40$. The horizontal dotted line is the deuteron binding energy.	78
2.24 The same SRG-evolved potentials as in Fig. 2.23 are used to generate energies, but with N fixed at (a) 8 and (b) 12 and no restriction on $\hbar\Omega$. Thus UV corrections are not negligible everywhere. The horizontal dotted line is the deuteron binding energy.	79
2.25 The IR energy correction ΔE_L versus L_2 for a Gaussian potential well Eq. 2.8 with $V_0 = 5$ (and $\hbar = \mu = R = 1$) using a wide range of N and $\hbar\Omega$. The energies are fitted with (a) exponential, (b) Gaussian, and (c) power law dependence on L_2	81
2.26 The IR energy correction ΔE_L versus L_2 for the deuteron calculated with the chiral EFT potential from Ref. [66] using a wide range of N and $\hbar\Omega$. The energies are fitted with (a) exponential, (b) Gaussian, and (c) power law dependence on L_2	82

2.27 Error plots of the energy correction at each L for (a) $l = 1$ and (b) $l = 2$ square-well states predicted at leading order by Eqs. 2.101 and 2.102 compared to the exact energy. Lines proportional to the expected L-NLO residual errors are plotted for comparison.	88
2.28 Residual error for the deuteron energy due to HO basis truncation as a function of $L = L_2$ (with $\hbar\Omega > 49$ MeV to eliminate UV contamination) after subtracting $l = 0$ energy corrections at different orders from Eq. 2.58 and the $l = 2$ correction from Eq. 2.102. For the parameter w_2 in Eq. 2.58 we use the value reported in [76].	89
2.29 Deuteron radius squared versus L_0 (top) and L_2 (bottom) for the Entem-Machleidt 500 MeV N ³ LO potential [66]. The horizontal dotted lines mark the exact radius squared $r_\infty^2 = 3.9006 \text{ fm}^2$. The insets show a magnification of data at smaller lengths L_n	90
2.30 Deuteron radius squared versus L_2 for the chiral N ³ LO (500 MeV) potential of Ref. [66]. To eliminate the UV contamination we only plot results for $\hbar\Omega > 49$ MeV. The solid, dot-dashed, and dashed lines are results from fitting Eq. 2.110 in the shaded region to find $\langle r^2 \rangle_\infty$ and one, two, or three of the c_i constants, respectively. The horizontal dotted line is the deuteron radius squared.	93
2.31 The ¹ S ₀ phase shifts (in degrees) of the N ³ LO chiral interaction (solid line) compared to the phase shifts computed directly in the harmonic oscillator basis (circles).	96
2.32 The ³ P ₁ phase shifts (in degrees) of the N ³ LO chiral interaction (solid line) compared to the phase shifts computed directly in the harmonic oscillator basis (circles).	97
2.33 Relative error of deuteron binding energy plotted vs. lengths Λ_2 , Λ_0 , and $\Lambda_{\kappa,\max}$ (multiplied by factors 2, 1, and 1/2, respectively, to separate the curves. Inset: The same values on a linear scale and without the separation factors.	101
2.34 Calculations of the relative error in the deuteron energy as a function of $\Lambda_2(N_{\max}, \hbar\Omega)$. Circles represent a wide range of oscillator parameters N_{\max} and $\hbar\Omega$ that are IR converged. The series of lines shows energies for which the Hamiltonian has been smoothly cutoff with exponent n . The solid line corresponds to a sharp cutoff.	102

2.35 Comparison of UV extrapolations for a deuteron state calculated with the AV18 potential of Ref. [12]. Circles: oscillator results. Dotted line: exponential extrapolation (Eq. 2.127). Dashed line: Gaussian extrapolation (Eq. 2.128). Solid line: simplest separable extrapolation (Eq. 2.126). Dotted horizontal lines indicate the exact result for the binding momentum.	106
2.36 Calculations of UV extrapolations for a deuteron state calculated with the Epelbaum <i>et al.</i> N3LO (550/600 MeV cutoff) potential of Ref. [51]. The legend description is the same as in Fig. 2.35.	106
2.37 Calculations of UV extrapolations for a deuteron state calculated with the Epelbaum <i>et al.</i> N3LO (550/600 MeV cutoff) potential of Ref. [51]. The legend description is the same as in Fig. 2.35.	107
2.38 Residual error for triton plotted as a function of L_2 (here calculated with the deuteron-neutron reduced mass) for the two- and three-nucleon potential in Ref. [97] unitarily evolved by the SRG to four different resolutions (specified by λ) with the same binding energy [27, 97]. k_∞ here is the lowest separation energy (triton breaking up into deuteron and neutron).	111
2.39 The ratio of the momentum distributions in nucleus to the deuteron momentum distributions. The dashed, dotted, dot-dashed, long dashed, dot-long dashed lines correspond to ${}^3\text{He}$, ${}^4\text{He}$, ${}^{16}\text{O}$, ${}^{56}\text{Fe}$, and nuclear matter respectively. Figure taken from [102].	112
2.40 Ground-state energy for ${}^7\text{Li}$ with IR (vertical dashed lines) and UV (vertical dotted lines) corrections from Eq. 2.129 added to predict E_∞ values. The horizontal dashed line is the global E_∞ . Figure taken from [107].	114
3.1 Schematic of a nucleon knockout reaction.	116
3.2 Schematic illustration of factorization between nuclear structure and reactions component.	117
3.3 Factorization in high-energy QCD. x is the Bjorken- x and it denotes the fraction of momentum of the nucleon carried by the parton under consideration. a denotes the parton flavor.	118

3.4	Parton distribution for the up quarks in the proton as a function of x and Q^2 . Figure taken from [110].	119
3.5	Schematic illustration of factorization in low-energy nuclear physics. .	120
3.6	Deuteron momentum distribution at different SRG resolutions λ . The evolved momentum distribution does not have the short-range correlations (SRCs). Figure from [110].	121
3.7	D -state wave functions for the deuteron for the AV18 potential and the AV18 potential evolved to two SRG λ 's.	121
3.8	High-momentum modes in intermediate states replaced by contact interactions. Figure from [110].	122
3.9	The SRG scale λ sets the natural scale for factorization.	123
3.10	The geometry of the electro-disintegration process in the lab frame. The virtual photon disassociates the deuteron into the proton and the neutron (not shown in this figure).	127
3.11	(a) The first term on the right side of Eq. 3.7. The outgoing nucleons do not interact. (b) The second term on the right side of Eq. 3.7. The outgoing nucleons interact through the NN potential. Figures taken from [139].	130
3.12	f_L calculated at various points on the quasi-free ridge for $\theta' = 15^\circ$ for the AV18 potential. Legends indicate which component of the matrix element in Eq. 3.35 used to calculate f_L is evolved. There are no appreciable evolution effects all along the quasi-free ridge. The effect due to evolution of the final state is small as well and is not shown here to avoid clutter. f_L calculated in the impulse approximation is also shown for comparison.	142
3.13	'Phase space' of kinematics for $\lambda = 1.5 \text{ fm}^{-1}$. The effects of evolution get progressively prominent as one moves further away from the quasi-free ridge. The kinematics of the labeled points are considered later .	143

3.14 f_L calculated for $E' = 100$ MeV and $\mathbf{q}^2 = 10$ fm $^{-2}$ (point “1” in Fig. 3.13) for the AV18 potential. Legends indicate which component of the matrix element in Eq. 3.35 used to calculate f_L is evolved. θ' is the angle of the outgoing proton in the center-of-mass frame. There are no discernible evolution effects for all angles. The effect due to evolution of the final state is small as well and is not shown here to avoid clutter. f_L calculated in the IA, $\langle \phi J_0 \psi_i \rangle$, is also shown for comparison.	144
3.15 f_L calculated for $E' = 10$ MeV and $\mathbf{q}^2 = 4$ fm $^{-2}$ (point “2” in Fig. 3.13) for the AV18 potential. Legends indicate which component of the matrix element in Eq. 3.35 used to calculate f_L is evolved. f_L calculated in the IA, $\langle \phi J_0 \psi_i \rangle$, is also shown for comparison. The effects due to evolution of individual components on f_L are discernible, but still small (compared to the FSI contribution). The effect due to evolution of the final state is small as well and is not shown here to avoid clutter.	145
3.16 f_L calculated for $E' = 30$ MeV and $\mathbf{q}^2 = 16$ fm $^{-2}$ (point “3” in Fig. 3.13) for the AV18 potential. Legends indicate which component of the matrix element in Eq. 3.35 used to calculate f_L is evolved. Prominent enhancement with evolution of the current only and suppression with evolution of the initial state and the final state only, respectively.	146
3.17 f_L calculated for $E' = 30$ MeV and $\mathbf{q}^2 = 25$ fm $^{-2}$ (point “3” in Fig. 3.13) for the AV18 potential. Legends indicate which component of the matrix element in Eq. 3.35 used to calculate f_L is evolved. Prominent enhancement with evolution of the current only and suppression with evolution of the initial state and the final state only, respectively.	147
3.18 Momentum distribution for the deuteron for the AV18 [12], CD-Bonn [19], and the Entem-Machleidt N ³ LO chiral EFT [66] potentials, and for the AV18 potential evolved to two SRG λ ’s.	148
3.19 f_L in IA ($\langle \psi_f \equiv \langle \phi $) calculated for $E' = 30$ MeV and $\mathbf{q}^2 = 16$ fm $^{-2}$ for the AV18 potential. Legends indicate which component of the matrix element in Eq. 3.35 used to calculate f_L are evolved.	150
3.20 f_L in IA ($\langle \psi_f \equiv \langle \phi $) calculated for $E' = 30$ MeV and $\mathbf{q}^2 = 25$ fm $^{-2}$ for the AV18 potential. Legends indicate which component of the matrix element in Eq. 3.35 used to calculate f_L are evolved.	151

3.21 f_L calculated for $E' = 30$ MeV and $\mathbf{q}^2 = 25$ fm $^{-2}$ (point “3” in Fig. 3.13) for the AV18 potential. Legends indicate which component of the matrix element in Eq. 3.35 used to calculate f_L is evolved. The evolution is to SRG (a) $\lambda = 4$ fm $^{-1}$ and (b) $\lambda = 2$ fm $^{-1}$	152
3.22 f_L in IA calculated at $\theta' = 15^\circ$ for $E' = 30$ MeV and $\mathbf{q}^2 = 25$ fm $^{-2}$ for the AV18 potential when the current operator in Eq. 3.35 used to calculate f_L is evolved to various SRG λ ’s. The horizontal dotted line is the unevolved answer.	153
3.23 f_L calculated for $E' = 100$ MeV and $\mathbf{q}^2 = 0.5$ fm $^{-2}$ (point “4” in Fig. 3.13) for the AV18 potential. Legends indicate which component of the matrix element in Eq. 3.35 used to calculate f_L is evolved. Opposite effects from the evolution of the initial state and the final state.	154
3.24 f_L in IA ($\langle \psi_f \equiv \langle \phi $) calculated for $E' = 100$ MeV and $\mathbf{q}^2 = 0.5$ fm $^{-2}$ for the AV18 potential. Legends indicate which component of the matrix element in Eq. 3.35 used to calculate f_L are evolved.	156
3.25 One-body current operator develops two- and higher-body components under SRG evolution.	157
3.26 Integrand of $\langle \psi_{\text{deut}}^\lambda (a_q^\dagger a_q)^\lambda \psi_{\text{deut}}^\lambda \rangle$ in the 3S_1 channel for $q = 3.02$ fm $^{-1}$. The initial potential is the chiral N 3 LO (500 MeV) potential [66]. Figure from [124].	157
3.27 Contour plot for the matrix element $\langle k_1 J_1 m_{J_d} L_1 S = 1 T_1 J_0^{-\lambda} k_2 J = 1 m_{J_d} L_2 S = 1 T = 0 \rangle$ for the quantum numbers indicated for $\lambda = \infty$ and $\lambda = 4$ fm $^{-1}$	159
3.28 Contour plot for the matrix element $\langle k_1 J_1 m_{J_d} L_1 S = 1 T_1 \Delta J^{-\lambda} k_2 J = 1 m_{J_d} L_2 S = 1 T = 0 \rangle$ for the quantum numbers indicated for $\lambda = 4$ and $\lambda = 1.5$ fm $^{-1}$. $\Delta J^{-\lambda} \equiv J_0^{-\lambda} - J_0$	160
3.29 Contour plot for the integrand of $\langle p' J_1=1 m_{J_d}=1 L_1=0 S=1 T_1=0 J_0^{-\lambda} \psi_{\text{deut}, {}^3S_1}^\lambda(k) \rangle$ for $\lambda = \infty$ and $\lambda = 1.5$ fm $^{-1}$	161
3.30 Factorization of U matrices demonstrated by plateaus at high q . Figure from [124].	163

3.31 Factorization of the evolved current J_0^λ demonstrated by plateaus at high q .	163
3.32 q -factorization of f_L .	164
3.33 f_L is a strong function of q . The box indicates the plateau region in Fig. 3.32a.	165
4.1 The EMC effect in different nuclei [153]. x is the Bjorken- x .	169
4.2 The relationship between the number of two-nucleon correlated pairs $a_2(A/d)$, and the strength of the EMC effect. The latter is characterized by the slope of EMC effect in $0.3 < x < 0.7$. Figure from [1].	170

List of Tables

Table	Page
2.1 Comparison between the lowest momentum κ_{\min} , π/L_2 , and π/L_0 for model spaces with up to N oscillator quanta.	48
2.2 Comparison of the exact lowest momentum κ with the analytical estimate x_l/L_2 for $l = 0, 1, 2$ and $0 \leq n \leq 10$	87
2.3 Coefficients from fitting Eq. 2.110 to the deuteron data using one, two, or three c_i constants as shown in Fig. 2.30a	94
2.4 Coefficients from fitting Eq. 2.110 to the deuteron data using one, two, or three c_i constants as shown in Fig. 2.30b	94

Chapter 1: Introduction

1.1 Overview of Nuclear Physics

Nuclear physics deals with the properties of atomic nuclei. The nuclear landscape shown in Fig. 1.1 has been the traditional playground for nuclear physics. The questions historically driving nuclear physics have been: how do protons and neutrons make stable nuclei and rare isotopes? What are the limits of nuclear existence? What are the nuclear binding energies, excitation spectra, radii and so on? We would also like to describe nuclear reactions, make predictions about the shape of the nuclei and understand how the shape dictates the nuclear properties.

By the mid-1970s, it was generally accepted that the nucleons (proton and neutrons) and other hadrons are composed of quarks, and that the quarks are held together through the exchange of gluons [2]. The following decades witnessed rapid development in the fundamental theory of strong interactions describing the interactions between quarks and gluons. This theory goes by the name of Quantum Chromodynamics (QCD) [3]. One of the active areas of investigation is obtaining the hadron structure from QCD. This includes, for example, understanding the origin of proton spin, which is studied experimentally at Jefferson Laboratory [4]. A related focus area is understanding the nature of the quark-gluon plasma (QGP)—the

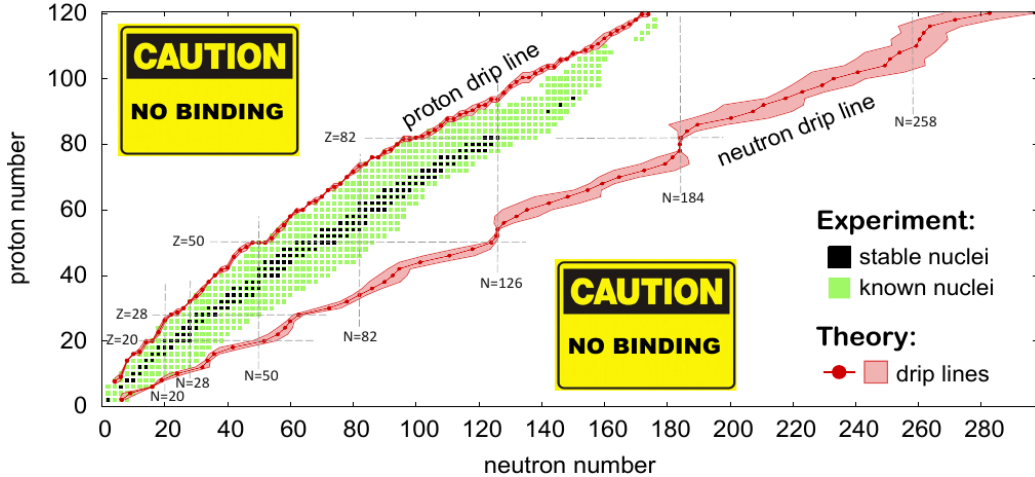


Figure 1.1: Nuclear landscape. A total of 288 isotopes (black squares) are stable on the time scale of the solar system. As more protons or neutrons are added to these stable nuclei, we enter the regime of short-lived radioactive nuclei (green squares). ‘Drip lines’ mark the limit of nuclear existence, where the last nucleon is no longer bound. The uncertainties around drip lines (in red) were obtained by averaging the results of different theoretical models. Figure from [1].

phase in which the universe is believed to exist for up to a few milliseconds after the Big Bang [5]. The energies involved in this subfield (few GeVs) are higher than the energies in ‘traditional’ nuclear physics (few MeVs) introduced in the opening paragraph. Therefore it is conventional to refer to the two subfields as high-energy nuclear physics and low-energy nuclear physics. The work in this thesis will mainly focus on questions in low-energy nuclear physics (LENP).

Apart from the questions at the core of LENP, mentioned in connection to Fig. 1.1, inputs from LENP are immensely important in other areas as well. One such broad area is that of nuclear astrophysics. The majority of the stable and known nuclei shown in Fig. 1.1 were formed in big bang, stellar, or supernova nucleosynthesis [6, 7]. Inputs from LENP are critical in understanding the processes involved in

nucleosynthesis and predicting the observed abundances of isotopes. Neutron stars are another fascinating astrophysical objects for low-energy nuclear physicists. We would like to determine the equation of state for neutron stars and understand how and why stars explode [8].

Finally, there are questions about the fundamental symmetries of the universe where nuclear physics hopes to make significant contributions. For instance, why is there more matter than antimatter in the universe? What is the nature of dark matter [9]? What is the nature of the neutrinos (Majorana or Dirac fermions) and how have they shaped the evolution of the universe? In fact, as we will see later, accurate calculations of nuclear matrix elements are critical for the experiments undertaken to understand the nature of neutrinos [10].

In addition to the broad scientific impact of nuclear physics that we have already mentioned, it also has many real-life applications. Our knowledge of nuclei and ability to produce them has led to an increase in the quality of life for humankind. Applications of nuclear physics encompass a diverse domain including but not limited to energy, security, medicine, radioisotope dating, and material sciences.

1.2 Checkered past; promising future

In 1935, Hideki Yukawa proposed the seminal idea of nuclear interactions being mediated by a massive boson [11]. This could explain how protons and neutrons would stay bound in a nucleus, overcoming the Coulomb repulsion between protons. The fact that such a model described scattering data well at low energies (few MeVs) and the eventual discovery of pions in 1947 led to a wide acceptance of this model. Very soon other heavy mesons (ρ , ω , σ) were discovered as well. Scattering experiments

also indicated that the strength of the nuclear potential depended on distance and at short distances the potential was repulsive.

By 1950, there emerged an industry for coming up with better nuclear potentials. These boson-exchange models shared some common features. The long-range part of the nucleonic interaction was given by pion exchange, the intermediate range was governed by multiple (mostly two) pion exchange, and short-range repulsion was thought to be because of overlap of nucleons. When heavy mesons were discovered, they were added to the intermediate range sector. The pion, being the lightest meson, has the longest range. These general considerations form the basis for phenomenological potentials used even today as seen in Fig. 1.2.

This intense effort is well summarized by Hans Bethe's quote in his essay 'What Holds the Nucleus Together?' in Scientific American (1953): "In the past quarter century physicists have devoted a huge amount of experimentation and mental labor to this problem – probably more man-hours than have been given to any other scientific question in the history of mankind." The boson models did not have a smooth sailing though. In particular the intermediate range multi-pion sector was beset with problems. The pessimism this resulted in is palpable in Marvin Goldberger's comment in 1960: "There are few problems in nuclear theoretical physics which have attracted more attention than that of trying to determine the fundamental interaction between two nucleons. It is also true that scarcely ever has the world of physics owed so little to so many...It is hard to believe that many of the authors are talking about the same problem or, in fact, that they know what the problem is." A running joke was that nuclear physics is really 'unclear' physics!

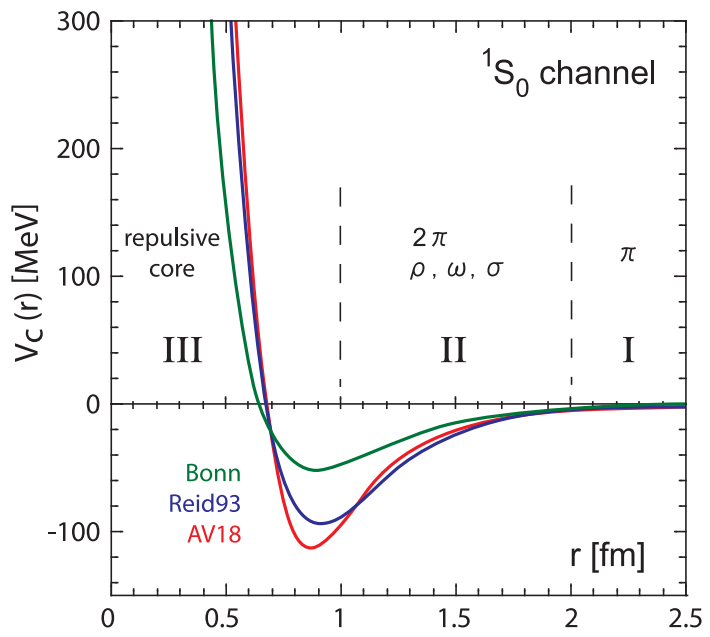


Figure 1.2: AV18 [12], Reid93 [13], and Bonn [14] potentials for 1S_0 channel as functions of internucleonic distance. These potentials accurately describe neutron-proton scattering up to laboratory energies of 300 MeV. Regions I, II, and III correspond to long-range, intermediate-range, and short-range parts discussed in the text. Figure from [15].

There was relatively slow progress with regards to the development of internucleonic potentials in 1970's and 80's. However, this period saw a rapid development of perturbative QCD. It was realized that the nucleons and pions are composed of quarks which are held together by exchange of gluons (cf. Fig. 1.3). This pushed the effort to derive the nuclear potential from the 'fundamental' theory of QCD.

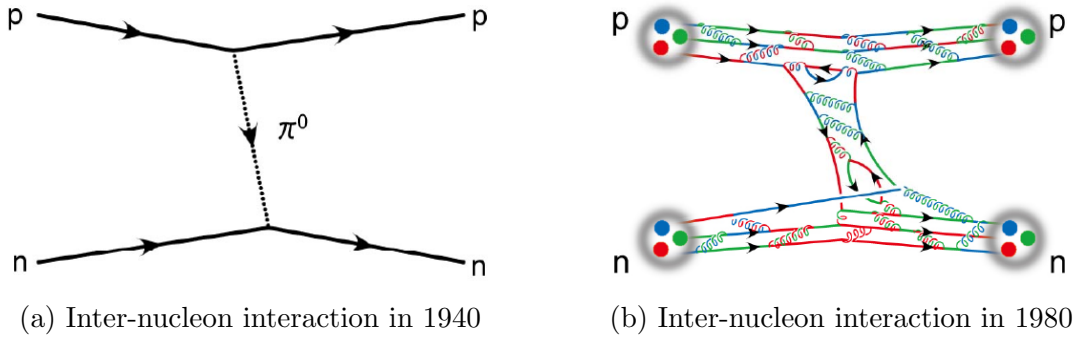


Figure 1.3: Evolution of the inter-nucleon interaction picture over time. Figures from a talk by Witold Nazarewicz.

However, the effort to replace the hadronic descriptions at ordinary nuclear densities with a quark description as in Fig. 1.3b was not very fruitful. As seen in Fig. 1.4, the strength of the QCD coupling α_s increases with decreasing energies. This makes QCD non-perturbative in the low-energy regime of nuclear physics, limiting the success of analytical calculations.

Another aspect that makes low-energy nuclear physics difficult is that it is a many-body problem. It exhibits some emergent phenomena that are difficult to capture in a reductionist approach. This issue has been well-summarized by the famous article 'More is different' by Phillip Anderson [17] (albeit with a focus on many-body problem in condensed matter).

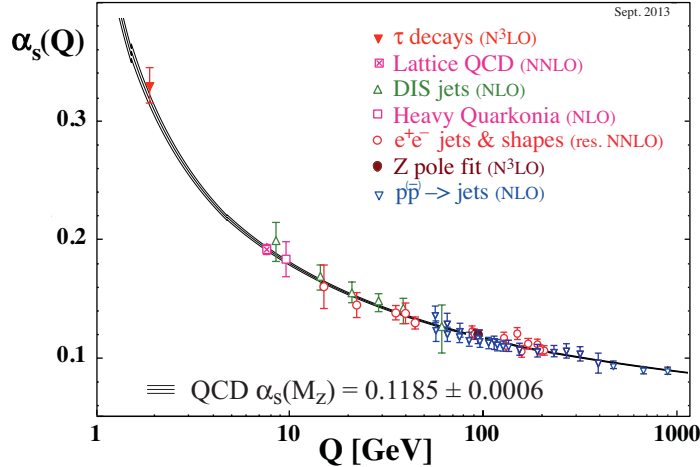


Figure 1.4: Summary of measurements of the QCD coupling α_s as a function of energy scale Q [16].

Despite all these challenges, great strides have been made in LENP in the last few decades. As indicated in Fig. 1.5 particularly the last few years have seen an explosion in the capabilities of low-energy nuclear theory. This phenomenal progress has been possible due to the combination of a few factors—new insights about the nuclear force, developments in many-body technology, and a surge in computational capabilities. In the following sections, we look briefly at each of these developments which will lead us to how the author’s PhD work fits into the bigger picture.

1.3 Understanding the Force

We saw that non-perturbativeness of QCD at low energies (cf. Fig. 1.4) motivated phenomenological descriptions of nuclear forces. The two popular categories of phenomenological interactions are the meson exchange models (which we touched upon

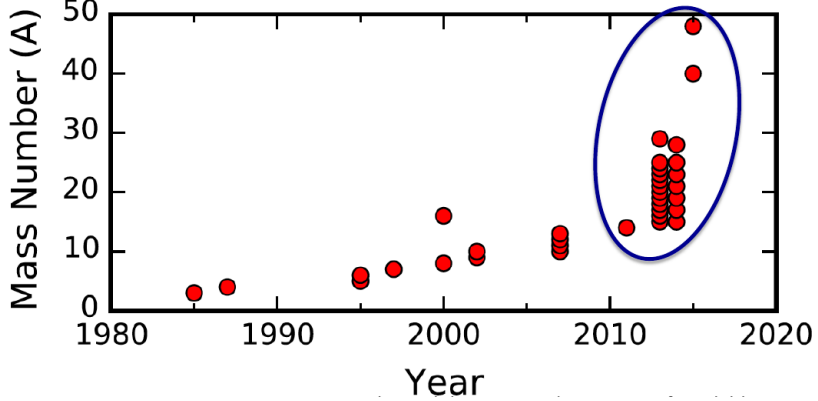


Figure 1.5: LENP version of Moore’s law and its violation. Y axis is the mass number of nuclei that can be calculated from ab-initio calculations. In past few years, it has been possible to push the ab-initio frontier to heavier nuclei. Figure from a talk by Gaute Hagen.

during discussion of Fig. 1.2) and local¹ phenomenological potentials. Examples of these include the Bonn potentials [14, 18, 19] and the Argonne potential [12].

The Argonne potential is probably the most widely used phenomenological potential. One of the reasons being that until recently, it was the only precision interaction usable for Quantum Monte Carlo calculations. The Argonne interactions are built by writing down all the operators that satisfy the required symmetries—translational and Galilean invariance, rotational invariance in space and spin, rotational invariance in isospin, time reversal, and spatial reflection. These operators are given below.

$$\hat{O}_i \in \{\mathbb{1}, \boldsymbol{\sigma}_1 \cdot \boldsymbol{\sigma}_2, S_{12}, \mathbf{L} \cdot \mathbf{S}, \mathbf{L}^2, \mathbf{L}^2 \boldsymbol{\sigma}_1 \cdot \boldsymbol{\sigma}_2, (\mathbf{L} \cdot \mathbf{S})^2\} \otimes \{\mathbb{1}, \boldsymbol{\tau}_1 \cdot \boldsymbol{\tau}_2\} \quad (1.1)$$

$S_{12} = 3(\boldsymbol{\sigma}_1 \cdot \hat{\mathbf{r}})(\boldsymbol{\sigma}_2 \cdot \hat{\mathbf{r}}) - \boldsymbol{\sigma}_1 \cdot \boldsymbol{\sigma}_2$ is the tensor force.

There are a total of 14 operators in Eq. 1.1. The AV18 potential has four more operators which are the charge-dependent and charge-symmetry breaking terms; they

¹The potential is local if $V(\mathbf{r}, \mathbf{r}') = V(\mathbf{r})\delta(\mathbf{r} - \mathbf{r}')$.

are small but needed to get $\chi^2/\text{dof} \approx 1$ for np, nn, and pp scattering. There are also AV8, AV6 potentials which use a limited set of operators.

The AV18 potential is written as

$$\widehat{V}_{18}(r) = \sum_{i=1}^{18} V_i(r) \widehat{O}_i , \quad (1.2)$$

where r is the inter-nucleon separation and $V_i(r) = V_{\text{EM}} + V_\pi + V_{\text{short range}}$. The coefficients in the potential are fit to nucleon scattering up to 350 MeV, and to deuteron bound state properties such as binding energy, radii, and quadrupole moment. A similar exercise has been done for 3N (3-body) interactions. However, the large number of possible three-body operators makes it difficult to get rid of model dependence.

Meson exchange models are formulated in terms of exchange of mesons taking into account the quantum nature of mesons (scalar, vector, pseudo-scalar, so on). The masses are those of real mesons, but couplings are fit parameters. In the simplest form, the interaction is a sum of Yukawa potentials,

$$V = \left(\frac{-g_s^2}{4\pi} \right) \frac{e^{-m_s r}}{r} + \gamma_1^\mu \gamma_{2\mu} \left(\frac{-g_\omega^2}{4\pi} \right) \frac{e^{-m_\omega r}}{r} + \gamma_1^5 \gamma_2^5 \boldsymbol{\tau}_1 \cdot \boldsymbol{\tau}_2 \left(\frac{-g_\pi^2}{4\pi} \right) \frac{e^{-m_\pi r}}{r} . \quad (1.3)$$

Meson exchange potentials and the AV18 potential share the common shortcoming that there is no scope for systematic improvements. It is also unclear how to seek model independence and do robust uncertainty quantification. Finally, these models offer limited guidance on the strength and relevance of three- and higher-body forces.

1.3.1 Chiral EFT

An intriguing aspect of the world we live in, is that there are interesting phenomena at virtually all energy and length scales we can probe. From TeV energies at the Large Hadron Collider (LHC) to the life-defining process of respiration which has the energy

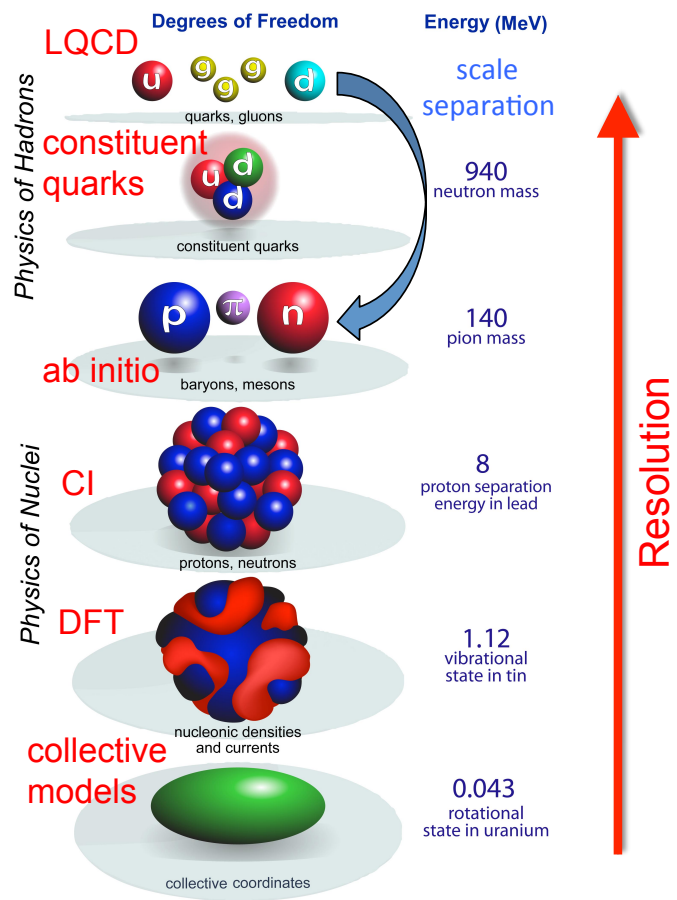


Figure 1.6: Hierarchy of degrees of freedom and associated energy scales in nuclear physics [20].

scale of only few meV, there are physical processes of interest at each step. Nuclear physics spans a wide range of energy and length scales (cf. Fig. 1.6); a wider range than most subfields. This hierarchy provides both challenges and opportunities.

Figure 1.6 indicates the relevant degrees of freedom for the given energy scales. Even though degrees of freedom are a matter of choice, in practice, appropriate degrees of freedom often dictate the success of a theory. To quote Steven Weinberg [21]: “You can use any degrees of freedom you want, but if you use the wrong ones, you’ll be sorry.” Weinberg in his seminal paper [22] applied the concept of effective field theory (EFT) to low-energy QCD. This effort proceeds by writing down the most general Lagrangian consistent with the (approximate) symmetries.

QCD has the expected symmetries of translational, Galilean, and rotational invariance, and spatial reflection and time reversal. Along with that, in the limit of vanishing quark masses, the QCD Lagrangian also possess an exact chiral symmetry [23]. If the chiral symmetry holds, “left”- and “right”-handed fields do not mix. As with any other continuous symmetry, spontaneous breaking of chiral symmetry leads to massless Goldstone boson(s). The masses of the up and down quark (quarks relevant in LENP) are both small ($\sim 2 - 6$ MeV [16]), but non-zero. Therefore the chiral symmetry of the QCD Lagrangian is only approximate and the resulting Goldstone boson—pion—is light (compared to mass of nucleon), but not massless.

Chiral EFT (χ -EFT) uses nucleons and pions as degrees of freedom ². Heavy mesons are “integrated out”. The crucial difference that distinguishes χ -EFTs from meson theories of the 1950s is that they are constrained by chiral symmetry. Broken

²Delta-full chiral EFTs also include the Δ —a resonant state of the nucleon—as a degree of freedom.

chiral symmetry serves as a connection with the underlying theory of QCD. A major advantage of χ -EFT is that it permits systematic improvements and allows the possibility of having reliable uncertainty quantification.

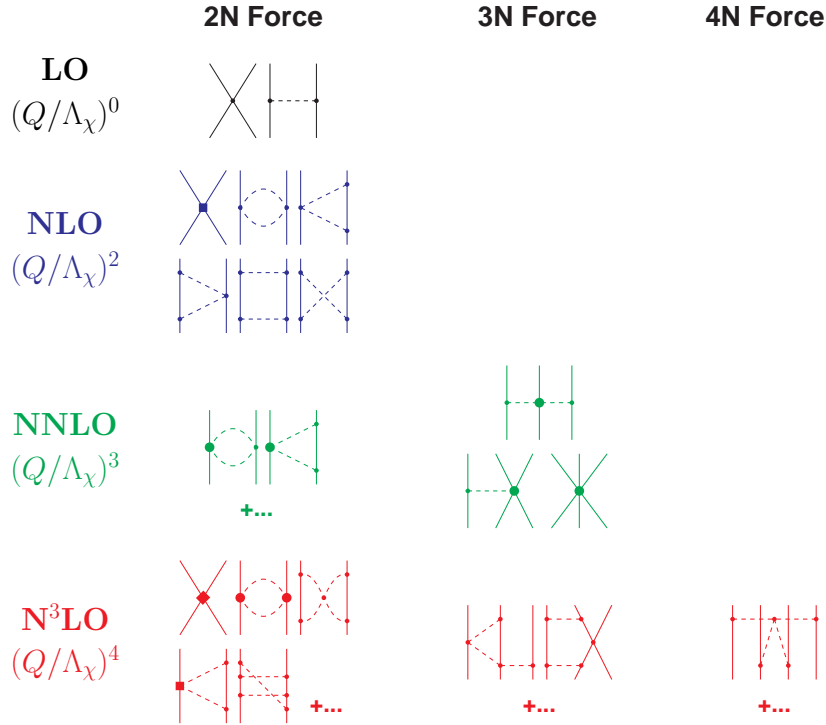


Figure 1.7: Diagrams for a chiral Lagrangian at each order. Solid lines are the nucleons and dashed lines pions. Figure from [24].

Diagrams in a χ -EFT are shown in Fig. 1.7. The three- and higher-body forces appear naturally in χ -EFT with an expected hierarchy (higher-body forces are suppressed successively). The coupling constants at the vertices in Fig. 1.7 are called low-energy coupling constants (LECs); they encode the QCD physics and cannot be calculated in χ -EFT. LECs are fit to experimental data. Lattice QCD provides a

promising method for extracting them in the near future (cf. Subsec. 1.4.1). Despite some concerns over power-counting (see Ref. [25] and references therein), it is fair to say that χ -EFT has been a major breakthrough in low-energy nuclear theory. For more details and applications of χ -EFT, please see Refs. [24] and [26].

1.4 Many-body methods

We learned in kindergarten quantum mechanics that a two-body problem can be solved by reducing it to a one-body problem. The many-body problem is far more relevant to the nuclear physics, and is more challenging. For the nuclear properties such as the bound state energies, the equation we need to solve is the time-independent Schrödinger equation

$$\hat{H}|\Psi\rangle = E|\Psi\rangle . \quad (1.4)$$

The Hamiltonian \hat{H} is given by

$$\hat{H} = \sum_{\text{particles}} \hat{T} + \sum_{\text{pairs}} \hat{V}_{\text{pair}}^{(2)} + \sum_{\text{triplets}} \hat{V}_{\text{triplets}}^{(3)} + \dots , \quad (1.5)$$

where \hat{T} is the kinetic energy and $\hat{V}^{(2)}$, $\hat{V}^{(3)}$ are two- and three-body nuclear potentials (e.g., from χ -EFT or phenomenological potentials).

Over the years various methods have been developed to tackle this problem. We will list some of the broad categories below. We only provide a brief explanation for each of them and refer the reader to the cited references for details.

- *Direct diagonalization:* This category involves expanding the many-body wave function $|\Psi\rangle$ in an appropriate complete basis. Very often this basis is chosen to be the Slater determinant of harmonic oscillator (HO) wave functions. HO wave functions form a complete basis with discrete energy levels that depend

on only one scale (the oscillator frequency). Moreover, HO wave functions are simple analytic functions that go to zero at large distance just as nuclear bound state wave functions.

Finite computational power forces us to truncate the infinite sum of Slater determinants at some point. One of the common truncation scheme is the N_{\max} truncation. It keeps all A particle states $|n_1 l_1 n_2 l_2 \dots n_A l_A\rangle$ such that

$$\sum_i 2n_i + l_i \leq N_{\max}. \quad (1.6)$$

With N_{\max} truncation, solving the many-body Schrödinger equation (Eq. 1.4) becomes a matrix diagonalization problem, and can be solved using standard algorithms. The N_{\max} truncation in HO basis also allows separation of center-of-mass motion from relative motion, ensuring that only intrinsic properties are being calculated.

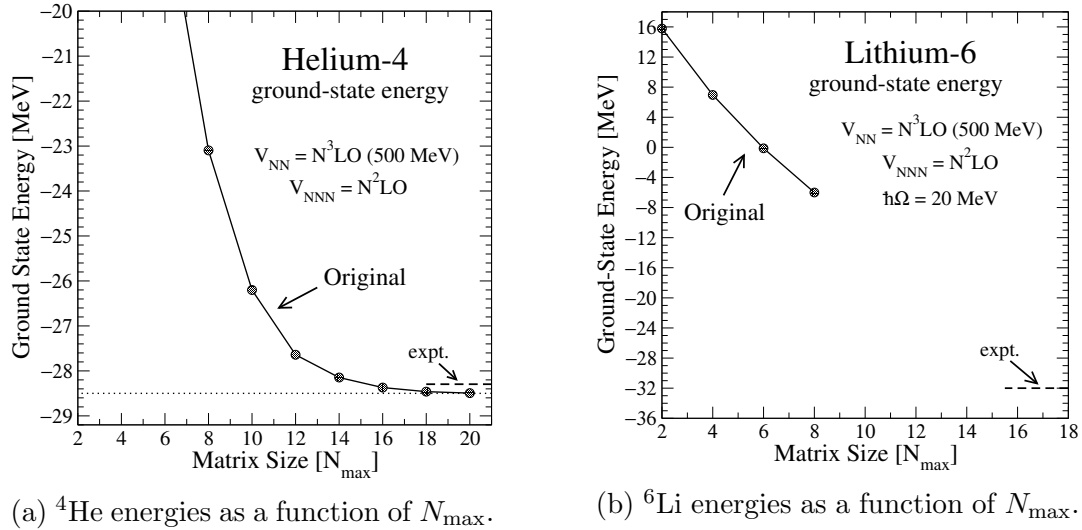


Figure 1.8: Convergence of energies as a function of the truncation parameter N_{\max} [27].

Figure 1.8 shows convergence plots for ground state energies for ^4He and ^6Li . As N_{\max} is increased the energies approach asymptotic values³. A limitation

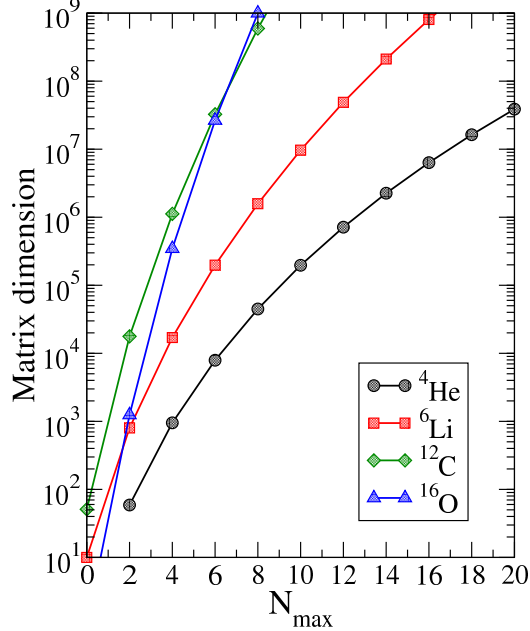


Figure 1.9: Matrix dimension grows factorially with the number of nucleons. Figure courtesy of Pieter Maris.

of the diagonalization method is that the size of the Hamiltonian matrix that we need to diagonalize grows factorially as we go to higher A and higher N_{\max} (cf. Fig. 1.9). This often forces us to truncate the basis before convergence is reached (cf. Fig. 1.8b), and necessitates development of reliable extrapolation schemes. Chapter 2 describes the author's original work devoted to the development of extrapolation schemes relevant to this problem.

³When the asymptotic value doesn't match the experimental value, it points to the shortcomings in the nuclear Hamiltonian.

Many different methods fall under the broad umbrella of diagonalization methods. This includes the traditional shell model [28], the No Core Shell Model (NCSM) [29], the No Core Full Configuration (NCFC) [30], and the Importance Truncated No Core Shell Model (IT-NCSM) [31]. The last three methods primarily differ in the nature of the truncation they employ.

- *Monte Carlo methods:* These methods use the imaginary time evolution of the Schrödinger equation

$$-\partial_\tau |\Psi(\tau)\rangle = \hat{H} |\Psi(\tau)\rangle . \quad (1.7)$$

This equation can be solved by making an ansatz for $|\Psi(\tau=0)\rangle \equiv |\Psi_{\text{trial}}\rangle$. $|\Psi_{\text{trial}}\rangle$ can be expanded in a complete basis of eigenvectors of \hat{H} as

$$|\Psi_{\text{trial}}\rangle = c_0 |\Psi_0\rangle + \sum_{i \neq 0} c_i |\Psi_i\rangle . \quad (1.8)$$

As long as the trial wave function is not orthogonal to the actual ground state, i.e., $c_0 \neq 0$ in Eq. 1.8, it can be shown that the imaginary time evolution (Eq. 1.7) projects out the ground state in the $\tau \rightarrow \infty$ limit. There are many different ways to do the stochastic time evolution of Eq. 1.7 to project out the ground state. The two most popular in nuclear physics are the Green's function Monte Carlo (GFMC) [32, 33] and the Auxiliary Field Diffusion Monte Carlo (AFDMC) [34, 35]. Monte Carlo methods work best with a local potential. The AV18 potential has been the potential of choice for these methods. Recently, it has been possible to derive the low-order χ -EFT in local form, making its use possible for Monte Carlo methods [35].

- *Coupled Cluster:* The energy of the many-body state Ψ is given by

$$E = \langle \Psi | \hat{H} | \Psi \rangle . \quad (1.9)$$

The coupled cluster (CC) method tries to build the state Ψ from the reference state Φ (which for instance can be a Hartree-Fock state) using the transformation

$$|\Psi\rangle = e^T |\Phi\rangle . \quad (1.10)$$

Thus, Eq. 1.9 becomes

$$E = \langle \Phi | e^{-T} \hat{H} e^T | \Phi \rangle . \quad (1.11)$$

The cluster operator T in Eq. 1.10 is defined with respect to the reference state.

$$T = T_1 + T_2 + \dots + T_A . \quad (1.12)$$

T_n generates n -particles- n -holes excitations. In practice, Eq. 1.12 is truncated at T_2 (more recently corrections from T_3 are included as well). CC scales much better than diagonalization or Monte Carlo methods discussed above and is therefore possible to use for medium-mass nuclei [36].

- *Density Functional Theory:* Density Functional Theory (DFT) is based on the principle that the many-body ground state $\Psi(\mathbf{r}_1, \mathbf{r}_2, \dots, \mathbf{r}_A)$ can be written as a functional of the density ρ , i.e., $\Psi = \Psi[\rho]$. Consequently, the energy (or any other observable) can be written as a functional of density

$$E[\rho] = \langle \Psi[\rho] | \hat{H} | \Psi[\rho] \rangle . \quad (1.13)$$

DFT proceeds by writing down an energy density functional (EDF) guided by intuition and general theoretical arguments [37, 38]. Inputs from experiments and exact calculations for simple few-body systems are also used for constructing the EDF. The properties of the physical system are then found by the two step minimization of the EDF—first minimization is at a fixed density $\rho(\mathbf{r})$ and the

second minimization is over $\rho(\mathbf{r})$. Once the EDF is decided upon, DFT does not scale prohibitively with the number of nucleons A , and is therefore the most popular for calculating properties of heavy-mass nuclei.

- *IM-SRG*: In-Medium Similarity Renormalization Group (IM-SRG) is based on the SRG technique we will look at in Subsec. 1.5.1. It uses a series of continuous unitary transformations to decouple the ground state of the many-body Hamiltonian from the excitations. IM-SRG has made it possible to apply the ab-initio (starting with 2N and 3N forces) methods to medium-mass nuclei and beyond. Please see the Ref. [39] for a recent review on progress achieved by IM-SRG.

1.4.1 “It from the bit”⁴ —lattice theories

Lattice QCD

We saw through Fig. 1.4 that the largeness of the QCD coupling at low-energies makes it unamenable to analytical calculations. A well-established non-perturbative approach in this regime is lattice QCD [40]. In lattice QCD, one discretizes space-time; fields representing quarks are defined at lattice sites and the gluon fields are defined on links connecting neighboring sites.

Ideally we would like the lattice size to be as large as possible and the lattice spacing to be as small as possible. However, lattice calculations are computationally extremely intensive, thereby severely constraining the lattice size and spacing. Moreover, the computational cost of simulations scales with the quark mass roughly as m_q^{-4} [41]. The simulations are therefore often done at quark masses larger than the

⁴The phrase “It from the bit” was originally used by John Wheeler while elucidating his ideas on digital physics.

physical quark masses. From the Gell-Mann-Oakes-Renner relation $m_\pi^2 \sim m_q$, and therefore the pion mass in the lattice calculations is larger than its physical value as well. The results are then extrapolated down to physical quark (or pion) mass. In the nuclear case, for accurate extrapolation one must also take into account the crucial non-analytic structure associated with chiral symmetry breaking [42].

Recent calculations have been able to use the physical pion mass though only for very light hadrons [43]. In near future, we hope to extract the low-energy constants in Fig. 1.7 from lattice QCD.

Lattice EFT

Quarks and gluons have many degrees of freedom in terms of spin, color charge, and flavor. This along with strong nonlinearity and non-perturbativeness of the problem makes getting nuclear physics from lattice QCD computationally difficult. An alternative approach is to have nucleons on the lattice site rather than the quarks. The difference between the two methods is illustrated in Fig. 1.10. Lattice EFT com-

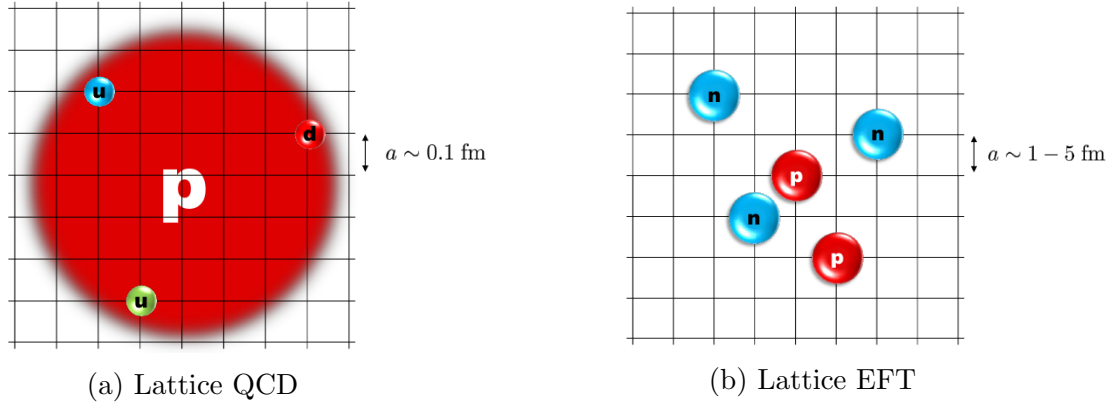


Figure 1.10: Lattice QCD vs. lattice EFT. Figures from a talk by Dean Lee.

bines the framework of effective field theory and computational lattice methods and is a promising tool for studying light nuclear systems.

Lattice theories inherently come with the associated graininess and the finite size. Thus, we have a cutoff for both the maximum length and the maximum momentum scale that we can have on a lattice. This is qualitatively similar to the harmonic oscillator basis truncation problem that we will look extensively at in Chapter 2. Various methods have been used to obtain the continuum limit from the lattice. We will touch upon these in Subsec. 2.3.1, where we look at similarities and differences between the lattice methods and our work with oscillator basis truncation.

1.5 RG techniques

We saw in Fig. 1.8 that the convergence in many-body calculations is slow. To understand why this is the case, recall from Fig. 1.2 that the nuclear potentials have a strong short-range repulsion. This hard core leads to high-momentum components in the potentials. This can be seen in Fig. 1.11 where we plot the AV18 potential in the

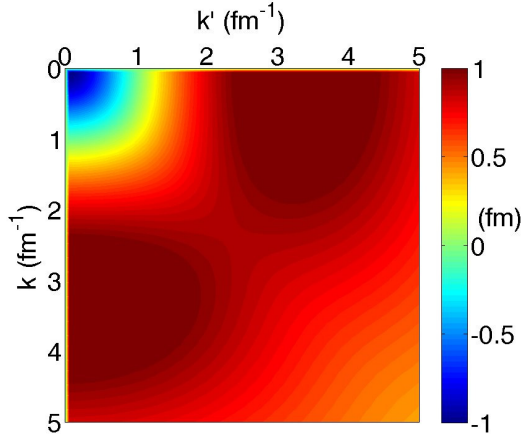


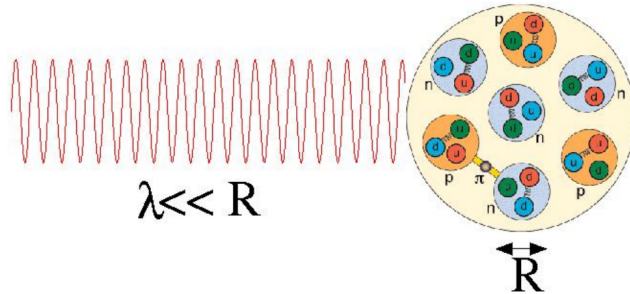
Figure 1.11: The 1S_0 AV18 potential in momentum space. Figure from [44].

1S_0 channel in momentum space. We note that for the AV18 potential, $V(k, k') \rightarrow 0$ only for $k, k' \gtrsim 25 \text{ fm}^{-1}$. However, the Fermi momentum of the nucleon in a heavy nucleus like ^{208}Pb is only about 1.2 fm^{-1} . The Fermi momentum sets the momentum scale of low-energy nuclear processes we wish to study. Thus, we have a mismatch of resolution scales; the processes we wish to describe are $1 - 2 \text{ fm}^{-1}$ ($200 - 400 \text{ MeV}$), whereas the momentum scale in the potential is much higher. To use the analogy due to Tom Banks, ‘it is like trying to understand the properties of waves in the ocean in terms of Feynmann diagrams’. Though in principle this can be done, it makes calculations intractably complicated.

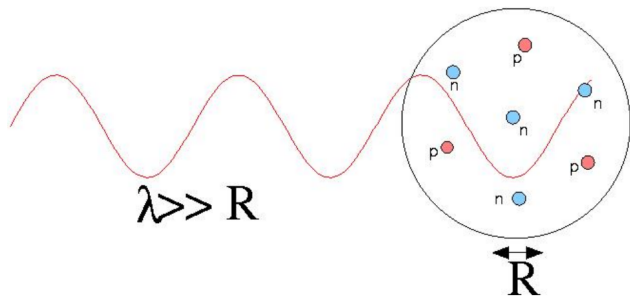
This bring us back to Fig. 1.6. The progression from top to bottom in Fig. 1.6 can be thought of as reduction in resolution. This can be established theoretically using renormalization group (RG) methods. As mentioned before, the focus in LENP is the intermediate region, where nucleons are the degrees of freedom. But even within this limited region, the concept of changing resolution by RG methods has been extremely advantageous [44].

We would like to stress that contrary to the popular notion, high resolution is not always the best thing, especially when the processes we are looking at are low-momentum. Also, though the value of the calculated observable is independent of the resolution, the physical interpretation often changes with the resolution. This is illustrated in Fig. 1.12.

One of the methods to get rid of the high-momentum components is to apply a ‘low-pass filter’ on the potential (cf. Fig. 1.13a). This is routinely done, for example, in image processing. Compression of a digital photograph is achieved by Fourier transforming it, setting the high-momentum modes in the Fourier transform equal to



(a) Nucleus under a high-resolution probe.

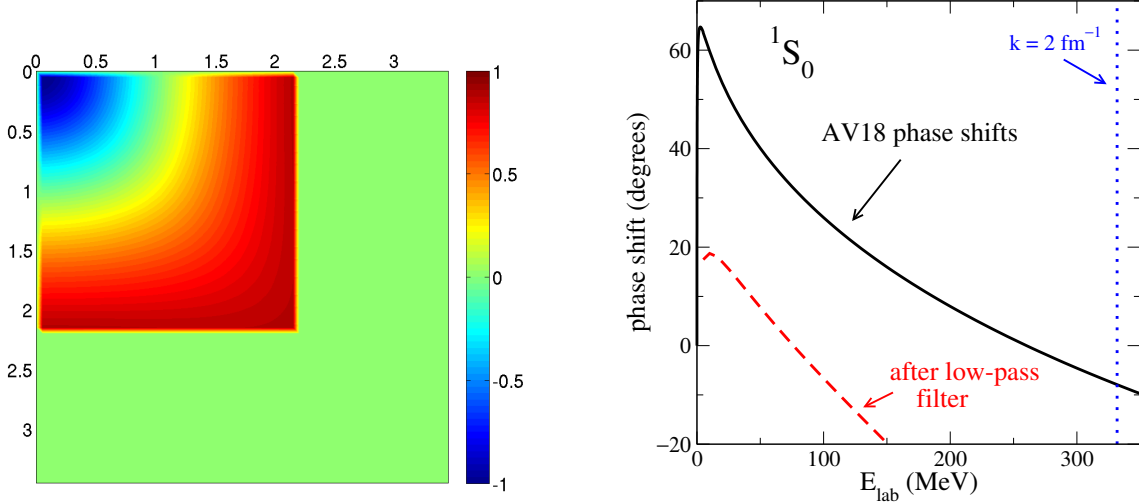


(b) Fine details (nucleon substructure) not resolved when probed at low energies.



(c) A painting by Georges Seurat, which is an example of pointillism. Small, distinct dots of color are applied to form a pattern. The pattern would be lost under a high-resolution probe. Image from Wikimedia Commons.

Figure 1.12: Physics interpretation often changes with resolution.



(a) An illustration of a low-pass filter.

(b) 1S_0 phase shifts for the AV18 potential and for the AV18 potential after the low-pass filter which sets $V(k, k') = 0$ for $k, k' > 2 \text{ fm}^{-1}$ [45].

Figure 1.13: Low-pass filter on nuclear potential—illustration and effect on phase shifts.

zero, and then transforming back. However, as seen in Fig. 1.13a, the straightforward application of a low-pass filter fails to reproduce nuclear phase shifts even at low energies.

This failure of a low-pass filter can be understood by recalling from Fig. 1.11 that the high and low-momentum modes are coupled. For instance, consider (schematically) the expression for the tangent of phase shift in perturbation theory

$$\langle k | \hat{V} | k \rangle + \sum_{k'} \frac{\langle k | \hat{V} | k' \rangle \langle k' | \hat{V} | k \rangle}{(k^2 - k'^2)/m} + \dots . \quad (1.14)$$

The second term in Eq. 1.14 involves a sum over off-diagonal matrix elements of \hat{V} . Therefore even phase shifts for small k will have significant contributions from high k' if the coupling matrix elements $\langle k | \hat{V} | k' \rangle$ are large.

A correct way to get rid of the high-momentum components is to use the RG evolution and lower the momentum cutoff in small steps. Two common choices for

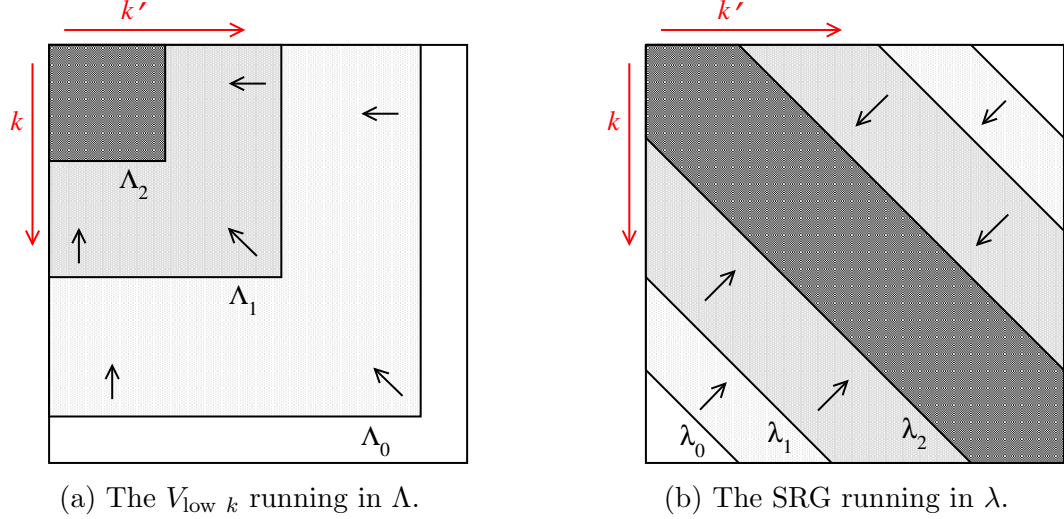


Figure 1.14: Schematic illustration of two types of RG evolution. For given Λ_i or λ_i the matrix elements outside the corresponding lines are negligible. This decouples the high-momentum modes from the low-momentum ones. Figure from [44].

RG running are shown in Fig. 1.14. The RG running shown in Fig. 1.14a is referred to as “ $V_{\text{low } k}$ ” was historically developed first for LENP. It attempts to get the potential in the low-pass-filter form through successive RG transformations [46, 47]. Though successful for two-nucleon forces, it has been difficult to systematically treat many-body forces in the $V_{\text{low } k}$ framework.

A more recent approach through the similarity renormalization group (SRG) is illustrated in Fig. 1.14b. SRG running drives the potential to a band-diagonal form. It is possible to systematically account for the many-body forces in the SRG framework. We will be using the SRG framework in our work presented in Chapter 3. Next we present a brief introduction to the SRG technique.

1.5.1 SRG

SRG for LENP was developed at Ohio State by S. Bogner (then a post-doc), R. Furnstahl, and R. Perry [48]. Their approach was inspired by the RG flows equations developed by Wegner for condensed matter applications [49]. The basic idea in SRG is to apply a series of unitary transformations U_s to transform the Hamiltonian \hat{H} into a band-diagonal form shown in Fig. 1.14b:

$$\hat{H}_s = \hat{U}_s \hat{H} \hat{U}_s^\dagger , \quad (1.15)$$

where s is the RG flow parameter. $U_{s=0} = \mathbb{1}$. In practice, instead of using Eq. 1.15, the SRG evolution is done through the flow equation

$$\frac{d\hat{H}_s}{ds} = \left[[\hat{G}_s, \hat{H}_s], \hat{H}_s \right] . \quad (1.16)$$

\hat{G}_s is the operator which generates the flow. \hat{T}_{rel} , the relative kinetic energy operator, is the most popular choice for \hat{G}_s , though other choices for \hat{G}_s have been explored [50].

Note that since we are just doing unitary transformations, eigenvalues such as energies are unchanged under SRG

$$E_n = \langle \Psi_n | \hat{H} | \Psi_n \rangle = (\langle \Psi_n | \hat{U}_s^\dagger \hat{U}_s H \hat{U}_s^\dagger (\hat{U}_s | \Psi_n \rangle) . \quad (1.17)$$

It is beneficial to change the flow parameter to λ , where $\lambda^2 = 1/\sqrt{s}$. λ has the units of momentum (fm^{-1}). With this change of variable and setting $\hat{G}_s = \hat{T}_{\text{rel}}$, for a given partial-wave channel, the Eq. 1.16 in momentum basis becomes

$$\frac{dV_\lambda}{d\lambda}(k, k') \propto -(\epsilon_k - \epsilon_{k'})^2 V_\lambda(k, k') + \sum_q (\epsilon_k + \epsilon_{k'} - 2\epsilon_q) V_\lambda(k, q) V_\lambda(q, k') . \quad (1.18)$$

The first term on the right side of Eq. 1.18 drives the potential to the band diagonal form shown in Fig. 1.14b and the second term on right side of Eq. 1.18 makes sure that the unitarity is maintained.

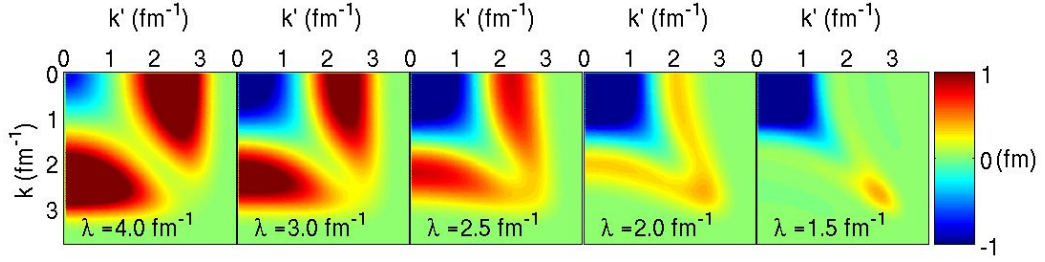


Figure 1.15: SRG evolution of the chiral N³LO potential [51] in the 3S_1 channel. Figure from [46].

Figure 1.15 shows Eq. 1.18 in action. We see that as we go to lower λ , we achieve the decoupling between high- and low-momentum components. Once this decoupling has been achieved, one can apply the low-pass filter and work with smaller matrices if desired.

Effects of SRG evolution

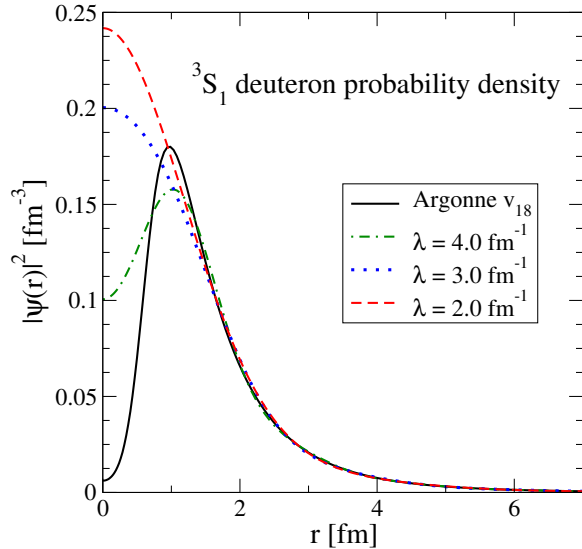


Figure 1.16: 3S_1 probability density in deuteron for the AV18 potential and the AV18 potential evolved to three SRG λ 's. Figure from [45].

The conventional nuclear potentials have a strong short-range repulsion. As a result, the wave functions at short distance are suppressed. This suppression is seen for the unevolved potential in Fig. 1.16. This suppression is called the short-range correlation (SRC). The RG evolution gets rid of the short-range repulsion in the potential (it shifts the strength from high-momentum modes into the low-momentum modes). The wave functions from the evolved potential therefore do not exhibit the SRC as seen in Fig. 1.16. It is also noteworthy that even though the deuteron wave functions change at short distances, the long-distance part is independent of the SRG λ . The long-distance part of the wave function is related to the asymptotic normalization coefficient (ANC), which is an observable. We will see later in Chapter 2 that the ANC being an observable plays an important role in establishing the universality of the extrapolation formulas derived in Chapter 2. The observables should be independent of the resolution scale, which at the end of the day is a theoretical choice.

In Fig. 1.17, we look at the effect of evolution on a few more (non-)observables. We see in Fig. 1.17a that the deuteron binding energy and the ratio of D -state ANC to the S -state ANC are independent of the resolution scale as expected. However, the D -state probability depends on the resolution. This indicates that the D -state probability of the deuteron is not an observable. We return to the phase shifts with a low-pass filter problem in Fig. 1.17b. We see that when the low-pass filter is applied to the SRG evolved potential, it reproduces the unevolved phase shifts up to the cut-off energy of the filter. This discussion also makes it clear that the nuclear potential itself is not an observable and there is no “correct” nuclear potential. In fact, there is more than one “correct” potential. For instance, all the potentials in Fig. 1.15 give the same values for observables such as binding energies, phase shifts, etc.

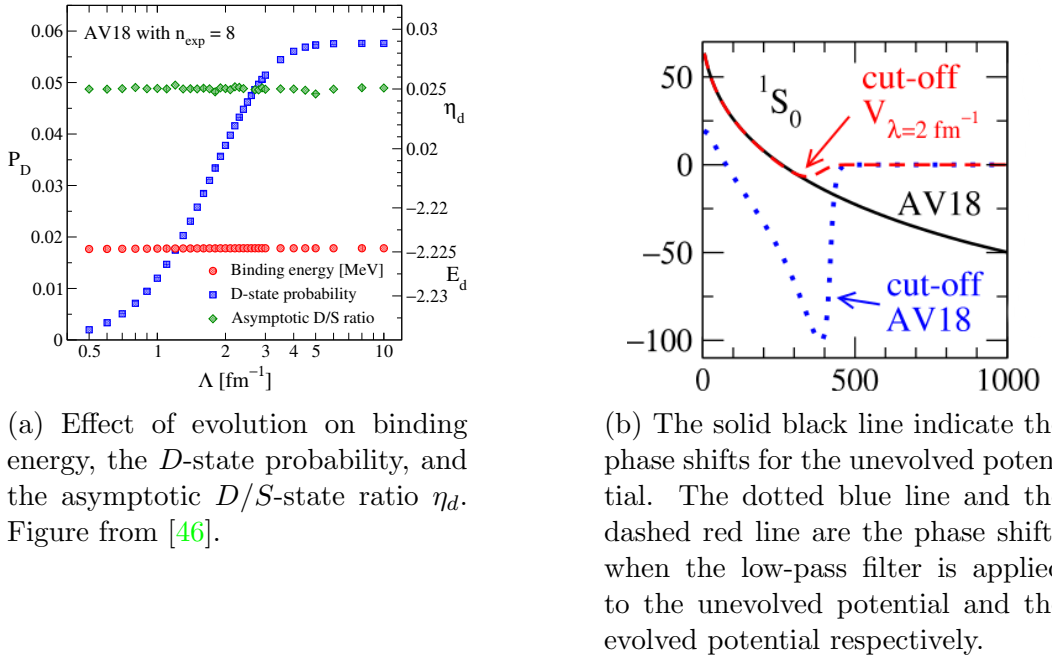


Figure 1.17: Effect of RG evolution on (non-)observables.

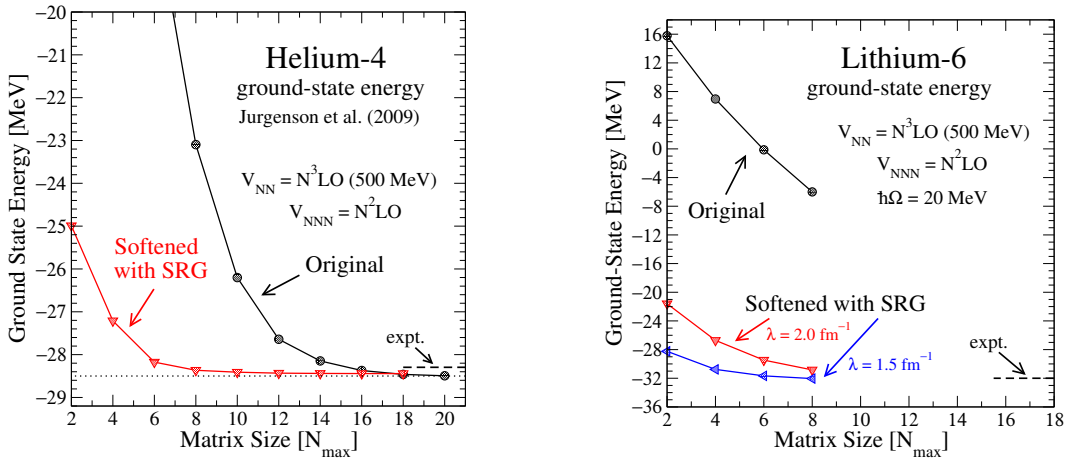


Figure 1.18: SRG evolution greatly accelerates the convergence in many-body calculations. Figure from [45].

Since the SRG evolved potentials only have low-momentum modes, they are amenable to numerical calculations. As seen in Fig. 1.18, SRG evolution greatly accelerates the convergence in many-body calculations.

We note that even when we start with just two-body forces, SRG evolution introduces three- and higher-body forces. This can be understood from the flow equation (Eq. 1.16)

$$\begin{aligned}\frac{d\hat{H}_s}{ds} &= \left[\sum_{\hat{G}_s} \underbrace{a^\dagger a}_{\text{2-body}}, \sum_{\text{2-body}} \underbrace{a^\dagger a^\dagger aa}_{\text{2-body}}, \sum_{\text{2-body}} \underbrace{a^\dagger a^\dagger aa}_{\text{2-body}} \right] \\ &= \cdots + \sum_{\text{3-body}} \underbrace{a^\dagger a^\dagger a^\dagger aaa}_{\text{3-body}} + \cdots\end{aligned}\quad (1.19)$$

The second equality in Eq. 1.19 demonstrates how the commutators give rise to three- and higher-body (up to A -body) forces. The initial potential in Fig. 1.18 includes both two- and three-body forces; it has been demonstrated that 3-body forces are crucial in getting the correct experimental values from theory [52]. To keep the invariance of energy with respect to the resolution scale (as in Fig. 1.17a), it is important to keep also the induced 3-body forces [27]. A major development in the SRG technology has been the ability to consistently evolve three-body forces [53, 54].

A related important development is that of In-Medium SRG (IM-SRG) [39]. IM-SRG uses a reference state $|\Phi\rangle$ which is different from the particle vacuum $|0\rangle$ used in SRG. For example, Φ can be a Slater determinant that is fair approximation to nucleus' ground state. Just like in SRG, IM-SRG then uses a series of unitary transformations to decouple the reference state from excitations. IM-SRG also maintains the hierarchy of many-body forces, namely $2N \gg 3N \gg 4N \dots$.

RG techniques have made possible calculations of medium-mass nuclei starting from inter-nucleonic interactions. However, if we keep pushing the calculations to

higher-mass nuclei, we run into the same problem as indicated in Fig. 1.8b, i.e, we run out of computational power before we reach convergence. So, along with RG techniques we also need reliable extrapolation techniques that will allow us to extrapolate the results from finite N_{\max} to $N_{\max} = \infty$. This problem will form the basis of Chapter 2.

1.6 Path forward for LENP

We have seen that nuclear theory has come a long way from the pion theories of the 1940's. The focus these days is on doing precision calculations and making reliable predictions. The tool box of a nuclear theorist includes a wide variety of techniques. In most cases, different techniques have complimentary strengths. In other cases, alternative methods provide a means to cross-check answers. Having made great strides in the evaluation of the bound state properties, the push recently has been on calculating resonant and scattering states, and using the improved understanding of nuclear structure to study nuclear reactions.

To pick a particular example, let's focus on the neutrinoless double beta decay ($0\nu\beta\beta$) example. $0\nu\beta\beta$ is of wide interest because of its potential to shed light on the nature of neutrinos (i.e, if neutrino is a Majorana or a Dirac fermion). $0\nu\beta\beta$ has not been observed yet and there are experiments around the world looking for this decay [55]. The experiments need guidance from theory to help design the experiment and to interpret the measurements. The theoretical calculation of $0\nu\beta\beta$ cross section involves computing a nuclear matrix element for the transition. Figure 1.19 indicates the current level of agreement for calculations from different methods. We see that these results differ by a factor of two. The reaction cross section is proportional to

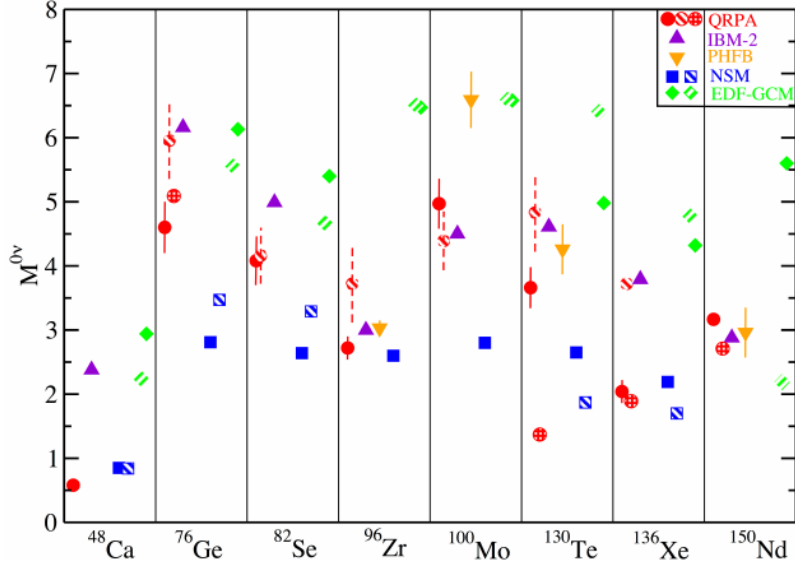


Figure 1.19: Nuclear matrix element for $0\nu\beta\beta$ for various nuclei calculated using different methods. The legends indicate the different methods used for calculations. Figure from a talk by Petr Vogel.

the matrix element squared, and therefore the current level of agreement translates to an uncertainty of factor four in the cost of the experiment.

We thus see that it is important that the theoretical calculations are accompanied by a reliable uncertainty estimate. The sources of uncertainty in a theoretical calculation can broadly be classified into two categories—uncertainty in the input (e.g., shortcomings in the potential, limitations of the assumptions made, etc.) and uncertainty arising from the method (e.g., errors due to various approximations made while solving). As presented in the next section, the work in this thesis focuses on investigating two common sources of uncertainties.

1.7 Thesis organization

The next two chapters in this thesis will present the author’s original work as a PhD student. As demonstrated in Fig. 1.8b, we often run out of computational power before the convergence is reached, necessitating a need for trustworthy extrapolation schemes. Chapter 2 describes our published work in this regard [56–58]. The extrapolation schemes we developed were physically motivated as opposed to phenomenological forms previously in use. The author of this thesis was a lead author on Ref. [56]. All authors of Ref. [57] contributed equally. We will therefore look in detail at the results presented in Refs. [56, 57] in this thesis. The author’s contribution to work presented in Ref. [58] was secondary, and hence only the summary from that work will be presented.

Theoretical calculations of nuclear cross sections involve evaluating nuclear structure (which involves description of the initial and final state) and nuclear reaction (which involves a description of the probe). To make accurate predictions, it is important to understand the uncertainty stemming from the renormalization scale and scheme dependence of nuclear structure and reaction components. We address this problem in Chapter 3 by using the SRG to look at the scale dependence of deuteron electrodisintegration. This effort was led by the author and has been published in Ref. [59].

Both these projects were the first of its kind, and are fertile grounds for further development. In fact, the work presented in Chapter 2 has already had a lot of impact as testified by the number of articles citing our publications. We believe that the work in Chapter 3 will also receive wide attention soon. We present the details

of our calculations in Appendix, which would enable anyone interested to reproduce our results.

Chapter 2: Extrapolation

As we have seen in the introduction, the harmonic oscillator (HO) basis is routinely used in low-energy nuclear physics (LENP) calculations. We also saw that the size of Hamiltonian matrix that we need to diagonalize grows factorially with the number of nucleons (cf. Fig. 1.9), severely restricting the number of terms that can be kept in the basis expansion. The single particle nuclear wave function with the N_{\max} truncation introduced in Chapter 1 is given by

$$\psi_{N_{\max}}^{\Omega}(r) = \sum_{\alpha=0}^{N_{\max}} c_{\alpha} \varphi_{\alpha}^{\Omega}(r) . \quad (2.1)$$

$\varphi_{\alpha}^{\Omega}(r)$ in Eq. 2.1 are the HO wave functions; Ω is the frequency of the HO ⁵. For reference, the S -wave HO wave function is given by

$$\varphi_{\alpha}^{\Omega}(r) = \mathcal{N} e^{-\frac{\mu\Omega}{2\hbar}r^2} L_{\alpha}^{1/2}\left(\frac{\mu\Omega}{\hbar}r^2\right) , \quad (2.2)$$

where \mathcal{N} is the normalization constant, μ is the reduced mass, and $L_{\alpha}^{1/2}$ denotes the generalized Laguerre polynomial.

The energy obtained in the HO basis— $E(N_{\max}, \Omega)$ —is a function of N_{\max} and Ω . This is illustrated in Fig. 2.1. We see that as we go to higher N_{\max} , the curves get flatter with respect to Ω , or in other words the dependence on Ω drops out.

⁵ In LENP, the oscillator frequency is often denoted by Ω rather than ω .

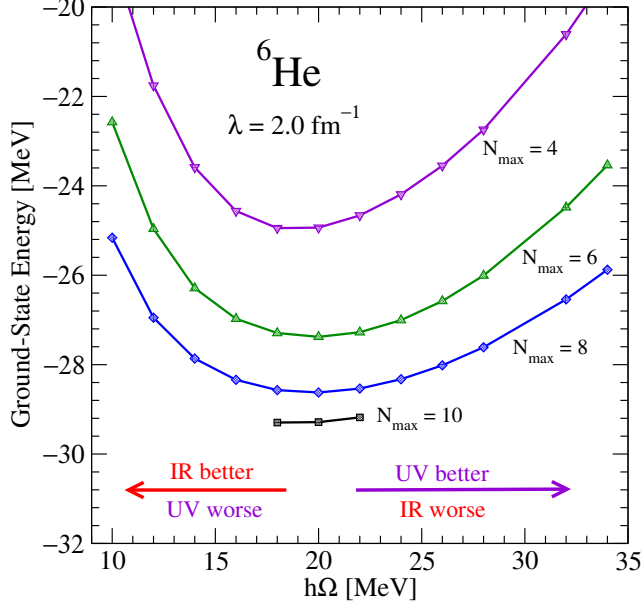


Figure 2.1: Ground state energy for ${}^6\text{He}$ as a function of N_{\max} and Ω . Figure taken from [60].

The goal is to extrapolate to $N_{\max} = \infty$ from a finite N_{\max} . The most widely used extrapolation scheme employs an exponential in N_{\max} form

$$E(N_{\max}) = E_{\infty} + ae^{-cN_{\max}}, \quad (2.3)$$

where a and c are determined separately for each $\hbar\Omega$ (with the option of constraining the fit to get the same asymptotic E_{∞} value). Figure 2.2 shows estimate for the ground state energy for ${}^6\text{He}$ obtained using the extrapolation form of Eq. 2.3.

The exponential in N_{\max} extrapolation is widely used in literature and seems to work quite well [30, 31, 62–64]. There are however many open questions about this extrapolation scheme such as the answer for E_{∞} depends on the oscillator frequency Ω and it is not clear which is the best choice for Ω . The terms a and c in Eq. 2.3 are fit to data. There is no way to extract these terms for one nucleus and use it

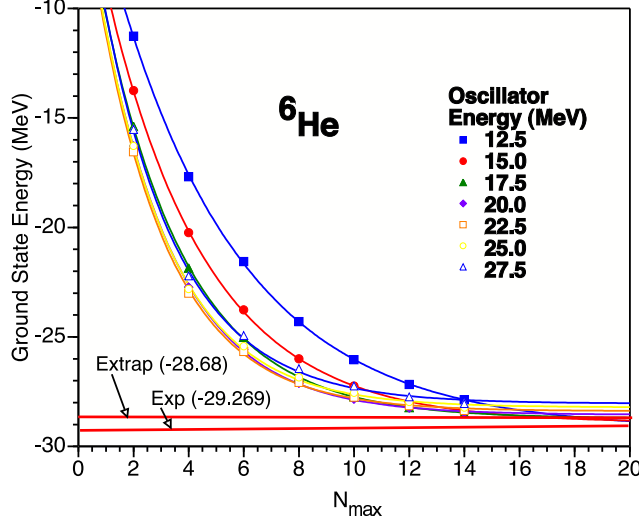


Figure 2.2: The estimate for exact ${}^6\text{He}$ ground state energy using Eq. 2.3. Extrapolated answer from the constrained fit and the experimental binding energy are indicated by horizontal lines. Figure from [61].

to predict something else. Moreover, the physical motivation for an exponential in N_{\max} extrapolation is slim at best. It has been claimed that for larger nuclei N_{\max} is a logarithmic measure of the number of states [63]. This would account for the exponential behavior, but there is no demonstration that it follows in general or with a specific logarithmic dependence.

An alternative approach to extrapolations is motivated by effective field theory (EFT) and based instead on explicitly considering the infrared (IR) and ultraviolet (UV) cutoffs imposed by a finite oscillator basis [65]. The truncation in the oscillator basis introduces a maximum length scale (or an IR cutoff) and also a maximum momentum scale (or an UV cutoff). These length and momentum scales can be motivated by the classical turning points denoted by L_0 and Λ_0 respectively. We have

$$L_0 = \sqrt{2(N_{\max} + 3/2)}b ,$$

$$\Lambda_0 = \sqrt{2(N_{\max} + 3/2)}\hbar/b . \quad (2.4)$$

b is the oscillator length given by $b = \sqrt{\hbar/m\Omega}$. The errors due the finite IR (UV) cutoff are called the IR (UV) errors. To draw a lattice analogy, IR errors stem from the finite box size, and the UV errors are a result of the finite lattice spacing (or the graininess of the lattice). Ideally, we would like the box size to be as large as possible and the lattice spacing to be as small as possible. Because of finite computational power, this is not always possible though and therefore we need reliable extrapolation schemes in both IR as well as UV.

This approach of thinking of the HO truncation in terms of IR and UV cutoffs has led to lot of development in the past three years. Note that b appears in the numerator for L_0 and in the denominator for Λ_0 , so it is not possible to make both cutoffs large simultaneously. We can choose the oscillator parameters such that one of the cutoffs in Eqs. 2.4 is large, making the errors due to that cutoff small and focus on the errors due to the other cutoff. The first attempt and test for a theoretically motivated IR correction was made in [60]. These corrections were made theoretically sound in [56, 57]. In [58] we looked at the UV correction for the deuteron. Our papers [56–58] have led to physically motivated extrapolation schemes and will form the basis of the next two sections. Insights from our work have also led to development of extrapolation schemes (both in IR and UV) for the many-body case by other groups. We will touch upon these developments in Subsec. 2.3.1.

2.1 Infrared story ⁶

As mentioned in the introduction, there was a lack of well motivated extrapolation schemes in LENP and this is where our work comes in. We started with the two-body case because it is more tractable mathematically. Note that extrapolation is usually not necessary for the two-body problem, because convergence is reached before we run out of computational power. This allows us to test our extrapolation formulas. Once we establish that the approach works for the two-body case, we can hope to extend the approach to few- and many-body case.

As mentioned earlier, IR cutoff effectively puts system in a finite box. We need to find appropriate box length such that

$$E(N_{\max}) = E(L_{\text{box}}) . \quad (2.5)$$

Note that our original problem was to find $E_{\infty} \equiv E(N_{\max} = \infty)$ given E at a finite N_{\max} . Once we make the correspondence in Eq. 2.5 and express energy as a function of box length, we can use various techniques (discussed later) to estimate $E(L_{\text{box}} = \infty)$ which equals $E(N_{\max} = \infty)$.

2.1.1 Tale of tails

The box size is usually bigger than the range of the potential. Thus imposing the IR cutoff modifies the asymptotic part (or tail) of the bound-state wave function. Our early work focused on trying to estimate the appropriate box size by matching the tails of wave functions in the truncated HO basis to the tails of wave functions in boxes of different lengths.

⁶Based on [56] and [57]

Our strategy was to use a range of model potentials for which the Schrödinger equation can be solved analytically or to any desired precision numerically to broadly test and illustrate various features, and then turn to the deuteron for a real-world example. In particular we considered:

$$V_{\text{sw}}(r) = -V_0 \theta(R - r) \quad [\text{square well}] , \quad (2.6)$$

$$V_{\text{exp}}(r) = -V_0 e^{-(r/R)} \quad [\text{exponential}] , \quad (2.7)$$

$$V_{\text{g}}(r) = -V_0 e^{-(r/R)^2} \quad [\text{Gaussian}] , \quad (2.8)$$

$$V_{\text{q}}(r) = -V_0 e^{-(r/R)^4} \quad [\text{quartic}] , \quad (2.9)$$

where for each of the models we work in units with $\hbar = 1$, reduced mass $\mu = 1$, and $R = 1$, but consider different values for V_0 . For the realistic potential we use the Entem-Machleidt 500 MeV chiral EFT N³LO potential [66] and unitarily evolve it with the similarity renormalization group (SRG). These potentials provide a diverse set of tests for universal properties. Because we can go to very high $\hbar\Omega$ and N_{\max} for the two-particle bound states (and therefore large Λ_{UV}), it is possible to always ensure that UV corrections are negligible.

We start with empirical considerations before presenting an analytical understanding. An example of how this correspondence between the HO truncation and a hard wall at specific length plays out is presented in Fig. 2.3. In the top panel, the exact ground-state radial wave function (dashed) for the square well in Eq. 2.6 is compared to the solution in an oscillator basis truncated at $N_{\max} = 4$ determined by diagonalization (solid). The truncated basis cuts off the tail of the exact wave function because the individual basis wave functions have a radial extent that depends on $\hbar\Omega$

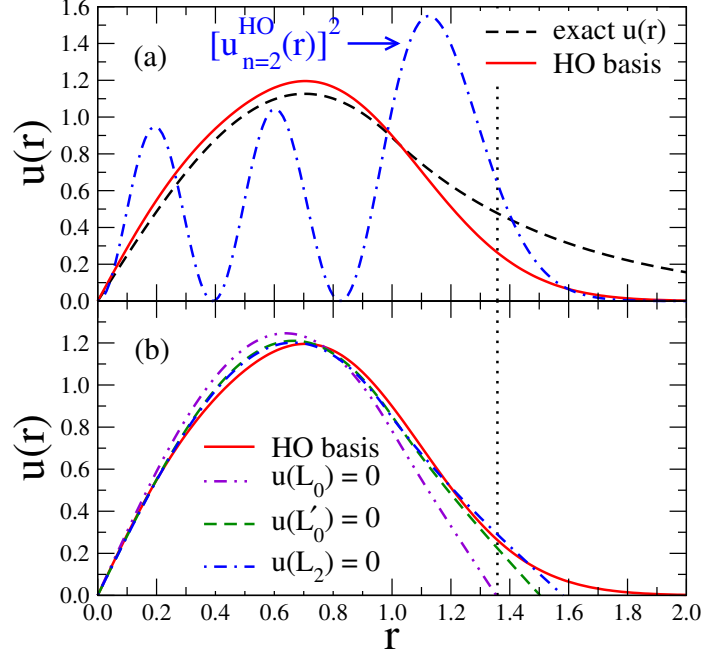


Figure 2.3: (a) The exact radial wave function (dashed) for a square well Eq. 2.6 with depth $V_0 = 4$ (and $\hbar = \mu = R = 1$) is compared to the wave function obtained from an HO basis truncated at $N_{\max} = 4$ with $\hbar\Omega = 6$ (solid). The spatial extent of the wave function obtained from the HO basis truncation is dictated by the square of HO wave function for the highest radial quantum number (dot-dashed). (b) The wave functions obtained from imposing a Dirichlet boundary condition (bc) at L_0 , L'_0 and L_2 are compared to the wave function in truncated HO basis.

(from the Gaussian part; cf. Eq. 2.2) and on the largest power of r (from the polynomial part). The latter is given by $N_{\max} = 2n + l$. With $N_{\max} = 4$ and $l = 0$, this means that $n = 2$ gives the largest power.

The cutoff will then be determined by the $n = 2$ oscillator wave function, $u_{n=2}^{\text{HO}}(r)$, whose square (which is the relevant quantity) is also plotted in the top panel (dot-dashed). It is evident that the tail of the wave function in the truncated basis is fixed by this squared wave function. Our premise is that the HO truncation is well modeled by a hard-wall (Dirichlet) bc at $r = L$. If so, the question remains how best

to *quantitatively* determine L given N_{\max} and $\hbar\Omega$. In the bottom panel of Fig. 2.3 we show the wave functions for several possible choices for L . L_0 corresponds to choosing the classical turning point (i.e. the half-height point of the tail of $[u_{n=2}^{HO}(r)]^2$); it is manifestly too small. The authors of [60] advocated an improved choice for L given by

$$L'_0 = L_0 + 0.54437 b (L_0/b)^{-1/3}. \quad (2.10)$$

The length L'_0 in Eq. 2.10 is obtained by linear extrapolation from the slope at the half-height point. However, choosing

$$L = L_2 \equiv \sqrt{2(N_{\max} + 3/2 + 2)}b \quad (2.11)$$

was found to work the best in almost all examples.

The most direct illustration of this conclusion comes from the bound-state energies. In the example in Fig. 2.3, the exact energy (in dimensionless units) is -1.51 while the result for the basis truncated at $N_{\max} = 4$ is -1.33 , which is therefore what we hope to reproduce. With L_0 , the energy is -0.97 , with L'_0 it is -1.21 , and with L_2 it is -1.29 . While this is only one example of a model problem, we have found that L_2 always gives a better energy estimate than L'_0 (and something like $L_3 \equiv \sqrt{2(N_{\max} + 3/2 + 3)}b$ is almost always worse).

Another signature that demonstrates the suitability of L_2 is that points from many different $\hbar\Omega$ and N_{\max} values all lie on the same curve. Figures 2.4 and 2.5 show the energies from a wide range of HO truncations for L_0 , L'_0 and L_2 for the Gaussian well and the square well potential, respectively. The energies for different $\hbar\Omega$ and N_{\max} lie on the same smooth and unbroken curve if we use L_2 but not with the other choices. For $L = L_0$ and $L = L'_0$, one finds that sets of points with different $\hbar\Omega$

but same N_{\max} fall on smooth, N_{\max} -dependent curves. For the square well, there are small discontinuities visible even for $L = L_2$. At the square well radius, the wave function's second derivative is not smooth, and this is difficult to approximate with a finite set of oscillator functions. This lack of UV convergence is likely the origin of the very small discontinuities. As a further test, we solve the Schrödinger

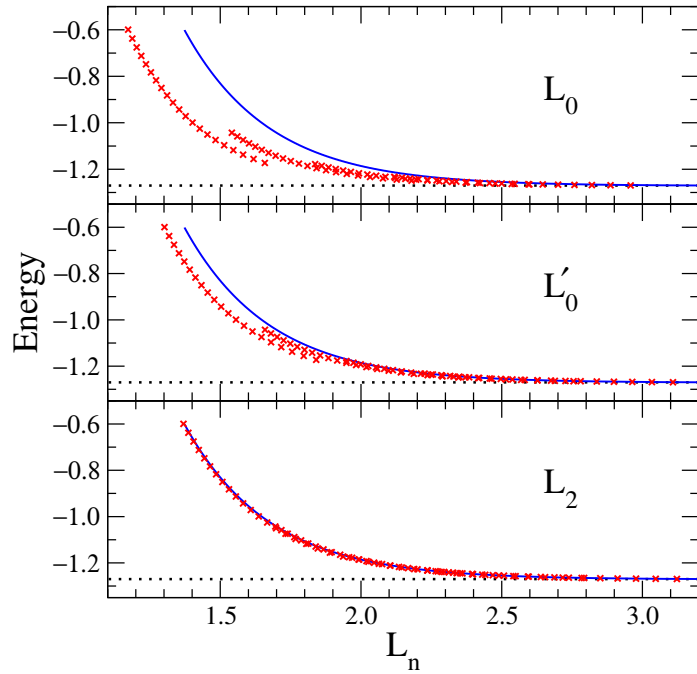


Figure 2.4: Ground-state energies versus L_0 (top), L'_0 (middle), and L_2 (bottom) for a Gaussian potential well Eq. 2.8 with $V_0 = 5$ and $R = 1$. The crosses are the energies from HO basis truncation. The energies obtained by numerically solving the Schrödinger equation with a Dirichlet bc at L lie on the solid line. The horizontal dotted lines mark the exact energy $E_\infty = -1.27$.

equation with a vanishing Dirichlet bc (solid lines in Figs. 2.4 and 2.5), and compare to the energies obtained from the HO truncations (crosses). The finite oscillator basis energies are well approximated by a Dirichlet bc with a mapping from the oscillator

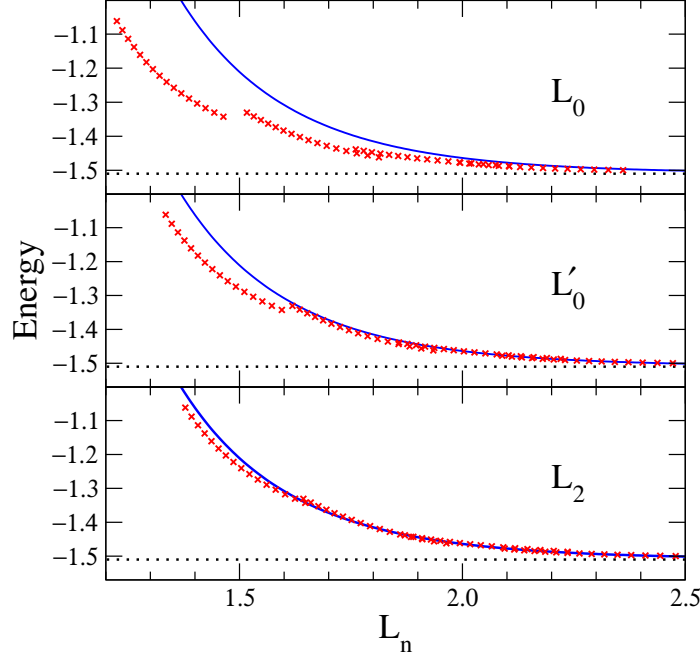


Figure 2.5: Ground-state energies versus L_0 (top), L'_0 (middle), and L_2 (bottom) for a square well potential well Eq. 2.6 with $V_0 = 4$ and $R = 1$. The crosses are the energies from HO basis truncation. The energies obtained by numerically solving the Schrödinger equation with a Dirichlet bc at L lie on the solid line. The horizontal dotted lines mark the exact energy $E_\infty = -1.51$.

$\hbar\Omega$ and N_{\max} to an equivalent length given by L_2 . Note that for large N_{\max} , the differences between L_0 , L'_0 and L_2 may be smaller than other uncertainties involved in nuclear calculations, but for practical calculations one will want to use small N_{\max} results, where these considerations are very relevant.

These results from model calculations are consistent with those from realistic potentials applied to the deuteron. To illustrate this, we use the N³LO 500 MeV potential of Entem and Machleidt [66]. We generate results in an HO basis with $\hbar\Omega$ ranging from 1 to 100 MeV and N_{\max} from 4 to 100 (in steps of 4 to avoid HO artifacts for the deuteron [63]). We then restrict the data to where UV corrections

are negligible (see Section 2.2). Figure 2.6 shows that the criterion of a continuous

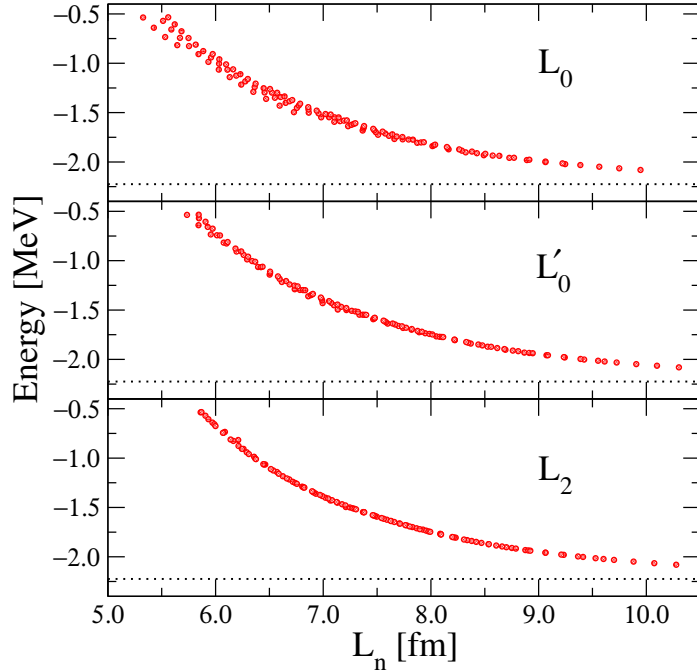


Figure 2.6: Ground-state energies versus L_0 (top), L'_0 (middle), and L_2 (bottom) for the Entem-Machleidt 500 MeV N^3LO potential [66]. The horizontal dotted lines mark the exact energy $E_\infty = -2.2246$ MeV.

curve with the smallest spread of points clearly favors L_2 .

Analytical derivation of L_2

In the asymptotic region (this is the region where IR cutoff is imposed), the potential is negligible and the only relevant part of the Hamiltonian is the kinetic energy or the p^2 operator. In what follows, we analytically compute the smallest eigenvalue κ_{\min}^2 of p^2 in a finite oscillator basis and will see that $\kappa_{\min} = \pi/L_2$. In the remainder of this Subsection, we set the oscillator length to one. We focus on s -waves and thus consider wave functions that are regular at the origin, i.e. the radial wave

functions are identical to the odd wave functions of the one-dimensional harmonic oscillator.

The localized eigenfunction of the operator p^2 with smallest eigenvalue κ^2 is

$$\psi_\kappa(r) = \begin{cases} \sin \kappa r, & 0 \leq r \leq \frac{\pi}{\kappa} \\ 0, & r > \frac{\pi}{\kappa} \end{cases}. \quad (2.12)$$

We employ the s -wave oscillator functions

$$\begin{aligned} \varphi_{2n+1}(r) &= (-1)^n \sqrt{\frac{2n!}{\Gamma(n+3/2)}} r L_n^{1/2}(r^2) e^{-\frac{r^2}{2}} \\ &= \left(\pi^{1/2} 2^{2n} (2n+1)! \right)^{-1/2} H_{2n+1}(r) e^{-\frac{r^2}{2}}, \end{aligned} \quad (2.13)$$

with energy $E = (2n+3/2)\hbar\Omega$. Here, $L_n^{1/2}$ denotes the Laguerre polynomial, and it is convenient to rewrite this function in terms of the Hermite polynomial H_n . We expand the eigenfunction in Eq. 2.12 as

$$\psi_\kappa(r) = \sum_{n=0}^{\infty} c_{2n+1}(\kappa) \varphi_{2n+1}(r). \quad (2.14)$$

Before we turn to the computation of the expansion coefficients $c_{2n+1}(\kappa)$, we consider the eigenvalue problem for the operator p^2 . We have

$$p^2 = a^\dagger a + \frac{1}{2} - \frac{1}{2} \left(a^2 + (a^\dagger)^2 \right), \quad (2.15)$$

where a and a^\dagger denote the annihilation and creation operator for the one-dimensional harmonic oscillator, respectively. The matrix of p^2 is tridiagonal in the oscillator basis. For the matrix representation, we order the basis states as $(\varphi_1, \varphi_3, \varphi_5, \dots)$. Thus, the eigenvalue problem $p^2 - \kappa^2 = 0$ becomes a set of rows of coupled linear equations. In an infinite basis, the eigenvector $(c_1(\kappa), c_3(\kappa), c_5(\kappa), \dots)$ identically satisfies every row of the eigenvalue problem for any value of κ . In a finite basis $(\varphi_1, \varphi_3, \varphi_5, \dots, \varphi_{2n+1})$, however, the last row of the eigenvalue problem

$$(2n+3/2 - \kappa^2) c_{2n+1}(\kappa) = \frac{1}{2} \sqrt{2n} \sqrt{2n+1} c_{2n-1}(\kappa), \quad (2.16)$$

can only be fulfilled for certain values of κ , and this is the quantization condition. To solve this eigenvalue problem we need expressions for the expansion coefficients $c_{2n+1}(\kappa)$ for $n \gg 1$. Those can be derived analytically as follows.

We rewrite the eigenfunction in Eq. 2.12 as a Fourier transform

$$\psi_\kappa(r) = \sqrt{\frac{2}{\pi}} \int_0^\infty dk \tilde{\psi}_\kappa(k) \sin kr , \quad (2.17)$$

and expand the sine function in terms of oscillator functions as

$$\sin kr = \sqrt{\frac{\pi}{2}} \sum_{n=0}^{\infty} (-1)^n \varphi_{2n+1}(r) \varphi_{2n+1}(k) . \quad (2.18)$$

Thus, the expansion coefficients in Eq. 2.14 are given in terms of the Fourier transform $\tilde{\psi}_\kappa(k)$ as

$$c_{2n+1}(\kappa) = (-1)^n \int_0^\infty dk \tilde{\psi}_\kappa(k) \varphi_{2n+1}(k) . \quad (2.19)$$

So far, all manipulations have been exact. We need an expression for $c_{2n+1}(\kappa)$ for $n \gg 1$ and use the asymptotic expansion

$$\varphi_{2n+1}(k) \approx \frac{(-1)^n \sqrt{2}}{\pi^{1/4}} \frac{(2n-1)!!}{\sqrt{(2n)!}} \sin(\sqrt{4n+3}k) , \quad (2.20)$$

which is valid for $|k| \ll \sqrt{2n}$, see [67]. Using this approximation, one finds (making use of Fourier transforms)

$$\begin{aligned} c_{2n+1}(\kappa) &\approx \pi^{1/4} \frac{(2n-1)!!}{\sqrt{(2n)!}} \psi_\kappa(\sqrt{4n+3}) \\ &= \pi^{1/4} \frac{(2n-1)!!}{\sqrt{(2n)!}} \sin(\sqrt{4n+3}\kappa) , \end{aligned} \quad (2.21)$$

with $\kappa \leq \pi/\sqrt{4n+3}$ due to Eq. 2.12.

Let us return to the solution of the quantization condition in Eq. 2.16. We make the ansatz

$$\kappa = \frac{\pi}{\sqrt{4n+3+2\Delta}} , \quad (2.22)$$

and must assume that $\Delta > 0$. This ansatz is well motivated, since the naive semi-classical estimate $\kappa = \pi/L_0$ yields $\Delta = 0$. We insert the expansion coefficients of Eq. 2.21 into Eq. 2.16 and consider its leading-order approximation for $n \gg 1$ and $n \gg \Delta$. This yields

$$\Delta = 2 \tag{2.23}$$

as the solution. Recalling that a truncation of the basis at φ_{2n+1} corresponds to the maximum energy $E = (2n + 3/2)\hbar\Omega$, we see that we must identify $N_{\max} \equiv N = 2n$. Thus, $\kappa_{\min} = \pi/L_2$ is the lowest momentum in a finite oscillator basis with $n \gg 1$ basis states (and not $1/b$ as stated in Ref. [65]). It is clear from its very definition that π/L_2 is also (a very precise approximation of) the infrared cutoff in a finite oscillator basis, and that L_2 (and not b as stated in Refs. [68, 69]) is the radial extent of the oscillator basis and the analog to the extent of the lattice in the lattice computations [70].

The derivation of our key result $\kappa_{\min} = \pi/L_2$ is based on the assumption that the number of shells N fulfills $N \gg 1$. Table 2.1 shows a comparison of numerical results for κ_{\min} in different model spaces. We see that π/L_2 is a very good approximation already for $N = 2$, with a deviation of about 1%.

Note that this approach can be generalized to other localized bases. The (numerical) computation of the lowest eigenvalue of the momentum operator p^2 yields the box size L corresponding to the employed Hilbert space.

EFT-like approach

We mentioned that the relevant operator for IR truncation is p^2 . To get a better understanding of the correspondence between the HO truncation and a hard wall at L_2 , let's compare the spectrum of p^2 in the two cases. In Fig. 2.7, we compare the

N	κ_{\min}	π/L_2	π/L_0
0	1.2247	1.1874	1.8138
2	0.9586	0.9472	1.1874
4	0.8163	0.8112	0.9472
6	0.7236	0.7207	0.8112
8	0.6568	0.6551	0.7207
10	0.6058	0.6046	0.6551
12	0.5651	0.5642	0.6046
14	0.5316	0.5310	0.5642
16	0.5035	0.5031	0.5310
18	0.4795	0.4791	0.5031
20	0.4585	0.4582	0.4791

Table 2.1: Comparison between the lowest momentum κ_{\min} , π/L_2 , and π/L_0 for model spaces with up to N oscillator quanta.

low-lying eigenfunctions of p^2 in the truncated HO basis to the eigenfunctions in a box of size L_2 . As we will see later, the asymptotic or near the wall difference between the two eigenfunctions are high-momentum effects irrelevant for the long-wavelength physics of the bound states.

Another way to look at this is to compute the number $M(k)$ of (*s*-wave) states up to a momentum k . We find

$$\begin{aligned} M(k) &= \text{Tr} \left[\Theta(\hbar^2 k^2 - p^2) \Theta \left(E - \frac{p^2}{2m} - \frac{m}{2} \Omega^2 r^2 \right) \right] \\ &\approx \frac{1}{2\pi\hbar} \int_{-\hbar k}^{\hbar k} dp \int_0^\infty dr \Theta(\hbar^2 k^2 - p^2) \Theta \left(E - \frac{p^2}{2m} - \frac{m}{2} \Omega^2 r^2 \right). \end{aligned} \quad (2.24)$$

Here, we apply the semiclassical approximation and write the trace as a phase-space integral. We assume $\hbar^2 k^2/(2m) \leq E$, perform the integrations and use $E/(\hbar\Omega) = N + 3/2$ ⁷. This yields

⁷For the sake of brevity we replace N_{\max} by N

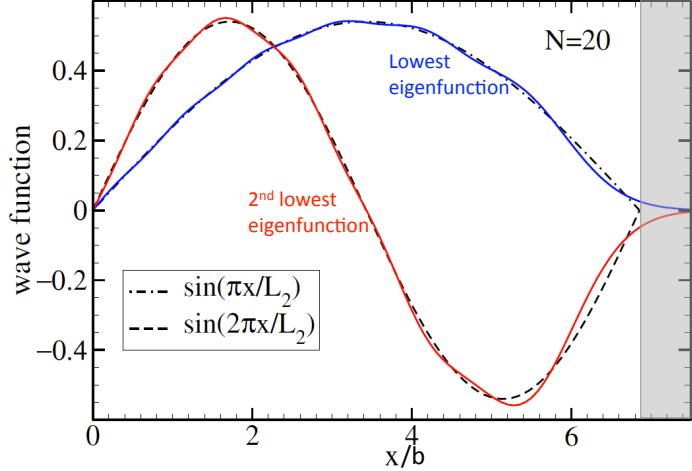


Figure 2.7: Eigenfunctions of p^2 in the truncated HO basis compared to those in a box of size L_2 .

$$M(k) = \frac{bk}{2\pi} \sqrt{2N + 3 - b^2 k^2} + \frac{N + 3/2}{\pi} \arcsin \frac{bk}{\sqrt{2N + 3}} , \quad (2.25)$$

where b is the oscillator length. Figure 2.8 shows a comparison between the quantum mechanical staircase function and the semiclassical estimate of Eq. 2.25 for $N = 32$. For sufficiently small values of $kb \ll \sqrt{2N}$, the number of s -wave momentum eigenstates grows linearly, and inspection of Eq. 2.25 shows that the slope at the origin is L_0/π semiclassically. The linear growth of the number of eigenstates of p^2 with k clearly demonstrate that — at not too large values of kb — the spectrum of p^2 in the oscillator basis is similar to the spectrum of p^2 in a spherical box.

As a final example of the correspondence between the HO truncation and the hard wall at L_2 , we look at the ground state wave functions of a square well in the two bases in Fig. 2.9. The binding momentum in this case is 1.7 (in units of $1/R$). The Fourier-transformed wave functions differ at much larger momentum and this difference is irrelevant for the long-wavelength physics of bound states. Thus the

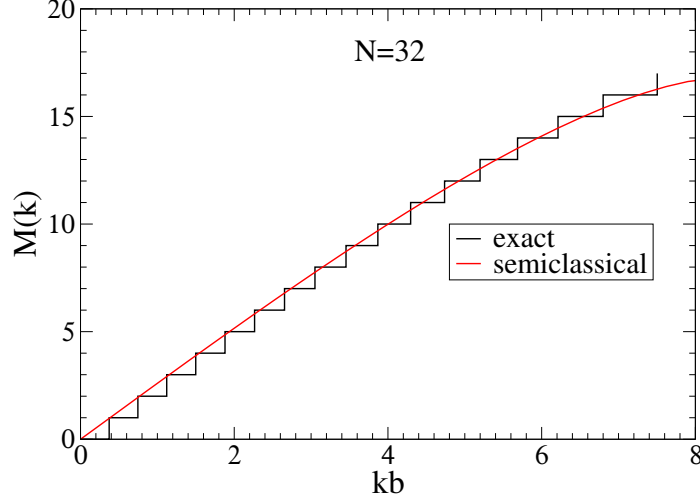


Figure 2.8: The staircase function of the s states of the operator p^2 in a finite oscillator basis with $N = 32$ (black) compared to its semiclassical estimate (smooth red curve). $M(k)$ denotes the number of states of the operator p^2 with eigenvalues $p^2 \leq \hbar^2 k^2$.

use of Dirichlet bc to take into account the HO truncation is similar in spirit to the use of contact interactions to describe the effect of unknown short-ranged forces on long-wavelength probes.

2.1.2 Cashing in on the hard wall correspondence

We have so far focused on establishing how HO truncation is analogous to putting the system in a spherical box of a specified radius. Now let's see how this correspondence helps us in getting the exact energy E_∞ .

Linear energy method

Our first approximation to the IR correction is based on what is known in quantum chemistry as the linear energy method [71]. Given a hard-wall bc at $r = L$ beyond the range of the potential, we write the energy compared to that for $L = \infty$ as

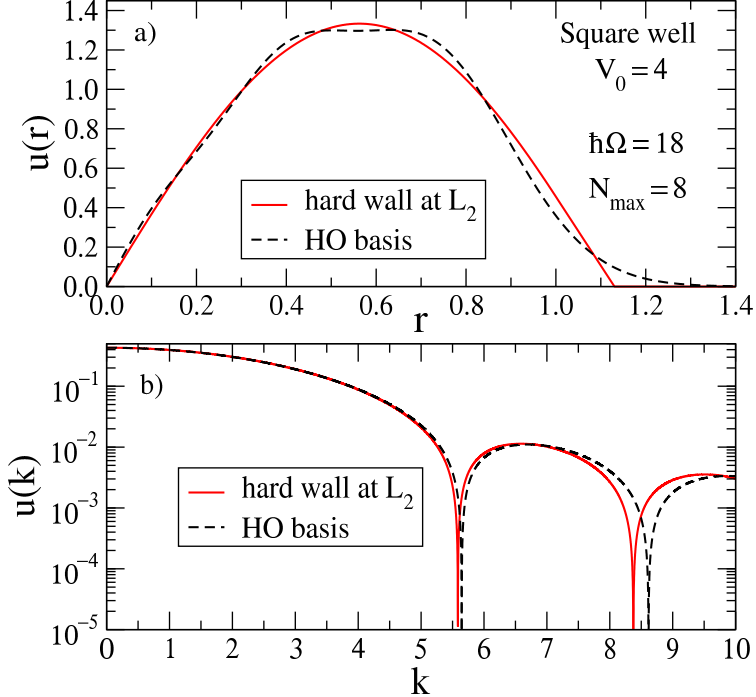


Figure 2.9: Ground-state wave functions for a square well potential of depth $V_0 = 4$ (see Eq. 2.6; lengths are in units of R and energies in units of $1/R^2$ with $\hbar^2/\mu = 1$) from solving the Schrödinger equation with a truncated harmonic oscillator basis with $\hbar\Omega = 18$ and $N = 8$ (dashed) and with a Dirichlet bc at $r = L_2$ given from Eq. 2.113 (solid). The coordinate-space radial wave functions in a) exhibit a difference at r near 1.5, but the Fourier-transformed wave functions in b) are in close agreement at low k , showing that the differences are high-momentum modes.

$$E_L = E_\infty + \Delta E_L . \quad (2.26)$$

We seek an estimate for ΔE_L , which is assumed to be small, based on an expansion of the wave function in ΔE_L . Let $u_E(r)$ be a radial solution with regular bc at the origin and energy E . For convenience in using standard quantum scattering formalism below, we choose the normalization corresponding to what is called the “regular solution” in Ref. [72], which means that $u_E(0) = 0$ and the slope at the origin is unity for all E . We denote the particular solutions $u_{E_L}(r) \equiv u_L(r)$ and

$u_{E_\infty}(r) \equiv u_\infty(r)$. Then there is a smooth expansion of u_E about $E = E_\infty$ at fixed r , so we approximate [71]

$$u_L(r) \approx u_\infty(r) + \Delta E_L \left. \frac{du_E(r)}{dE} \right|_{E_\infty} + \mathcal{O}(\Delta E_L^2), \quad (2.27)$$

for $r \leq L$. By evaluating Eq. 2.27 at $r = L$ with the bc $u_L(L) = 0$, we find

$$\Delta E_L \approx -u_\infty(L) \left(\left. \frac{du_E(L)}{dE} \right|_{E_\infty} \right)^{-1}, \quad (2.28)$$

which is the estimate for the IR correction.

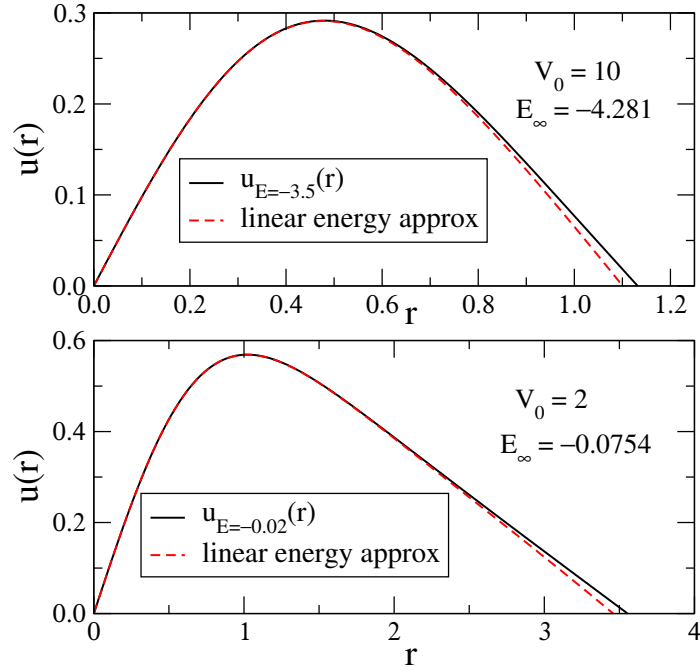


Figure 2.10: Testing the linear energy approximation Eq. 2.27 for (a) deep ($V_0 = 10$) and (b) shallow ($V_0 = 2$) Gaussian potential well Eq. 2.8 ($\hbar = \mu = R = 1$). The solid lines are the exact solutions $u_L(r)$ for energies -3.5 and -0.020 , respectively, whose zero crossings determine the corresponding values for L .

We can check the accuracy of the linear energy approximation (Eq. 2.27) by numerically solving the Schrödinger equation with a specified energy. This determines

L as the radius at which the resulting wave function vanishes. Then we compare this wave function for $r \leq L$ to the right side of Eq. 2.27, with the derivative calculated numerically. Figure 2.10 shows representative examples for a deep and shallow Gaussian potential. In these examples and other cases, the approximation to the wave function is good, particularly in the interior. The estimates for ΔE_L using the right side of Eq. 2.28 are within a few to ten percent: 0.68 versus 0.70 and 0.050 versus 0.055 for the two cases.

The good approximation to the wave function suggests that for the calculation of other observables the linear energy approximation will be useful. For observables most sensitive to the long distance (outer) part of the wave function, such as the radius, this has already been shown to be true [73]. But the good approximation to the wave function at small r means that corrections for short-range observables should also be controlled, with the dominant contribution in an extrapolation formula coming from the normalization.

Next we derive an expression for the derivative in Eq. 2.28. To start with we assume we have a single partial-wave channel. For general $E < 0$, the asymptotic form of the radial wave function for r greater than the range of the potential is

$$u_E(r) \xrightarrow{r \gg R} A_E(e^{-k_E r} + \alpha_E e^{+k_E r}), \quad (2.29)$$

with $u_\infty(r) \xrightarrow{r \gg R} A_\infty e^{-k_\infty r}$ for $E = E_\infty$. We take the derivative of Eq. 2.29 with respect to energy, evaluate at $E = E_\infty$ using $\alpha_{E_\infty} = 0$ and $dk_E/dE = -\mu/(\hbar^2 k_E)$, to find

$$\frac{du_E(r)}{dE} \Big|_{E_\infty} = A_\infty \frac{d\alpha_E}{dE} \Big|_{E_\infty} e^{+k_\infty r} + A_\infty \frac{\mu}{\hbar^2 k_\infty} \frac{r}{e^{-k_\infty r}} + \frac{dA_E}{dE} \Big|_{E_\infty} e^{-k_\infty r}. \quad (2.30)$$

We now evaluate at $r = L$ and anticipate that the $e^{+k_\infty L}$ term dominates:

$$\frac{du_E(L)}{dE} \Big|_{E_\infty} \approx A_\infty \frac{d\alpha_E}{dE} \Big|_{E_\infty} e^{+k_\infty L} + \mathcal{O}(e^{-k_\infty L}) . \quad (2.31)$$

Substituting Eq. 2.31 into Eq. 2.28, we obtain

$$\Delta E_L \approx - \left[\frac{d\alpha_E}{dE} \Big|_{E_\infty} \right]^{-1} e^{-2k_\infty L} + \mathcal{O}(e^{-4k_\infty L}) . \quad (2.32)$$

Note that this result is independent of the normalization of the wave function.

To calculate the derivative explicitly, we turn to scattering theory, following the notation and discussion in Ref. [72]. In particular, the asymptotic form of the regular scattering wave function $\phi_{l,k}$ for orbital angular momentum l and for positive energy $E \equiv \hbar^2 k^2 / 2\mu$ is given in terms of the Jost function $\mathfrak{f}_l(k)$ [72],

$$\phi_{l,k}(r) \longrightarrow \frac{i}{2} [\mathfrak{f}_l(k) \hat{h}_l^-(kr) - \mathfrak{f}_l(-k) \hat{h}_l^+(kr)] , \quad (2.33)$$

where the \hat{h}_l^\pm functions (related to Hankel functions) behave asymptotically as

$$\hat{h}_l^\pm(kr) \xrightarrow{r \rightarrow \infty} e^{\pm i(kr - l\pi/2)} . \quad (2.34)$$

The ratio of the Jost functions appearing in Eq. 2.33 gives the partial wave S -matrix $s_l(k)$:

$$s_l(k) = \frac{\mathfrak{f}_l(-k)}{\mathfrak{f}_l(+k)} , \quad (2.35)$$

which is in turn related to the partial-wave scattering amplitude $f_l(k)$ by

$$f_l(k) = \frac{s_l(k) - 1}{2ik} . \quad (2.36)$$

We will restrict ourselves to $l = 0$ for simplicity; the generalization to higher l is straightforward and will be considered later.

To apply Eq. 2.33 to negative energies, we analytically continue from real to (positive) imaginary k . So,

$$\begin{aligned}\phi_{0,ik_E}(r) &\xrightarrow{r \gg R} \frac{i}{2} (\mathfrak{f}_0(ik_E)e^{k_E r} - \mathfrak{f}_0(-ik_E)e^{-k_E r}) \\ &= -\frac{i}{2} \mathfrak{f}_0(-ik_E) (e^{-k_E r} - \frac{\mathfrak{f}_0(-ik_E)}{\mathfrak{f}_0(ik_E)} e^{k_E r}),\end{aligned}\quad (2.37)$$

where R is the range of the potential. Upon comparing to Eq. 2.29 we conclude that

$$\alpha_E = -\frac{\mathfrak{f}_0(ik_E)}{\mathfrak{f}_0(-ik_E)} = -\frac{1}{s_0(ik_E)}. \quad (2.38)$$

Note that Eq. 2.38 is consistent with the bound-state limit of Eq. 2.29: at a bound state where $E_\infty = -\hbar^2 k_\infty^2 / 2\mu$ there is a simple pole in the S matrix, which means $\alpha_E = 0$ as expected (no exponentially rising piece).

From Ref. [72] we learn that the residue as a function of E of the partial wave amplitude $f_l(E)$ at the bound-state pole is $(-1)^{l+1} \gamma_\infty^2 \hbar^2 / 2\mu$, where γ_∞ is the asymptotic normalization coefficient (ANC). The ANC is defined by the large- r behavior of the *normalized* bound-state wave function:

$$u_{\text{norm}}(r) \xrightarrow{r \gg R} \gamma_\infty e^{-k_\infty r}. \quad (2.39)$$

Thus, near the bound-state pole (with $E = \hbar^2 k^2 / 2\mu$),

$$f_0(k) \approx \frac{-\hbar^2 \gamma_\infty^2}{2\mu(E - E_\infty)} = \frac{-\gamma_\infty^2}{k^2 + k_\infty^2}. \quad (2.40)$$

or, using Eqs. 2.36 and 2.38,

$$\alpha_E(k) \approx -\frac{k^2 + k_\infty^2}{k^2 + k_\infty^2 - 2ik\gamma_\infty^2}. \quad (2.41)$$

Now,

$$\left. \frac{d\alpha_E}{dE} \right|_{E_\infty} = \left. \frac{d\alpha_E/dk}{dE/dk} \right|_{k=ik_\infty}, \quad (2.42)$$

so using Eq. 2.41 we find

$$\left. \frac{d\alpha_E}{dk} \right|_{k=ik_\infty} = \frac{-i}{\gamma_\infty^2}, \quad (2.43)$$

and therefore

$$\frac{d\alpha_E}{dE} \Big|_{E_\infty} = \frac{-\mu}{\hbar^2 k_\infty \gamma_\infty^2} . \quad (2.44)$$

Putting it all together, we have

$$\Delta E_L = \frac{\hbar^2 k_\infty \gamma_\infty^2}{\mu} e^{-2k_\infty L} + \mathcal{O}(e^{-4k_\infty L}) . \quad (2.45)$$

Equation 2.45 matches the result

$$E(L) = E_\infty + A e^{-2k_\infty L} + \mathcal{O}(e^{-4k_\infty L}) \quad (2.46)$$

in [60], but now we have identified $A = \hbar^2 k_\infty \gamma_\infty^2 / \mu$.

In [56], we advocated including second term in Eq. 2.30 for weakly bound states (small k_∞ makes the term $A_\infty \frac{\mu}{\hbar^2} \frac{r}{k_\infty} e^{-k_\infty r}$ non-negligible). Including this term was also seen to give better prediction for weakly bound states like deuteron. As we pointed out in [57], a better way to arrange an expression for ΔE is to have a systematic expansion in powers of $e^{-2k_\infty L}$. Keeping the second term in Eq. 2.30, generates terms in higher powers of $\mathcal{O}(e^{-2k_\infty L})$. However, these higher order terms also arise from the $\mathcal{O}(\Delta E_L^2)$ term in Eq. 2.27 and to be consistent we need to take in account contributions up to a given order from both the sources (i.e., Eqs. 2.27 and 2.30). As we will see below, relating k_L (k_L is the binding momentum when we have a hard wall at length L) directly to the S -matrix allows us to transparently obtain systematic expansion for ΔE in powers of $e^{-2k_\infty L}$.

The S -matrix way

In [57], we returned to Eq. 2.29 and noted that the bc uniquely fixed the coefficient α_E . We need $u_E(r = L) = 0$ which fixes

$$\alpha_E = -e^{-2k_E L} . \quad (2.47)$$

To make the L dependence explicit, we modify the notation and let $k_L \equiv k_E$. Comparing Eqs. 2.47 and 2.38, we have

$$e^{-2k_L L} = [s_0(ik_L)]^{-1}. \quad (2.48)$$

We then use appropriate parametrization for s_0 valid in the complex k region and solve the transcendental equation 2.48 for k_L and thereby find E_L .

If the potential has no long-range part that introduces a singularity in the complex k plane nearer to the origin than the bound-state pole (which is the case, for example, for the deuteron when we assume that the longest-ranged interaction is from pion exchange), then the continuation of the positive-energy partial-wave S-matrix (i.e., the phase shifts) to the pole should be unique. Because $|k_L| < |k_\infty|$, $s_0(ik_L)$ and therefore k_L and the energy shift E_L should be determined solely by observables.

The leading term in an expansion of $k_L - k_\infty$ using Eq. 2.48 comes from the bound-state pole, at which s_0 behaves like [74]

$$s_0(k) \approx \frac{-i\gamma_\infty^2}{k - ik_\infty}. \quad (2.49)$$

Note that γ_∞ here is the asymptotic normalization coefficient (ANC) defined in Eq. 2.39. Substituting Eq. 2.49 into Eq. 2.48 yields

$$k_L - k_\infty \approx -\gamma_\infty^2 e^{-2k_L L} \approx -\gamma_\infty^2 e^{-2k_\infty L}. \quad (2.50)$$

This is the leading-order (LO) result for k_L obtained in Eq. 2.45. Note that in Eq. 2.45, $\Delta E_L \equiv E_L - E_\infty = k_\infty^2/2 - k_L^2/2$. We set $\hbar^2/\mu = 1$. The notation k_∞ for the exact binding momentum make sense in this context, because in the exact case, the hard wall is at $L = \infty$.

Iterations of the intermediate equation in 2.50 motivate the NLO parameterization of k_L as

$$k_L = k_\infty + A e^{-2k_\infty L} + (BL + C) e^{-4k_\infty L} + \mathcal{O}(e^{-6k_\infty L}), \quad (2.51)$$

with $A = -\gamma_\infty^2$. In general we can substitute this expansion into Eq. 2.48 using an parametrized form of the S-matrix, then expand in powers of $e^{-2k_\infty L}$ and equate $e^{-2k_\infty L}$, $L e^{-4k_\infty L}$, and $e^{-4k_\infty L}$ terms on both sides of the equation. However, while both A and B are uniquely determined by the pole in $s_0(k)$ at $k = ik_\infty$, C is only determined unambiguously if $s_0(k)$ is consistently parameterized away from the pole.

For example, the two parametrizations

$$s_0(ik_L) \approx \frac{k_\infty^2 - k_L^2 + 2k_L\gamma_\infty^2}{k_\infty^2 - k_L^2} \quad (2.52)$$

and

$$s_0(k) \approx \frac{-\gamma_\infty^2}{2k_\infty} \frac{k + ik_\infty}{k - ik_\infty} \quad (2.53)$$

yield different results for C . The first parametrization (Eq. 2.52) is based on a particular form for the partial-wave scattering amplitude near the pole [72], and was employed in Ref. [56]. The second paramerization (Eq. 2.53) correctly incorporates that the S-matrix also has a zero at $-ik_\infty$ [74]. In neither case, however, do we have a sufficiently general parametrization that allows us to unambiguously determine C .

For the complete NLO energy correction, we start from the general expression for the S-matrix

$$s_0(k) = \frac{k \cot \delta_0(k) + ik}{k \cot \delta_0(k) - ik}, \quad (2.54)$$

and use an effective range expansion to substitute for $k \cot \delta_0(k)$. In particular, we use an expansion around the bound-state pole rather than about zero energy, namely [75, 76],

$$k \cot \delta_0(k) = -k_\infty + \frac{1}{2} \rho_d (k^2 + k_\infty^2) + w_2 (k^2 + k_\infty^2)^2 + \dots . \quad (2.55)$$

To match the residue at the S-matrix pole as in Eq. 2.49, we identify

$$\rho_d = \frac{1}{k_\infty} - \frac{2}{\gamma_\infty^2} . \quad (2.56)$$

w_2 is a low-energy observable like γ_∞ and k_∞ . Now we substitute Eq. 2.55 into Eq. 2.54 and use Eq. 2.51 to expand both sides of Eq. 2.48, equating terms with equal powers of $e^{-2k_\infty L}$ and L . The resulting expansion for the binding momentum to NLO is

$$\begin{aligned} [k_L]_{\text{NLO}} &= k_\infty - \gamma_\infty^2 e^{-2k_\infty L} - 2L\gamma_\infty^4 e^{-4k_\infty L} \\ &\quad - \gamma_\infty^2 \left(1 - \frac{\gamma_\infty^2}{2k_\infty} - \frac{\gamma_\infty^4}{4k_\infty^2} + 2k_\infty w_2 \gamma_\infty^4 \right) e^{-4k_\infty L} . \end{aligned} \quad (2.57)$$

Using $\Delta E_L \equiv E_L - E_\infty = k_\infty^2/2 - k_L^2/2$, the correction for the energy due to finite L is

$$\begin{aligned} [\Delta E_L]_{\text{NLO}} &= k_\infty \gamma_\infty^2 e^{-2k_\infty L} + 2k_\infty L \gamma_\infty^4 e^{-4k_\infty L} \\ &\quad + k_\infty \gamma_\infty^2 \left(1 - \frac{\gamma_\infty^2}{k_\infty} - \frac{\gamma_\infty^4}{4k_\infty^2} + 2k_\infty w_2 \gamma_\infty^4 \right) e^{-4k_\infty L} . \end{aligned} \quad (2.58)$$

In what follows we use LO to refer to the first term in this expansion and L-NLO to refer to the first two terms (the second term should dominate the full NLO expression when $k_\infty L$ is large). We also note that higher-order terms in Eq. 2.55 (e.g., terms proportional to $(k^2 + k_\infty^2)^3$ and higher powers) do not affect the binding momentum or energy predictions Eqs. 2.57 and 2.58 at NLO.

As a special case, let us consider the zero-range limit of a potential. In this case $\rho_d = w_2 = 0$, $\gamma_\infty^2 = 2k_\infty$, and

$$[s_0(i k_L)]^{-1} = \frac{k_\infty - k_L}{k_\infty + k_L} . \quad (2.59)$$

The expansion for k_L in a form similar to Eq. 2.51 can be extended to arbitrary order using Eq. 2.48.

We note finally that the leading corrections beyond NLO scale as $L^2 e^{-6k_\infty L}$. While we do not pursue a derivation of such high-order corrections here, the knowledge of the leading form is useful in some of the error analysis we present in Subsec. 2.1.3.

Differential method

Because we seek the change in energy with respect to a cutoff, it is natural to formulate the problem in the spirit of renormalization group methods by seeking a flow equation for the bound-state energy as a function of L . Such an approach is already documented in the literature, for example in Refs. [77] and [78], and it provides us with an alternative method that does not directly reference the S-matrix.

The basic equation is

$$\frac{\partial E_L}{\partial L} = -\frac{1}{2} \frac{|u'_L(L)|^2}{\int_0^L |u_L(r)|^2 dr} . \quad (2.60)$$

Here the prime denotes a derivative with respect to r . Given an expression for the right-hand side in terms of observables (k_∞ , γ_∞ , and so on) and L , we can simply integrate to find the energy correction for a bc at L

$$\Delta E_L \equiv E_L - E_\infty = \int_{E_\infty}^{E_L} dE = \int_\infty^L \frac{\partial E_L}{\partial L} dL . \quad (2.61)$$

To derive Eq. 2.60, we start with

$$\frac{\partial}{\partial L} \left[\int_0^L u_L(r) H u_L(r) dr \right] = E_L \int_0^L dr u_L(r)^2 , \quad (2.62)$$

which yields (after some cancellations)

$$\frac{1}{2} \left(\frac{\partial u_L(r)}{\partial r} \frac{\partial u_L(r)}{\partial L} \right) \Big|_0^L = \frac{\partial E_L}{\partial L} \int_0^L dr u_L(r)^2 . \quad (2.63)$$

The left-hand side is a surface term from partially integrating the kinetic energy in H . The lower limit vanishes because $u_L(0) = 0$ for any L . Finally, we replace the partial derivative with respect to L at the upper limit using

$$\frac{\partial u_L(L)}{\partial L} = -\frac{\partial u_L(L)}{\partial r}, \quad (2.64)$$

which follows from expanding $u_{L'}(L') = 0$ about $u_L(L) = 0$ for $L' = L + \Delta L$.

To apply Eq. 2.60, we start with $u_L(r)$ in the asymptotic region, as given by

$$u_L(r) \xrightarrow{r \gg R} (e^{-k_L r} - e^{-2k_L L} e^{k_L r}). \quad (2.65)$$

The normalization constant γ_L is chosen so that the integral of $u_L(r)^2$ from 0 to L is unity; it becomes the ANC γ_∞ as $L \rightarrow \infty$. Thus

$$u'_L(L) = -2\gamma_L k_L e^{-k_L L}. \quad (2.66)$$

Now we need to expand k_L and γ_L about k_∞ and γ_∞ , respectively. The leading term is trivial: $k_L \rightarrow k_\infty$ and $\gamma_L \rightarrow \gamma_\infty$, so the only L dependence in $u'_L(L)^2$ is in $e^{-2k_\infty L}$ and the integration in 2.60 is immediate:

$$\Delta E_L = \int_\infty^L \frac{\partial E_L}{\partial L} dL = -2\gamma_\infty^2 k_\infty^2 \int_\infty^L e^{-2k_\infty L} dL = k_\infty \gamma_\infty^2 e^{-2k_\infty L} + \mathcal{O}(e^{-4k_\infty L}). \quad (2.67)$$

This is the same LO result for ΔE_L found by other methods.

To go to NLO we need an expression for γ_L . In the zero-range (zr) limit, γ_L is given completely in terms of k_L using the normalization condition (because the asymptotic form in Eq. 2.65 holds over the entire range of the integral)

$$\gamma_L^2 = \left[\int_0^L dr (e^{-k_L r} - e^{-2k_L L} e^{k_L r})^2 \right]^{-1} = 2k_L (1 + 4k_L L e^{-2k_L L}) + \mathcal{O}(e^{-4k_L L}). \quad (2.68)$$

We expand k_L everywhere in Eq. 2.60 using Eq. 2.66 and our LO result

$$k_L = k_\infty (1 - 2e^{-2k_\infty L}). \quad (2.69)$$

Here, we neglected terms that are $\mathcal{O}(e^{-6k_\infty L})$ or smaller. We need to expand $e^{-2k_L L}$ in $u'_L(L)$ to get

$$e^{-2k_L L} = e^{-2k_\infty L}(1 + 4k_\infty L e^{-2k_\infty L}) + \mathcal{O}(e^{-6k_\infty L}). \quad (2.70)$$

(Elsewhere it suffices to replace $e^{-2k_L L}$ by $e^{-2k_\infty L}$ to NLO.) So we find that

$$\begin{aligned} \frac{\partial E_L}{\partial L} &= -\frac{1}{2}(4\gamma_L^2 k_L^2 e^{-2k_L L}) \\ &\approx -2[2k_\infty(1 - 2e^{-2k_\infty L})(1 + 4k_\infty L e^{-2k_\infty L})] \\ &\quad \times [k_\infty^2(1 - 4e^{-2k_\infty L})][e^{-2k_\infty L}(1 + 4k_\infty L e^{-2k_\infty L})] \\ &\approx -4k_\infty^3 e^{-2k_\infty L} - 8k_\infty^3(4k_\infty L - 3)e^{-4k_\infty L} + \mathcal{O}(e^{-6k_\infty L}), \end{aligned} \quad (2.71)$$

and then finally

$$\begin{aligned} [\Delta E_L]_{\text{zr,NLO}} &= \int_\infty^L \frac{\partial E_L}{\partial L} dL \\ &= 2k_\infty^2 e^{-2k_\infty L} + 4k_\infty^2(2k_\infty L - 1)e^{-4k_\infty L} + \mathcal{O}(e^{-6k_\infty L}), \end{aligned} \quad (2.72)$$

in agreement with Eq. 2.58 with $\gamma_\infty^2 = 2k_\infty$ and $w_2 = 0$. We can take this procedure to higher order by using a more general expansion for k_L .

To extend the differential method to higher order for nonzero range, we must parametrize γ_L to account for the part of the integration within the range of the potential; e.g., in terms of the effective range. However, we have not found a clear advantage in doing this compared to the straightforward S-matrix method.

2.1.3 The proof is in the pudding

In this subsection we will test the Eq. 2.58 for various test models and for the deuteron. Note that for the cases that we test Eq. 2.58, the exact answer E_∞ is already known (either by exact analytical calculation or by using large number of basis

states). So we can compare how good the prediction from Eq. 2.58 is by comparing to exact answer. In cases where the exact values for E_∞ and γ_∞ are not known, our approach suggests that we can use the exponential in L fit of Eq. 2.46 to extract E_∞ and k_∞ .

Based on the results presented in Subsec. 2.1.1, we use L_2 in all our further analyses. It is important that we isolate the IR corrections in making these tests. The truncation in the HO basis also introduces an ultraviolet error inversely proportional to the ultraviolet cutoff $\Lambda_{\text{UV}} \approx \sqrt{2\mu\hbar\Omega(N+3/2)}$. In the results here we use combinations of $\hbar\Omega$ and N values such that the UV error in each case can be neglected compared to the IR error.

For each of the model potentials, the radial Schrödinger equation is accurately solved numerically in coordinate space for the energy, which yields k_∞ , and the wave functions. The asymptotic normalization coefficient γ_∞ is found by multiplying the wave function by $e^{k_\infty r}$ and reading off its asymptotic value. This is illustrated in the inset of Fig. 2.11, which also shows the onset of the plateau that defines the asymptotic region in L_2 where we expect our correction formulas to hold. For the deuteron, the Hamiltonian is diagonalized in momentum space to find k_∞ , and then an extrapolation to the pole is used to find the s -wave and d -wave ANC [79]. In the present subsection we use only the s -wave ANC for the deuteron.

The derivations in Subsec. 2.1.2 imply that the energy corrections should have the same exponential form and functional dependence on the radius L at which the wave function is zero, independent of the potential and for any bound state. Here we make some representative tests of a direct fit of Eq. 2.46 in comparison to applying Eq. 2.45.

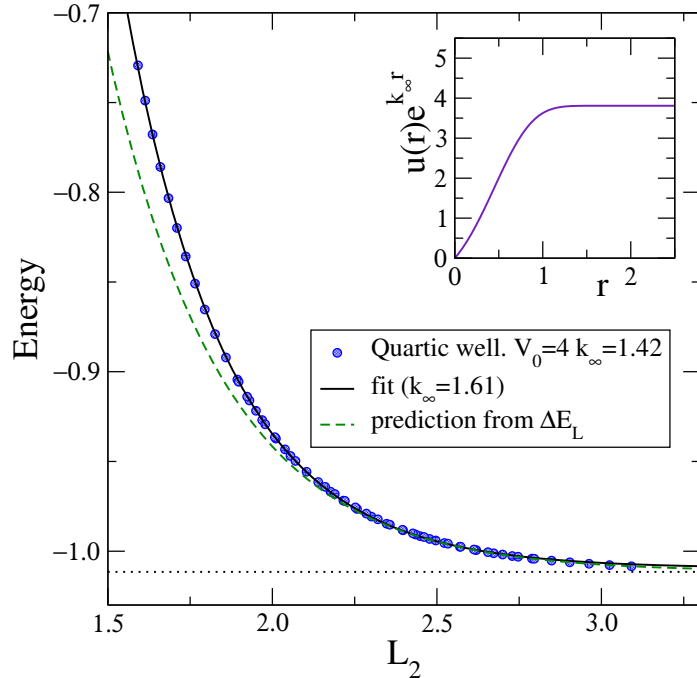


Figure 2.11: Energy versus L_2 for a quartic potential well Eq. 2.9 for a wide range of N and $\hbar\Omega$ (circles) ($\hbar = \mu = R = 1$). The solid line is a fit to Eq. 2.46 with A , k_∞ and E_∞ as fit parameters while the dashed line is the prediction from Eq. 2.45. The horizontal line is the exact energy, $E_\infty = -1.0115$. The inset illustrates the calculation of the asymptotic normalization coefficient (ANC) from the (normalized) wave function.

Figure 2.11 shows results for a quartic potential with a moderate depth. The fit to Eq. 2.46 is very good over a large range in L_2 for which the energy changes by 30%, and the prediction for E_∞ is accurate to 0.2%. However, the fit value of k_∞ is 1.61 compared to the exact value of 1.42. The dashed curve shows the prediction from Eq. 2.45 using the exact k_∞ and γ_∞ . It is evident that the approximation is very good above $L_2 > 2$ but increasingly deviates at smaller L_2 .

In Fig. 2.12, examples are shown for square well and Gaussian potentials with a moderate depth. Again we find a good fit to an exponential fall-off in L_2 , but in these

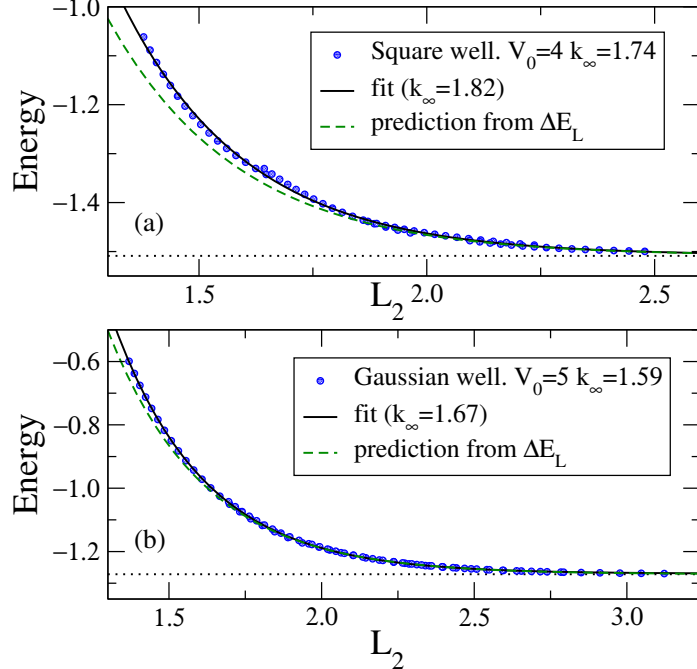


Figure 2.12: Energy versus L_2 for moderate-depth (a) square well Eq. 2.6 and for (b) Gaussian potential well Eq. 2.8 ($\hbar = \mu = R = 1$) for a wide range of N and $\hbar\Omega$ (circles). The solid line is a fit to Eq. 2.46 with A , k_∞ and E_∞ as fit parameters while the dashed line is the prediction from Eq. 2.45. The horizontal dotted lines are the exact energies; square well: $E_\infty = -1.5088$, Gaussian well: $E_\infty = -1.2717$

cases not only are the energies well predicted (again to better than 0.2%) but the fit values of k_∞ are within 5% of the exact results. For deeply bound states, Eq. 2.45 fails for a different reason. The error in Eq. 2.45 is proportional to $e^{-4k_\infty L}$, so one might expect that the prediction to become increasingly accurate as the state becomes more bound. However, as seen in Figs. 2.13 and 2.14, results for deep Gaussian and exponential potential wells do not match this expectation. In deriving the energy corrections we used the asymptotic form of the wave functions. This is valid only in the region $r \gg R$, where R is the range of the potential. The potentials at the smaller values of L_2 shown in the figures are not negligible. Indeed, it is evident from the

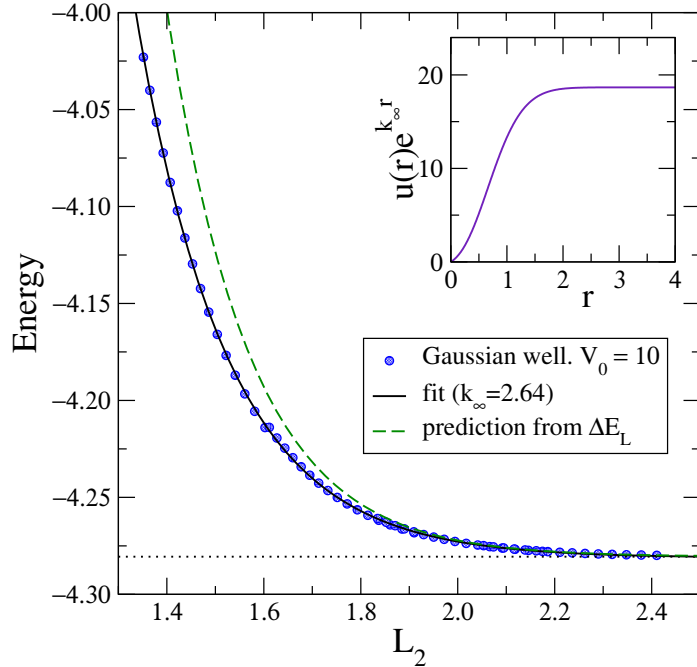


Figure 2.13: Energy versus L_2 for the deeply bound ground state of a Gaussian potential for a wide range of N and $\hbar\Omega$ (circles) ($\hbar = \mu = R = 1$). These are compared to the prediction of Eq. 2.45 (dashed). The solid line is a fit to Eq. 2.46 with A , k_∞ and E_∞ as fit parameters. The horizontal dotted line is the exact energy, $E_\infty = -4.2806$.

insets in Figs. 2.13 and 2.14 that we are not in the asymptotic region for those values of L . The lesson is that when applying the IR extrapolation schemes discussed in the present paper we need to make sure that the two conditions for its applicability are fulfilled. First, we need N sufficiently large for L_2 to be the correct box size (see Table 2.1). Second we need L_2 to be the largest length scale in the problem under consideration.

The results so far are for the ground state of the potential. However, the derivations in the Subsec. 2.1.2 should also hold for excited states. This is so because the generalization of the results in Subsec. 2.1.1 shows that $(j\pi/L_2)^2$ is a very good

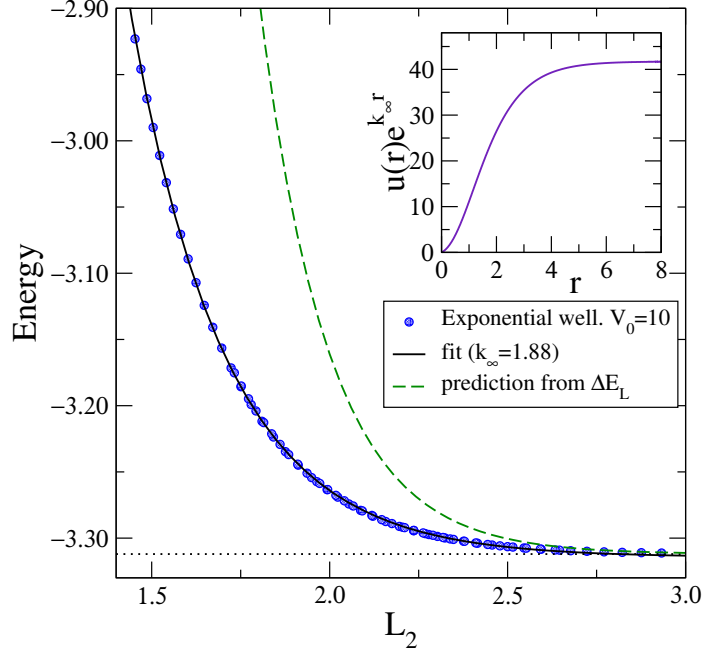


Figure 2.14: Energy versus L_2 for the deeply bound ground state of an exponential potential well for a wide range of N and $\hbar\Omega$ (circles) ($\hbar = \mu = R = 1$). These are compared to the predictions of Eq. 2.45 (dashed). The solid line is a fit to Eq. 2.46 with A , k_∞ and E_∞ as fit parameters. The horizontal dotted line is the exact energy, $E_\infty = -3.3121$.

approximation to the j^{th} eigenvalue of the operator p^2 for $j \ll N$. In Fig. 2.15 representative results for excited states from two model potentials are shown. We find the same systematics as with the ground-state results: the exponential fit works very well but the extracted k_∞ is only correct at about the 10% level. In assessing the success of Eq. 2.45, we note that these excited states in deep potentials are comparable to the ground states in moderate-depth potentials shown in Fig. 2.12. The discussion there applies here as well, namely that the prediction from Eq. 2.45 is very good at large L_2 , but increasingly deviates at smaller L_2 .

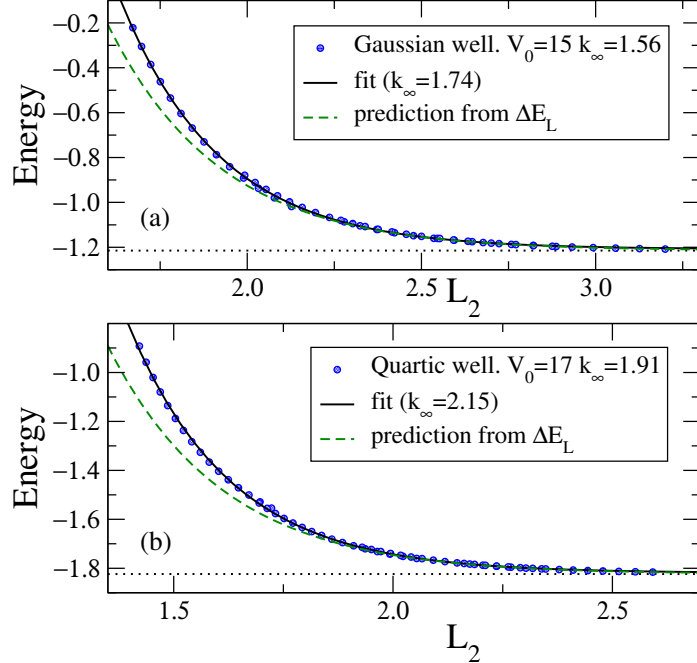


Figure 2.15: Energy versus L_2 for the first excited states of deep (a) Gaussian Eq. 2.8 and (b) quartic Eq. 2.9 potential wells for a wide range of N and $\hbar\Omega$ (circles) ($\hbar = \mu = R = 1$). The solid line is a fit to Eq. 2.46 with A , k_∞ and E_∞ as fit parameters while the dashed line is the prediction from Eqs. 2.45. The horizontal dotted lines are the exact energies for the first excited states; Gaussian well: $E_\infty = -1.2147$, quartic well: $E_\infty = -1.8236$

The case of weakly bound states is of special interest because of the correspondence to deuteron which is also a weakly bound shallow state. Figure 2.16 (a) shows ground-state energies for many different N and $\hbar\Omega$ versus L_2 using Gaussian model potentials whose parameters are chosen so that the energies are the same as the deuteron binding energy (scaled to units with $\hbar = 1$, $\mu = 1$, $R = 1$). In Fig. 2.16 (b) we have a ‘deuteron-like’ square well. The energies in this case are obtained by solving the Schrödinger equation exactly with a Dirichlet bc on wave functions at $r = L$. The prediction from Eq. 2.45 fails to reproduce the data except at the highest values of

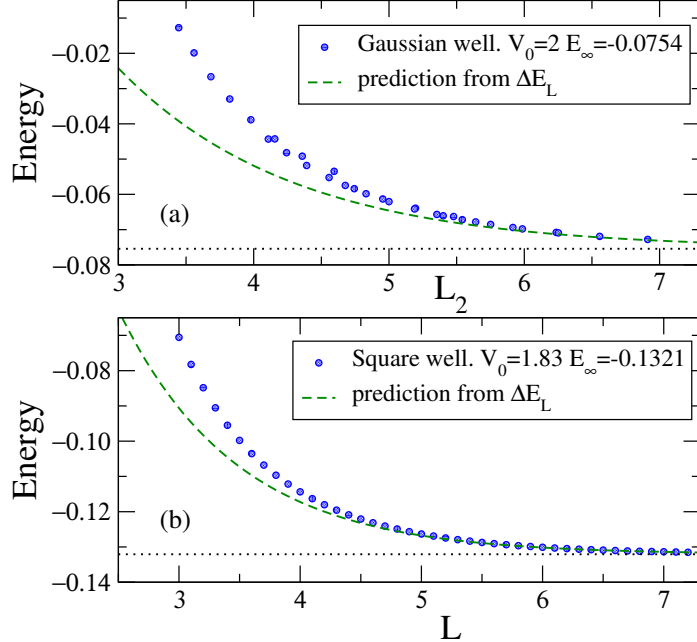


Figure 2.16: (a) Ground-state energy versus L_2 for model Gaussian potential. (b) Energy versus L for the square well. The energies for the square well are from solving the Schrödinger equation exactly with a Dirichlet bc on wave functions at $r = L$. The dashed line is the prediction from Eqs. 2.45. The depths of these model potentials are chosen so that the scaled energies (with $\hbar = \mu = R = 1$) are the same as the deuteron binding energy.

L_2 . Eq. 2.45 keeps only the leading-order (LO) corrections to ΔE . For the weakly bound states, the higher-order corrections become important. The corrections to the energy up to the next to leading order (NLO) were noted in Eq. 2.58. Note that the NLO correction involves the low-energy constant w_2 . In certain cases, this constant w_2 can be calculated and ΔE up to NLO can be obtained. Now we turn to the test of Eq. 2.58.

NLO and systematics of the correction

For the square-well potential of Eq. 2.6, the parameters in Eq. 2.58 can be calculated easily. The S -wave scattering phase shift for the square well is

$$\delta_0(k) = \tan^{-1} \left[\sqrt{\frac{k^2}{k^2 + \eta^2}} \tan(\sqrt{k^2 + \eta^2} R) \right] - kR , \quad (2.73)$$

with $\eta = \sqrt{2V_0}$. Analytically continuing the effective range expansion by taking $k \rightarrow ik_L$ in Eqs. 2.55 and 2.73, we obtain

$$\begin{aligned} \frac{ik_L \sqrt{\eta^2 - k_L^2} - k_L^2 \tan(\sqrt{\eta^2 - k_L^2} R) \tan(ik_L R)}{ik_L \tan(\sqrt{\eta^2 - k_L^2} R) - \sqrt{\eta^2 - k_L^2} \tan(ik_L R)} &= \\ -k_\infty + \frac{1}{2} \rho_d(k_\infty^2 - k_L^2) + w_2(k_\infty^2 - k_L^2)^2 + \mathcal{O}((k_\infty^2 - k_L^2)^3) . \end{aligned} \quad (2.74)$$

The branch for the square-root is fixed by the requirement that $\tan \delta(ik_\infty) = -i$. Note from Eq. 2.54 that this builds in the requirement that the S -matrix has a pole at ik_∞ . To get ρ_d (w_2) we differentiate once (twice) each side of Eq. 2.74 with respect to k_L and then set $k_L = k_\infty$. The ρ_d obtained in this way is consistent with Eq. 2.56 when γ_∞ is obtained by the large r behavior of the bound-state wave function as defined in Eq. 2.39.

The square well with a Dirichlet bc at $L > R$ can be solved analytically. The wave functions inside and outside the square well are

$$u_L^<(r) = C \sin \kappa_L r , \quad u_L^>(r) = D(e^{-k_L r} - e^{-2k_L L} e^{+k_L r}) , \quad (2.75)$$

which builds in the boundary condition $u_L^>(L) = 0$. The interior wave number $\kappa_L = \sqrt{\eta^2 - k_L^2}$ and $k_L = \sqrt{2|E_L|}$. Matching the logarithmic derivatives at $r = R$ for $E = E_\infty$ yields

$$\kappa_\infty \cot \kappa_\infty R = -k_\infty \quad (2.76)$$

and with the boundary condition at L we get:

$$\kappa_L \cot \kappa_L R = -k_L \frac{1 + e^{-2k_L(L-R)}}{1 - e^{-2k_L(L-R)}}. \quad (2.77)$$

We expand both sides of Eq. 2.77 in powers of

$$\Delta k \equiv k_L - k_\infty. \quad (2.78)$$

We write the left-hand side of Eq. 2.77 as

$$\kappa_L \cot \kappa_L R = \kappa_\infty \cot \kappa_\infty R + \mathcal{A}(\Delta k) + \mathcal{B}(\Delta k)^2 + \dots, \quad (2.79)$$

and obtain the coefficients \mathcal{A} , \mathcal{B} by Taylor expanding $\kappa_L \cot(\kappa_L R)$ around k_∞ . We write Δk as

$$\Delta k = k_{(1)} + k_{(2)} + \dots. \quad (2.80)$$

Here $k_{(1)} \sim e^{-2k_\infty L}$ is the LO correction, $k_{(2)} \sim e^{-4k_\infty L}$ is the NLO correction and so on, and we truncate the expressions consistently to obtain the energy correction for the square well to the desired order. The results of the general S-matrix and square-well-only Taylor expansion methods of calculating energy corrections are found to match explicitly at LO, L-NLO, and NLO. We remind the reader that we use L-NLO to denote terms proportional to $Le^{-4k_\infty L}$.

Figure 2.17 compares the energy corrections for the general S-matrix method at LO and NLO for a representative square-well potential with one bound state to the exact energies. The Taylor expansion results for the square well at NLO and N2LO (which is proportional to $e^{-6k_\infty L}$) are also plotted. We note that the predictions are systematically improved as higher-order terms are included and that keeping terms only up to L-NLO overestimates the energy correction. Also as seen in Fig. 2.17, the full NLO energy correction predicted by Eq. 2.58, with w_2 determined by Eq. 2.74,

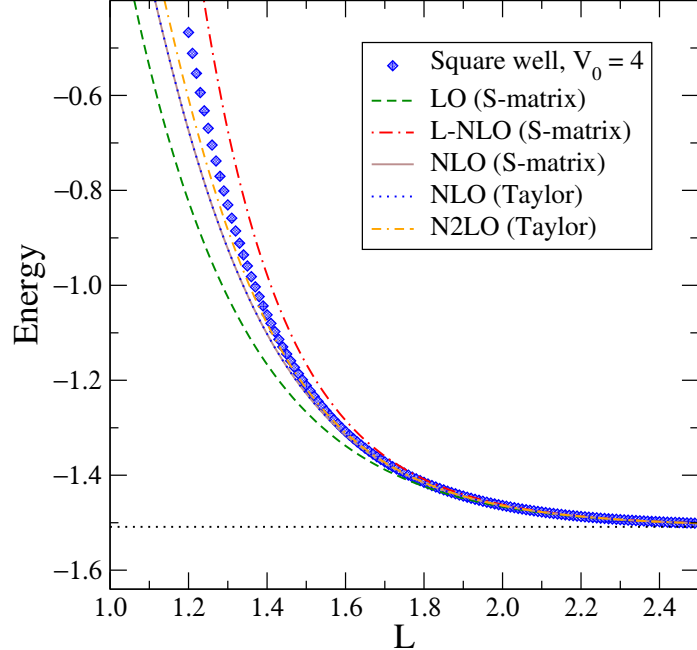


Figure 2.17: Bound-state energy for a square well of depth $V_0 = 4$ (lengths are in units of R and energies in units of $1/R^2$ with $\hbar^2/\mu = 1$) from solving the Schrödinger equation with a Dirichlet bc at $r = L$. The diamonds are exact results for each L while the horizontal dotted line is the energy for $L \rightarrow \infty$, $E_\infty = -1.5088$. The dashed, dot-dashed and solid lines are predictions for the energy using the systematic correction formula Eq. 2.58 at LO (first term only), L-NLO (first two terms), and full NLO (all terms), respectively. The dotted curve on top of the solid line and the dot-double-dashed lines are respectively the NLO and N2LO predictions for the square well from the Taylor expansion using Eqs. 2.77 and 2.79.

matches the ‘exact’ NLO result obtained by Taylor expansion. This confirms that Eq. 2.58 is indeed the complete energy correction at NLO.

To see if the errors decrease with the implied systematics, we plot the difference of actual energy corrections and the energy corrections predicted at different orders on a log-linear scale in Fig. 2.18. We observe that the errors successively decrease at each fixed L as we go from LO to NLO to N2LO. The up triangles in Fig. 2.18 are $\Delta E_{\text{actual}} - \Delta E_{\text{LO}}$. From Eq. 2.58 the dominant omitted correction in ΔE_{LO} is

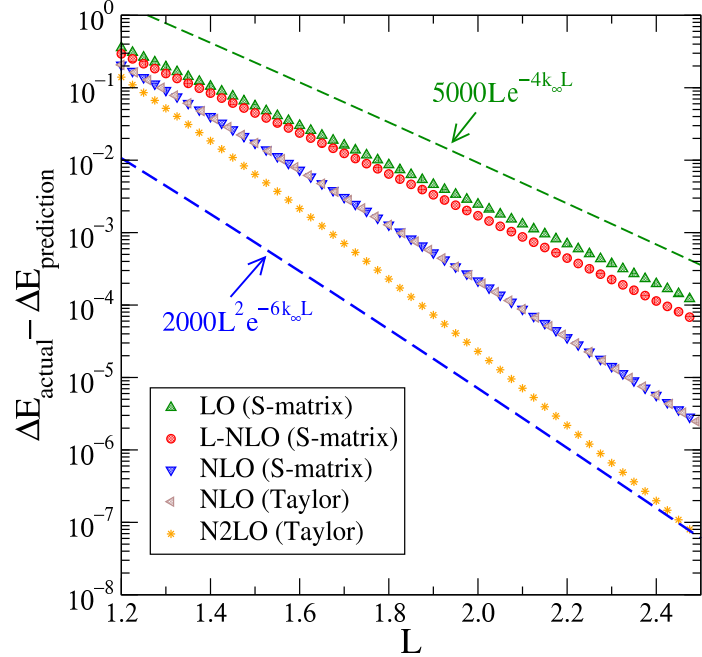


Figure 2.18: Error plots of the energy correction at each L for the square well of Fig. 2.17 ($V_0 = 4$) predicted at different orders by Eq. 2.58 and by the Taylor expansion method, each compared to the exact energy. Lines proportional to $Le^{-4k_\infty L}$ (dashes) and $L^2e^{-6k_\infty L}$ (with arbitrary normalization) are plotted for comparison to anticipated error slopes.

proportional to $Le^{-4k_\infty L}$. As seen in Fig. 2.18, the slope of $\Delta E_{\text{actual}} - \Delta E_{\text{LO}}$ is roughly $Le^{-4k_\infty L}$, as expected. We also note that $\Delta E_{\text{L-NLO}}$ is only a marginal improvement over ΔE_{LO} and that $\Delta E_{\text{actual}} - \Delta E_{\text{NLO}}$ has the expected slope of $L^2e^{-6k_\infty L}$. We again see a perfect agreement between the results obtained from the S-matrix method (Eq. 2.58) and those obtained from the Taylor expansion of Eq. 2.77. We have also studied deeper square wells with more than one bound state and verified that our results apply even in the presence of excited states.

In Figs. 2.19 and 2.20, the same analysis is done but now with the depth of the square well adjusted so that the exact binding energy is the same as the deuteron

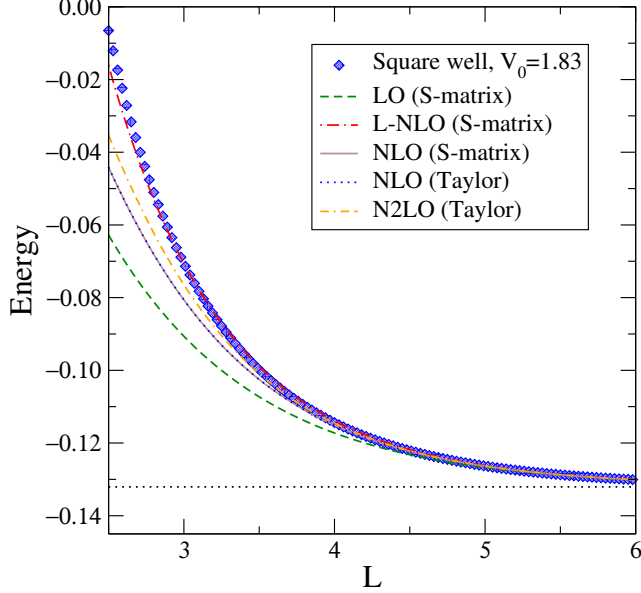


Figure 2.19: Bound-state energy for a square well of depth $V_0 = 1.83$ (units with $R = 1$), which simulates a deuteron, from solving the Schrödinger equation with a Dirichlet bc at $r = L$. The horizontal dotted line is the exact energy, $E_\infty = -0.1321$ and the other curves are as the same as in Fig. 2.17.

binding energy scaled to the units $\hbar = 1$, $\mu = 1$ and $R = 1$. An important difference in this case compared to the deeper square well is that the L-NLO prediction gives a very close estimate for the truncated energies. However as seen in Fig. 2.20, the improvement achieved by the L-NLO prediction is not systematic with L . At large L , $\Delta E - \Delta E_{\text{L-NLO}}$ has the same slope as $\Delta E - \Delta E_{\text{LO}}$ and is not the dominant NLO correction. In this regard, the proximity of L-NLO prediction to the actual data in Fig. 2.19 should not be over-emphasized. Figures 2.21 and 2.22 show analogous results for the deuteron calculated with the chiral EFT potential of Ref. [66]. We use the HO basis and predict the ($l = 0$) energy correction from Eq. 2.58 assuming a Dirichlet bc at L_2 given by Eq. 2.113. We only include energies for which $\hbar\Omega > 49$ MeV, which is sufficient to render UV corrections negligible. For the parameter

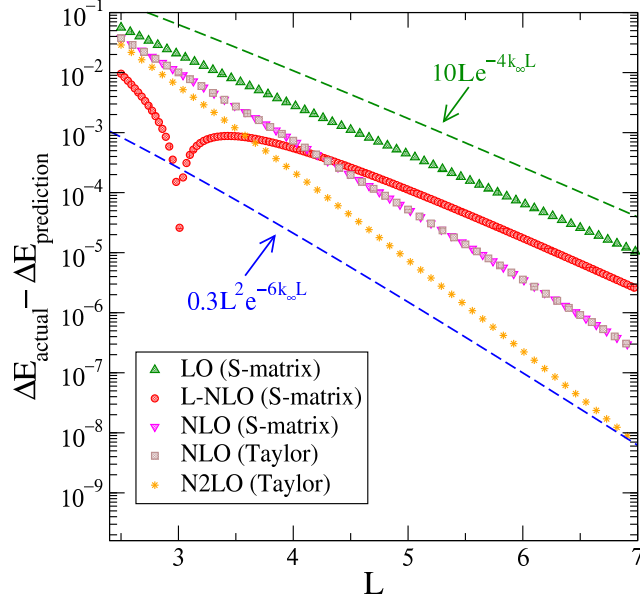


Figure 2.20: Comparison of the actual energy correction due to truncation to the energy correction predicted to different orders by Eq. 2.58 for a square well (Eq. 2.6) with $V_0 = 1.83$ and $R = 1$.

w_2 in Eq. 2.58 we use $w_2 = 0.389$ as reported in [76]. We also note that the ρ_d value reported in [76] satisfies Eq. 2.56, where γ_∞ now is the s -wave ANC. The y -axis minimum is dictated by the limited precision of the ANC and w_2 values. We notice again that the close agreement of the L-NLO prediction to the deuteron data is not systematic while the full corrections to the LO and NLO predictions have the anticipated slopes except at large L_2 . In the next Subsec. 2.1.4 we extend our formulas to $l > 0$, which enables us to include contributions from the d -wave at LO. This becomes noticeable on the error plot for large L_2 (see Fig. 2.28).

As a final test of the universal applicability of the correction formula Eq. 2.58, we consider a sequence of unitarily equivalent potentials for the deuteron. In particular,

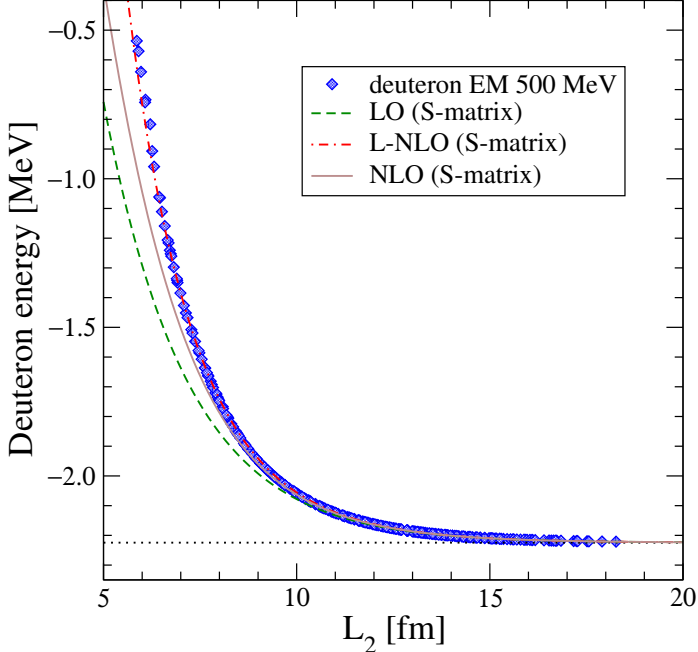


Figure 2.21: Deuteron energy versus L_2 (see Eq. 2.113) for the chiral $N^3\text{LO}$ (500 MeV) potential of Ref. [66]. To eliminate the UV contamination we only plot results for $\hbar\Omega > 49$ MeV. The dashed, dot-dashed and solid lines are respectively the LO (first term in Eq. 2.58), L-NLO (first two terms in Eq. 2.58) and the full NLO (all the terms in Eq. 2.58) predictions for the energy correction. The horizontal dotted line is the deuteron energy.

we use the similarity renormalization group (SRG) [46] to evolve the initial Entem-Machleidt potential to four values of the SRG evolution parameter λ . Because the transformation is exactly unitary (up to very small numerical errors) at the two-body level, the measurable quantities such as phase shifts, bound-state energies, and ANCs are unchanged. From Eq. 2.58 or more generally from Eq. 2.48, we see that the IR energy correction can be written in terms of observables (S -matrix near the bound state can be parametrized in terms of low-energy observables) and therefore should be independent of the SRG scale. This is verified in Fig. 2.23.

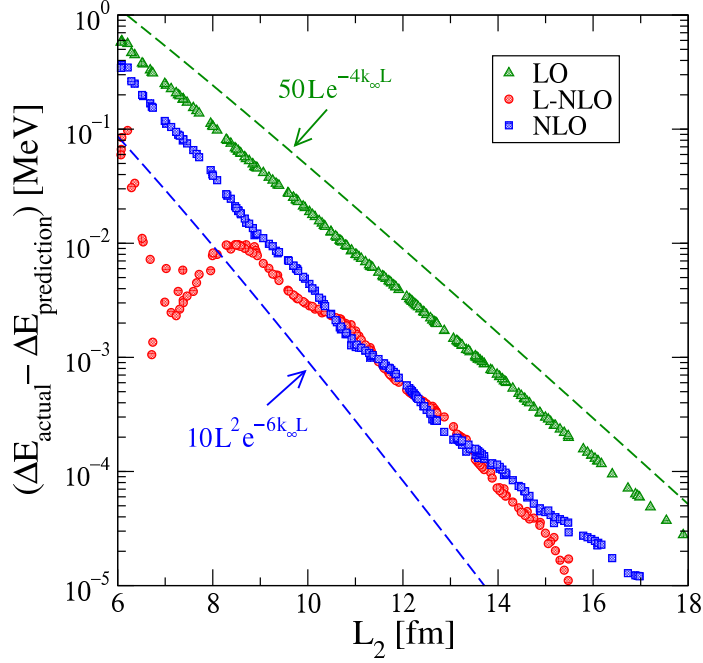


Figure 2.22: Comparison of the actual energy correction due to HO basis truncation ($\hbar\Omega$ restricted to be greater than 49 MeV to eliminate UV contamination) for the deuteron to the energy correction predicted to different orders from Eq. 2.58. For the parameter w_2 in Eq. 2.58 we use the value reported in [76].

As λ decreases, the SRG systematically reduces the coupling between high-momentum and low-momentum potential matrix elements, thereby lowering the effective UV cutoff. Thus these potentials are useful tools to assess the role of UV corrections. This is exploited in Fig. 2.24 where we relax the condition that the UV corrections are small compared to IR corrections. In particular, we fix N at 8 and 12 and scan through the full range of $\hbar\Omega$. We observe that with increasing L_2 , each of the curves with a given λ eventually deviates from the universal curve, first with $\lambda = 3.0 \text{ fm}^{-1}$ and then later with decreasing λ or with higher N . We can understand this in terms of the behavior of the induced UV cutoff. For fixed N , Eq. 2.113 tells us that increasing L_2 means increasing b (or decreasing $\hbar\Omega$). But at fixed N ,

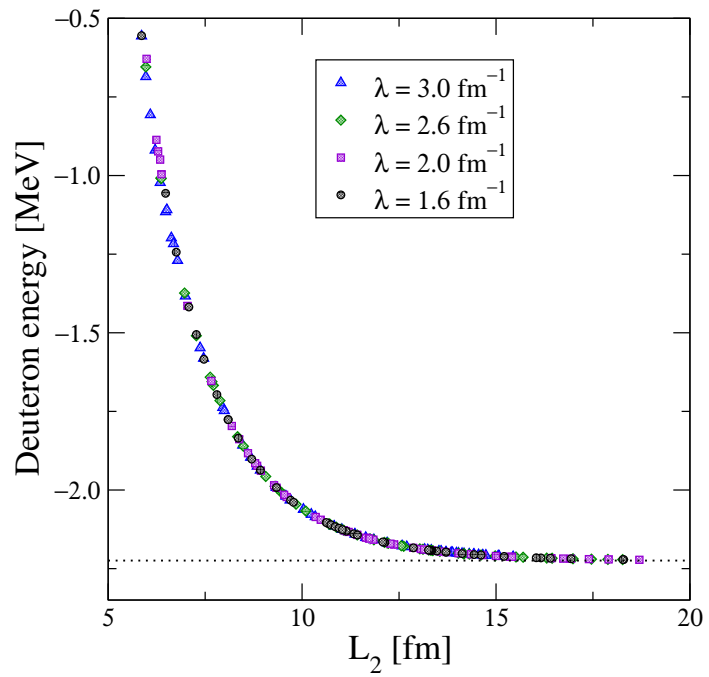


Figure 2.23: Deuteron energy versus L_2 for the potential of Ref. [66] evolved by the SRG to four different resolutions (specified by λ). To eliminate the UV contamination we only keep points for which $\hbar\Omega > 40$. The horizontal dotted line is the deuteron binding energy.

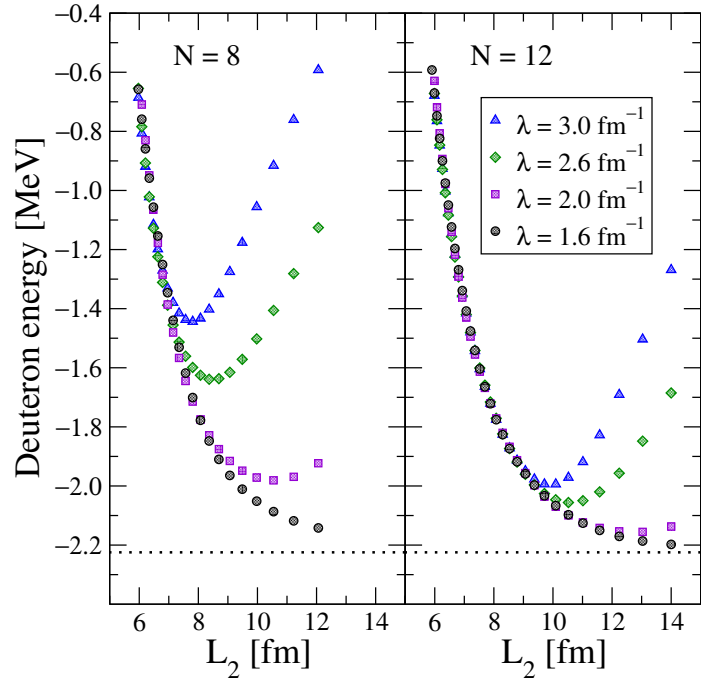


Figure 2.24: The same SRG-evolved potentials as in Fig. 2.23 are used to generate energies, but with N fixed at (a) 8 and (b) 12 and no restriction on $\hbar\Omega$. Thus UV corrections are not negligible everywhere. The horizontal dotted line is the deuteron binding energy.

$\Lambda_{\text{UV}} \propto 1/b$, so the UV cutoff will be decreasing and the corresponding UV energy correction increasing. Thus the curves at fixed λ correspond to the curves seen in conventional plots of energy versus $\hbar\Omega$ (e.g., see Ref. [63]). The softer potentials (lower λ) will have lower intrinsic UV cutoffs and therefore they are only affected for larger L_2 . The minima for each λ are when IR and UV corrections are roughly equal.

Comparison to conventional extrapolation schemes

The extrapolation formulas in Eqs. 2.45 and 2.58 with $L = L_2$ are theoretically founded. Thus the functional form for the energy extrapolation that we have is an exponential in L . As mentioned in the introduction to this chapter, a popular phenomenological choice is an exponential in N extrapolation (Eq. 2.3). From Eq. 2.113 we see that exponential in N extrapolation corresponds to gaussian in L . Authors of Ref. [80] investigated the convergence properties of genuine and smeared contact interactions in an effective theory of trapped bosons and found that the smearing changed a power law dependence of the convergence to an exponential dependence. Here we will consider all three functional dependences on L : exponential, Gaussian, and power law. A purely empirical test can be made for our models and the deuteron because we can calculate the exact E_∞ , plot $\Delta E(L_2) \equiv E(L_2) - E_\infty$ against L_2 , and then attempt to fit each of the three choices of $\Delta E(L_2)$. Figure 2.25 shows the results for a representative model potential (a Gaussian) with moderate depth while Fig. 2.26 shows the results for the deuteron. The plots are made so that the candidate form would yield a straight line if followed precisely. We see that the exponential form is an excellent fit for the model throughout the range of L_2 and a reasonable but not perfect fit for the deuteron. The not perfect fit for the deuteron can be explained

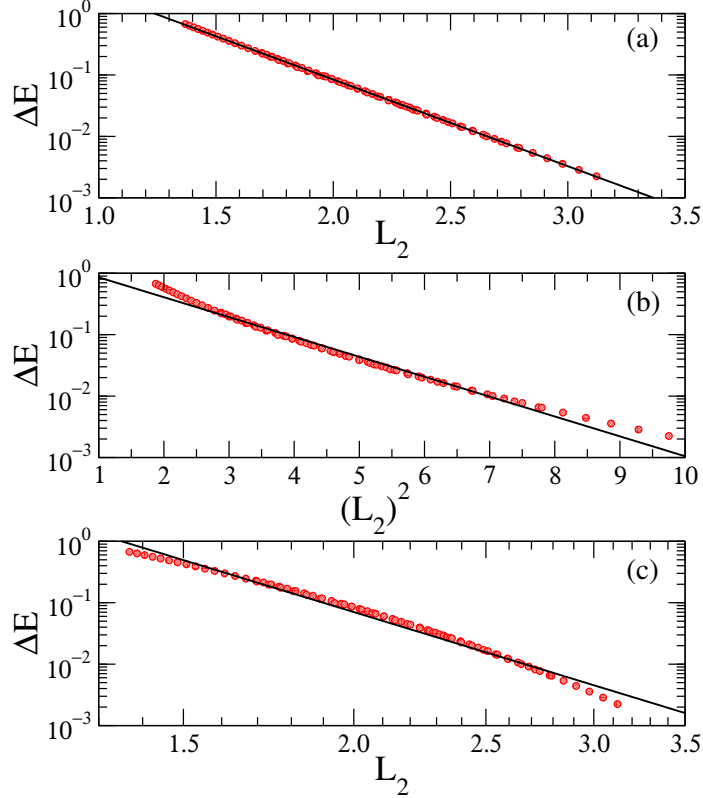


Figure 2.25: The IR energy correction ΔE_L versus L_2 for a Gaussian potential well Eq. 2.8 with $V_0 = 5$ (and $\hbar = \mu = R = 1$) using a wide range of N and $\hbar\Omega$. The energies are fitted with (a) exponential, (b) Gaussian, and (c) power law dependence on L_2 .

by noting that it is a weakly bound state. We see from Figs. 2.21 and 2.22 that for deuteron, the correction will be a sum of exponential terms. In contrast to the exponential extrapolation, Gaussian and power law fits fail over the full range of L_2 . This is consistent with Tolle *et al.* [80]. For limited ranges of L_2 a Gaussian does provide a reasonable fit (and should give a good extrapolation for E_∞ if close enough to convergence). This is consistent with the apparent success of exponential in N extrapolation observed in the literature. However, we see that globally exponential in L is clearly superior. Moreover, the exponent and coefficient (see Eq. 2.45) are

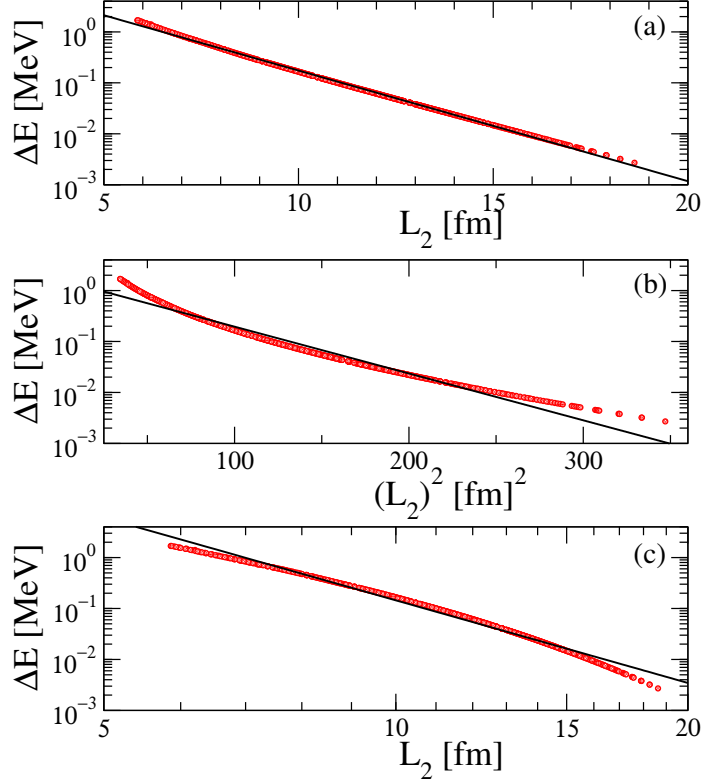


Figure 2.26: The IR energy correction ΔE_L versus L_2 for the deuteron calculated with the chiral EFT potential from Ref. [66] using a wide range of N and $\hbar\Omega$. The energies are fitted with (a) exponential, (b) Gaussian, and (c) power law dependence on L_2 .

physically motivated whereas in the exponential in N case (Eq. 2.3) these parameters are fit to data.

2.1.4 Higher angular momenta

The deuteron ground state is a mixture of an s and a d state, and the s and d asymptotic normalization coefficients (as well as the d -to- s state ratio of about 2.5%) are observables. The extrapolation formulas so far were derived for s states, and it is of interest to extend these to nonzero angular momenta l . We do so in two steps.

First, we show that L_2 is also the relevant effective hard-wall radius for oscillator wave functions with nonzero angular momenta. Second, we derive the energy correction for nonzero angular momenta.

L for nonzero angular momenta

For the derivation of the relevant IR length scale at $l > 0$ we closely follow the derivation for $l = 0$ presented in Subsec. 2.1.1. We compute the smallest eigenvalue κ^2 of the squared momentum operator \hat{p}^2 in a finite oscillator basis and identify $\kappa = x_l/L$ (with x_l being the smallest positive zero of the spherical Bessel function j_l). This identification, and the form of the corresponding eigenfunctions are, of course, guided by the Dirichlet bc at $r = L$. We set the oscillator length $b = 1$. Because this is the only length scale here, the results are general and can be extended to any b with simple rescaling. The normalized radial oscillator wave function of energy

$$E = 2n + l + 3/2 \quad (2.81)$$

is $\psi_{nl}(r) = u_{nl}(r)/r$ with

$$u_{nl}(r) = \sqrt{\frac{2n!}{\Gamma(n+l+3/2)}} r^{l+1} e^{-r^2/2} L_n^{l+1/2}(r^2). \quad (2.82)$$

Here, $L_n^{l+1/2}$ denotes the generalized Laguerre polynomial.

In this basis, the operator \hat{p}^2 of the momentum squared is tridiagonal with matrix elements

$$\begin{aligned} \langle u_{ml} | \hat{p}^2 | u_{nl} \rangle &= (2n + l + 3/2) \delta_m^n \\ &+ \sqrt{n+1} \sqrt{n+l+3/2} \delta_m^{n+1} \\ &+ \sqrt{n} \sqrt{n+l+1/2} \delta_m^{n-1}. \end{aligned} \quad (2.83)$$

For the eigenfunction of \hat{p}^2 with smallest eigenvalue κ^2 at angular momentum l , we make the ansatz $\psi_{\kappa l}(r)/r$ with

$$\psi_{\kappa l}(r) = \begin{cases} \kappa r j_l(\kappa r) , & 0 \leq \kappa r \leq x_l , \\ 0 , & \kappa r > x_l . \end{cases} \quad (2.84)$$

Here, j_l is the regular spherical Bessel function and x_l is its smallest positive zero. Clearly, these eigenfunctions are those of a particle in a spherical cavity with a Dirichlet bc at x_l/κ . In an infinite basis, the wave function $\psi_{\kappa l}(r)/r$ is an eigenfunction of \hat{p}^2 for any non-negative value of κ . In a finite oscillator basis, only discrete momenta κ are allowed. For their computation we expand the eigenfunction as

$$\psi_{\kappa l}(r) = \sum_{m=0}^n c_m(\kappa) u_{ml}(r) , \quad (2.85)$$

where we suppress the dependence of the admixture coefficients $c_m(\kappa)$ on l , which is kept fixed throughout this derivation.

The last row of the matrix eigenvalue problem for \hat{p}^2 is

$$(2n + l + 3/2 - \kappa^2) c_n(\kappa) = -\sqrt{n} \sqrt{n + l + 1/2} c_{n-1} , \quad (2.86)$$

and this becomes the quantization condition for κ . The direct computation of the coefficients $c_n(\kappa)$ seems difficult. Instead, we make a Fourier-Bessel expansion

$$\psi_{\kappa l}(r) = \sqrt{\frac{2}{\pi}} \int_0^\infty dk \tilde{\psi}_{\kappa l}(k) kr j_l(kr) , \quad (2.87)$$

and use

$$kr j_l(kr) = \sqrt{\frac{\pi}{2}} \sum_{n=0}^{\infty} (-1)^n u_{nl}(k) u_{nl}(r) . \quad (2.88)$$

Thus,

$$\psi_{\kappa l}(r) = \sum_{n=0}^{\infty} (-1)^n u_{nl}(r) \int_0^\infty dk \tilde{\psi}_{\kappa l}(k) u_{nl}(k) , \quad (2.89)$$

and the admixture coefficients are therefore

$$c_n(\kappa) = (-1)^n \int_0^\infty dk \tilde{\psi}_{\kappa l}(k) u_{nl}(k) . \quad (2.90)$$

So far, our formal manipulations have been exact. We now employ an asymptotic approximation of the generalized Laguerre polynomials (which enters the $u_{nl}(k)$) in terms of Bessel functions, valid for $n \gg 1$, see Eq. 15 of Ref. [81]. This yields

$$u_{nl}(k) \approx \frac{2^{1-n}}{\pi^{1/4}} \sqrt{\frac{(2n+2l+1)!}{(n+l)!n!}} (4n+2l+3)^{-\frac{l+1}{2}} \sqrt{4n+2l+3} k j_l(\sqrt{4n+2l+3}k) , \quad (2.91)$$

and

$$c_n(\kappa) \approx C_{nl} \sqrt{\frac{2}{\pi}} \int_0^\infty dk \tilde{\psi}_{\kappa l}(k) \sqrt{4n+2l+3} k j_l(\sqrt{4n+2l+3}k) . \quad (2.92)$$

Here, C_{nl} is a constant that does not depend on κ . The key point is that the asymptotic expansion in terms of Bessel functions allows us now to employ the definition in Eq. 2.87 to evaluate the integral

$$\begin{aligned} & \sqrt{\frac{2}{\pi}} \int_0^\infty dk \tilde{\psi}_{\kappa l}(k) \sqrt{4n+2l+3} k j_l(\sqrt{4n+2l+3}k) \\ &= \tilde{\psi}_{\kappa l}(\sqrt{4n+2l+3}) \\ &= \sqrt{4n+2l+3} \kappa j_l(\sqrt{4n+2l+3}\kappa) . \end{aligned} \quad (2.93)$$

Putting it all together, we find

$$c_n(\kappa) = \frac{2^{1/2-n}(-1)^n \pi^{1/4}}{(4n+2l+3)^{l/2}} \sqrt{\frac{(2n+2l+1)!}{(n+l)!n!}} \kappa j_l(\sqrt{4n+2l+3}\kappa) . \quad (2.94)$$

We insert this expression for $c_n(\kappa)$ into the quantization condition of Eq. 2.86 and make the ansatz

$$\kappa = \frac{x_l}{\sqrt{4n+2l+3+2\Delta}} . \quad (2.95)$$

Assuming the limit $n \gg 1$ and $n \gg l$ in the quantization condition then yields

$$\Delta = 2 . \quad (2.96)$$

Thus, Δ does not depend on l in this limit, and the result is consistent with the $l = 0$ result of Ref. [56]. In other words, the extent of the position space in finite oscillator basis with maximum radial quantum number n and angular momentum l is

$$\begin{aligned} L_2 &= \sqrt{2(2n + l + 3/2 + 2)}b \\ &= \sqrt{2(N + 3/2 + 2)}b , \end{aligned} \quad (2.97)$$

in accord with Eq. 2.113.

Table 2.2 shows numerical comparisons for $l = 0, 1, 2$ and a range of n of the exact minimum momentum κ and the estimate x_l/L_2 (with $x_0 = \pi$, $x_1 \approx 4.49341$, $x_2 \approx 5.76346$). The estimates are accurate approximations of the exact results even for small $N = 2n + l$, but the accuracy decreases somewhat with increasing orbital angular momentum. In some practical calculations it might thus be of advantage to directly employ the numerical results for L_2 instead of the approximate analytical expression (Eq. 2.97).

Energy correction for finite angular momentum

Let us extend our $l = 0$ result for $[\Delta E]_{\text{LO}}$ to $l > 0$ following the S -matrix method in Subsec. 2.1.2. For orbital angular momentum l , the asymptotic wave function is

$$u_L(r) \xrightarrow{r \gg R} k_L r \left(h_l^{(1)}(ik_L r) - \frac{h_l^{(1)}(ik_L L)}{h_l^{(1)}(-ik_L L)} h_l^{(1)}(-ik_L r) \right) . \quad (2.98)$$

Here, $h_l^{(1)}$ denotes the spherical Hankel function of the first kind (or the spherical Bessel function of the third kind) [82]. By definition $u_L(L) = 0$.

l	n	κ	x_l/L_2	l	n	κ	x_l/L_2	l	n	κ	x_l/L_2
0	0	1.2247	1.1874	1	0	1.5811	1.4978	2	0	1.8708	1.7378
0	1	0.9586	0.9472	1	1	1.2764	1.2463	2	1	1.5423	1.4881
0	2	0.8163	0.8112	1	2	1.1047	1.0898	2	2	1.3509	1.3222
0	3	0.7236	0.7207	1	3	0.9892	0.9805	2	3	1.2191	1.2018
0	4	0.6568	0.6551	1	4	0.9042	0.8987	2	4	1.1207	1.1092
0	5	0.6058	0.6046	1	5	0.8382	0.8344	2	5	1.0432	1.0352
0	6	0.5651	0.5642	1	6	0.7850	0.7822	2	6	0.9801	0.9742
0	7	0.5316	0.5310	1	7	0.7408	0.7387	2	7	0.9274	0.9229
0	8	0.5035	0.5031	1	8	0.7033	0.7018	2	8	0.8824	0.8789
0	9	0.4795	0.4791	1	9	0.6711	0.6698	2	9	0.8435	0.8407
0	10	0.4585	0.4582	1	10	0.6429	0.6419	2	10	0.8093	0.8070

Table 2.2: Comparison of the exact lowest momentum κ with the analytical estimate x_l/L_2 for $l = 0, 1, 2$ and $0 \leq n \leq 10$.

In complete analogy to the case of s waves (e.g., using Eqs. 2.48 and 2.49 for general l), the correction ΔE of the energy at leading order is

$$[\Delta E]_{\text{LO}} = -k_\infty (\gamma_\infty^{(l)})^2 \frac{h_l^{(1)}(ik_L L)}{h_l^{(1)}(-ik_L L)} . \quad (2.99)$$

We note that

$$\frac{h_l^{(1)}(ix)}{h_l^{(1)}(-ix)} \approx -e^{-2x} \quad (2.100)$$

for $x \gg 1$. In particular, for $l = 1$

$$[\Delta E]_{\text{LO}} = k_\infty (\gamma_\infty^{(1)})^2 \frac{k_\infty L + 1}{k_\infty L - 1} e^{-2k_\infty L} , \quad (2.101)$$

and for $l = 2$

$$[\Delta E]_{\text{LO}} = k_\infty (\gamma_\infty^{(2)})^2 \frac{(k_\infty L)^2 + 3k_\infty L + 3}{(k_\infty L)^2 - 3k_\infty L + 3} e^{-2k_\infty L} . \quad (2.102)$$

These corrections are tested in Fig. 2.27. For coupled channels, the leading energy correction will be the sum of the LO corrections for the individual angular momenta.

We note that lattices with periodic bc lead to energy shifts that depend on the

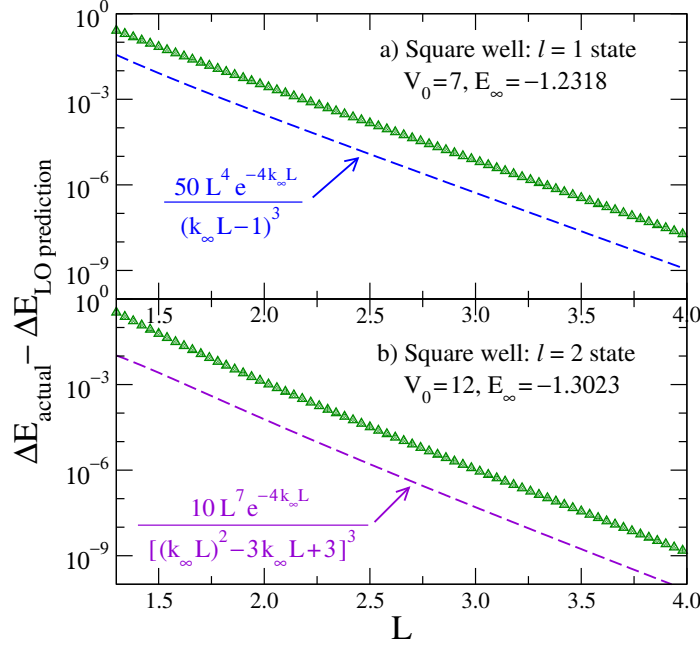


Figure 2.27: Error plots of the energy correction at each L for (a) $l = 1$ and (b) $l = 2$ square-well states predicted at leading order by Eqs. 2.101 and 2.102 compared to the exact energy. Lines proportional to the expected L-NLO residual errors are plotted for comparison.

angular momentum [83]. In contrast, the basis truncations we consider in this work are variational and thus always yield a positive energy correction.

We return to the deuteron and take $|\gamma_\infty^{(2)} / \gamma_\infty^{(0)}| \approx 0.0226 / 0.8843$ from Ref. [24].

Then

$$[\Delta E]_{\text{LO}} = k_\infty (\gamma_\infty^{(0)})^2 e^{-2k_\infty L} \left[1 + \left| \frac{\gamma_\infty^{(2)}}{\gamma_\infty^{(0)}} \right|^2 \frac{(k_\infty L)^2 + 3k_\infty L + 3}{(k_\infty L)^2 - 3k_\infty L + 3} \right]. \quad (2.103)$$

This formula is tested in Fig. 2.28 with the same deuteron calculations as in Fig. 2.22.

We note that the deviation after subtraction of the NLO ($l = 0$) result does not exhibit the $\exp(-6k_\infty L)$ falloff but is rather consistent with an $\exp(-4k_\infty L)$ falloff at large L . We attribute this to the missing LO d -state correction. Due to the small value

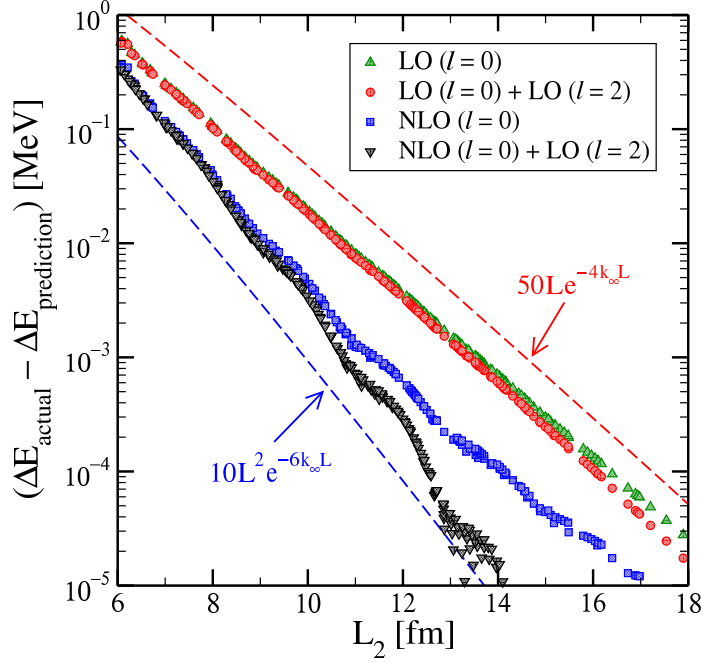


Figure 2.28: Residual error for the deuteron energy due to HO basis truncation as a function of $L = L_2$ (with $\hbar\Omega > 49$ MeV to eliminate UV contamination) after subtracting $l = 0$ energy corrections at different orders from Eq. 2.58 and the $l = 2$ correction from Eq. 2.102. For the parameter w_2 in Eq. 2.58 we use the value reported in [76].

of the d -to- s state ratio, the d -wave correction is small, but it makes a perceptible shift of the s -wave LO result. When added to the NLO $l = 0$ correction, the large L_2 behavior of the error is brought somewhat closer in line with the predicted dependence of $L^2 e^{-6k_\infty L}$. We note, however, that the NLO correction is not complete due to the missing $l = 2$ correction. Calculating NLO corrections for $l > 0$ remains an open question. Particularly, because that would entail taking into account the admixture between different channels.

2.1.5 Radii and phase shifts

Radii

Along with binding energies, another nuclear observable that we looked at was the radius squared. Figure 2.29 shows the numerical results for the squared radius for the deuteron calculated in the HO basis. Analogous to Figs. 2.5 and 2.6, we see that the results for the squared radius fall on a continuous curve with minimal spread when plotted as a function of L_2 (but not as a function of L_0).

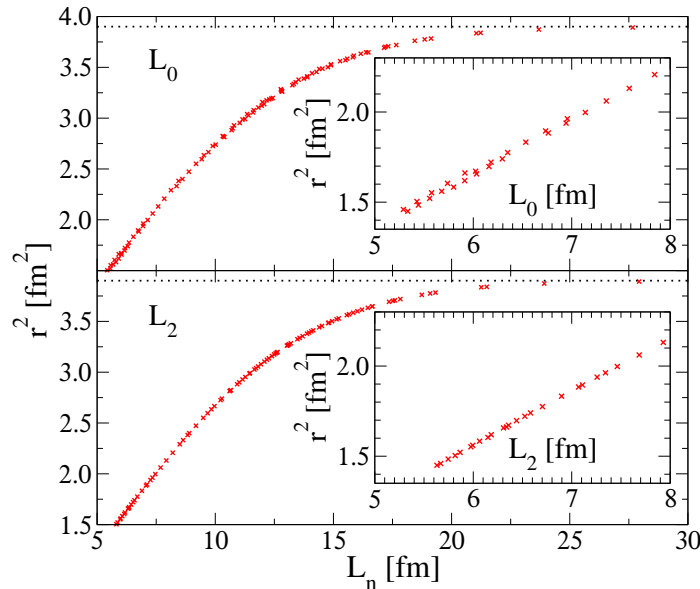


Figure 2.29: Deuteron radius squared versus L_0 (top) and L_2 (bottom) for the Entem-Machleidt 500 MeV N³LO potential [66]. The horizontal dotted lines mark the exact radius squared $r_\infty^2 = 3.9006 \text{ fm}^2$. The insets show a magnification of data at smaller lengths L_n .

Though the squared radius is a long-ranged operator, its matrix elements will still be modified at short distances by renormalizations or similarity transformations of the Hamiltonian, see, e.g., Ref. [84]. Thus we cannot expect an extrapolation law

for the radius that depends entirely on observables. Instead, we seek a formula that identifies the L dependence but leaves parameters to be fit. We define

$$\langle r^2 \rangle_L = \langle r^2 \rangle_\infty + \Delta \langle r^2 \rangle_L , \quad (2.104)$$

where

$$\Delta \langle r^2 \rangle_L = \frac{\int_0^L |u_L(r)|^2 r^2 dr}{\int_0^L |u_L(r)|^2 dr} - \frac{\int_0^\infty |u_\infty(r)|^2 r^2 dr}{\int_0^\infty |u_\infty(r)|^2 dr} . \quad (2.105)$$

The strategy is to isolate the polynomial L dependence by splitting the necessary integrals into an interior part and an exterior part:

$$\int_0^L r^n |u_L(r)|^2 dr = \int_0^R r^n |u_L(r)|^2 dr + \int_R^L r^n |u_L(r)|^2 dr , \quad (2.106)$$

where R is sufficiently large so that the asymptotic form of $u_L(r)$ from Eq. 2.65 can be used in the second integral. Our expression for $\Delta \langle r^2 \rangle_L$ is independent of the normalization of $u_L(r)$, so we are free to choose it so that the large r form is exactly given by Eq. 2.65.

The first integral in Eq. 2.106 will depend on the details of the interior wave function and therefore on the potential, but the linear energy method shows us that to $\mathcal{O}(e^{-2k_\infty L})$ the L dependence is isolated. In particular, the dependence on L of $u_L(r)$ in Eq. 2.27 is confined to $\Delta E_L = k_\infty \gamma_\infty^2 e^{-2k_\infty L}$ because $du_E(r)/dE|_{E_\infty}$ for $r < R$ is independent of L with our choice of normalization. Thus the integral over r cannot introduce polynomial L dependence and we can conclude that

$$\int_0^R r^n |u_L(r)|^2 dr = \mathcal{O}(L^0) e^{-2k_\infty L} + \mathcal{O}(e^{-4k_\infty L}) . \quad (2.107)$$

The $\mathcal{O}(L^0)$ coefficient will depend on the potential, so we will treat it as a parameter to be fit.

The second integral can be directly evaluated to $\mathcal{O}(e^{-2k_\infty L})$ using Eq. 2.65 and

$[k_L]_{LO} = k_\infty - \gamma_\infty^2 e^{-2k_\infty L}$ to expand $|u_L(r)|^2$. For $n = 0$ we find

$$\int_R^L |u_L(r)|^2 dr = \frac{1}{2k_\infty} e^{-2k_\infty R} + \left[\frac{\gamma_\infty^2}{k_\infty} \left(R + \frac{1}{2k_\infty} \right) e^{-2k_\infty R} + 2R - 2L \right] e^{-2k_\infty L} + \mathcal{O}(e^{-4k_\infty L}), \quad (2.108)$$

and for $n = 2$ we find

$$\begin{aligned} \int_R^L r^2 |u_L(r)|^2 dr &= \frac{1}{2k_\infty^3} \left[\frac{1}{2} + k_\infty R + (k_\infty R)^2 \right] e^{-2k_\infty R} \\ &\quad + \left[\frac{\gamma_\infty^2}{k_\infty^4} \left(\frac{3}{4} + \frac{3}{2} k_\infty R + \frac{3}{2} (k_\infty R)^2 + (k_\infty R)^3 \right) e^{-2k_\infty R} \right. \\ &\quad \left. + \frac{1}{k_\infty^3} \left(\frac{2}{3} (k_\infty R)^3 - k_\infty L - \frac{2}{3} (k_\infty L)^3 \right) \right] e^{-2k_\infty L} + \mathcal{O}(e^{-4k_\infty L}). \end{aligned} \quad (2.109)$$

Note that it is necessary to keep the expansion of $|u_L(r)|^2$ up to $e^{-4k_\infty L}$ until after doing the integrals because terms proportional to $e^{-4k_\infty L} e^{2k_\infty r}$ will be leading order.

When we use Eqs. 2.108 and 2.109 and our previous result for the interior integrals in Eq. 2.105, expanding consistently to $\mathcal{O}(e^{-2k_\infty L})$, we will mix R -dependent terms with the L dependence. However, we can immediately conclude that the general form to this order is (with $\beta \equiv 2k_\infty L$)

$$\langle r^2 \rangle_L \approx \langle r^2 \rangle_\infty [1 - (c_0 \beta^3 + c_1 \beta + c_2) e^{-\beta}]. \quad (2.110)$$

Here, $\langle r^2 \rangle_\infty$, c_0 , c_1 , and c_2 are fit parameters while k_∞ should be determined from fitting the energy. This form has been verified explicitly for finite-range model potentials (e.g., square well and delta shell). The approximation in Eq. 2.110 should be valid in the asymptotic regime $\beta \gg 1$. In practice, one needs $\beta \gtrsim 3$ so that the dominant β^3 correction is approximately an order of magnitude larger than the subleading terms (with c_1 and c_2 expected to be roughly the same size as c_0 or smaller).

If we take the zero-range limit $R \rightarrow 0$ of the potential, we arrive at the simple expression

$$\frac{\Delta \langle r^2 \rangle_L}{\langle r^2 \rangle_\infty} \approx - \left(\frac{(2k_\infty L)^3}{3} - 4 \right) e^{-2k_\infty L}. \quad (2.111)$$

Note that in this limit the correction becomes independent of the potential. Equation 2.111 suggests that for a short-range potential, the c_1 and c_2 terms will give comparable contributions for moderate β , and therefore will be difficult to determine reliably.

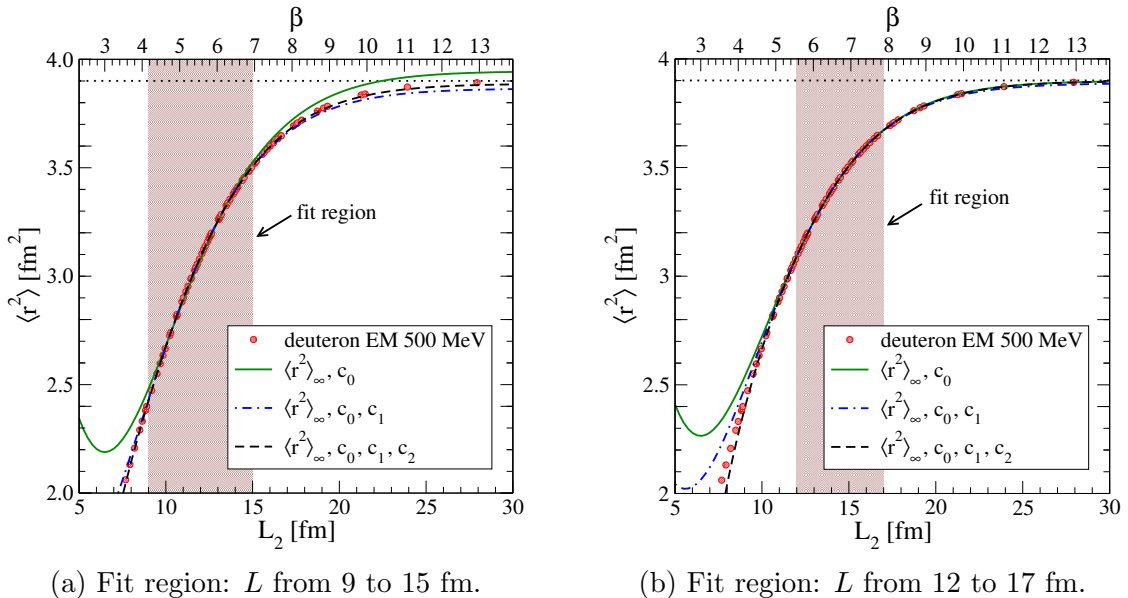


Figure 2.30: Deuteron radius squared versus L_2 for the chiral N^3LO (500 MeV) potential of Ref. [66]. To eliminate the UV contamination we only plot results for $\hbar\Omega > 49$ MeV. The solid, dot-dashed, and dashed lines are results from fitting Eq. 2.110 in the shaded region to find $\langle r^2 \rangle_\infty$ and one, two, or three of the c_i constants, respectively. The horizontal dotted line is the deuteron radius squared.

Sample fits of Eq. 2.110 for the deuteron are shown in Fig. 2.30. Results are obtained for fitting one, two, and all three c_i constants to radii calculated with the same truncated oscillator basis parameters used for Fig. 2.21. The fit region is for L_2 between 9 and 15 fm, where the calculations only show a small amount of curvature

and between 12 and 17 fm. All points are equally weighted. The values for $\langle r^2 \rangle_\infty$

fit region: L from 9 to 15 fm. Exact: $\langle r^2 \rangle_\infty = 3.901 \text{ fm}^2$, $k_\infty = 0.232 \text{ fm}^{-1}$				
	$\langle r^2 \rangle_\infty$	c_0	c_1	c_2
1 term	3.945 ± 0.006	0.331 ± 0.002	—	—
2 terms	3.865 ± 0.001	0.266 ± 0.001	1.131 ± 0.018	—
3 terms	3.887 ± 0.001	0.308 ± 0.002	-1.239 ± 0.135	7.167 ± 0.408

Table 2.3: Coefficients from fitting Eq. 2.110 to the deuteron data using one, two, or three c_i constants as shown in Fig. 2.30a

and the coefficients c_i 's from the fits in Fig. 2.30 are reported in Tables 2.3 and 2.4.

For all of these fits, the value of c_0 is fairly stable, ranging from 0.27 to 0.33 (note that $c_0 = 1/3$ in the zero-range limit). In contrast, c_1 and c_2 are not well determined (even the sign of c_1 varies). This is consistent with fits using the square-well potential, where analytic expressions for the c_i 's can be found. We find that $\langle r^2 \rangle_\infty$ and c_0 are well determined by fits in analogous regions but that c_1 and c_2 are not. If we push the analysis by taking the fit region between 7 and 13 fm, the $\langle r^2 \rangle_\infty$ prediction using only c_0 breaks down, giving 4.21 fm^2 . However, the fit with all three c_i 's is still reasonable, giving 3.86 fm^2 . This indicates the importance of using the correct functional form

fit region: L from 12 to 17 fm. Exact: $\langle r^2 \rangle_\infty = 3.901 \text{ fm}^2$, $k_\infty = 0.232 \text{ fm}^{-1}$				
	$\langle r^2 \rangle_\infty$	c_0	c_1	c_2
1 term	3.899 ± 0.001	0.312 ± 0.000	—	—
2 terms	3.888 ± 0.001	0.293 ± 0.001	0.503 ± 0.026	—
3 terms	3.898 ± 0.001	0.339 ± 0.006	-3.577 ± 0.508	15.339 ± 1.908

Table 2.4: Coefficients from fitting Eq. 2.110 to the deuteron data using one, two, or three c_i constants as shown in Fig. 2.30b

for extrapolation. Further studies are needed to test how these trends might carry over to $A > 2$ nuclei. It is worthwhile to note that this approach can be generalized to any coordinate space operator.

Phase shifts

The argument for computing scattering phase shifts is as follows: The oscillator basis appears as a spherical box of size L . For low momenta we have $L = L_2$, but at higher momentum L deviates slightly from L_2 , and can be determined from the eigenvalues of the operator p^2 . Thus, the positive-energy states computed in the oscillator basis can be used to extract phase shifts.

In a fixed harmonic oscillator basis ($N, \hbar\Omega$), the computation of the phase shifts for a given partial wave $^{2S+1}l_J$ with orbital angular momentum l proceeds as follows: First, one computes the discrete eigenvalues p_i^2 of the operator p^2 for orbital angular momentum l . Second, we need to determine the momentum dependent box size $L_i = L(p_i)$. Assuming that the i^{th} momentum eigenstate is the i^{th} eigenstate of a spherical box, we must determine the i^{th} zero of the spherical Bessel function. Thus $j_l(p_i L_i / \hbar) = 0$ determines $L(p_i)$. We evaluate the smooth function $L(p)$ for arbitrary momentum p by interpolating between the discrete momenta p_i . Third, we compute the discrete positive energies $E_i = \hbar^2 k_i^2 / (2m)$ of the neutron-proton system in relative coordinates for the partial wave $^{2S+1}l_J$, and compute the phase shifts from the Dirichlet boundary condition at $r = L$, i.e.

$$\tan \delta_l(k_i) = \frac{j_l(k_i L(\hbar k_i))}{\eta_l(k_i L(\hbar k_i))}. \quad (2.112)$$

Here η_l is the spherical Neumann function. In practice one repeats this procedure for several values of $\hbar\Omega$ in order to get sufficiently many datapoints that fall onto

a smooth curve. Note that for E_i or k_i are obtained from diagonalizing the nuclear Hamiltonian in HO basis whereas p_i are obtained from diagonalizing the momentum squared operator.

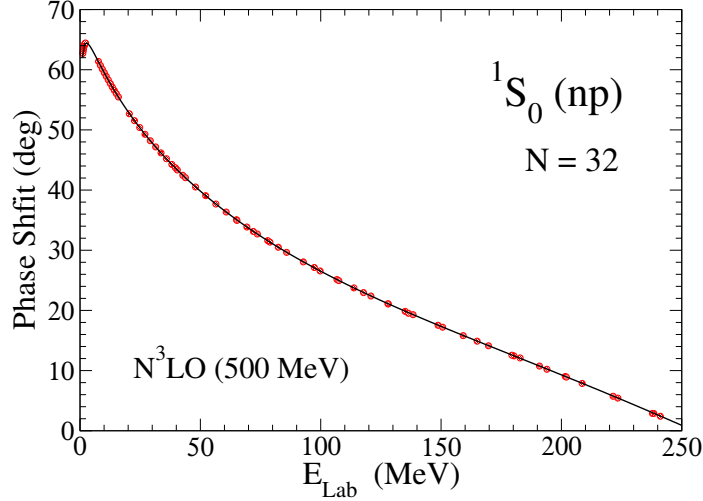


Figure 2.31: The ${}^1\text{S}_0$ phase shifts (in degrees) of the N^3LO chiral interaction (solid line) compared to the phase shifts computed directly in the harmonic oscillator basis (circles).

As examples we compute the scattering phase shifts for the ${}^1\text{S}_0$ and ${}^3\text{P}_1$ partial waves in model spaces with $N = 32$ and $\hbar\Omega = 20, 22, \dots, 40$ MeV. Our calculations are based on the Entem-Machleidt 500 MeV chiral EFT N^3LO potential [66]. Figures 2.31 and 2.32 show the results and compares them to the numerically exact phase shifts. For smaller N than our current choice, the computed phase shifts start to deviate from exact phase shifts at higher energies. However, if one is interested only in low-energy phase shifts and observables such as the scattering length and the effective range, a smaller harmonic oscillator basis is sufficient.

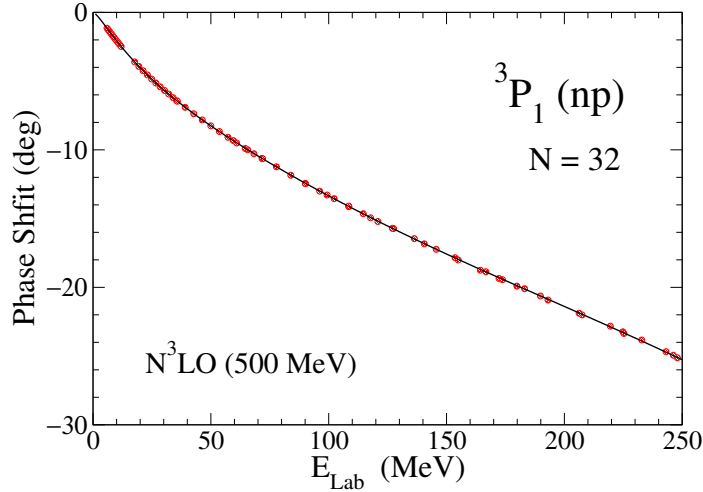


Figure 2.32: The 3P_1 phase shifts (in degrees) of the N^3LO chiral interaction (solid line) compared to the phase shifts computed directly in the harmonic oscillator basis (circles).

There are other methods to compute scattering phase shifts in the harmonic oscillator basis. Bang *et al.* [85] used the method of harmonic oscillator representation of scattering equations (HORSE) for this purpose, and more recent works [86, 87] computed phase shifts to develop an EFT for nuclear interactions directly in the oscillator basis [68]. References [86, 87] build on the results by Busch *et al.* [88] and their generalization [89] to finite range corrections, and extract scattering information from the energy shifts of bound states in a harmonic oscillator potential. The resulting EFTs are quite efficient for contact interactions and systems such as ultracold trapped fermions, but nuclear potentials with a finite range require an extrapolation of $\Omega \rightarrow 0$ [86]. The approach presented in this Subsection is more direct, as no external oscillator potential is employed. We note that the phase shift analysis presented here can be extended to coupled channels as well.

Finally, we note again that the approach of this Section can be utilized in other localized basis sets. All that is required is the diagonalization of the operator p^2 in the employed basis set, which yields the (momentum dependent) box size.

2.2 Ultraviolet story⁸

In Sec. 2.1 we worked in the region where the UV errors were small and focused on the IR errors. However, for many methods full suppression of the UV errors is not feasible and the need to understand UV corrections remains. In all cases the UV effect is a systematic error that must be quantified. In addition, this error worsens for harder nucleon–nucleon potentials that may still be of interest. The understanding of the UV errors formed the focus of our work in Ref. [58]. The author of this thesis contributed to the work presented in [58]. However, the UV effort was mainly spearheaded by Sebastian König, the post-doc in the group. To avoid misappropriation of credit, only a summary of results from [58] will be presented in this section. The summary presented here hopes to elucidate how the UV results tie into our broader agenda of developing reliable extrapolations schemes for nuclear calculations. We refer the reader to [58] for the additional UV extrapolation details.

We follow the strategy of Sec. 2.1 by focusing on the two-body problem and exactly solvable examples to establish the true UV behavior for the simple systems and then make correspondence to the nuclear systems.

⁸Based on [58]

2.2.1 Duality and momentum-space boxes

To briefly recap results in Subsec. 2.1.1—we demonstrated there that a truncated oscillator basis with highest excitation energy $N\Omega$ effectively imposes a spherical hard-wall boundary condition at a radius depending on N and b . The optimal effective radius L_{eff} can be determined by matching the smallest eigenvalue κ^2 of the squared momentum operator p^2 in the finite basis to the corresponding eigenvalue of the spherical box, namely $\kappa = \pi/L$ (for $\ell = 0$). The value can be established numerically, but an accurate approximation for the two-body system is

$$L_{\text{eff}} = L_2 \equiv \sqrt{2(N + 3/2 + 2)b}. \quad (2.113)$$

Note that L_2 differs by $\mathcal{O}(1/N)$ from the naive estimate $L_0 \equiv \sqrt{2(N + 3/2)b}$. In localized bases that differ from the harmonic oscillator, L can also be determined from a numerical diagonalization of the operator p^2 .

The dual nature of the harmonic oscillator Hamiltonian

$$H_{\text{HO}} = \frac{p^2}{2\mu} + \frac{\mu\Omega^2 r^2}{2} \quad (2.114)$$

(*i.e.*, under $p \leftrightarrow \mu\Omega r$) implies that the truncation of the basis will effectively impose a sharp cutoff at a momentum Λ_{eff} depending only on N and b . The analog matching condition leads us to consider the smallest eigenvalue (denoted ρ) of the operator r^2 evaluated in that truncated basis. This eigenvalue is identical to the smallest (squared) distance that can be realized in the oscillator basis. Thus it corresponds to a lattice spacing on a grid and therefore sets the highest momentum available. As we see in Fig. 2.33, the square root of the largest eigenvalue of the squared momentum operator, which might be a natural guess for the effective UV cutoff, is not an accurate estimate for Λ_{eff} . From steps completely analogous (dual) to those given

in Subsec. 2.1.1 for the IR case, we find that the solution (in a subspace with fixed angular momentum ℓ) is

$$\rho = \frac{x_\ell b}{\sqrt{2}} \left(N_{\max} + \frac{3}{2} + \Delta \right)^{-1/2} \quad (2.115)$$

with $\Delta = 2$ to leading order. The constant x_ℓ in the prefactor is the first positive zero of the spherical Bessel function j_ℓ . Since the UV cutoff is given by x_ℓ/ρ , it drops out again in our final result:

$$\Lambda_2 \equiv \sqrt{2(N_{\max} + 3/2 + 2)}/b. \quad (2.116)$$

Hence, we have shown that the proper effective UV cutoff imposed by the basis truncation is given by Λ_2 , which differs by a correction term from the naive estimate

$$\Lambda_0 \equiv \sqrt{2(N_{\max} + 3/2)}/b \quad (2.117)$$

that one obtains by simply considering the maximum single-particle energy level represented by the truncated basis. We note that subleading corrections to $\Delta = 2$, which by duality apply equally to the IR and UV cutoff, are derived in Appendix of Ref. [58].

Fig. 2.33 shows the relative error when plotted against three cutoff variables, Λ_2 , Λ_0 , and $\Lambda_{\kappa_{\max}}$. The calculations use the 500 MeV N³LO nucleon-nucleon NN potential of Ref. [66], evolved by the SRG [48] to $\lambda = 2$ fm⁻¹. $\Lambda_{\kappa_{\max}}$ is defined as the square root of the largest eigenvalue of the squared momentum operator in the finite oscillator basis, which one might naively expect to be a natural choice. However, of the cases considered this actually gives the largest scatter in data. From the fact that we get an essentially smooth curve only for Λ_2 , we conclude that this identification of the relevant UV cutoff is correct. In Fig. 2.34, deuteron calculations are plotted as

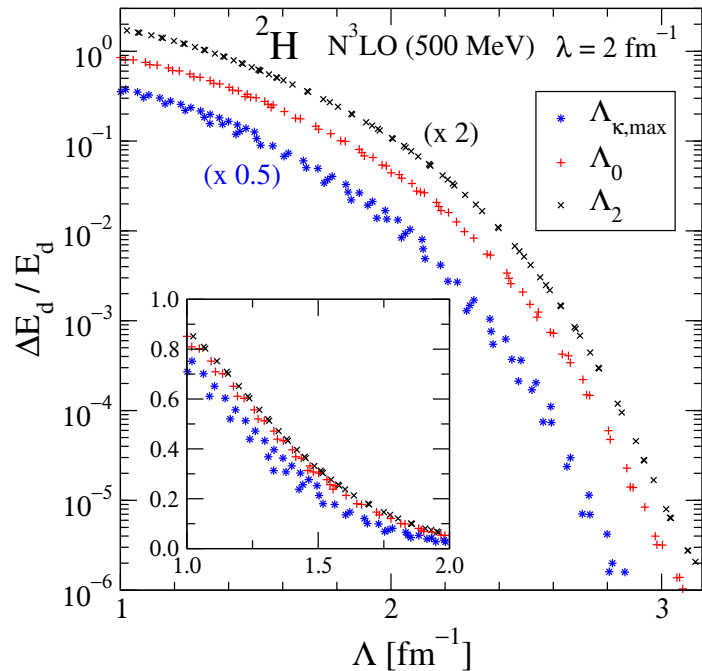


Figure 2.33: Relative error of deuteron binding energy plotted vs. lengths Λ_2 , Λ_0 , and $\Lambda_{\kappa,\text{max}}$ (multiplied by factors 2, 1, and 1/2, respectively, to separate the curves. Inset: The same values on a linear scale and without the separation factors.

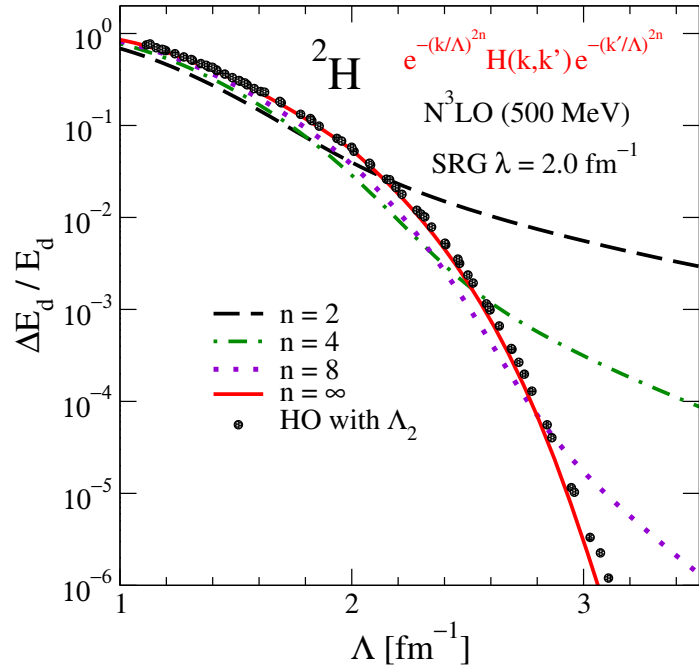


Figure 2.34: Calculations of the relative error in the deuteron energy as a function of $\Lambda_2(N_{\max}, \hbar\Omega)$. Circles represent a wide range of oscillator parameters N_{\max} and $\hbar\Omega$ that are IR converged. The series of lines shows energies for which the Hamiltonian has been smoothly cutoff with exponent n . The solid line corresponds to a sharp cutoff.

a function of $\Lambda = \Lambda_2(N_{\max}, \Omega)$ along with several other functions of Λ given by the relative error from the same Hamiltonian, but now smoothly cut off as

$$H_{\text{cut}}(k, k') = e^{-(k^2/\Lambda^2)^n} H(k, k') e^{-(k'^2/\Lambda^2)^n}, \quad (2.118)$$

for $n = 2, 4, 8$ and ∞ . The latter corresponds to a sharp cutoff. We find that the curve from a sharp cutoff tracks the truncated-oscillator points through many orders of magnitude. This validates the claim that the error from oscillator basis truncation is well reproduced by applying instead a sharp cutoff in momentum at Λ_2 .

2.2.2 Separable approximations

We showed in Ref. [58] that for a separable interaction of the form

$$V(k', k) = g \eta(k') \eta(k), \quad (2.119)$$

UV energy correction formula can be exactly derived. For potential in Eq. 2.119, the cutoff dependent binding momentum κ_λ is given by the quantization condition

$$-1 = 4\pi a \int_0^\Lambda dk \frac{k^2 \eta_\lambda^2(k)}{\kappa_\Lambda^2 + k^2}, \quad (2.120)$$

which is straightforward to solve numerically.

However, most interactions used in practical calculations do not have this convenient simple form (at least not in nuclear physics). Still, as shown in Ref. [58], Eq. 2.120 can be put to some use using separable approximations. Methods to obtain separable approximations for a given potential have been known and used for quite a while (see, *e.g.*, Refs. [90–92]). The technique we use is called *unitary pole approximation (UPA)* [91, 93]. Assuming that for an arbitrary potential \hat{V} we know a (bound) eigenstate $|\psi\rangle$, we can construct a rank-1 separable approximation in momentum

space by setting

$$\hat{V}_{\text{sep}} = \frac{|\eta\rangle\langle\eta|}{\langle\psi|\hat{V}|\psi\rangle} = \frac{\hat{V}|\psi\rangle\langle\psi|\hat{V}}{\langle\psi|\hat{V}|\psi\rangle}. \quad (2.121)$$

In other words, we have

$$\eta(k) = \langle k|\hat{V}|\psi\rangle \quad (2.122)$$

for the momentum-space “form factor,” and the coupling strength $g = \langle\psi|\hat{V}|\psi\rangle$ is, of course, independent of any particular representation. From Eq. 2.121 one immediately sees that

$$\hat{V}_{\text{sep}}|\psi\rangle = \hat{V}|\psi\rangle. \quad (2.123)$$

This means that the separable approximation is constructed in such a way that it exactly reproduces the state $|\psi\rangle$ used for its construction. The potential from Eq. 2.121 reproduces the exact half off-shell T-matrix at the energy corresponding to the state ψ , and more sophisticated approximations (separable potential of rank > 1) can be constructed by using more than a single state [91]. Since we are only interested in performing the UV extrapolation for a single state, however, the rank-1 approximation is sufficient. To assess to what extent it actually reflects the UV behavior of a calculation based on the *original* potential, we first considered some examples where the separable approximation can be constructed analytically such as the square well (Eq. 2.6) and the Pöschl-Teller potential of the form

$$V_{\text{PT}}(r) = -\frac{\alpha^2\beta(\beta-1)}{\cosh^2(\alpha r)}. \quad (2.124)$$

For given values of α and β , this potential has an analytically known bound-state spectrum. Motivated by the success of the separable approximation (Eq. 2.121) for the toy models, we moved on to the deuteron. Here we will just look at a few representative results for the deuteron.

A difficulty in applying the separable approximation directly to the deuteron is that the form factor $n(k)$ in Eq. 2.122 depends on the deuteron wave function. The exact wave function of course can not be calculated due to the truncation in the HO basis. We use the best wave function available from the largest oscillator space and set

$$\eta(k) = \langle k | \hat{V} | \psi \rangle_{\text{HO, best}} . \quad (2.125)$$

As we know, deuteron has both S - and D -wave components. This is taken into account by letting $\eta \rightarrow \eta_S^2 + \eta_D^2$.

As derived in Ref. [58], the simplest fit formula inspired by separable approximation is

$$\kappa_\Lambda = \kappa_\infty - A \int_\Lambda^\infty dk \eta(k)^2 , \quad (2.126)$$

In Figs. 2.35, 2.36, and 2.37 we show the results obtained for the deuteron from fitting to Eq. 2.126. We compare the result for separable fit to two phenomenological choices. The exponential fit

$$\kappa_\Lambda = \kappa_\infty - a e^{-b\Lambda} , \quad (2.127)$$

and the gaussian fit

$$\kappa_\Lambda = \kappa_\infty - a e^{-b\Lambda^2} . \quad (2.128)$$

We see from Figs. 2.35, 2.36, and 2.37 that the fit from the separable approximation is superior to phenomenological fits. The separable approximation allows extrapolation even when we are far from convergence (this is especially evident in Fig. 2.35). It is also worthwhile to note that the separable fit (Eq. 2.126) has just two fit parameters κ_∞ and A , whereas the phenomenological fits have three free parameters κ_∞ , a , and

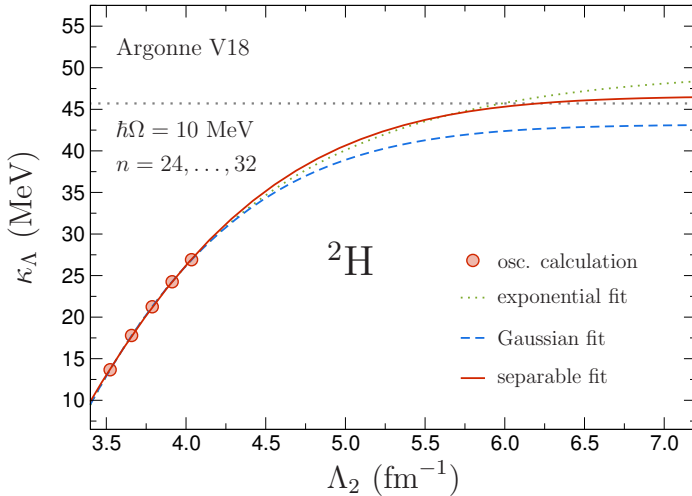


Figure 2.35: Comparison of UV extrapolations for a deuteron state calculated with the AV18 potential of Ref. [12]. Circles: oscillator results. Dotted line: exponential extrapolation (Eq. 2.127). Dashed line: Gaussian extrapolation (Eq. 2.128). Solid line: simplest separable extrapolation (Eq. 2.126). Dotted horizontal lines indicate the exact result for the binding momentum.

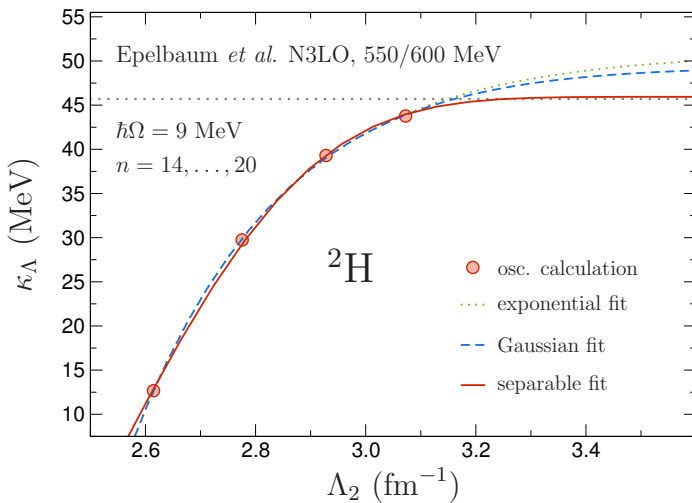


Figure 2.36: Calculations of UV extrapolations for a deuteron state calculated with the Epelbaum *et al.* N3LO (550/600 MeV cutoff) potential of Ref. [51]. The legend description is the same as in Fig. 2.35.

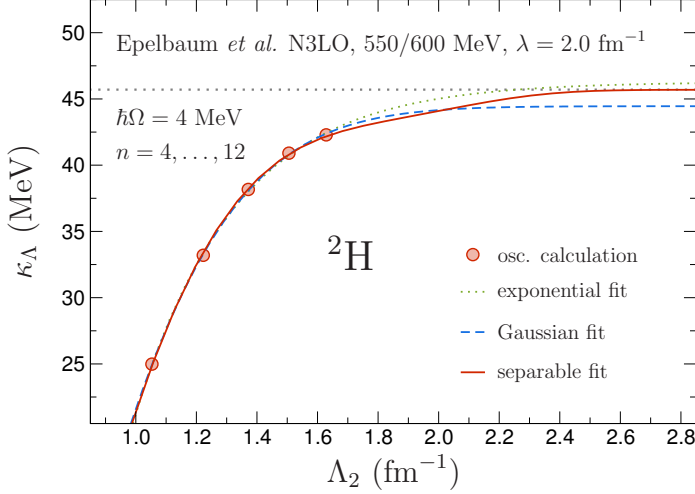


Figure 2.37: Calculations of UV extrapolations for a deuteron state calculated with the Epelbaum *et al.* N3LO (550/600 MeV cutoff) potential of Ref. [51]. The legend description is the same as in Fig. 2.35.

b. The reason that the separable fit does well is that it puts in the information we already know about the state through Eq. 2.125.

The IR and UV corrections exhibit a complementary mix of universal and non-universal characteristics. The IR corrections are dictated by asymptotic behavior and are consequently determined by observables, independent of the details of the interaction. So unitarily equivalent potentials—such as those generated by renormalization-group running—will have the same corrections. In contrast, because they probe short-range features, UV corrections depend on the details of the interaction (and the state under consideration). However, the IR correction depends on the number of nucleons, whereas as we will see in Subsec. 2.3.2 the UV correction is expected to scale simply with the number of particles.

2.3 Moving forward and related developments

In this section, we will list the open questions with respect to both IR and UV extrapolations. As mentioned before, this approach of mapping the HO truncation to IR and UV cutoffs and using them to obtain physically motivated extrapolation formulas was rigorously developed for the first time by us [56–58]. This pioneering work has sprouted many new developments by extending our work. We will briefly touch upon some of these related developments.

2.3.1 IR front

Open questions

As discussed towards the end of Subsec. 2.1.4, the NLO IR correction is incomplete due to the missing $l = 2$ correction. It might be challenging to derive NLO corrections to the binding energies for nuclei with $A > 2$, particular for nuclei with nonzero ground-state spin. Here, many different orbital angular momenta can contribute to the ground-state wave function, and one would presumably need to know the admixture of the different channels quite accurately. Our results show that nonzero orbital angular momenta yield corrections in inverse powers of $k_\infty L$ to the LO energy extrapolation. On the other hand, the leading contributions to bound-state energies in finite model spaces fall off as $\exp(-2k_\infty L)$ for all orbital angular momenta. This makes extrapolations feasible in practice.

The formulation in terms of S-matrix analytic structure is closely related to methods used to analyze break-up reactions, which provides a link to $A > 2$ extrapolations. Indeed, in Ref. [73] the basic form of the LO extrapolation proportional to $e^{-2k_\infty L}$ was based on interpreting k_∞ in terms of the one-particle separation energy. More

generally, the asymptotic many-body wave function is dominated by configurations corresponding to the break-up channels with the lowest separation energies and it is their modification by the hard wall at L that will be associated with the energy shift ΔE_L . This is in turn dominantly described by the S-matrix near poles at the corresponding separation binding momenta. Future work will seek to clarify the precise nature of the more general expansion (including the effects of the Coulomb interaction) and whether it will be possible to quantitatively extract asymptotic normalization constants.

Relation to Lüscher-type formulas We saw in Subsec. 1.4.1 that lattice theories have an inherent IR and UV cutoff. Starting with the seminal work of Lüscher [70], a wide variety of formulas have been derived for the energy shift of bound states in finite-volume lattice calculations. The usual application is to simulations that use periodic boundary conditions in cubic boxes (e.g., see Ref. [94]). The recent work by Pine and Lee [95, 96] extend the derivation to hard-wall boundary conditions using effective field theory for zero-range interactions and the method of images. The result for ΔE_L in a three-dimensional cubic box has a different functional form than found here (the leading exponential is multiplied by $1/L$ with that geometry) and the subleading corrections are parametrically larger.

However, because the HO truncation we consider is in partial waves, the one-dimensional analysis and formula from Ref. [96] are applicable (because k_∞ and γ_∞ are asymptotic quantities, the result for zero-range interaction is actually general for short-range interactions). The method of images can be applied in a one-dimensional box of size $2L$ after specializing to a particular partial wave and then extending

the space to odd solutions in r from $-\infty$ to $+\infty$. The leading-order finite-volume correction agrees with Eq. 2.45, and the first omitted term is of the same order. The methods presented in [95, 96] can be used to extend the present formulas to higher orders and more general cases, including coupled channels. This area is ripe for investigation.

Another area of investigation is how the trends for operator extrapolation carry over for $A > 2$.

Related developments

The results presented in this chapter have exclusively been for the two-body case. Figure 2.38 shows $\Delta E = E_{\text{HO}} - E_\infty$ for triton plotted as a function of L_2 . Recall from Eq. 2.113 that evaluating L_2 involves calculating the oscillator length b . In Fig. 2.38, we use the deuteron-neutron reduced mass, $\mu = 2/3M_N$, to calculate b and thereby L_2 . There are a few interesting observations to be made about Fig. 2.38. Triton energies when plotted as a function of L_2 lie on a single line. Also, as in Fig. 2.23, triton energies from potentials evolved to various SRG λ 's, fall on the same line. This indicates that L_2 is the correct length even for the three-body case and the three-body IR correction can also be written in terms of observables. Moreover the falloff is proportional to $e^{-2k_\infty L_2}$, with k_∞ being the lowest separation energy, as expected.

There has been a lot of work on extending the results for IR energy corrections presented in this thesis to the many-body case. This has been documented in Refs. [98, 99]. In Subsec. 2.1.5 we looked at the extrapolation of the radius-squared operator. The authors of Ref. [100] extended this to the extrapolation of quadrupole moments and transitions for the deuteron.

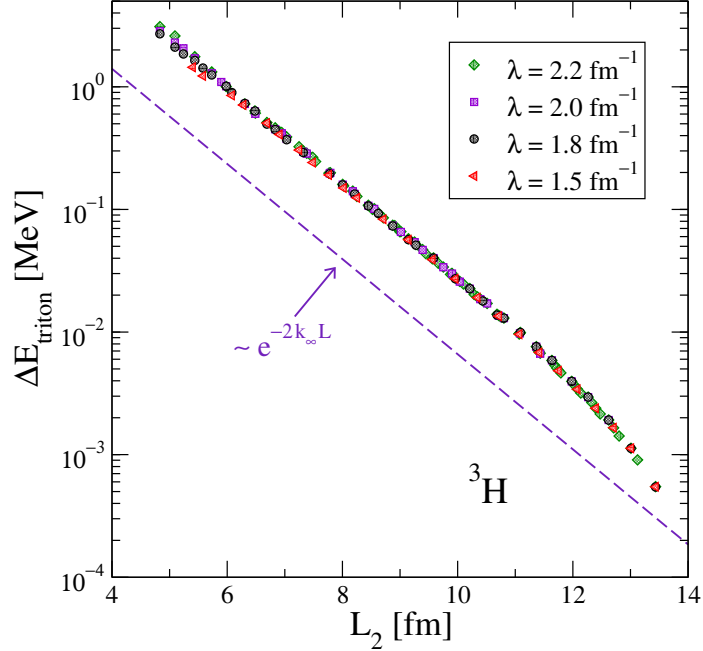


Figure 2.38: Residual error for triton plotted as a function of L_2 (here calculated with the deuteron-neutron reduced mass) for the two- and three-nucleon potential in Ref. [97] unitarily evolved by the SRG to four different resolutions (specified by λ) with the same binding energy [27, 97]. k_∞ here is the lowest separation energy (triton breaking up into deuteron and neutron).

As mentioned previously, the approach of mapping the HO truncation into a hard-wall boundary condition (in both position as well as momentum space) can be used for any localized basis. This has been explored for the case of Coulomb-Sturmian basis [101].

2.3.2 UV front

The dependence of UV corrections on the number of nucleons A is not yet established theoretically, but the tests in [58] seem to indicate that the cutoff dependence of ΔE for the many-body case is the same as in the two-body case, just scaled by an A -dependent overall constant. This can be understood from general considerations of

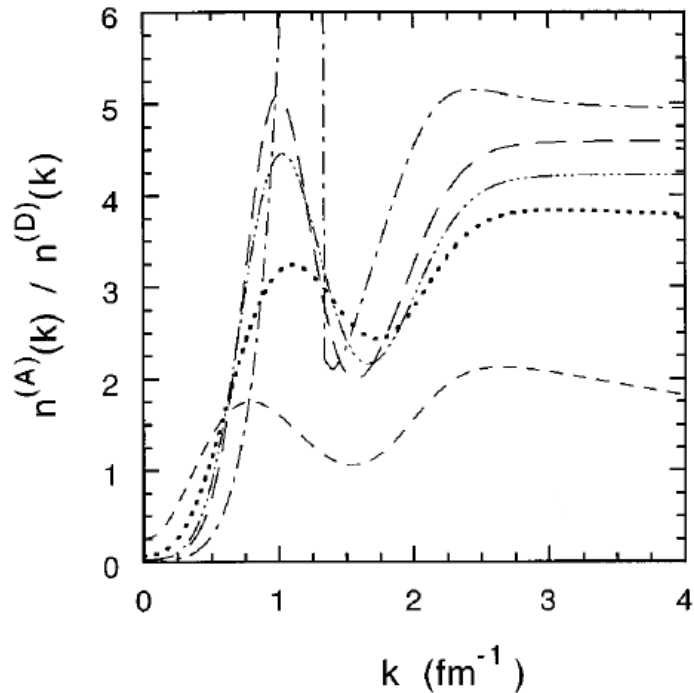


Figure 2.39: The ratio of the momentum distributions in nucleus to the deuteron momentum distributions. The dashed, dotted, dot-dashed, long dashed, dot-long dashed lines correspond to ${}^3\text{He}$, ${}^4\text{He}$, ${}^{16}\text{O}$, ${}^{56}\text{Fe}$, and nuclear matter respectively. Figure taken from [102].

short-range correlations [103] or more systematically using the operator product expansion [104, 105]. If there is a common two-body part, it may determine the dominant Λ_2 dependence with the rest providing the A -dependent scale factor. This behavior would be consistent with the observation of a universal shape for high-momentum tails in momentum distributions in Fig. 2.39 (or the corresponding short-distance behavior) [102, 106]. Connecting the two-body UV extrapolation results to the many-body case remains an open question.

In this chapter we worked in the region where either the IR or the UV errors were dominant. We saw in Fig. 2.24 how UV contamination spoils the data collapse for IR extrapolation. However, it is not always possible to isolate the IR and the UV contributions. We therefore need reliable extrapolation schemes which can be employed when both the IR and UV errors are comparable. Ref. [107] combined phenomenological UV errors⁹ with leading IR errors and used extrapolation of the form

$$E(\Lambda_2, L_2) = E_\infty + B_0 e^{-2\Lambda_2^2/B_1^2} + B_2 e^{-2k_\infty L_2}. \quad (2.129)$$

As seen in Fig. 2.40 this simple addition of IR and UV errors seems to work well. More work will be needed to place this on a sound theoretical foundation.

The authors of Ref. [108] developed interactions from chiral EFT that are tailored to the HO basis. In their approach, the UV convergence with respect to the model space is implemented by construction (through refitting of LECs) and IR convergence is achieved by enlarging the model space for the kinetic energy. This exhibited a fast convergence of ground-state energies and radii for nuclei up to ^{132}Sn . Thus, the

⁹Phenomenological form for the UV error is found to be Gaussian in the cutoff Λ_2 . Ref. [58] discusses how the Gaussian form arises.

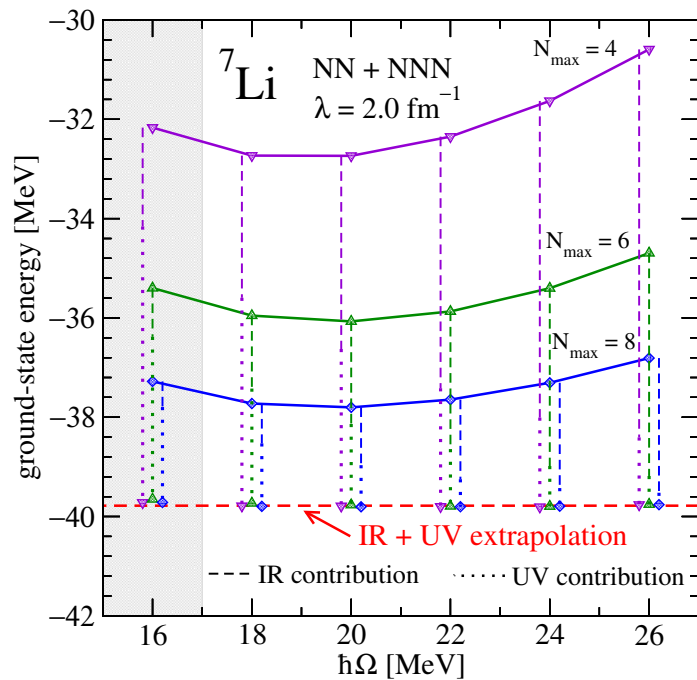


Figure 2.40: Ground-state energy for ^7Li with IR (vertical dashed lines) and UV (vertical dotted lines) corrections from Eq. 2.129 added to predict E_∞ values. The horizontal dashed line is the global E_∞ . Figure taken from [107].

development of reliable extrapolation schemes is indeed pushing the ab-initio frontier to heavier nuclei.

Chapter 3: Factorization ¹⁰

3.1 Motivation

Most of the information we know about nuclear interactions and the properties of the nuclei comes from some kind of scattering experiments (either elastic or inelastic). In such experiments we scatter a known probe off a nucleus and extract information about nuclear interactions by looking at the final outcome of the scattering experiment. Figure 3.1 shows a schematic for a nucleon knockout reaction where the probe

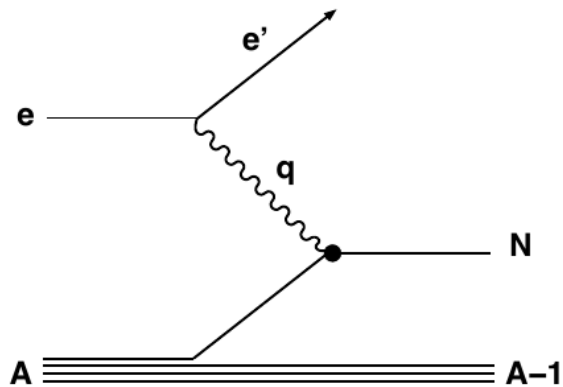


Figure 3.1: Schematic of a nucleon knockout reaction.

is electrons, which interact with the nucleus by emitting virtual photons.

¹⁰Based on [59]

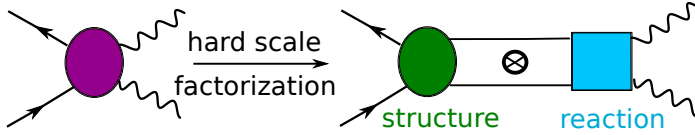


Figure 3.2: Schematic illustration of factorization between nuclear structure and reactions component.

The process of extracting nuclear properties from such experiments relies on the assumption that the effects of the probe are well understood and can be separated from the nuclear interactions we are trying to study. This is the *factorization* between the nuclear structure and the nuclear reaction components illustrated schematically in Fig. 3.2. The reaction component describes the probe and the structure includes the description of the initial and final states. This factorization between the structure and reaction components depends on the renormalization scale and scheme. In some physical systems (e.g., in cold atoms near unitarity [109]), the scale and scheme dependence is very weak and can be safely neglected. In some other physical systems such as in deep inelastic scattering (DIS) in high-energy QCD, the scale and scheme dependence is very manifest. Figure 3.3 illustrates the factorization in DIS. The form factor F_2 of the nucleon (which up to some kinematic factors is the cross section) is given by the convolution of the long-distance parton density and the short-distance Wilson coefficient. In this case, the parton density forms the structure part which is non-perturbative and the Wilson coefficient form the reactions part which can be calculated in perturbative QCD. This separation between long- and short-distance physics is not unique, and is defined by the factorization scale μ_f . To minimize the contribution of logarithms that can disturb the perturbative expansion, μ_f is

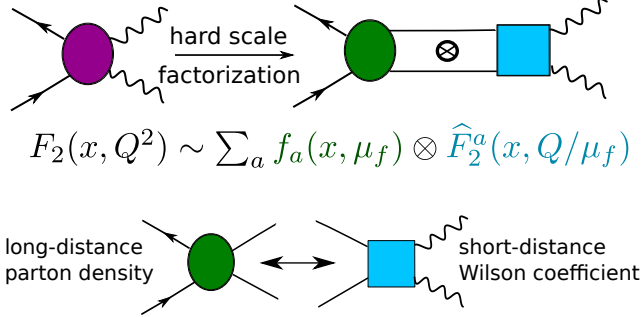


Figure 3.3: Factorization in high-energy QCD. x is the Bjorken- x and it denotes the fraction of momentum of the nucleon carried by the parton under consideration. a denotes the parton flavor.

chosen to be equal to the magnitude of the four-momentum transfer Q . The form factor F_2 (because it is related to the observable cross section) is independent of μ_f , but the individual components are not. As a consequence, the parton density (or distribution) function $f_a(x, Q^2)$ runs with Q^2 . This is demonstrated in Fig. 3.4. The parton distributions $f_a(x, Q^2)$ and $f_a(x, Q_0^2)$ at two different Q^2 are related by DGLAP evolution or the Altarelli-Parisi equations [111]. Thus the scale dependence of the structure and reaction components is well understood in high-energy QCD.

The situation is far from well settled in low-energy nuclear physics. Nuclear structure has conventionally been treated largely separate from nuclear reactions (e.g., the two volumes of Feshbach's *Theoretical Nuclear Physics* are divided this way). The nuclear structure community usually dealt with calculating time-independent properties such as nuclear binding energies, excitation spectra, radii, so on whereas the nuclear reaction experts worked on disintegration, knock-out, and transfer reactions. However, both the communities invariably use inputs from the other side, and the consistency and universality of different components is not always guaranteed. To

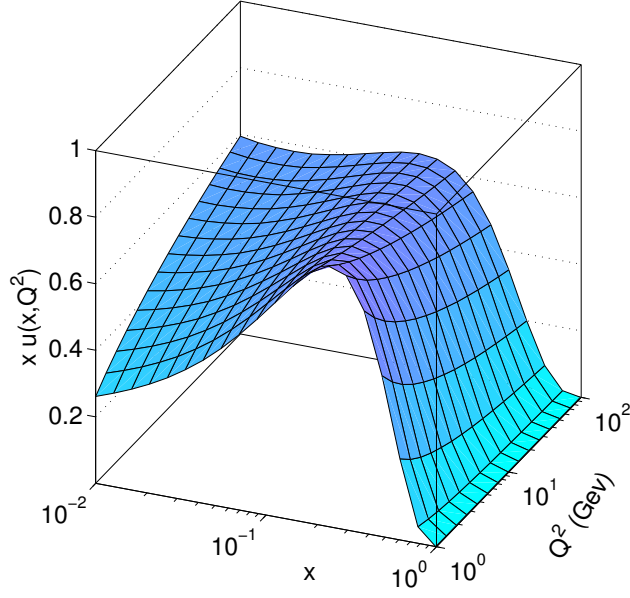


Figure 3.4: Parton distribution for the up quarks in the proton as a function of x and Q^2 . Figure taken from [110].

go back to the high-energy QCD analogy, the parton distribution functions (PDFs) $f_a(x, Q)$ extracted from the DIS are universal, in the sense that they are process-independent. For instance, the PDFs extracted from the DIS can be used for making prediction for the Drell-Yan process. The analogous process independence in the extracted quantities has not yet been demonstrated in low-energy nuclear physics. This leads to ambiguous uncertainty quantification when the nuclear properties extracted from one process (cf. Fig. 3.2) are used as an input to predict something else.

The assumed factorization in low-energy nuclear physics is illustrated in Fig. 3.5. The observable cross section in this case is written as a convolution of the spectroscopic factor and the single-particle cross section. However, there are many open

$$\begin{array}{ccc}
 \text{Observable:} & \text{Structure model:} & \text{Reaction model:} \\
 \text{cross section} & \text{spectroscopic factor} & \text{single-particle} \\
 & & \text{cross section}
 \end{array}
 \rightarrow \sigma^{if} = \sum_{|J_i - J_f| \leq j \leq J_i + J_f} S_j^{if} \sigma_{sp}$$

Figure 3.5: Schematic illustration of factorization in low-energy nuclear physics.

questions such when does this factorization hold and how can we justify it theoretically? In cases that it does hold what are the nuclear properties that we can extract and what is the scale/scheme dependence of these extracted properties?

The Similarity Renormalization Group (or the SRG) transformations were introduced in Subsec. 1.5.1. We noted that SRG transformations are a class of unitary transformations that soften nuclear Hamiltonians and lead to accelerated convergence of observables. Figure 3.6 shows the momentum distribution for the deuteron as a function of the SRG scale and momentum. Note that Fig. 3.6 is analogous to Fig. 3.4. The SRG evolution gets rid of the high-momentum components and therefore the evolved momentum distributions don't have the short-range correlations (SRCs). Figure 3.6 makes it clear that the high-momentum tail of the momentum distribution is dramatically resolution dependent. Yet it is common in the literature that high-momentum components are treated as measurable, at least implicitly [112–115]. In fact, what can be extracted is the momentum distribution at some scale, and with the specification of a scheme. This makes momentum distributions model dependent [116, 117].

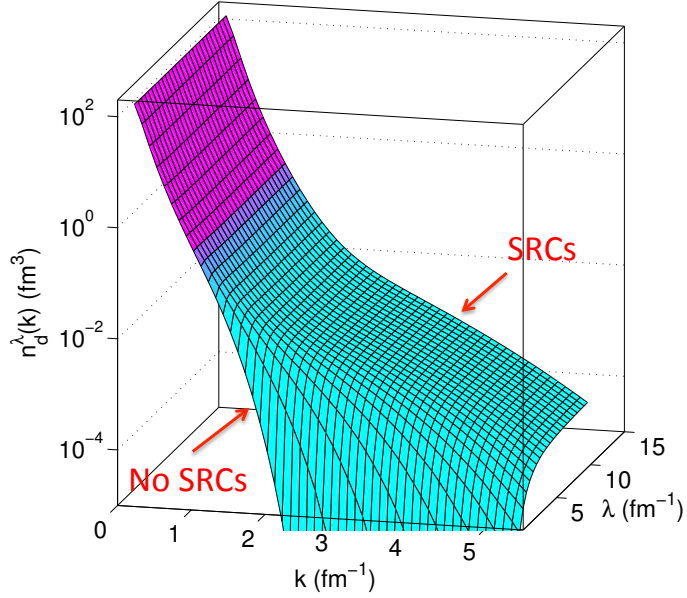


Figure 3.6: Deuteron momentum distribution at different SRG resolutions λ . The evolved momentum distribution does not have the short-range correlations (SRCs). Figure from [110].

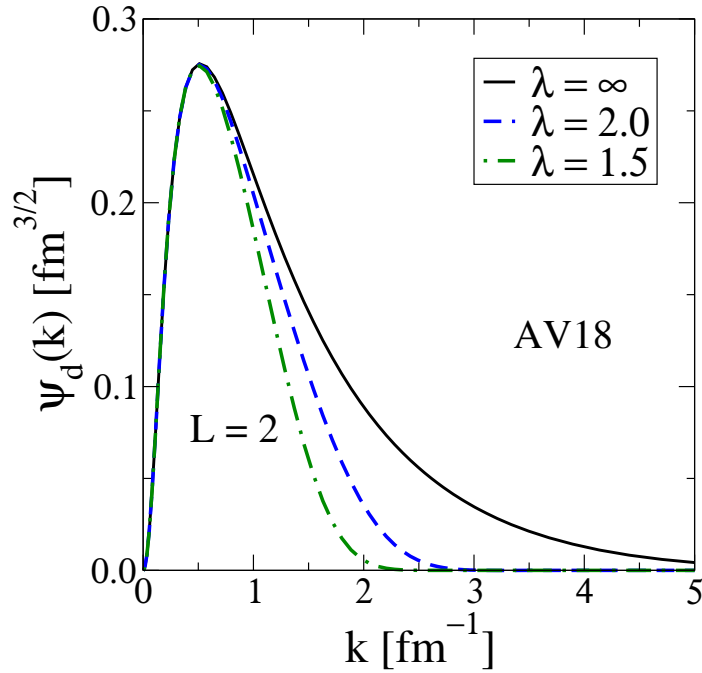


Figure 3.7: D -state wave functions for the deuteron for the AV18 potential and the AV18 potential evolved to two SRG λ 's.

Figure 3.7 shows the D -state wave function for deuteron. We see that just like the momentum distributions, SRG transformed wave functions do not have the high-momentum components. Therefore, if we use the SRG evolved wave function for calculating the cross section for a process involving high-momentum probe, then the only way we get the same answer as with the unevolved wave function is if the relevant operator changed as well. Thus, with SRG evolution, the high-momentum physics is shuffled from the wave function (nuclear structure) to the operator (nuclear reaction component). This is reminiscent of chiral EFTs where the renormalization replaces the high-momentum modes in intermediate states by contact interactions (see Fig. 3.8). The discussion so far shows how the SRG makes the scale dependence

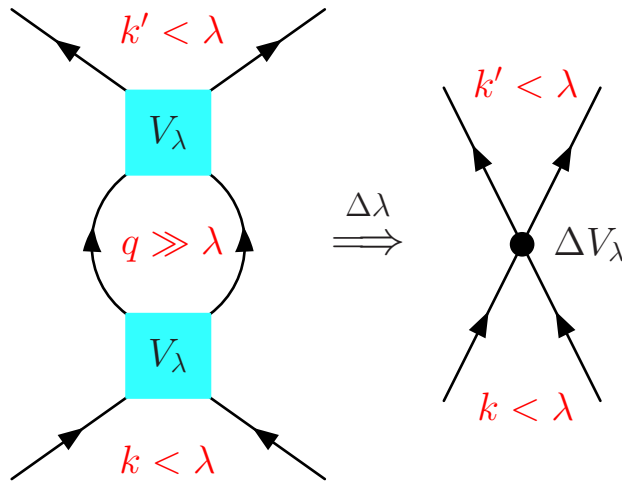


Figure 3.8: High-momentum modes in intermediate states replaced by contact interactions. Figure from [110].

of factorization explicit. SRG transformations come with the momentum scale λ and this sets the scale for factorization. As seen in the Fig. 3.9, we have a natural separation that the piece which involves momenta less than λ forms the long-distance

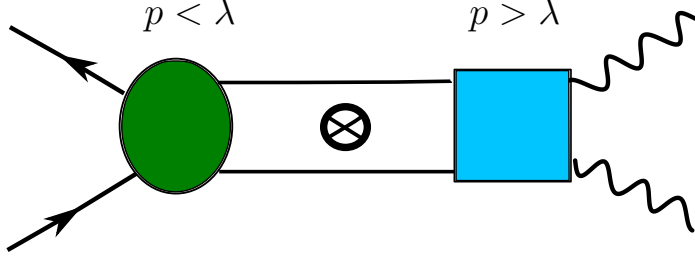


Figure 3.9: The SRG scale λ sets the natural scale for factorization.

part and the piece that involves momenta greater than λ forms the short-distance part.

Consider the differential cross section given by the overlap matrix element of initial and final states.

$$\frac{d\sigma}{d\Omega} \propto \left| \langle \psi_f | \hat{O} | \psi_i \rangle \right|^2. \quad (3.1)$$

The SRG evolved wave function is given by $|\psi_i^\lambda\rangle = U_\lambda |\psi_i\rangle$, where U_λ is the unitary matrix associated with the SRG transformation. The cross section is an experimental observable and should be independent of our choice of the SRG scale. If we evolve all the components of the matrix element consistently

$$\langle \psi_f | \hat{O} | \psi_i \rangle = \underbrace{\langle \psi_f^\lambda |}_{\psi_f^\lambda} \underbrace{| U_\lambda \hat{O} U_\lambda^\dagger |}_{\hat{O}^\lambda} \underbrace{| U_\lambda \psi_i \rangle}_{\psi_i^\lambda}, \quad (3.2)$$

then the evolved matrix element is same as the unevolved one and the observable cross section is unchanged.

In general, to be consistent between structure and reactions one must calculate cross sections or decay rates within a single framework. That is, one must use the same Hamiltonian and consistent operators throughout the calculation (which means the same scale and scheme). Such consistent calculations have existed for some time for few-body nuclei (e.g., see [52, 118–120]) and are becoming increasingly feasible

for heavier nuclei because of advances in reaction technology, such as using complex basis states to handle continuum physics. Recent examples in the literature include the No Core Shell Model Resonating Group Method (NCSM/RGM) [121], coupled cluster [122], and lattice EFT calculations [123]. But there are many open questions about constructing consistent currents and how to compare results from two such calculations. Some work along this direction which includes the evolution of the operator has recently been done. Anderson *et al.* looked at the static properties of the deuteron such as momentum distributions, radii, and form factors under SRG evolution; they found no pathologies in the evolved operators, and the evolution effects were small for low-momentum observables [124]. Schuster *et al.* found in their work on radii and dipole transition matrix elements in light nuclei that the evolution effects are as important as three-body forces [125, 126]. Neff *et al.* looked at the SRG transformed density operators and concluded that it is essential to use evolved operators for observables sensitive to short-range physics [127]. But all this work was done for expectation values of the operator, i.e, the state on the either side of the matrix element was the same. In particular, there was no work which dealt with the issues related to operator evolution when we have a transition to continuum. This is what we sought to address in [59].

The electron scattering knock-out process is particularly interesting because of the connection to past, present, and planned experiments [128, 129]. The conditions for clean factorization of structure and reactions in this context is closely related to the impact of 3N forces, two-body currents, and final-state interactions, which have not

been cleanly understood as yet [130]. All of this becomes particularly relevant for high-momentum-transfer electron scattering.¹¹ This physics is conventionally explained in terms of short-range correlation (SRC) phenomenology [112, 131]. SRCs are two- or higher-body components of the nuclear wave function with high relative momentum and low center-of-mass momentum. These explanations would seem to present a puzzle for descriptions of nuclei with low-momentum Hamiltonians, for which SRCs are essentially absent from the wave functions.

This puzzle is resolved by the unitary transformations that mandate the invariance of the cross section (cf. Eq. 3.2). The physics that was described by SRCs in the wave functions must shift to a different component, such as a two-body contribution from the current (cf. Fig. 3.8). This may appear to complicate the reaction problem just as we have simplified the structure part, but past work and analogies to other processes suggests that factorization may in fact become cleaner [104, 124]. One of our goals is to elucidate this issue, although we have only begun to do so in [59].

In particular, we take the first steps in exploring the interplay of structure and reaction as a function of kinematic variables and SRG decoupling scale λ in a controlled calculation of a knock-out process. There are various complications for such processes. With RG evolution, a Hamiltonian—even with only a two-body potential initially—will develop many-body components as the decoupling scale decreases (cf. Eq. 1.19). Similarly, a one-body current will develop two- and higher-body components.

Our strategy is to avoid dealing with all of these complications simultaneously by considering the cleanest knock-out process: deuteron electrodisintegration with only

¹¹Note that high-momentum transfers imply high-resolution *probes*, which is different from the resolution induced by the SRG scale. How the latter should be chosen to best accommodate the former is a key unanswered question.

an initial one-body current. With a two-body system, there are no three-body forces or three-body currents to contend with. Yet it still includes several key ingredients to investigate: i) the wave function will evolve with changes in resolution; ii) at the same time, the one-body current develops two-body components, which are simply managed; and iii) there are final-state interactions (FSI). It is these ingredients that will mix under the RG evolution. We can focus on different effects or isolate parts of the wave function by choice of kinematics. For example, we can examine when the impulse approximation is best and to what extent that is a resolution-dependent assessment.

3.2 Test ground: Deuteron disintegration

3.2.1 Formalism

Deuteron electrodisintegration is the simplest nucleon-knockout process and has been considered as a test ground for various NN models for a long time (see, for example, Refs. [115, 132]). It has also been well studied experimentally [133, 134]. The absence of three-body currents and forces makes it an ideal starting point for studying the interplay with SRG evolution of the deuteron wave function, current, and final-state interactions.

We follow the approach of Ref. [135], which we briefly review. The kinematics for the process in the laboratory frame is shown in Fig. 3.10. The virtual photon from electron scattering transfers enough energy and momentum to break up the deuteron into a proton and neutron. The differential cross section for deuteron electrodisintegration for unpolarized scattering in the lab frame is given by [136]

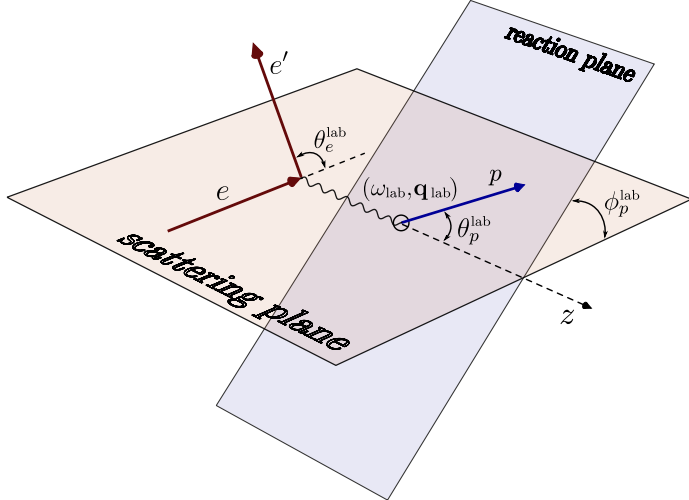


Figure 3.10: The geometry of the electro-disintegration process in the lab frame. The virtual photon disassociates the deuteron into the proton and the neutron (not shown in this figure).

$$\frac{d^3\sigma}{dk'^{\text{lab}} d\Omega_e^{\text{lab}} d\Omega_p^{\text{lab}}} = \frac{\alpha}{6\pi^2} \frac{k'^{\text{lab}}}{k^{\text{lab}}(Q^2)^2} \left[v_L f_L + v_T f_T + v_{TT} f_{TT} \cos 2\phi_p^{\text{lab}} + v_{LT} f_{LT} \cos \phi_p^{\text{lab}} \right]. \quad (3.3)$$

Here Ω_e^{lab} and Ω_p^{lab} are the solid angles of the electron and the proton, k^{lab} and k'^{lab} are the magnitude of incoming and outgoing electron 3-momenta, Q^2 is the 4-momentum-squared of the virtual photon, and α is the fine structure constant. ϕ_p^{lab} is the angle between the scattering plane containing the electrons and the plane spanned by outgoing nucleons. v_L, v_T, \dots are electron kinematic factors, and f_L, f_T, \dots are the deuteron structure functions. These structure functions contain all the dynamic information about the process. The four structure functions are independent and can be separated by combining cross-section measurements carried out with appropriate kinematic settings [137]. Structure functions are thus cross sections up to kinematic factors and are independent of the SRG scale λ . They are analogous to form factor

F_2 we saw in the DIS case (cf. Fig. 3.3). In our work we focus on the longitudinal structure function f_L , following the approach of Ref. [135].

Calculating f_L

As in Ref. [135], we carry out the calculations in the center-of-mass frame of the outgoing proton-neutron pair. In this frame the photon four-momentum is (ω, \mathbf{q}) , which can be obtained from the initial electron energy and θ_e , the electron scattering angle. We denote the momentum of the outgoing proton by \mathbf{p}' and take \mathbf{q} to be along the z -axis. The angles of \mathbf{p}' are denoted by $\Omega_{\mathbf{p}'} = (\theta', \varphi')$.

The longitudinal structure function can be written as

$$f_L = \sum_{\substack{S_f, m_{s_f} \\ m_{J_d}}} \mathcal{T}_{S_f, m_{s_f}, \mu=0, m_{J_d}}(\theta', \varphi') \mathcal{T}_{S_f, m_{s_f}, \mu=0, m_{J_d}}^*(\theta', \varphi'), \quad (3.4)$$

where S_f and m_{s_f} are the spin quantum numbers of the final neutron-proton state, μ is the polarization index of the virtual photon, and m_{J_d} is the angular momentum of the initial deuteron state. The amplitude \mathcal{T} is given by [138]

$$\mathcal{T}_{S_f, m_{s_f}, \mu, m_{J_d}} = -\pi \sqrt{2\alpha |\mathbf{p}'| E_p E_d / M_d} \langle \psi_f | J_\mu(\mathbf{q}) | \psi_i \rangle, \quad (3.5)$$

where $\langle \psi_f |$ is the final-state wavefunction of the outgoing neutron-proton pair, $|\psi_i\rangle$ is the initial deuteron state, and $J_\mu(\mathbf{q})$ is the current operator that describes the momentum transferred by the photon. The variables in Eq. 3.5 are:

- fine-structure constant α ;
- outgoing proton (neutron) 3-momentum $\mathbf{p}' (-\mathbf{p}')$;
- proton energy $E_p = \sqrt{M^2 + \mathbf{p}'^2}$, where M is the average of proton and neutron mass

- deuteron energy $E_d = \sqrt{M_d^2 + \mathbf{q}^2}$, where M_d is the mass of the deuteron.

As mentioned before, all of these quantities are in the center-of-mass frame of the outgoing nucleons.

For $f_L, \mu = 0$ and therefore only J_0 contributes. The one-body current matrix element is given by

$$\begin{aligned} \langle \mathbf{k}_1 T_1 | J_0(\mathbf{q}) | \mathbf{k}_2 T=0 \rangle &= \frac{1}{2} (G_E^p + (-1)^{T_1} G_E^n) \delta(\mathbf{k}_1 - \mathbf{k}_2 - \mathbf{q}/2) \\ &\quad + \frac{1}{2} ((-1)^{T_1} G_E^p + G_E^n) \delta(\mathbf{k}_1 - \mathbf{k}_2 + \mathbf{q}/2), \end{aligned} \quad (3.6)$$

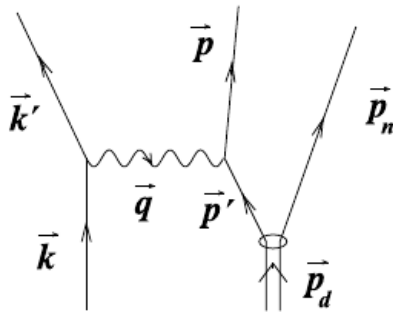
where G_E^p and G_E^n are the electric form factors of the proton and the neutron, and the deuteron state has isospin $T = 0$.

The final-state wave function of the outgoing proton-neutron pair can be written as

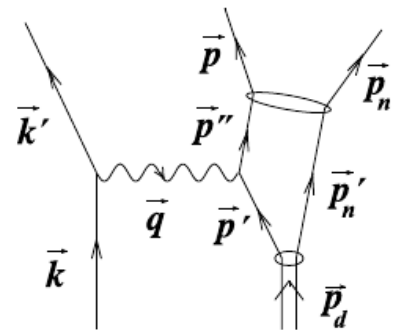
$$|\psi_f\rangle = |\phi\rangle + G_0(E') t(E') |\phi\rangle, \quad (3.7)$$

where $|\phi\rangle$ denotes a relative plane wave, G_0 and t are the Green's function and the t -matrix respectively, and $E' = \mathbf{p}'^2/M$ is the energy of the outgoing nucleons. The second term in Eq. 3.7 describes the interaction between the outgoing nucleons. As the momentum associated with the plane wave $|\phi\rangle$ is p' , the t -matrix $t(E')$ that enters our calculation is always half on-shell.

In the impulse approximation (IA) as defined here, the interaction between the outgoing nucleons is ignored and $|\psi_f\rangle_{\text{IA}} \equiv |\phi\rangle$. A schematic of IA and FSI contributions is shown in Fig. 3.11. The plane wave $|\phi\rangle$ will have both isospin 0 and 1 components. The current J_0 , G_0 , and the t -matrix are diagonal in spin space. The deuteron has spin $S = 1$ and therefore the final state will also have $S = 1$. Hence, we



(a) Impulse Approximation (IA)



(b) Final State Interaction (FSI)

Figure 3.11: (a) The first term on the right side of Eq. 3.7. The outgoing nucleons do not interact. (b) The second term on the right side of Eq. 3.7. The outgoing nucleons interact through the NN potential. Figures taken from [139].

have

$$\begin{aligned} |\phi\rangle &\equiv |\mathbf{p}' S=1 m_{s_f} \psi_T\rangle \\ &= \frac{1}{2} \sum_{T=0,1} (|\mathbf{p}' S=1 m_{s_f}\rangle + (-1)^T |-\mathbf{p}' S=1 m_{s_f}\rangle) |T\rangle. \end{aligned} \quad (3.8)$$

Using Eqs. 3.6 and 3.8, the overlap matrix element in IA becomes

$$\begin{aligned} \langle \psi_f | J_0 | \psi_i \rangle_{\text{IA}} &= \sqrt{\frac{2}{\pi}} \sum_{L_d=0,2} \langle L_d m_{J_d} - m_{s_f} S=1 m_{s_f} | J=1 m_{J_d} \rangle \\ &\times \left[G_E^p \psi_{L_d}(|\mathbf{p}' - \mathbf{q}/2|) Y_{L_d, m_{J_d} - m_{s_f}}(\Omega_{\mathbf{p}' - \mathbf{q}/2}) \right. \\ &\quad \left. + G_E^n \psi_{L_d}(|\mathbf{p}' + \mathbf{q}/2|) Y_{L_d, m_{J_d} - m_{s_f}}(\Omega_{\mathbf{p}' + \mathbf{q}/2}) \right], \end{aligned} \quad (3.9)$$

where $\Omega_{\mathbf{p}' \pm \mathbf{q}/2}$ is the solid angle between the unit vector \hat{z} and $\mathbf{p}' \pm \mathbf{q}/2$. ψ_{L_d} is the deuteron wave function in momentum space defined as

$$\langle k_1 J_1 m_{J_1} L_1 S_1 T_1 | \psi_i \rangle = \psi_{L_1}(k_1) \delta_{J_1,1} \delta_{m_{J_1}, m_{J_d}} \delta_{L_1, L_d} \delta_{S_1, 1} \delta_{T_1, 0}. \quad (3.10)$$

The S -wave ($L = 0$) and D -wave ($L = 2$) components of the deuteron wave function satisfy the normalization condition

$$\frac{2}{\pi} \int dp p^2 (\psi_0^2(p) + \psi_2^2(p)) = 1. \quad (3.11)$$

In deriving Eq. 3.9 we have used the property of the spherical harmonics that

$$Y_{lm}(\pi - \theta, \phi + \pi) = (-1)^l Y_{lm}(\theta, \phi). \quad (3.12)$$

In our work we follow the conventions of Ref. [140]. Deriving Eq. 3.9 also uses partial wave expansion

$$|\mathbf{k}\rangle = \sqrt{\frac{2}{\pi}} \sum_{l,m} Y_{lm}^*(\Omega_{\mathbf{k}}) |k l m\rangle, \quad (3.13)$$

the normalization condition

$$\langle p | k \rangle = \frac{\pi}{2} \frac{\delta(p - k)}{p^2}, \quad (3.14)$$

and, the Clebsch-Gordan completeness relation

$$|l m S=1 m_s\rangle = \sum_{J, m_J} |J m_J l S=1\rangle \langle J m_J l S=1|l m S=1 m_s\rangle . \quad (3.15)$$

Because θ' and φ' are the angles of \mathbf{p}' , $\Omega_{\mathbf{p}'-\mathbf{q}/2} \equiv (\alpha'(p', \theta', q), \varphi')$ and $\Omega_{\mathbf{p}'+\mathbf{q}/2} \equiv (\alpha''(p', \theta', q), \varphi')$, where

$$\alpha'(p', \theta', q) = \cos^{-1}\left(\frac{p' \cos \theta' - q/2}{\sqrt{p'^2 - p'q \cos \theta' + q^2/4}}\right) \quad (3.16)$$

and

$$\alpha''(p', \theta', q) = \cos^{-1}\left(\frac{p' \cos \theta' + q/2}{\sqrt{p'^2 + p'q \cos \theta' + q^2/4}}\right) . \quad (3.17)$$

The expressions for α' and α'' can be obtained by elementary trigonometry. Note that Eqs. 3.16 and 3.17 reproduce the correct $p' = 0$ and $q = 0$ limit.

The overlap matrix element including the final-state interactions (FSI) is given by

$$\langle \psi_f | J_0 | \psi_i \rangle = \underbrace{\langle \phi | J_0 | \psi_i \rangle}_{\text{IA}} + \underbrace{\langle \phi | t^\dagger G_0^\dagger J_0 | \psi_i \rangle}_{\text{FSI}} . \quad (3.18)$$

The first term on the right side of Eq. 3.18 has already been evaluated in Eq. 3.9. Therefore, the term we still need to evaluate is $\langle \phi | t^\dagger G_0^\dagger J_0 | \psi_i \rangle$. The t -matrix is most conveniently calculated in a partial-wave basis. Hence, the FSI term is evaluated by inserting complete sets of states in the form

$$1 = \frac{2}{\pi} \sum_{\substack{L, S \\ J, m_J}} \sum_{T=0,1} \int dp p^2 |p J m_J L S T\rangle \langle p J m_J L S T| . \quad (3.19)$$

The outgoing plane-wave state in the partial-wave basis is given by

$$\begin{aligned} \langle \phi | k_1 J_1 m_{J_1} L_1 S=1 T_1 \rangle &= \frac{1}{2} \sqrt{\frac{2}{\pi}} \frac{\pi}{2} \frac{\delta(p' - k_1)}{k_1^2} \langle L_1 m_{J_1} - m_{s_f} S=1 m_{s_f} | J_1 m_{J_1} \rangle \\ &\times (1 + (-1)^{T_1} (-1)^{L_1}) Y_{L_1, m_{J_1} - m_{s_f}}(\theta', \varphi') . \end{aligned} \quad (3.20)$$

The Green's function is diagonal in J , m_J , L , S , and T , so we have

$$\langle k_1 | G_0^\dagger | k_2 \rangle = \frac{\pi}{2} \frac{\delta(k_1 - k_2)}{k_1^2} \frac{M}{p'^2 - k_1^2 - i\epsilon}. \quad (3.21)$$

We also need to express the current in Eq. 3.6 in the partial-wave basis. To begin with, let us just work with first term in Eq. 3.6, which we denote by J_0^- . In the partial-wave basis, it is written as

$$\begin{aligned} \langle k_1 J_1 m_{J_d} L_1 S=1 T_1 | J_0^- | k_2 J=1 m_{J_d} L_2 S=1 T=0 \rangle &= \frac{\pi^2}{2} (G_E^p + (-1)^{T_1} G_E^n) \\ &\times \sum_{\tilde{m}_s=-1}^1 \int d\cos\theta \langle J_1 m_{J_d} | L_1 m_{J_d} - \tilde{m}_s S=1 \tilde{m}_s \rangle P_{L_1}^{m_{J_d} - \tilde{m}_s}(\cos\theta) \\ &\times P_{L_2}^{m_{J_d} - \tilde{m}_s}(\cos\alpha'(k_1, \theta, q)) \frac{\delta(k_2 - \sqrt{k_1^2 - k_1 q \cos\theta + q^2/4})}{k_2^2} \\ &\times \langle L_2 m_{J_d} - \tilde{m}_s S=1 \tilde{m}_s | J=1 m_{J_d} \rangle. \end{aligned} \quad (3.22)$$

Here m_{J_d} is the deuteron quantum number, which is preserved throughout. We have used the deuteron quantum numbers in the ket in anticipation that we will always evaluate the matrix element of J_0 with the deuteron wave function on the right. α' is as defined in Eq. 3.16. In deriving Eq. 3.22 we have also made use of the relation [141]

$$\int Y_{lm}^*(\theta, \varphi) Y_{l'm'}(\alpha', \varphi) d\cos\theta d\varphi = 2\pi \delta_{mm'} \int d\cos\theta P_l^m(\cos\theta) P_{l'}^m(\cos\alpha'). \quad (3.23)$$

Equations 3.20, 3.21, and 3.22 can be combined to obtain

$$\begin{aligned}
\langle \phi | t^\dagger G_0^\dagger J_0^- | \psi_i \rangle &= \sqrt{\frac{2}{\pi}} \frac{M}{\hbar c} \sum_{T_1=0,1} (G_E^p + (-1)^{T_1} G_E^n) \sum_{L_1=0}^{L_{\max}} (1 + (-1)^{T_1} (-1)^{L_1}) \\
&\times Y_{L_1, m_{J_d} - m_{s_f}}(\theta', \varphi') \sum_{J_1=|L_1-1|}^{L+1} \langle L_1 m_{J_d} - m_{s_f} S=1 m_{s_f} | J_1 m_{J_d} \rangle \sum_{L_2=0}^{L_{\max}} \int dk_2 k_2^2 \\
&\times t^*(k_2, p', L_2, L_1, J_1, S=1, T_1) \sum_{\tilde{m}_s=-1}^1 \langle J_1 m_{J_d} | L_2 m_{J_d} - \tilde{m}_s S=1 \tilde{m}_s \rangle \\
&\times \sum_{L_d=0,2} \langle L_d m_{J_d} - \tilde{m}_s S=1 \tilde{m}_s | J=1 m_{J_d} \rangle \int d\cos \theta \frac{1}{p'^2 - k_2^2 - i\epsilon} \\
&\times P_{L_2}^{m_{J_d} - \tilde{m}_s}(\cos \theta) P_{L_d}^{m_{J_d} - \tilde{m}_s}(\cos \alpha'(k_2, \theta, q)) \psi_{L_d}\left(\sqrt{k_2^2 - k_2 q \cos \theta + q^2/4}\right). \quad (3.24)
\end{aligned}$$

Note that the matrix element of the t -matrix in Eq. 3.24 should strictly be written as $t^*(E' = p'^2/M; k_2, p', L_2, L_1, J_1, S=1, T_1)$. However, keeping in mind that the t -matrix in this chapter is always evaluated half on-shell, we drop the E' index for the sake of brevity. To evaluate the hermitian conjugate, we use the property

$$t^\dagger(p', k_2, L_1, L_2, J_1, S=1, T_1) = t^*(k_2, p', L_2, L_1, J_1, S=1, T_1). \quad (3.25)$$

We denote the second term in the one-body current Eq. 3.6 by J_0^+ . The expression for $\langle \phi | t^\dagger G_0^\dagger J_0^+ | \psi_i \rangle$ is analogous to Eq. 3.24, the only differences being that the form-factor coefficient is $(-1)^{T_1} G_E^p + G_E^n$ and the input arguments for the second associated Legendre polynomial and the deuteron wave function are different. The two factors respectively become $P_{L_d}^{m_{J_d} - \tilde{m}_s}(\cos \alpha''(k_2, \theta, q))$ and $\psi_{L_d}\left(\sqrt{k_2^2 + k_2 q \cos \theta + q^2/4}\right)$, where α'' is defined in Eq. 3.17. It can be shown that $\langle \phi | t^\dagger G_0^\dagger J_0^+ | \psi_i \rangle = \langle \phi | t^\dagger G_0^\dagger J_0^- | \psi_i \rangle$. Thus,

$$\langle \phi | t^\dagger G_0^\dagger J_0 | \psi_i \rangle = 2 \langle \phi | t^\dagger G_0^\dagger J_0^- | \psi_i \rangle. \quad (3.26)$$

Using this we can evaluate the overlap matrix element in Eq. 3.18. As outlined in Eqs. 3.4 and 3.5, this matrix element is related to the longitudinal structure function

f_L . Recall that the deuteron spin is conserved throughout and therefore $S_f = 1$ in Eq. 3.4.

In Subsec. 3.2.4 we present results for f_L both in the IA and including the FSI. These results match those of Ref. [135, 138], verifying the accuracy of the calculations presented above.

3.2.2 Evolution setup

As outlined previously, we want to investigate the effect of unitary transformations on calculations of f_L . Let us start by looking at the IA matrix element:

$$\begin{aligned} \langle \phi | J_0 | \psi_i \rangle &= \langle \phi | U^\dagger U J_0 U^\dagger U | \psi_i \rangle \\ &= \underbrace{\langle \phi | \tilde{U}^\dagger J_0^\lambda | \psi_i^\lambda \rangle}_A + \underbrace{\langle \phi | J_0^\lambda | \psi_i^\lambda \rangle}_B, \end{aligned} \quad (3.27)$$

where we decompose the unitary matrix U into the identity and a residual \tilde{U} ,

$$U = I + \tilde{U}. \quad (3.28)$$

The matrix \tilde{U} is smooth and therefore amenable to interpolation. The U matrix is calculated following the approach in [124]. The terms in Eq. 3.27 can be further split into

$$\langle \phi | J_0^\lambda | \psi_i^\lambda \rangle = \underbrace{\langle \phi | \tilde{U} J_0 \tilde{U}^\dagger | \psi_i^\lambda \rangle}_{B_1} + \underbrace{\langle \phi | \tilde{U} J_0 | \psi_i^\lambda \rangle}_{B_2} + \underbrace{\langle \phi | J_0 \tilde{U}^\dagger | \psi_i^\lambda \rangle}_{B_3} + \underbrace{\langle \phi | J_0 | \psi_i^\lambda \rangle}_{B_4} \quad (3.29)$$

and

$$\langle \phi | \tilde{U}^\dagger J_0^\lambda | \psi_i^\lambda \rangle = \underbrace{\langle \phi | \tilde{U}^\dagger \tilde{U} J_0 \tilde{U}^\dagger | \psi_i^\lambda \rangle}_{A_1} + \underbrace{\langle \phi | \tilde{U}^\dagger \tilde{U} J_0 | \psi_i^\lambda \rangle}_{A_2} + \underbrace{\langle \phi | \tilde{U}^\dagger J_0 \tilde{U}^\dagger | \psi_i^\lambda \rangle}_{A_3} + \underbrace{\langle \phi | \tilde{U}^\dagger J_0 | \psi_i^\lambda \rangle}_{A_4}. \quad (3.30)$$

The B_4 term is the same as in Eq. 3.9, but with the deuteron wave function replaced by the evolved version $\psi_{L_d}^\lambda$. Inserting complete sets of partial-wave basis states as in

Eq. 3.19 and using Eqs. 3.20 and 3.22, we can obtain the expressions for B_1 , B_2 , B_3 and A_1, \dots, A_4 . These expressions are given in Appendix B.1.

Using the expressions for A_1, \dots, A_4 and B_1, \dots, B_4 , we can obtain results for f_L in the IA with one or more components of the overlap matrix element $\langle\phi|J_0|\psi\rangle$ evolved. When calculated in IA, f_L with all components evolved matches its unevolved counterpart, as shown later in Subsec. 3.2.4. The robust agreement between the evolved and unevolved answers indicates that the expressions derived for A_1, \dots, B_4 are correct and that there is no error in generating the U -matrices. In Sec. 3.2.3 we provide some details about the numerical implementation of the equations presented here.

Let us now take into account the FSI and study the effects of evolution. The overlap matrix element should again be unchanged under evolution,

$$\langle\psi_f|J_0|\psi_i\rangle = \langle\psi_f^\lambda|J_0^\lambda|\psi_i^\lambda\rangle, \quad (3.31)$$

where ψ_f is given by Eq. 3.7. Furthermore,

$$|\psi_f^\lambda\rangle = |\phi\rangle + G_0 t_\lambda |\phi\rangle, \quad (3.32)$$

where t_λ is the evolved t -matrix, *i.e.*, the t -matrix obtained by solving the Lippmann–Schwinger equation using the evolved potential, as discussed in Appendix B.2. Thus

$$\langle\psi_f^\lambda|J_0^\lambda|\psi_i^\lambda\rangle = \underbrace{\langle\phi|J_0^\lambda|\psi_i^\lambda\rangle}_B + \underbrace{\langle\phi|t_\lambda^\dagger G_0^\dagger J_0^\lambda|\psi_i^\lambda\rangle}_F. \quad (3.33)$$

The term B is the same that we already encountered in Eq. 3.27. The term F can also be split up into four terms:

$$\langle \phi | t_\lambda^\dagger G_0^\dagger J_0^\lambda | \psi_i^\lambda \rangle = \underbrace{\langle \phi | t_\lambda^\dagger G_0^\dagger \widetilde{U} J_0 \widetilde{U}^\dagger | \psi_i^\lambda \rangle}_{F_1} + \underbrace{\langle \phi | t_\lambda^\dagger G_0^\dagger \widetilde{U} J_0 | \psi_i^\lambda \rangle}_{F_2} \\ + \underbrace{\langle \phi | t_\lambda^\dagger G_0^\dagger J_0 \widetilde{U}^\dagger | \psi_i^\lambda \rangle}_{F_3} + \underbrace{\langle \phi | t_\lambda^\dagger G_0^\dagger J_0 | \psi_i^\lambda \rangle}_{F_4}. \quad (3.34)$$

The expression for F_4 can easily be obtained from Eqs. 3.24 and 3.26 by replacing the deuteron wave function and the t -matrix by their evolved counterparts. As before, we insert complete sets of partial-wave basis states using Eq. 3.19 and evaluate F_3 , F_2 , and F_1 ; see Eqs. B.6, B.7, and B.8. Figures in Subsec. 3.2.4 compare f_L calculated from the matrix element with all components evolved to the unevolved f_L . We find an excellent agreement, validating the expressions for F_1, \dots, F_4 .

First-order analytical calculation

Recall that from Eqs. 3.4 and 3.5 we have

$$f_L \propto \sum_{m_{s_f}, m_{J_d}} |\langle \psi_f | J_0 | \psi_i \rangle|^2. \quad (3.35)$$

When all three components—the final state, the current, and the initial state—are evolved consistently, then f_L is unchanged. However, if we miss evolving a component, then we obtain a different result. It is instructive to illustrate this through a first-order analytical calculation.¹²

Let us look at the effects due to the evolution of individual components for a general matrix element $\langle \psi_f | \hat{O} | \psi_i \rangle$. The evolved initial state is given by

$$|\psi_i^\lambda\rangle \equiv U |\psi_i\rangle = |\psi_i\rangle + \widetilde{U} |\psi_i\rangle, \quad (3.36)$$

where \widetilde{U} is the smooth part of the U -matrix defined in Eq. 3.28. Similarly, we can write down the expressions for the evolved final state and the evolved operator as

$$\langle \psi_f^\lambda | \equiv \langle \psi_f | U^\dagger = \langle \psi_f | - \langle \psi_f | \widetilde{U} \quad (3.37)$$

¹²An analogous calculation based on field redefinitions appears in Ref. [142].

and

$$\hat{O}^\lambda \equiv U \hat{O} U^\dagger = \hat{O} + \tilde{U} \hat{O} - \hat{O} \tilde{U} + \mathcal{O}(\tilde{U}^2). \quad (3.38)$$

We assume here that \tilde{U} is small compared to I (which can always be ensured by choosing the SRG λ large enough) and therefore keep terms only up to linear order in \tilde{U} . Using Eqs. 3.36, 3.37, and 3.38, we get an expression for the evolved matrix element in terms of the unevolved one and changes to individual components due to evolution:

$$\begin{aligned} \langle \psi_f^\lambda | \hat{O}^\lambda | \psi_i^\lambda \rangle &= \langle \psi_f | \hat{O} | \psi_i \rangle - \underbrace{\langle \psi_f | \tilde{U} \hat{O} | \psi_i \rangle}_{\delta \langle \psi_f |} \\ &\quad + \underbrace{\langle \psi_f | \tilde{U} \hat{O} | \psi_i \rangle - \langle \psi_f | \hat{O} \tilde{U} | \psi_i \rangle}_{\delta \hat{O}} + \underbrace{\langle \psi_f | \hat{O} \tilde{U} | \psi_i \rangle}_{\delta |\psi_i\rangle} \end{aligned} \quad (3.39)$$

$$\implies \langle \psi_f^\lambda | \hat{O}^\lambda | \psi_i^\lambda \rangle = \langle \psi_f | \hat{O} | \psi_i \rangle + \mathcal{O}(\tilde{U}^2). \quad (3.40)$$

We see that the change due to evolution in the operator is equal and opposite to the sum of changes due to the evolution of the initial and final states. We also find that changes in each of the components are of the same order, and that they mix; this feature persists to higher order. Therefore, if one misses evolving an individual component, one will not reproduce the unevolved answer. It is interesting to analyze how this is a function of kinematics and will be a subject of Subsec. 3.2.4.

3.2.3 Numerical implementation

There are various practical issues in the calculation of evolved matrix elements that are worth detailing. We use C++11 for our numerical implementation of the expressions discussed in the previous section. Matrix elements with a significant number of components evolved are computationally quite expensive due to a large number of nested sums and integrals (see in particular Appendix B.1).

The deuteron wave function and NN t -matrix are obtained by discretizing the Schrödinger and Lippmann–Schwinger equations, respectively; these equations are also used to interpolate the t -matrix and wave function to points not on the discretized mesh. For example, if we write the momentum-space Schrödinger equation—neglecting channel coupling here for simplicity—as

$$\begin{aligned}\psi(p) = & \int dq q^2 G_0(-E_B, q) V(p, q) \psi(q) \\ \rightarrow & \sum_i w_i q_i^2 G_0(-E_B, q_i) V(p, q_i) \psi(q_i),\end{aligned}\quad (3.41)$$

it can be solved numerically as a simple matrix equation by setting $p \in \{q_i\}$. For any $p = p_0$ not on this mesh, the sum in Eq. 3.41 can then be evaluated to get $\psi(p_0)$. This technique is based on what has been introduced in connection with contour-deformation methods in break-up scattering calculations [143, 144]. For more details on interpolation of the t -matrix and wave function, please refer to Appendix A.

To interpolate the potential, which is stored on a momentum-space grid, we use the two-dimensional cubic spline algorithm from ALGLIB [145]. In order to avoid unnecessary recalculation of expensive quantities—in particular of the off-shell t -matrix—while still maintaining an implementation very close to the expressions given in this paper, we make use of transparent caching techniques.¹³ For most integrations, in particular those involving a principal value, we use straightforward nested Gaussian quadrature rules; only in a few cases did we find it more efficient to use adaptive routines for multi-dimensional integrals.

¹³This means that the expensive calculation is only carried out once, the first time the corresponding function is called for a given set of arguments, while subsequent calls with the same arguments return the result directly, using a fast lookup. All this is done without the *calling* code being aware of the caching details.

With these optimizations, the calculations can in principle still be run on a typical laptop computer. In practice, we find it more convenient to use a small cluster, with parallelization implemented using the TBB library [146]. On a node with 48 cores, generating data for a meaningful plot (like those shown in Subsec. 3.2.4) can then be done in less than an hour. For higher resolution and accuracy, we used longer runs with a larger number of data and integration mesh points.

3.2.4 Results

For our analysis, we studied the effect of evolution of individual components on f_L for selected kinematics in the ranges $E' = 10\text{--}100$ MeV and $\mathbf{q}^2 = 0.25\text{--}25$ fm $^{-2}$, where E' is the energy of outgoing nucleons and \mathbf{q}^2 is the three-momentum transferred by the virtual photon; both are taken in the center-of-mass frame of the outgoing nucleons. This range was chosen to cover a variety of kinematics and motivated by the set covered in Ref. [135]. We use the Argonne v_{18} potential (AV18) [12] for our calculations. It is one of the widely used potentials for nuclear few-body reaction calculations, particularly those involving large momentum transfers [119, 147].

How strong the evolution of individual components (or a subset thereof) affects the result for f_L depends on the kinematics. One kinematic configuration of particular interest is the so-called quasi-free ridge. As discussed in Subsec. 3.2.1, the four-momentum transferred by the virtual photon in the center-of-mass frame is (ω, \mathbf{q}) . The criterion for a configuration to lie on the quasi-free ridge is $\omega = 0$. Physically, this means that the nucleons in the deuteron are on their mass shell. As shown in Ref. [135], at the quasi-free ridge the energy of the outgoing nucleons (E') and the photon momentum transfer are related by

$$E' = \sqrt{M_d^2 + \mathbf{q}^2} - 2M, \quad (3.42)$$

which reduces to

$$E' \text{ (in MeV)} \approx 10 \mathbf{q}^2 \text{ (in fm}^{-2}\text{).} \quad (3.43)$$

The quasi-free condition in the center-of-mass frame is the same as the quasi-elastic condition in the lab frame. There, the quasi-elastic ridge is defined by $W^2 = m_p^2 \Rightarrow Q^2 = 2\omega_{\text{lab}} m_p$, where W is the invariant mass. On the quasi-elastic ridge, the so-called missing momentum¹⁴ vanishes, $p_{\text{miss}} = 0$.

In Fig. 3.12 we plot f_L along the quasi-free ridge both in the impulse approximation (IA) and with the final-state interactions (FSI) included as a function of energy of the outgoing nucleons for a fixed angle, $\theta' = 15^\circ$ of the outgoing proton. E' and \mathbf{q}^2 in Fig. 3.12 are related by Eq. 3.42. Comparing the solid curve labeled $\langle \psi_f | J_0 | \psi_i \rangle$ in the legend to the dashed curve (labeled $\langle \phi | J_0 | \psi_i \rangle$) we find that FSI effects are minimal for configurations on the quasi-free ridge especially at large energies.

In an intuitive picture, this is because after the initial photon is absorbed, both the nucleons in the deuteron are on their mass shell at the quasi-free ridge, and therefore no FSI are needed to make the final-state particles real. As we move away from the ridge, FSI become more important, as additional energy-momentum transfer is required to put the neutron and the proton on shell in the final state. The difference between full f_L and f_L in IA at small energies is also seen to hold for few-body nuclei [148].

Figure 3.12 also shows f_L calculated from evolving only one of the components of the matrix element in Eq. 3.35. We note that the effects of SRG evolution of the

¹⁴The missing momentum is defined as the difference of the measured proton momentum and the momentum transfer, $\mathbf{p}_{\text{miss}} \equiv \mathbf{p}_{\text{lab}}^{\text{proton}} - \mathbf{q}_{\text{lab}}$.

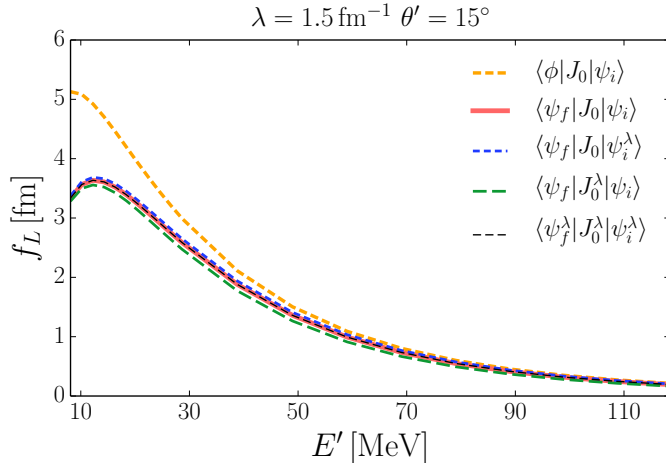


Figure 3.12: f_L calculated at various points on the quasi-free ridge for $\theta' = 15^\circ$ for the AV18 potential. Legends indicate which component of the matrix element in Eq. 3.35 used to calculate f_L is evolved. There are no appreciable evolution effects all along the quasi-free ridge. The effect due to evolution of the final state is small as well and is not shown here to avoid clutter. f_L calculated in the impulse approximation is also shown for comparison.

individual components are minimal at the quasi-free ridge as well. The kinematics at the quasi-free ridge are such that only the long-range (low-momentum) part of the deuteron wave function is probed, the FSI remains small under evolution, and then unitarity implies minimal evolution of the current. As one moves away from the quasi-free ridge, the effects of evolution of individual components become prominent. Note that $\langle \psi_f | J_0 | \psi_i \rangle = \langle \psi_f^\lambda | J_0^\lambda | \psi_i^\lambda \rangle$ and therefore the unevolved vs. all-evolved f_L overlap in Fig. 3.12.

Figure 3.13 shows the ‘phase space’ of kinematics for SRG $\lambda = 1.5 \text{ fm}^{-1}$. The quasi-free ridge is along the solid line in Fig. 3.13. In the shaded region the effects generated by the evolution of individual components are weak (only a few percent relative difference). As one moves away from the quasi-free ridge, these differences

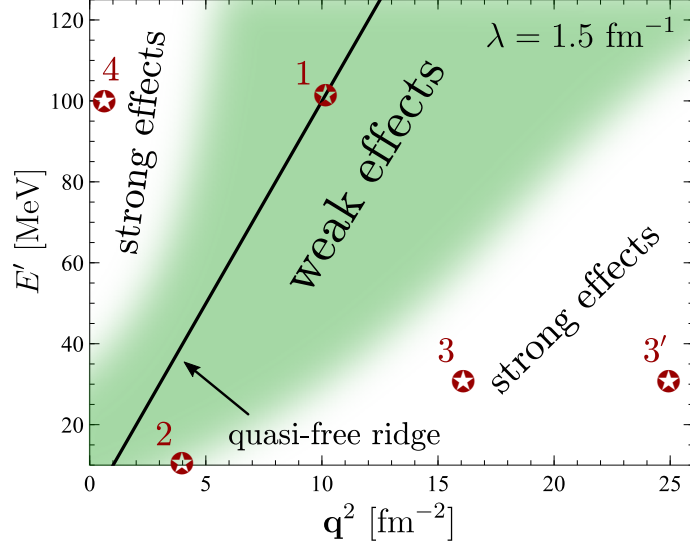


Figure 3.13: ‘Phase space’ of kinematics for $\lambda = 1.5 \text{ fm}^{-1}$. The effects of evolution get progressively prominent as one moves further away from the quasi-free ridge. The kinematics of the labeled points are considered later

get progressively more prominent. The terms ‘small’ and ‘weak’ in Fig. 3.13 are used in a qualitative sense. In the shaded region denoted by ‘weak effects’, the effects of evolution are not easily discernible on a typical f_L versus θ' plot, as seen in Fig. 3.14, whereas in the region labeled by ‘strong effects’, the differences due to evolution are evident on such a plot (e.g., see Fig. 3.16). The size of the shaded region in Fig. 3.13 depends on the SRG λ . It is large for high λ ’s and gets smaller as the λ is decreased (note that smaller SRG λ means greater evolution). Next, we look in detail at a few representative kinematics, indicated by points in Fig. 3.13.

At the quasifree ridge

As a representative of quasi-free kinematics, we choose $E' = 100 \text{ MeV}$ and $\mathbf{q}^2 = 10 \text{ fm}^{-2}$ and plot f_L as a function of angle in Fig. 3.14. The effect of including FSI

is small for this configuration for all angles. Also, the effects due to evolution of the individual components are too small to be discernible. All this is consistent with the discussion in the previous section.

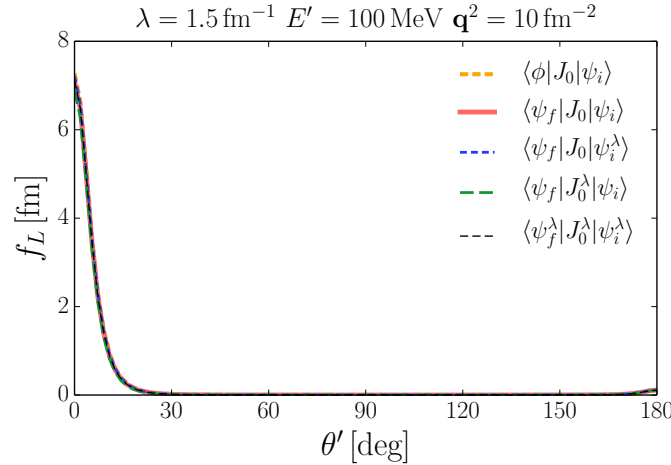


Figure 3.14: f_L calculated for $E' = 100$ MeV and $\mathbf{q}^2 = 10$ fm $^{-2}$ (point “1” in Fig. 3.13) for the AV18 potential. Legends indicate which component of the matrix element in Eq. 3.35 used to calculate f_L is evolved. θ' is the angle of the outgoing proton in the center-of-mass frame. There are no discernible evolution effects for all angles. The effect due to evolution of the final state is small as well and is not shown here to avoid clutter. f_L calculated in the IA, $\langle \phi | J_0 | \psi_i \rangle$, is also shown for comparison.

Near the quasi-free ridge

Next we look at the kinematics $E' = 10$ MeV and $\mathbf{q}^2 = 4$ fm $^{-2}$, which is near the quasi-free ridge. This is the point “2” in Fig. 3.13. As seen in Fig. 3.15, the different curves for f_L obtained from evolving different components start to diverge. Figure 3.15 also shows f_L calculated in IA. Comparing this to the full f_L including FSI, we see that the effects due to evolution are small compared to the FSI contributions. This smallness prevents us from making any systematic observations about the effects

due to evolution at this kinematics. We thus move on to kinematics which show more prominent effects.

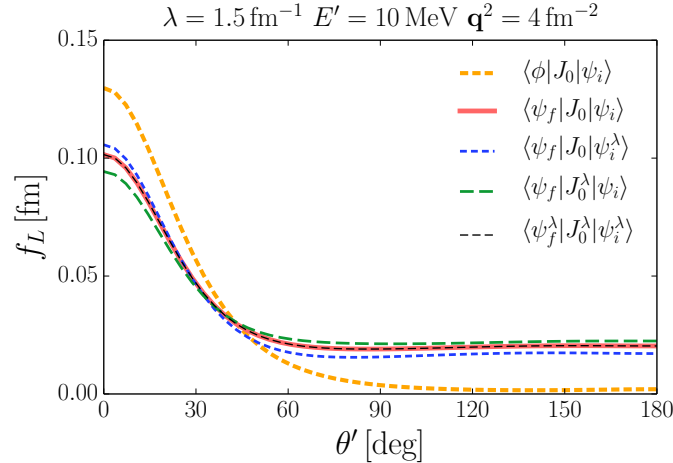


Figure 3.15: f_L calculated for $E' = 10$ MeV and $\mathbf{q}^2 = 4$ fm $^{-2}$ (point “2” in Fig. 3.13) for the AV18 potential. Legends indicate which component of the matrix element in Eq. 3.35 used to calculate f_L is evolved. f_L calculated in the IA, $\langle \phi | J_0 | \psi_i \rangle$, is also shown for comparison. The effects due to evolution of individual components on f_L are discernible, but still small (compared to the FSI contribution). The effect due to evolution of the final state is small as well and is not shown here to avoid clutter.

Below the quasi-free ridge

We next look in the region where E' (in MeV) $\ll 10 \mathbf{q}^2$ (in fm $^{-2}$), *i.e.*, below the quasi-free ridge in Fig. 3.13. We look at two momentum transfers $\mathbf{q}^2 = 16$ fm $^{-2}$ and $\mathbf{q}^2 = 25$ fm $^{-2}$ for $E' = 30$ MeV, which are points “3” and “3” in Fig. 3.13. Figures 3.16 and 3.17 indicate the effects on f_L from evolving individual components of the matrix elements. It is noteworthy that in both cases evolution of the current gives a prominent enhancement, whereas evolution of the initial and final state gives a suppression. When all the components are evolved consistently, these changes

combine and we recover the unevolved answer for f_L . This verifies the accurate implementation of the equations derived in Subsec. 3.2.2.

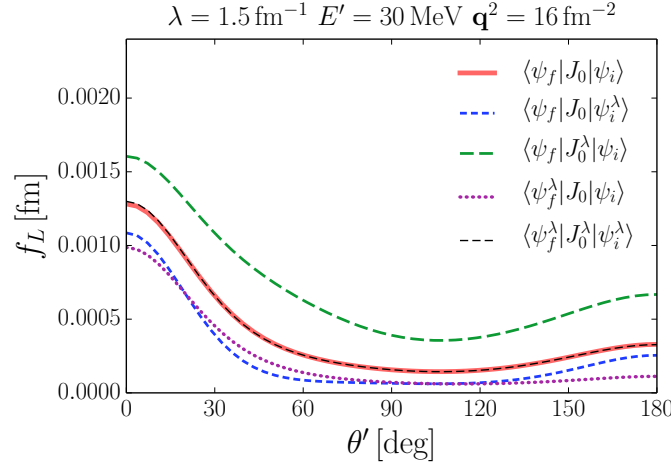


Figure 3.16: f_L calculated for $E' = 30$ MeV and $\mathbf{q}^2 = 16$ fm $^{-2}$ (point “3” in Fig. 3.13) for the AV18 potential. Legends indicate which component of the matrix element in Eq. 3.35 used to calculate f_L is evolved. Prominent enhancement with evolution of the current only and suppression with evolution of the initial state and the final state only, respectively.

It is possible to qualitatively explain the behavior seen in Figs. 3.16 and 3.17. As noted in Eq. 3.18, the overlap matrix element is given by the sum of the IA part and the FSI part. Below the quasi-free ridge these two terms add constructively. In this region, f_L calculated in impulse approximation is smaller than f_L calculated by including the final-state interactions.

(a) Evolving the initial state Let us first consider the effect of evolving the initial state only. We have

$$\langle \psi_f | J_0 | \psi_i^\lambda \rangle = \langle \phi | J_0 | \psi_i^\lambda \rangle + \langle \phi | t^\dagger G_0^\dagger J_0 | \psi_i^\lambda \rangle . \quad (3.44)$$

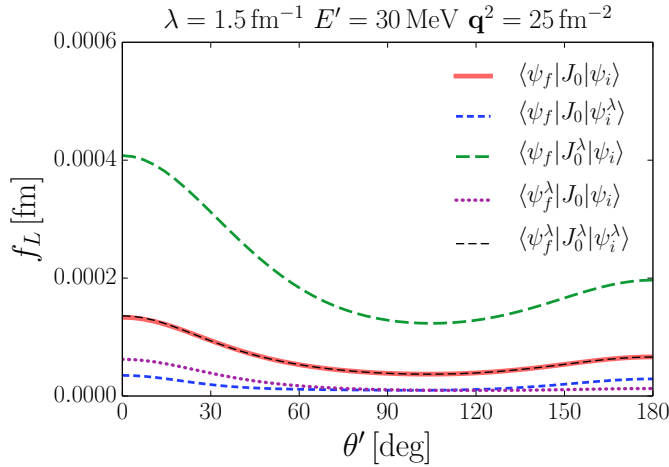


Figure 3.17: f_L calculated for $E' = 30$ MeV and $\mathbf{q}^2 = 25$ fm $^{-2}$ (point “3” in Fig. 3.13) for the AV18 potential. Legends indicate which component of the matrix element in Eq. 3.35 used to calculate f_L is evolved. Prominent enhancement with evolution of the current only and suppression with evolution of the initial state and the final state only, respectively.

As seen in Eq. 3.9, in the term $\langle \phi | J_0 | \psi_i^\lambda \rangle$ the deuteron wave function is probed between $|p' - q/2|$ and $p' + q/2$. These numbers are $(1.2, 2.9)$ fm $^{-1}$ and $(1.7, 3.4)$ fm $^{-1}$ for $E' = 30$ MeV, $\mathbf{q}^2 = 16$ fm $^{-2}$ and $E' = 30$ MeV, $\mathbf{q}^2 = 25$ fm $^{-2}$, respectively. The evolved deuteron wave function is significantly suppressed at these high momenta. This behavior is reflected in the deuteron momentum distribution plotted in Fig. 3.18. The deuteron momentum distribution $n(k)$ is proportional to the sum of the squares of S - and D - state deuteron wave functions. Thus, the first (IA) term in Eq. 3.44 is much smaller than its unevolved counterpart in Eq. 3.18, for all angles. We note that even though we only use the AV18 potential to study changes due to evolution, these changes will be significant for other potentials as well.

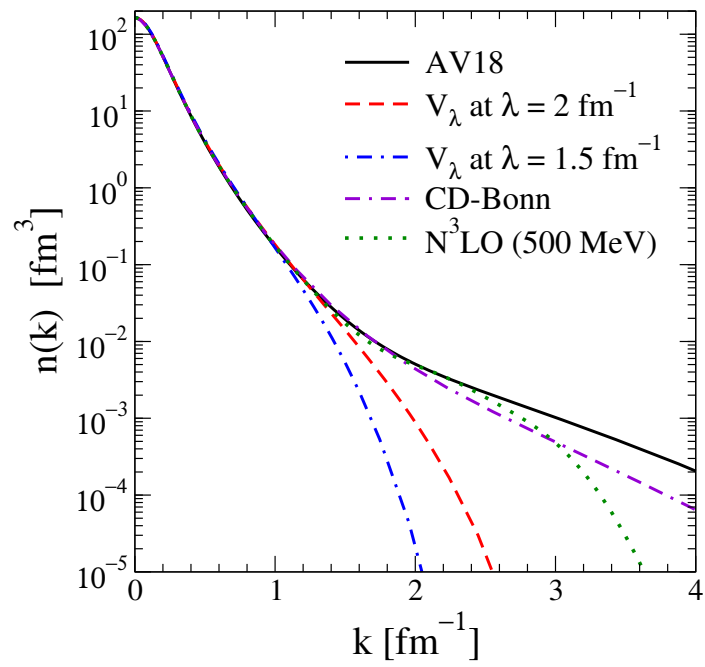


Figure 3.18: Momentum distribution for the deuteron for the AV18 [12], CD-Bonn [19], and the Entem-Machleidt $N^3\text{LO}$ chiral EFT [66] potentials, and for the AV18 potential evolved to two SRG λ 's.

Evaluation of the second (FSI) term in Eq. 3.44 involves an integral over all momenta, as indicated in Eq. 3.24. We find that $|\langle \phi | t^\dagger G_0^\dagger J_0 | \psi_i^\lambda \rangle| < |\langle \phi | t^\dagger G_0^\dagger J_0 | \psi_i \rangle|$. As mentioned before, because the terms $\langle \phi | J_0 | \psi_i \rangle$ and $\langle \phi | t^\dagger G_0^\dagger J_0 | \psi_i \rangle$ add constructively below the quasi-free ridge and because the magnitude of both these terms decreases upon evolving the wave function, we have

$$|\langle \psi_f | J_0 | \psi_i^\lambda \rangle| < |\langle \psi_f | J_0 | \psi_i \rangle|. \quad (3.45)$$

The above relation holds for most combinations of m_{J_d} and m_{s_f} . For those m_{J_d} and m_{s_f} for which Eq. 3.45 does not hold, the absolute value of the matrix element is much smaller than for those for which the Eq. 3.45 *does* hold, and therefore we have f_L calculated from $\langle \psi_f | J_0 | \psi_i^\lambda \rangle$ smaller than the f_L calculated from $\langle \psi_f | J_0 | \psi_i \rangle$, as seen in Figs. 3.16 and 3.17.

(b) Evolving the final state As indicated in Eq. 3.32, evolving the final state entails the evolution of the t -matrix. The overlap matrix element therefore is

$$\langle \psi_f^\lambda | J_0 | \psi_i \rangle = \langle \phi | J_0 | \psi_i \rangle + \langle \phi | t_\lambda^\dagger G_0^\dagger J_0 | \psi_i \rangle. \quad (3.46)$$

The IA term is the same as in the unevolved case. The SRG evolution leaves the on-shell part of the t -matrix—which is directly related to observables—Invariant. The magnitude of the relevant off-shell t -matrix elements decreases on evolution, though. As a result we have

$$|\langle \psi_f^\lambda | J_0 | \psi_i \rangle| < |\langle \psi_f | J_0 | \psi_i \rangle|. \quad (3.47)$$

This is reflected in f_L as calculated from the evolved final state, and seen in Figs. 3.16 and 3.17.

The effect of evolution of the initial state and the final state is to suppress f_L . When all the three components are evolved, we reproduce the unevolved answer as indicated in Fig. 3.16 and 3.17. It is therefore required that we find a huge enhancement when just the current is evolved.

The kinematics $E' = 30$ MeV, $\mathbf{q}^2 = 25$ fm $^{-2}$ is further away from the quasi-free ridge than $E' = 30$ MeV, $\mathbf{q}^2 = 16$ fm $^{-2}$. The evolution effects discussed above get progressively more prominent the further away one is from the quasifree ridge. This can be verified by comparing the effects due to evolution of individual components in Figs. 3.16 and 3.17.

As remarked earlier, away from the quasi-free ridge the FSI become important. Nonetheless, it is still instructive to look at f_L calculated in the IA at these kinematics. Note that the (unevolved) f_L calculated in the IA, shown in Figs. 3.19 and 3.20, is

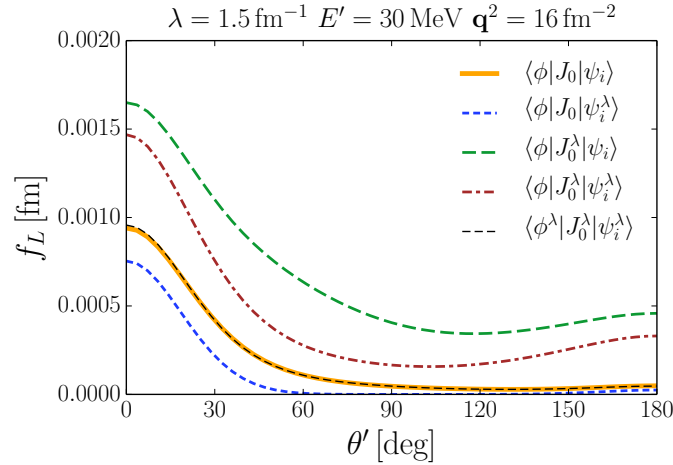


Figure 3.19: f_L in IA ($\langle\psi_f|\equiv\langle\phi|$) calculated for $E' = 30$ MeV and $\mathbf{q}^2 = 16$ fm $^{-2}$ for the AV18 potential. Legends indicate which component of the matrix element in Eq. 3.35 used to calculate f_L are evolved.

smaller than the full f_L that takes into account the final state interactions (cf. the corresponding curves in Figs. 3.16 and 3.17). This is consistent with the claim made earlier that below the quasi-free ridge the two terms in Eq. 3.18 add constructively.

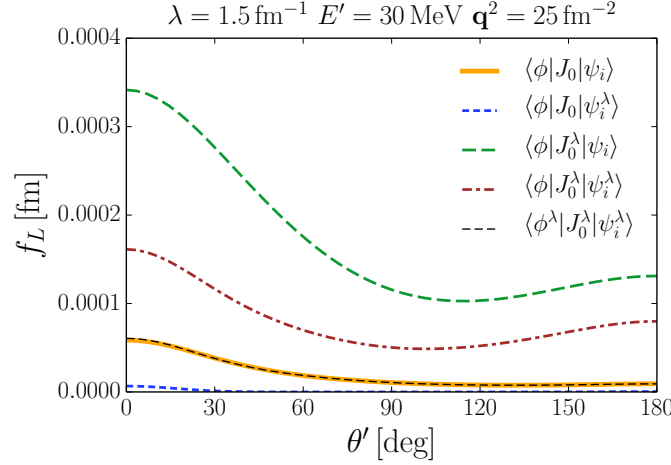
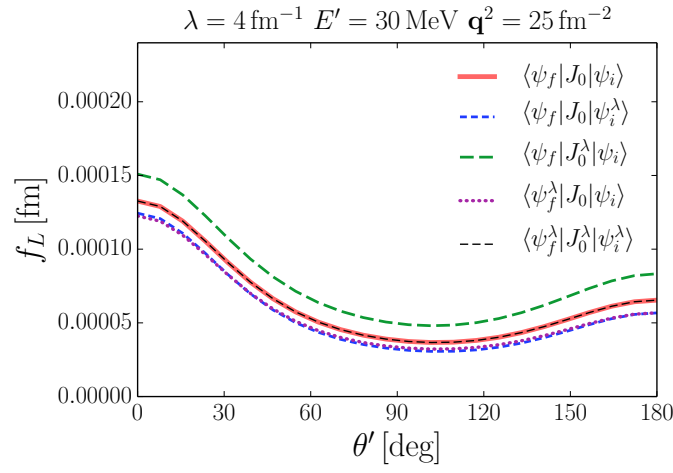


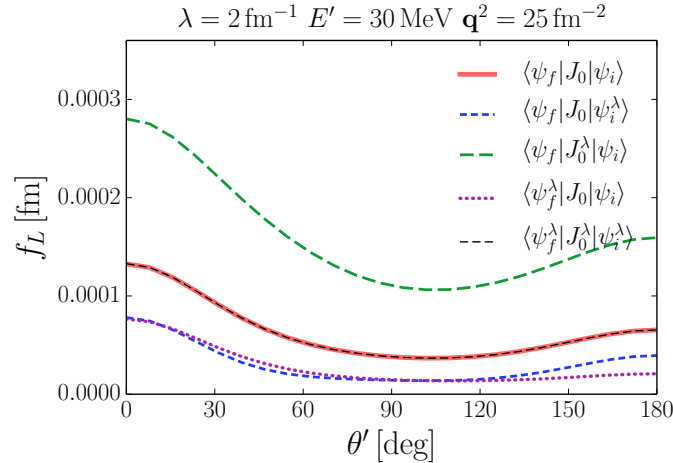
Figure 3.20: f_L in IA ($\langle \psi_f | \equiv \langle \phi |$) calculated for $E' = 30$ MeV and $\mathbf{q}^2 = 25$ fm $^{-2}$ for the AV18 potential. Legends indicate which component of the matrix element in Eq. 3.35 used to calculate f_L are evolved.

The results in Figs. 3.19 and 3.20 can again be qualitatively explained based on our discussion above. The evolution of the deuteron wave function leads to suppression as the evolved wave function does not have strength at high momentum. The evolved current thus leads to enhancement. Evolution of both the current and the initial state decreases f_L from just the evolved current value, but it is not until we evolve all three components—final state, current, and the initial state—that we recover the unevolved answer.

As expected, the effect due to evolution increases with further evolution. This can be seen by comparing the plots in Fig. 3.21 to Fig. 3.17. In Fig. 3.22 we look at



(a) SRG $\lambda = 4 \text{ fm}^{-1}$



(b) SRG $\lambda = 2 \text{ fm}^{-1}$

Figure 3.21: f_L calculated for $E' = 30 \text{ MeV}$ and $\mathbf{q}^2 = 25 \text{ fm}^{-2}$ (point “3” in Fig. 3.13) for the AV18 potential. Legends indicate which component of the matrix element in Eq. 3.35 used to calculate f_L is evolved. The evolution is to SRG (a) $\lambda = 4 \text{ fm}^{-1}$ and (b) $\lambda = 2 \text{ fm}^{-1}$.

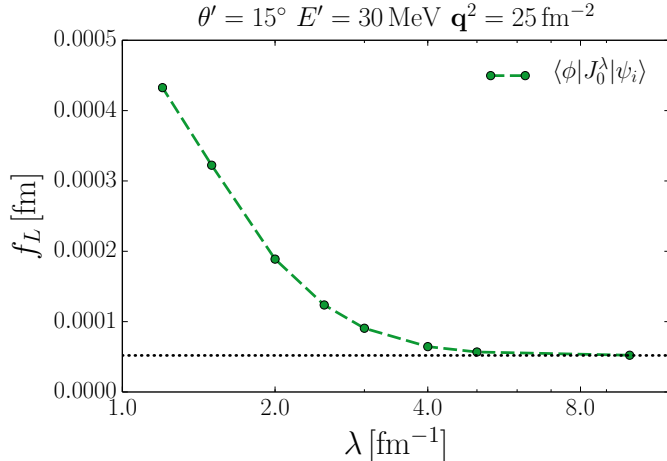


Figure 3.22: f_L in IA calculated at $\theta' = 15^\circ$ for $E' = 30$ MeV and $\mathbf{q}^2 = 25$ fm $^{-2}$ for the AV18 potential when the current operator in Eq. 3.35 used to calculate f_L is evolved to various SRG λ 's. The horizontal dotted line is the unevolved answer.

effects of the current-operator evolution on f_L as a function of the SRG λ . To isolate the effect of operator evolution, we only look at f_L calculated in IA at a specific angle in Fig. 3.22. Investigating details of the operator evolution forms the basis of ongoing work. A few preliminary results along those lines are presented in Subsec. 3.2.5.

Above the quasi-free ridge

Finally, we look at an example from above the quasi-free ridge. Figure 3.23 shows the effect of evolution of individual components on f_L for $E' = 100$ MeV and $\mathbf{q}^2 = 0.5$ fm $^{-2}$, which is point “4” in Fig. 3.13. The effects of evolution in this case are qualitatively different from those found below the quasi-free ridge. For instance, we see a peculiar suppression in f_L calculated from the evolved deuteron wave function at small angles, but an enhancement at large angles. An opposite behavior is observed for the final state. It is again possible to qualitatively explain these findings.

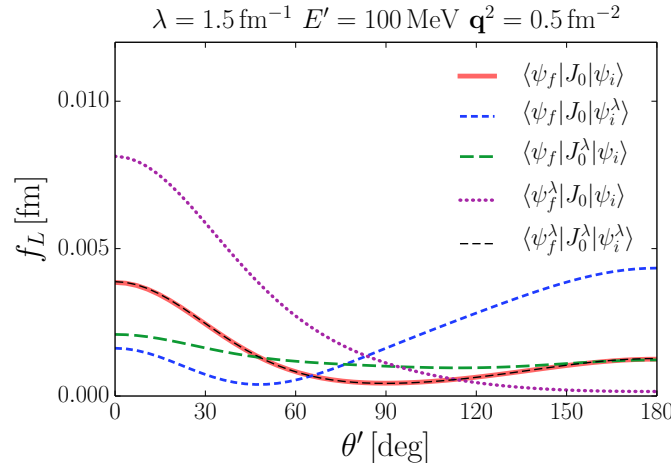


Figure 3.23: f_L calculated for $E' = 100$ MeV and $\mathbf{q}^2 = 0.5$ fm $^{-2}$ (point “4” in Fig. 3.13) for the AV18 potential. Legends indicate which component of the matrix element in Eq. 3.35 used to calculate f_L is evolved. Opposite effects from the evolution of the initial state and the final state.

(a) Evolving the initial state Above the quasi-free ridge, the IA and FSI terms in Eq. 3.18 add destructively. This can be seen by comparing the unevolved f_L curves in Figs. 3.23 and 3.24. Including the FSI brings down the value of f_L when one is above the quasi-free ridge.

At small angles, the magnitude of the IA term in Eq. 3.18 is larger than that of the FSI term. The deuteron wave function for this kinematics is probed between 1.2 and 1.9 fm $^{-1}$. With the wave-function evolution, the magnitude of the IA term in Eq. 3.44 decreases, whereas the magnitude of the FSI term in that equation slightly increases compared to its unevolved counterpart. Still, at small angles, we have $|\langle \phi | J_0 | \psi_i^\lambda \rangle| > |\langle \phi | t^\dagger G_0^\dagger J_0 | \psi_i^\lambda \rangle|$, which leads to

$$|\langle \psi_f | J_0 | \psi_i^\lambda \rangle| < |\langle \psi_f | J_0 | \psi_i \rangle|, \quad (3.48)$$

and thus to the suppression of f_L at small angles observed in Fig. 3.23.

At large angles, the magnitude of the IA term in Eq. 3.18 is smaller than that of the FSI term. With the wave-function evolution, the magnitude of IA term decreases substantially (large momenta in the deuteron wave function are probed at large angles, cf. Eq. 3.9), whereas the FSI term in Eq. 3.18 remains almost the same. This results in increasing the difference between the two terms in Eq. 3.18 as the SRG λ is decreased. As mentioned before, above the quasi-free ridge, the IA and FSI terms in Eq. 3.18 add destructively and we therefore end up with $|\langle \psi_f | J_0 | \psi_i^\lambda \rangle| > |\langle \psi_f | J_0 | \psi_i \rangle|$, leading to the observed enhancement at large angles upon evolution of the wave function (see Fig. 3.23).

(b) Evolving the final state The expression to consider is Eq. 3.46. With the evolution of the t -matrix, the magnitude of the term $\langle \phi | t_\lambda^\dagger G_0^\dagger J_0 | \psi_i \rangle$ decreases, and because of the opposite relative signs of the two terms in Eq. 3.46—and because at small angles the magnitude of the IA term is larger than the FSI term—the net effect is $|\langle \psi_f^\lambda | J_0 | \psi_i \rangle| > |\langle \psi_f | J_0 | \psi_i \rangle|$. This leads to an enhancement of f_L with evolved final state at small angles, as seen in Fig. 3.23.

At large angles the magnitude of the IA term in Eq. 3.46 is smaller than that of the FSI term. With the evolution of the t -matrix, the magnitude of the FSI term decreases and the difference between the IA and the FSI terms decreases as well. This leads to the observed overall suppression in f_L at large angles due to the evolution of the final state seen in Fig. 3.23. For those few (m_{s_f} , m_{J_d}) combinations for which the above general observations do not hold, the value of individual components is too small to make any qualitative difference.

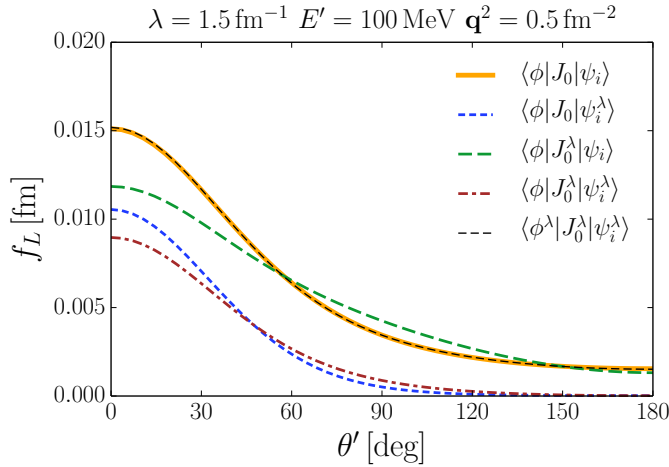


Figure 3.24: f_L in IA ($\langle\psi_f|\equiv\langle\phi|$) calculated for $E'=100$ MeV and $\mathbf{q}^2=0.5$ fm $^{-2}$ for the AV18 potential. Legends indicate which component of the matrix element in Eq. 3.35 used to calculate f_L are evolved.

Figure 3.24 shows the effect of evolution of individual components on f_L calculated in the IA for the kinematics under consideration. Again the evolved deuteron wave function does not have strength at high momenta and therefore f_L calculated from $\langle\phi|J_0|\psi_i^\lambda\rangle$ has a lower value than its unevolved counterpart.

Unitary evolution means that the effect of the evolved current is always such that it compensates the effect due to the evolution of the initial and final states. As mentioned before, varying λ shuffles the physics between long- and short-distance parts (cf. Fig. 3.9). As SRG λ decreases the blob size in Fig. 3.25 increases, the high-momentum interaction between the nucleons can no longer be resolved, and thus the one-body current operator develops two- and higher-body components. Our ongoing work examines more directly the behavior of the current as it evolves to better understand how to carry over the results observed here to other reactions.

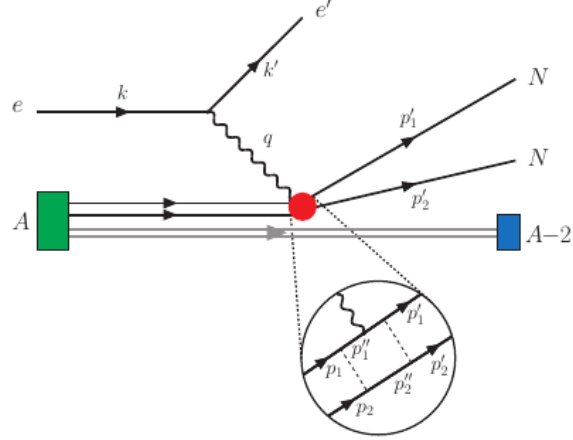


Figure 3.25: One-body current operator develops two- and higher-body components under SRG evolution.

3.2.5 Operator evolution and q -factorization

The first work on operator evolution via the SRG evolution was done in Ref. [124]. Among other things the authors of Ref. [124] looked at the effect of evolution on the momentum distribution in the deuteron (cf. Fig. 3.26). As seen in Fig. 3.26,

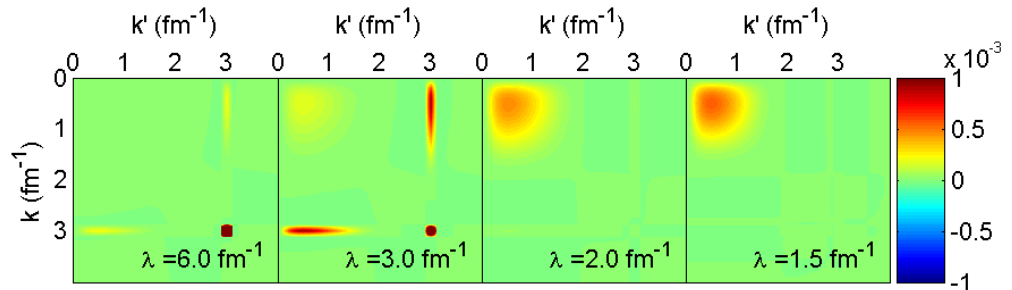


Figure 3.26: Integrand of $\langle \psi_{\text{deut}}^\lambda | (a_q^\dagger a_q)^\lambda | \psi_{\text{deut}}^\lambda \rangle$ in the 3S_1 channel for $q = 3.02 \text{ fm}^{-1}$. The initial potential is the chiral N³LO (500 MeV) potential [66]. Figure from [124].

the unevolved momentum operator which is peaked at large momentum develops

strength at low momentum on evolution. The high-momentum one-body part of the operator $a_q^\dagger a_q$ is unchanged by the evolution, but it is suppressed by the evolved wave function, which is why only the two-body part survives in the matrix element $\langle \psi_{\text{deut}}^\lambda | (a_q^\dagger a_q)^\lambda | \psi_{\text{deut}}^\lambda \rangle$ at lower λ .

We follow the approach of [124], but focus instead on the current relevant to the deuteron disintegration. The relevant current matrix element is given by Eq. 3.22. The δ function in Eq. 3.22 can be used to do the integral analytically, giving a condition over the allowed momenta.

$$\begin{aligned}
\langle k_1 J_1 m_{J_d} L_1 S = 1 T_1 | J_0^- | k_2 J = 1 m_{J_d} L_2 S = 1 T = 0 \rangle &= \frac{\pi^2}{2} (G_E^p + (-1)^{T_1} G_E^n) \\
&\times \sum_{\tilde{m}_s=-1}^1 \langle J_1 m_{J_d} | L_1 m_{J_d} - \tilde{m}_s S = 1 \tilde{m}_s \rangle P_{L_1}^{m_{J_d} - \tilde{m}_s} \left(\frac{k_1^2 - k_2^2 + q^2/4}{k_1 q} \right) \frac{2}{k_1 k_2 q} \\
&\times P_{L_2}^{m_{J_d} - \tilde{m}_s} \left(\frac{k_1^2 - k_2^2 - q^2/4}{k_2 q} \right) \langle L_2 m_{J_d} - \tilde{m}_s S = 1 \tilde{m}_s | J = 1 m_{J_d} \rangle \\
&\quad \cdots \text{for } k_2 \in (|k_1 - q/2|, k_1 + q/2) \\
&= 0 \text{ otherwise}
\end{aligned} \tag{3.49}$$

In deriving Eq. 3.49 from Eq. 3.22 we have used the property of the δ function that

$$\delta(f(x)) = \frac{\delta(x - x_0)}{|f'(x_0)|}, \tag{3.50}$$

where x_0 is the zero of $f(x)$.

Equation 3.49 along with the expressions in Appendix B.3 can be used to study the effects of evolution on the deuteron disintegration current operator. In what follows, we will look at some representative graphs. For convenience we set $G_E^p = 1$ and $G_E^n = 0$; it should not qualitatively affect the results.

Figure 3.27 looks at the strength distribution of the unevolved and evolved current in a specific channel. The unevolved current is a one-body operator and is peaked

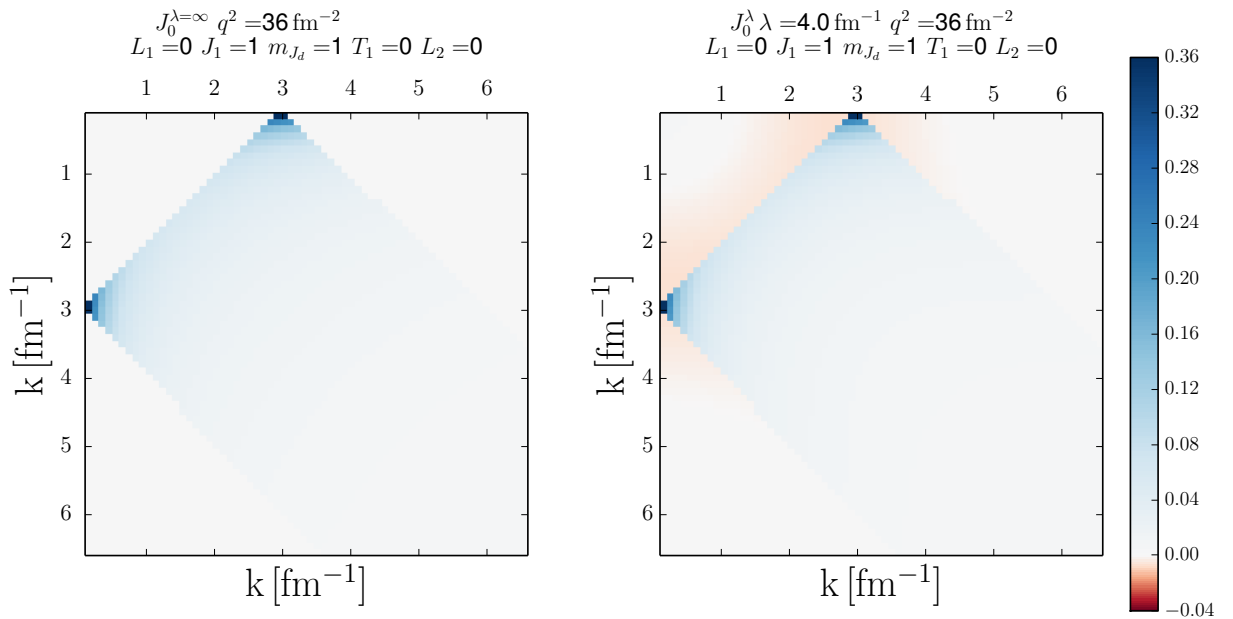


Figure 3.27: Contour plot for the matrix element $\langle k_1 J_1 m_{J_d} L_1 S = 1 T_1 | J_0^{-\lambda} | k_2 J = 1 m_{J_d} L_2 S = 1 T = 0 \rangle$ for the quantum numbers indicated for $\lambda = \infty$ and $\lambda = 4 \text{ fm}^{-1}$.

at $(0, q/2)$ and $(q/2, 0)$. With SRG evolution, the current develops two-body components. As seen in Figs. 3.27 and 3.28, the changes due to evolution are rather distributed. The evolved current doesn't become pathologically large at high momentum. This is important because for practical calculations the evolved current will be used in conjunction with the evolved wave function. The evolved wave functions have negligible strength at high momentum and the absence of pathologies in the evolved current make sure that the calculations with SRG in the reduced basis are possible. To illustrate this we turn to Fig. 3.29.

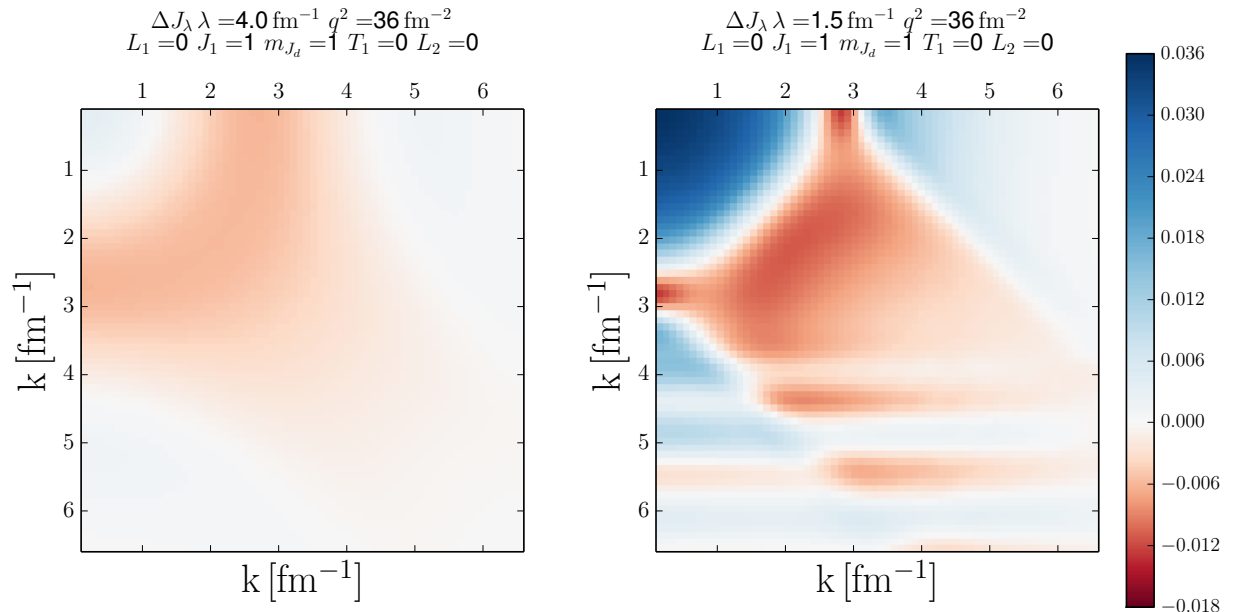


Figure 3.28: Contour plot for the matrix element $\langle k_1 J_1 m_{J_d} L_1 S = 1 T_1 | \Delta J^{-\lambda} | k_2 J = 1 m_{J_d} L_2 S = 1 T = 0 \rangle$ for the quantum numbers indicated for $\lambda = 4$ and $\lambda = 1.5 \text{ fm}^{-1}$. $\Delta J^{-\lambda} \equiv J_0^{-\lambda} - J_0$.

Figure 3.29 shows the contour plot for the integrand of $\langle p'; {}^3S_1 | J_0^\lambda(q) | \psi_{\text{deut}, {}^3S_1}^\lambda \rangle$. The ket is the deuteron state and the bra state corresponds to the outgoing nucleons (up to factors of Spherical Harmonics and Clebsch-Gordan coefficients) without the final state interactions. We find that as we evolve to lower SRG λ , the strength in

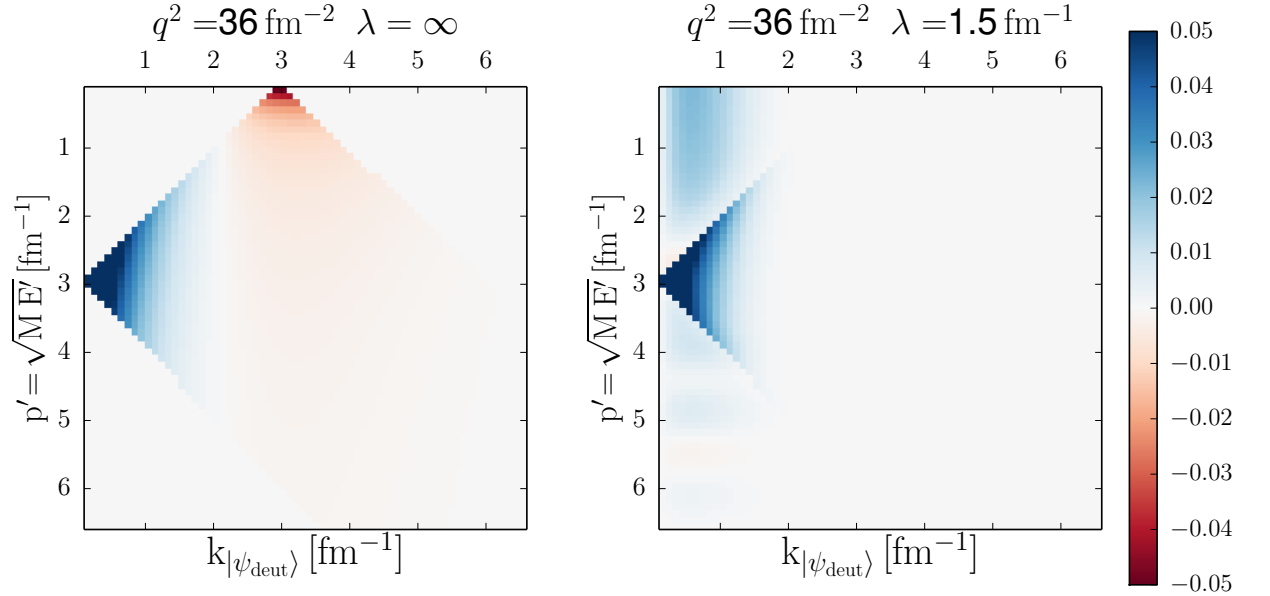


Figure 3.29: Contour plot for the integrand of $\langle p' J_1=1 m_{J_d}=1 L_1=0 S=1 T_1=0 | J_0^{-\lambda} | \psi_{\text{deut}, {}^3S_1}^\lambda(k) \rangle$ for $\lambda = \infty$ and $\lambda = 1.5 \text{ fm}^{-1}$.

the integrand shifts to lower momenta in deuteron. It is also possible to qualitatively explain the results in Subsec. 3.2.4 on the basis of Fig. 3.29. For a given $p' = p_0$, the value for $\langle p_0; {}^3S_1 | J_0^\lambda(q) | \psi_{\text{deut}, {}^3S_1}^\lambda \rangle$ is obtained by adding all the points along the horizontal axis $p' = p_0$ in Fig. 3.29.

The kinematics at the quasi-free ridge corresponds to $p_0 = q/2$ (can be derived from Eq. 3.43). We see from Fig. 3.29 that for $p_0 = q/2$, the contribution to the matrix element $\langle p_0; {}^3S_1 | J_0(q) | \psi_{\text{deut}, {}^3S_1} \rangle$ comes from the low momentum components in the deuteron. These low-momentum components are unchanged under SRG evolution and therefore we see hardly any scale dependence at the quasi-free ridge in the results presented in Subsec. 3.2.4. Next consider $p_0 = 1 \text{ fm}^{-1}$. For this case, the contribution to $\langle p_0; {}^3S_1 | J_0(q) | \psi_{\text{deut}, {}^3S_1} \rangle$ comes from the high-momentum components in the deuteron, which change substantially under evolution. Moreover, we see from Fig. 3.29 that the changes due to evolution are smooth low-momentum effects. This indicates that the changes due to evolution are of the form of contact terms as expected from an EFT approach (cf. Fig. 3.8).

q-factorization of f_L

It was observed and explained in Refs. [124, 149] that for $k < \lambda$ and $q \gg \lambda$ the unitary evolution operator factorizes: $U_\lambda(k, q) \rightarrow K_\lambda(k)Q_\lambda(q)$. This factorization was observed by looking at the ratio of $U(k_i, q)/U(k_0, q)$ for small k'_i s and k_0 , and noting that the ratio plateaus at high q (cf. Fig. 3.30).

Similar behavior is observed for the evolved current in Fig. 3.31. Preliminary analysis indicates that the scaling

$$J_0^\lambda(k, k'; q) \rightarrow Z_\lambda(k, k') A(q) \quad (3.51)$$

is a result of both the form of the unevolved current and the momentum factorization of U matrices.

Note that $f_L \sim \sum_{m_s, m_J} |\langle \psi_f^\lambda | J_0^\lambda | \psi_i^\lambda \rangle|^2$. The “q-factorization” of J_0^λ and U matrices indicates that the observable f_L should scale with q as well. We see in Fig. 3.32a that

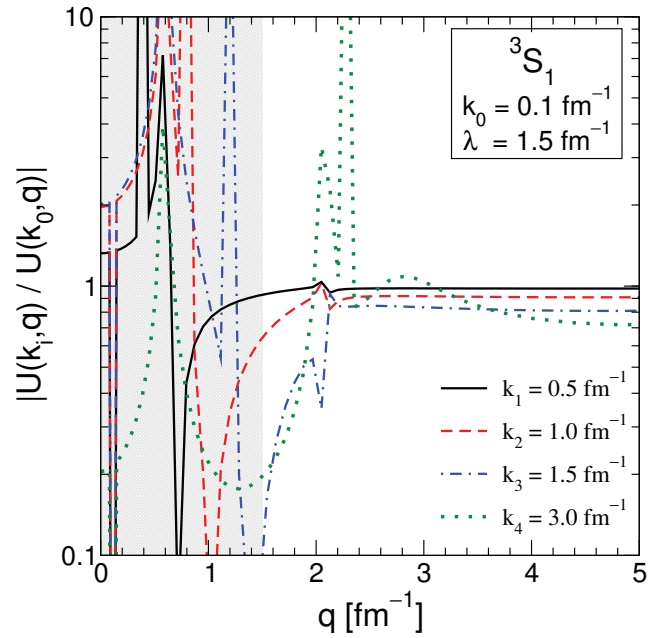


Figure 3.30: Factorization of U matrices demonstrated by plateaus at high q . Figure from [124].

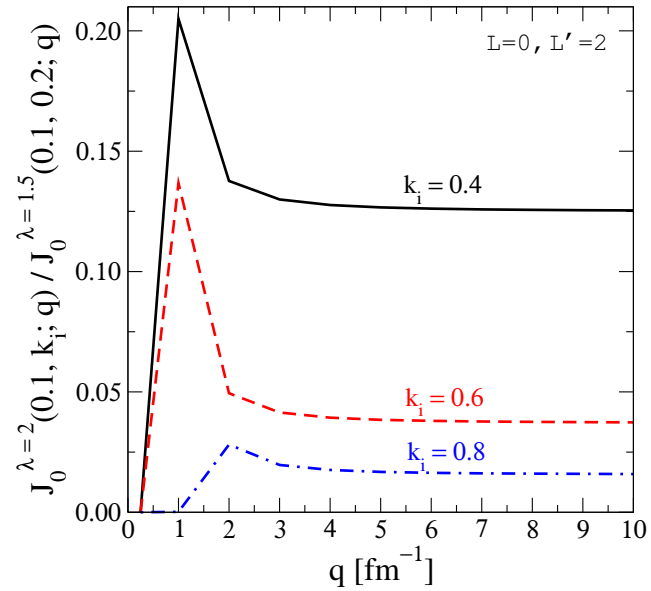


Figure 3.31: Factorization of the evolved current J_0^λ demonstrated by plateaus at high q .

this indeed is the case. f_L is a function of the outgoing nucleon momentum (p'), the

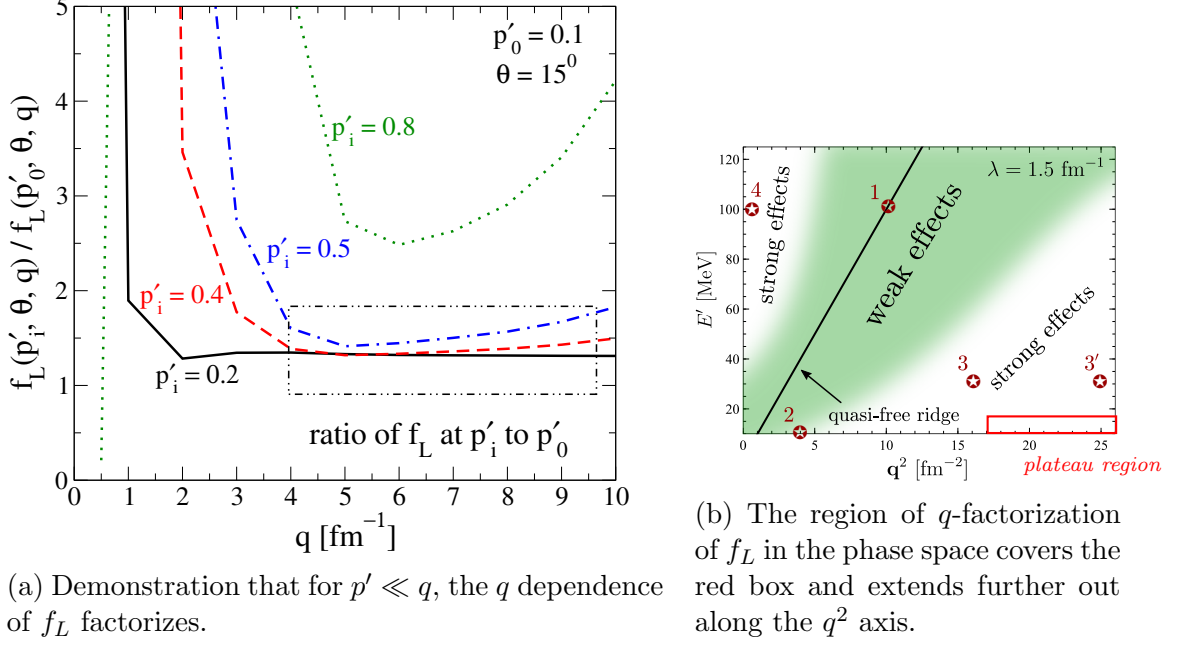


Figure 3.32: q -factorization of f_L .

proton emission angle (θ'), and the momentum transferred by the photon (q). For $p' \ll q$, Fig. 3.32a tells us that

$$f_L(p', \theta'; q) \rightarrow g(p', \theta) B(q) . \quad (3.52)$$

Figure 3.32b shows the region in the phase space where Eq. 3.52 holds.

Figure 3.33 indicates that f_L by itself is a strong function of q . In the plateau region of Fig. 3.32a, the denominator of the ratio varies by over two orders of magnitude. Given this and the complicated nature of f_L calculations (results here include the FSIs), the scaling observed in Fig. 3.32a is non-trivial.

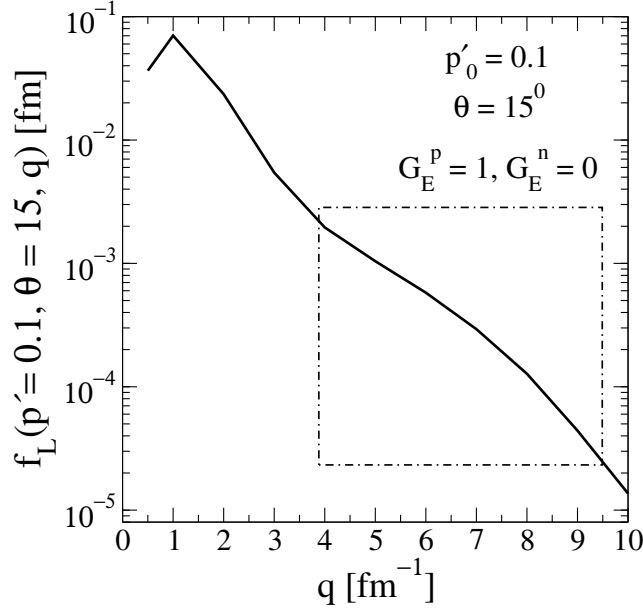


Figure 3.33: f_L is a strong function of q . The box indicates the plateau region in Fig. 3.32a.

It seems that the observed q -factorization of f_L can be explained from the SRG perspective by invoking the factorization of U matrices. It remains to be seen how the q -factorization could be explained starting from the unevolved matrix element. This offers an interesting scenario, where the observation in Eq. 3.52 can be explained by two different interpretations.

3.3 Summary and Outlook

Nuclear properties such as momentum distributions are extracted from experiment by invoking the factorization of structure, which includes descriptions of initial and final states, and reaction, which includes the description of the probe components. The factorization between reaction and structure depends on the scale and scheme chosen for doing calculations. Unlike in high-energy QCD, this scale and scheme

dependence of factorization is often not taken into account in low-energy nuclear physics calculations, but is potentially critical for interpreting experiment. In our work we investigated this issue by looking at the simplest knockout reaction: deuteron electrodisintegration. We used SRG transformations to test the sensitivity of the longitudinal structure function f_L to evolution of its individual components: initial state, final state, and the current.

We find that the effects of evolution depend on kinematics, but in a *systematic* way. Evolution effects are negligible at the quasi-free ridge, indicating that the scale dependence of individual components is minimal there. This is consistent with the quasi-free ridge mainly probing the long-range part of the wave function, which is largely invariant under SRG evolution. This is also the region where contributions from FSI to f_L are minimal. The effects get progressively more pronounced the further one moves away from the quasifree ridge. The nature of these changes depends on whether one is above or below the quasifree ridge in the phase-space plot (Fig. 3.13). As indicated in Subsec. 3.2.4, these changes can also be explained qualitatively by looking at the overlap matrix elements. This allows us to predict the effects due to evolution depending on kinematics.

Our results demonstrate that scale dependence needs to be taken into account for low-energy nuclear calculations. While we showed this explicitly only for the case of the longitudinal structure function in deuteron disintegration, we expect the results should qualitatively carry over for other knock-out reactions as well. An area of active investigation is the extension of the formalism presented here to hard scattering processes.

SRG transformations are routinely used in nuclear structure calculations because they lead to accelerated convergence for observables like binding energies. We demonstrated that SRG transformations can be used for nuclear knock-out reactions as well as long as the operator involved is also consistently evolved. Naively, one would expect the evolved operator to be more complicated than the unevolved one. However, as we saw in Subsec. 3.2.5, the SRG evolution makes interpretation of the high q -factorization of observables easy. It sets the stage for exploiting the operator product expansion as in Refs. [104, 124]. Moreover, we saw that the changes due to evolution are regulated contact terms as expected from an EFT perspective.

We plan to use pionless EFT as a framework to quantitatively study the effects of operator evolution. It should be a good starting point to understand in detail how a one-body operator develops strength in two- and higher-body sectors upon evolution. This can give insight on the issue of power counting of operator evolution. Pionless EFT has been employed previously to study deuteron electrodisintegration in Ref. [150], where it was used to resolve a discrepancy between theory and experiment.

Extending our work to many-body nuclei requires inclusion of 3N forces and 3N currents. Consistent evolution in that case would entail evolution in both two and three-body sectors. However, SRG transformations have proven to be technically feasible for evolving three-body forces [27, 53, 54, 97]. Thus, extending our calculations to many-body nuclei would be computationally intensive, but is feasible in the existing framework. Including the effects of FSI is challenging for many-body systems and has been possible only recently for light nuclei [148, 151]. It would be interesting to investigate if the scale and scheme dependence of factorization allows us to choose a scale where the FSI effects are minimal.

Chapter 4: Epilogue

This thesis presented the author’s original work over the past four years. Most of the work has already been published. The thesis offers more motivation for our work, added details about calculations, and presents new insights along with recent developments.

The work in Chapter 2 started as author’s warm-up problem during the summer following his first year. We kept finding interesting results, and the warm-up problem turned into a full-fledged project resulting in three publications [56–58]. The key development was the mapping between the basis truncation and the hard-wall boundary condition. This mapping led to development of extrapolation schemes for energy, radii, and allowed extraction of phase shifts. Our work focused on two-body systems, though in principle, the two-body results usually don’t need extrapolation. However, availability of exact answers allowed us to test our results. Our results pioneered the development of physically motivated extrapolation schemes in LENP. The work in Refs. [98, 99, 108] showed a way to extend our work to many-body nuclei.

The uncertainty in the scale and scheme dependence of nuclear structure and reactions components made it difficult to make robust predictions for experiments (cf. Fig. 1.19). To tackle this issue, we followed the same approach as in Chapter 2, i.e., we started with a two-body system which is more tractable. We found that

the scale dependence depends strongly on kinematics, but in a systematic way and therefore can be understood.

In Sec. 3.3, we listed some of the direct extensions of our work. Here we will discuss some of the broader topics relevant to our analysis in Chapter 3. To begin with we looked at the deuteron disintegration reaction. Its time-reversed version $n+p \rightarrow d+\gamma$ is appealing as well due to its relevance to the big bang nucleosynthesis. It would be instructive to see how our analysis carries over to this reaction.

One of the outstanding mysteries of nuclear physics is the *EMC effect*, named after the European Muon Collaboration that discovered it 32 years ago [152]. They observed that the probability of deep inelastic scattering (DIS) off a quark is significantly different from the same probability in a free nucleon. Figure 4.1 shows the

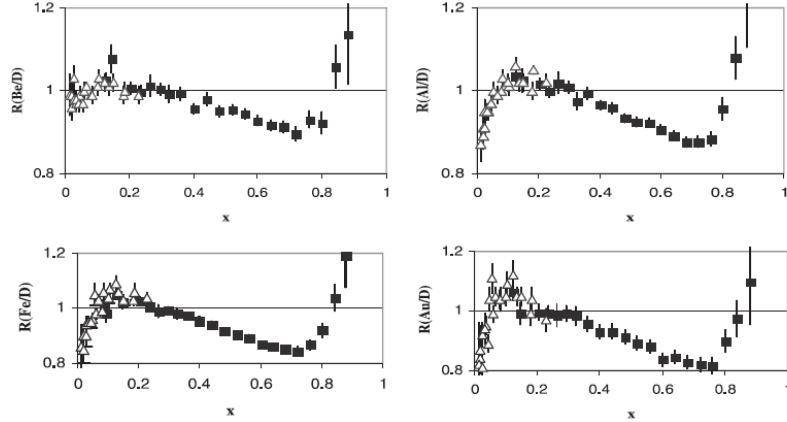


Figure 4.1: The EMC effect in different nuclei [153]. x is the Bjorken- x .

EMC effect for various nuclei. Given that nuclei are weakly bound (maximum of 8.8 MeV per nucleon) compared to the energy transfer in DIS (order of GeV), the

deviation of ratio in Fig. 4.1 by up to 20% from unity was unexpected. A complete understanding of this curious EMC effect still remains elusive.

Experiments at Jefferson Lab indicate that there is a correlation between the two-nucleon short-range correlations and the EMC effect (cf. Fig. 4.2). However, as

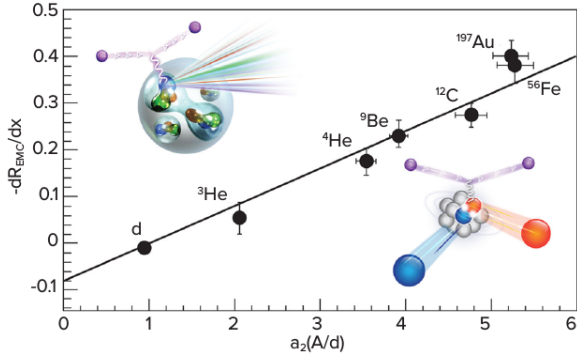


Figure 4.2: The relationship between the number of two-nucleon correlated pairs $a_2(A/d)$, and the strength of the EMC effect. The later is characterized by the slope of EMC effect in $0.3 < x < 0.7$. Figure from [1].

we have already seen (cf. Figs. 1.16 and 3.7), SRG evolved wave functions do not have the SRCs. Instead the SRC physics is accounted for by the evolution of the operator. Our results in Subsec. 3.2.5 suggest that the relationship in Fig. 4.2 might be explained by both the quantities being dominantly given by the leading two-body (contact) operator. Studies analogous to the one presented in Chapter 3 will help elucidate the model dependence of SRCs, and will be valuable for understanding the EMC effect.

An on-going debate in the LENP community is the nature and interpretation of the spectroscopic factors [130]. Spectroscopic factors involve overlap of nuclear wave functions. The short-range parts of the wave functions are scale and scheme

dependent (cf. Fig. 1.16) and therefore so are the spectroscopic factors. Nonetheless, in experimental analysis they are often treated as observables with no scale/scheme dependence. This is often because the dependence is unclear. An exercise similar to our analysis in Chapter 3 will shed a light on the scale/scheme dependence of the spectroscopic factors. This in essence, will bridge the gap between theory and experiments resolving the issues associated with the extraction of nuclear properties from the experiments.

Bibliography

- [1] Long range plan for nuclear science. <http://science.energy.gov/np/nsac/>, September 2015.
- [2] J. J. Aubert et al. Experimental Observation of a Heavy Particle *J. Phys. Rev. Lett.*, 33:1404–1406, 1974.
- [3] D. J. Gross. The discovery of asymptotic freedom and the emergence of QCD. *Proc. Nat. Acad. Sci.*, 102:9099–9108, 2005. [Rev. Mod. Phys.77,837(2005)].
- [4] F. Myhrer and A. W. Thomas. Understanding the proton’s spin structure. *J. Phys.*, G37:023101, 2010.
- [5] Gines Martinez. Advances in Quark Gluon Plasma. 2013.
- [6] Richard H. Cyburt, Brian D. Fields, Keith A. Olive, and Tsung-Han Yeh. Big Bang Nucleosynthesis: 2015. *Rev. Mod. Phys.*, 88:015004, 2016.
- [7] Amanda I. Karakas and John C. Lattanzio. The dawes review 2: Nucleosynthesis and stellar yields of low- and intermediate-mass single stars. *PASA - Publications of the Astronomical Society of Australia*, 31:e030 (62 pages), 2014.
- [8] James M. Lattimer. Introduction to neutron stars. *AIP Conf. Proc.*, 1645:61–78, 2015.
- [9] Jonathan L. Feng. Dark Matter Candidates from Particle Physics and Methods of Detection. *Ann. Rev. Astron. Astrophys.*, 48:495–545, 2010.
- [10] Frank T. Avignone, III, Steven R. Elliott, and Jonathan Engel. Double Beta Decay, Majorana Neutrinos, and Neutrino Mass. *Rev. Mod. Phys.*, 80:481–516, 2008.
- [11] Hideki Yukawa. On the Interaction of Elementary Particles I. *Proc. Phys. Math. Soc. Jap.*, 17:48–57, 1935. [Prog. Theor. Phys. Suppl.1,1(1935)].
- [12] Robert B. Wiringa, V. G. J. Stoks, and R. Schiavilla. An Accurate nucleon-nucleon potential with charge independence breaking. *Phys. Rev.*, C51:38–51, 1995.

- [13] V. G. J. Stoks, R. A. M. Klomp, C. P. F. Terheggen, and J. J. de Swart. Construction of high quality N N potential models. *Phys. Rev.*, C49:2950–2962, 1994.
- [14] R. Machleidt. The Meson theory of nuclear forces and nuclear structure. *Adv. Nucl. Phys.*, 19:189–376, 1989.
- [15] S. Aoki, T. Hatsuda, and N. Ishii. Nuclear Force from Monte Carlo Simulations of Lattice Quantum Chromodynamics. *Comput. Sci. Dis.*, 1:015009, 2008.
- [16] K. A. Olive et al. Review of Particle Physics. *Chin. Phys.*, C38:090001, 2014.
- [17] P. W. Anderson. More Is Different. *Science*, 177(4047):393–396, 1972.
- [18] R. Machleidt, K. Holinde, and C. Elster. The Bonn Meson Exchange Model for the Nucleon Nucleon Interaction. *Phys. Rept.*, 149:1–89, 1987.
- [19] R. Machleidt. The high-precision, charge-dependent Bonn nucleon-nucleon potential (CD-Bonn). *Phys. Rev. C*, 63:024001, 2001.
- [20] *DOE/NSF Nuclear Science Advisory Committee, The Frontiers of Nuclear Science: A Long-Range Plan*, 2007.
- [21] Alan H. Guth, K. Huang, and R. L. Jaffe, editors. *ASYMPTOTIC REALMS OF PHYSICS. ESSAYS IN HONOR OF FRANCIS E. LOW. PROCEEDINGS, SYMPOSIUM, CAMBRIDGE, USA, OCTOBER 16, 1984*.
- [22] Steven Weinberg. Phenomenological Lagrangians. *Physica*, A96:327–340, 1979.
- [23] Michael E Peskin and Daniel V Schroeder. *An Introduction to Quantum Field Theory*. Westview Press, 1995.
- [24] R. Machleidt and D.R. Entem. Chiral effective field theory and nuclear forces. *Phys. Rept.*, 503:1–75, 2011.
- [25] Harald W. Grieshammer. Assessing Theory Uncertainties in EFT Power Countings from Residual Cutoff Dependence. In *8th International Workshop on Chiral Dynamics (CD 2015) Pisa, Italy, June 29-July 3, 2015*, 2015.
- [26] Evgeny Epelbaum. Few-nucleon forces and systems in chiral effective field theory. *Prog. Part. Nucl. Phys.*, 57:654–741, 2006.
- [27] E. D. Jurgenson, P. Navratil, and R. J. Furnstahl. Evolving Nuclear Many-Body Forces with the Similarity Renormalization Group. *Phys. Rev.*, C83:034301, 2011.

- [28] B. A. Brown. The nuclear shell model towards the drip lines. *Prog. Part. Nucl. Phys.*, 47:517–599, 2001.
- [29] Bruce R. Barrett, Petr Navratil, and James P. Vary. Ab initio no core shell model. *Prog. Part. Nucl. Phys.*, 69:131–181, 2013.
- [30] P. Maris, J. P. Vary, and A. M. Shirokov. Ab initio no-core full configuration calculations of light nuclei. *Phys. Rev. C*, 79:014308, 2009.
- [31] Robert Roth. Importance Truncation for Large-Scale Configuration Interaction Approaches. *Phys. Rev. C*, 79:064324, 2009.
- [32] Steven C. Pieper, K. Varga, and Robert B. Wiringa. Quantum Monte Carlo calculations of $A=9, A=10$ nuclei. *Phys. Rev.*, C66:044310, 2002.
- [33] Steven C. Pieper. Quantum Monte Carlo calculations of light nuclei. *Riv. Nuovo Cim.*, 31:709–740, 2008. [,111(2007)].
- [34] S. Gandolfi, F. Pederiva, S. Fantoni, and K. E. Schmidt. Auxiliary Field Diffusion Monte Carlo calculation of nuclei with $A \neq 40$ with tensor interactions. *Phys. Rev. Lett.*, 99:022507, 2007.
- [35] A. Gezerlis, I. Tews, E. Epelbaum, M. Freunek, S. Gandolfi, K. Hebeler, A. Nogga, and A. Schwenk. Local chiral effective field theory interactions and quantum Monte Carlo applications. *Phys. Rev.*, C90(5):054323, 2014.
- [36] G. Hagen, T. Papenbrock, M. Hjorth-Jensen, and D. J. Dean. Coupled-cluster computations of atomic nuclei. *Rept. Prog. Phys.*, 77(9):096302, 2014.
- [37] J. E. Drut, R. J. Furnstahl, and L. Platter. Toward ab initio density functional theory for nuclei. *Prog. Part. Nucl. Phys.*, 64:120–168, 2010.
- [38] Jacek Dobaczewski. Current Developments in Nuclear Density Functional Methods. *J. Phys. Conf. Ser.*, 312:092002, 2011.
- [39] H. Hergert, S. K. Bogner, T. D. Morris, A. Schwenk, and K. Tsukiyama. The In-Medium Similarity Renormalization Group: A Novel Ab Initio Method for Nuclei. *Phys. Rept.*, 621:165–222, 2016.
- [40] Martin J. Savage. Nuclear Physics from Lattice Quantum Chromodynamics. In *12th Conference on the Intersections of Particle and Nuclear Physics (CIPANP 2015) Vail, Colorado, USA, May 19-24, 2015*, 2015.
- [41] William Detmold, W. Melnitchouk, and Anthony William Thomas. Extraction of parton distributions from lattice QCD. *Mod. Phys. Lett.*, A18:2681–2698, 2003.

- [42] William Detmold, W. Melnitchouk, John W. Negele, Dru Bryant Renner, and Anthony William Thomas. Chiral extrapolation of lattice moments of proton quark distributions. *Phys. Rev. Lett.*, 87:172001, 2001.
- [43] S. Durr, Z. Fodor, C. Hoelbling, S. D. Katz, S. Krieg, T. Kurth, L. Lellouch, T. Lippert, K. K. Szabo, and G. Vulvert. Lattice QCD at the physical point: Simulation and analysis details. *JHEP*, 08:148, 2011.
- [44] R. J. Furnstahl and K. Hebeler. New applications of renormalization group methods in nuclear physics. *Rept. Prog. Phys.*, 76:126301, 2013.
- [45] R. J. Furnstahl. The Renormalization Group in Nuclear Physics. *Nucl. Phys. Proc. Suppl.*, 228:139–175, 2012.
- [46] S. K. Bogner, R. J. Furnstahl, and A. Schwenk. From low-momentum interactions to nuclear structure. *Prog. Part. Nucl. Phys.*, 65:94–147, 2010.
- [47] S. K. Bogner, T. T. S. Kuo, and A. Schwenk. Model independent low momentum nucleon interaction from phase shift equivalence. *Phys. Rept.*, 386:1–27, 2003.
- [48] S. K. Bogner, R. J. Furnstahl, and R. J. Perry. Similarity renormalization group for nucleon-nucleon interactions. *Phys. Rev. C*, 75:061001, 2007.
- [49] F. J. Wegner. Flow equations for Hamiltonians. *Nucl. Phys. Proc. Suppl.*, 90:141–146, 2000. [,141(2000)].
- [50] W. Li, E. R. Anderson, and R. J. Furnstahl. The Similarity Renormalization Group with Novel Generators. *Phys. Rev.*, C84:054002, 2011.
- [51] E. Epelbaum, W. Glockle, and Ulf-G. Meissner. The Two-nucleon system at next-to-next-to-next-to-leading order. *Nucl. Phys.*, A747:362–424, 2005.
- [52] Hans-Werner Hammer, Andreas Nogga, and Achim Schwenk. Three-body forces: From cold atoms to nuclei. *Rev. Mod. Phys.*, 85:197, 2013.
- [53] K. Hebeler. Momentum space evolution of chiral three-nucleon forces. *Phys. Rev. C*, 85:021002, 2012.
- [54] Kyle A. Wendt. Similarity Renormalization Group Evolution of Three-Nucleon Forces in a Hyperspherical Momentum Representation. *Phys. Rev. C*, 87:061001, 2013.
- [55] Alberto Garfagnini. Neutrinoless Double Beta Decay Experiments. In *12th Conference on Flavor Physics and CP Violation (FPCP 2014) Marseille, France, May 26-30, 2014*, 2014.

- [56] S. N. More, A. Ekström, R. J. Furnstahl, G. Hagen, and T. Papenbrock. Universal properties of infrared oscillator basis extrapolations. *Phys. Rev.*, C87(4):044326, 2013.
- [57] R. J. Furnstahl, S. N. More, and T. Papenbrock. Systematic expansion for infrared oscillator basis extrapolations. *Phys. Rev.*, C89(4):044301, 2014.
- [58] S. König, S. K. Bogner, R. J. Furnstahl, S. N. More, and T. Papenbrock. Ultraviolet extrapolations in finite oscillator bases. *Phys. Rev.*, C90(6):064007, 2014.
- [59] S. N. More, S. König, R. J. Furnstahl, and K. Hebeler. Deuteron electrodisintegration with unitarily evolved potentials. *Phys. Rev.*, C92(6):064002, 2015.
- [60] R. Furnstahl, G. Hagen, and T. Papenbrock. Corrections to nuclear energies and radii in finite oscillator spaces. *Physical Review C*, 86(3):1–6, sep 2012.
- [61] P. Maris, J. Vary, and A. Shirokov. Ab initio no-core full configuration calculations of light nuclei. *Physical Review C*, 79(1):014308, jan 2009.
- [62] G. Hagen, D. J. Dean, M. Hjorth-Jensen, T. Papenbrock, and A. Schwenk. Benchmark calculations for ^3H , ^4He , ^{16}O and ^{40}Ca with ab- initio coupled-cluster theory. *Phys. Rev. C*, 76:044305, 2007.
- [63] S. K. Bogner, R. J. Furnstahl, P. Maris, R. J. Perry, A. Schwenk, and J. P. Vary. Convergence in the no-core shell model with low-momentum two-nucleon interactions. *Nucl. Phys. A*, 801:21–42, 2008.
- [64] C. Forssén, J.P. Vary, E. Caurier, and P. Navratil. Converging sequences in the ab initio no-core shell model. *Phys. Rev. C*, 77:024301, 2008.
- [65] Sidney A. Coon, Matthew I. Avetian, Michael K.G. Kruse, U. van Kolck, Pieter Maris, et al. Convergence properties of *ab initio* calculations of light nuclei in a harmonic oscillator basis. *Phys. Rev. C*, 86:054002, 2012.
- [66] D. R. Entem and R. Machleidt. Accurate charge-dependent nucleon-nucleon potential at fourth order of chiral perturbation theory. *Phys. Rev. C*, 68:041001, 2003.
- [67] L. S. Gradshteyn and L. M. Ryzhik. *Tables of integrals, series, and products*. Academic Press, San Diego, 6th edition, 2000.
- [68] I. Stetcu, B. R. Barrett, and U. van Kolck. No-core shell model in an effective-field-theory framework. *Phys. Lett. B*, 653:358–362, 2007.

- [69] I. Stetcu, B. R. Barrett, U. van Kolck, and J. P. Vary. Effective Theory for Trapped Few-Fermion Systems. *Phys. Rev. A*, 76:063613, 2007.
- [70] M. Luscher. Volume Dependence of the Energy Spectrum in Massive Quantum Field Theories. 1. Stable Particle States. *Commun. Math. Phys.*, 104:177, 1986.
- [71] David Djajaputra and Bernard R Cooper. Hydrogen atom in a spherical well: linear approximation. *European Journal of Physics*, 21(3):261, 2000.
- [72] J.R. Taylor. *Scattering Theory: The Quantum Theory of Nonrelativistic Collisions*. Dover, 2006.
- [73] R. J. Furnstahl, G. Hagen, and T. Papenbrock. Corrections to nuclear energies and radii in finite oscillator spaces. *Phys. Rev.*, C86:031301, 2012.
- [74] R.G. Newton. *Scattering theory of waves and particles*. Dover, 2002.
- [75] T.-Y. Wu and T. Ohmura. *Quantum Theory of Scattering*. Dover, New York, 2011.
- [76] Daniel R. Phillips, Gautam Rupak, and Martin J. Savage. Improving the convergence of N N effective field theory. *Phys. Lett. B*, 473:209–218, 2000.
- [77] Gustavo Alberto Arteca, Francisco M. Fernández, and Eduardo A. Castro. *J. of Chem. Phys.*, 80:1569, 1984.
- [78] Francisco M. Fernández and Eduardo A. Castro. Hypervirial analysis of enclosed quantum mechanical systems. i. dirichlet boundary conditions. *Int. J. of Quantum Chem.*, 19(4):521–532, 1981.
- [79] Ralph D. Amado. Problems in determining nuclear bound state wave functions. *Phys. Rev. C*, 19:1473–1481, 1979.
- [80] S. Tolle, H. W. Hammer, and B. Ch. Metsch. Convergence Properties of the Effective Theory for Trapped Bosons. *J. Phys.*, G40:055004, 2013.
- [81] Alfredo Deaño, Edmundo J. Huertas, and Francisco Marcellán. Strong and ratio asymptotics for Laguerre polynomials revisited. *J. Math. Anal. Appl.*, 403:477–486, 2013.
- [82] Milton Abramowitz and Irene A. Stegun. *Handbook of Mathematical Functions*. Dover, New York, 1972.
- [83] Sebastian Koenig, Dean Lee, and H.-W. Hammer. Volume Dependence of Bound States with Angular Momentum. *Phys. Rev. Lett.*, 107:112001, 2011.

- [84] Ionel Stetcu, Bruce R. Barrett, Petr Navratil, and James P. Vary. Effective operators within the ab initio no-core shell model. *Phys. Rev. C*, 71:044325, 2005.
- [85] J. M. Bang, A. I. Mazur, A. M. Shirokov, Y. F. Smirnov, and S. A. Zaytsev. P-Matrix and J-Matrix Approaches: Coulomb Asymptotics in the Harmonic Oscillator Representation of Scattering Theory. *Annals of Physics*, 280:299–335, March 2000.
- [86] Thomas Luu, Martin J. Savage, Achim Schwenk, and James P. Vary. Nucleon-Nucleon Scattering in a Harmonic Potential. *Phys. Rev.*, C82:034003, 2010.
- [87] I. Stetcu, J. Rotureau, B. R. Barrett, and U. van Kolck. Effective interactions for light nuclei: An Effective (field theory) approach. *J. Phys.*, G37:064033, 2010.
- [88] Thomas Busch, Berthold-Georg Englert, Kazimierz Rzazewski, and Martin Wilkens. Two cold atoms in a harmonic trap. *Foundations of Physics*, 28:549–559, 1998.
- [89] Anirban Bhattacharyya and T. Papenbrock. Density functional theory for fermions close to the unitary regime. *Phys. Rev.*, A74:041602, 2006.
- [90] Edward Harms. Convenient Expansion for Local Potentials. *Phys. Rev. C*, 1:1667–1679, 1970.
- [91] D.J. Ernst, C.M. Shakin, and R.M. Thaler. Separable Representations of Two-Body Interactions. *Phys. Rev. C*, 8:46–52, 1973.
- [92] Ø. Elgarøy and M. Hjorth-Jensen. Nucleon-nucleon phase shifts and pairing in neutron matter and nuclear matter. *Phys. Rev. C*, 57:1174–1177, Mar 1998.
- [93] C. Lovelace. Practical theory of three particle states. 1. Nonrelativistic. *Phys. Rev.*, 135:B1225–B1249, 1964.
- [94] Sebastian Koenig, Dean Lee, and H.-W. Hammer. Non-relativistic bound states in a finite volume. *Annals Phys.*, 327:1450–1471, 2012.
- [95] Dean Lee and Michelle Pine. How quantum bound states bounce and the structure it reveals. *Eur. Phys. J. A*, 47:41, 2011.
- [96] Michelle Pine and Dean Lee. Effective Field Theory for Bound State Reflection. *Annals Phys.*, 331:24–50, 2013.
- [97] E. D. Jurgenson, P. Navratil, and R. J. Furnstahl. Evolution of Nuclear Many-Body Forces with the Similarity Renormalization Group. *Phys. Rev. Lett.*, 103:082501, 2009.

- [98] R. J. Furnstahl, G. Hagen, T. Papenbrock, and K. A. Wendt. Infrared extrapolations for atomic nuclei. *J. Phys.*, G42(3):034032, 2015.
- [99] K. A. Wendt, C. Forssn, T. Papenbrock, and D. Sf. Infrared length scale and extrapolations for the no-core shell model. *Phys. Rev.*, C91(6):061301, 2015.
- [100] D. Odell, T. Papenbrock, and L. Platter. Infrared extrapolations of quadrupole moments and transitions. 2015.
- [101] Mark Caprio. private communication.
- [102] Claudio Ciofi degli Atti and S. Simula. Realistic model of the nucleon spectral function in few and many nucleon systems. *Phys. Rev.*, C53:1689, 1996.
- [103] J.C. Kimball. Short-Range Correlations and Electron-Gas Response Functions. *Phys. Rev. A*, 7:1648–1652, 1973.
- [104] S. K. Bogner and D. Roscher. High-momentum tails from low-momentum effective theories. *Phys. Rev. C*, 86:064304, 2012.
- [105] Johannes Hofmann, Marcus Barth, and Wilhelm Zwerger. Short-distance properties of Coulomb systems. *Phys. Rev. B*, 87:235125, 2013.
- [106] H. Feldmeier, W. Horiuchi, T. Neff, and Y. Suzuki. Universality of short-range nucleon-nucleon correlations. *Phys. Rev. C*, 84:054003, 2011.
- [107] E. D. Jurgenson, P. Maris, R. J. Furnstahl, P. Navratil, W. E. Ormand, and J. P. Vary. Structure of p -shell nuclei using three-nucleon interactions evolved with the similarity renormalization group. *Phys. Rev.*, C87(5):054312, 2013.
- [108] S. Binder, A. Ekström, G. Hagen, T. Papenbrock, and K. A. Wendt. Effective field theory in the harmonic oscillator basis. 2015.
- [109] Sascha Hoinka, Marcus Lingham, Kristian Fenech, Hui Hu, Chris J. Vale, Joaquin E. Drut, and Stefano Gandolfi. Precise determination of the structure factor and contact in a unitary Fermi gas. *Phys. Rev. Lett.*, 110(5):055305, 2013.
- [110] R. J. Furnstahl. High-resolution probes of low-resolution nuclei. In *Proceedings, International Conference on Nuclear Theory in the Supercomputing Era (NTSE-2013)*, page 371, 2013.
- [111] Guido Altarelli and G. Parisi. Asymptotic Freedom in Parton Language. *Nucl. Phys.*, B126:298, 1977.

- [112] Leonid Frankfurt, Misak Sargsian, and Mark Strikman. Recent observation of short range nucleon correlations in nuclei and their implications for the structure of nuclei and neutron stars. *Int. J. Mod. Phys. A*, 23:2991–3055, 2008.
- [113] J. Arrington, D.W. Higinbotham, G. Rosner, and M. Sargsian. Hard probes of short-range nucleon-nucleon correlations. *Prog. Part. Nucl. Phys.*, 67:898–938, 2012.
- [114] A. Rios, A. Polls, and W. H. Dickhoff. Density and isospin asymmetry dependence of high-momentum components. *Phys. Rev.*, C89(4):044303, 2014.
- [115] Werner Boeglin and Misak Sargsian. Modern Studies of the Deuteron: from the Lab Frame to the Light Front. *Int. J. Mod. Phys.*, E24(03):1530003, 2015.
- [116] William P. Ford, Sabine Jeschonnek, and J. W. Van Orden. Momentum distributions for $^2\text{H}(e, e'p)$. *Phys. Rev.*, C90(6):064006, 2014.
- [117] Francesca Sammarruca. Short-range correlations in the deuteron: chiral effective field theory, meson-exchange, and phenomenology. *Phys. Rev.*, C92(4):044003, 2015.
- [118] Evgeny Epelbaum, Hans-Werner Hammer, and Ulf-G. Meißner. Modern Theory of Nuclear Forces. *Rev. Mod. Phys.*, 81:1773–1825, 2009.
- [119] J. Carlson, S. Gandolfi, F. Pederiva, Steven C. Pieper, R. Schiavilla, K. E. Schmidt, and R. B. Wiringa. Quantum Monte Carlo methods for nuclear physics. 2014.
- [120] L. E. Marcucci, F. Gross, M. T. Pena, M. Piarulli, R. Schiavilla, I. Sick, A. Stadler, J. W. Van Orden, and M. Viviani. Electromagnetic Structure of Few-Nucleon Ground States. *J. Phys.*, G43:023002, 2016.
- [121] S. Quaglioni, G. Hupin, A. Calci, P. Navratil, and R. Roth. Ab initio calculations of reactions with light nuclei. *EPJ Web Conf.*, 113:01005, 2016.
- [122] Sonia Bacca, Nir Barnea, Gaute Hagen, Giuseppina Orlandini, and Thomas Papenbrock. First Principles Description of the Giant Dipole Resonance in ^{16}O . *Phys. Rev. Lett.*, 111(12):122502, 2013.
- [123] Michelle Pine, Dean Lee, and Gautam Rupak. Adiabatic projection method for scattering and reactions on the lattice. *Eur. Phys. J.*, A49:151, 2013.
- [124] E. R. Anderson, S. K. Bogner, R. J. Furnstahl, and R. J. Perry. Operator Evolution via the Similarity Renormalization Group I: The Deuteron. *Phys. Rev.*, C82:054001, 2010.

- [125] Micah D Schuster, Sofia Quaglioni, Calvin W. Johnson, Eric D. Jurgenson, and Petr Navratil. Operator evolution for ab initio nuclear theory. *Phys. Rev.*, C90(1):011301, 2014.
- [126] Micah D. Schuster, Sofia Quaglioni, Calvin W. Johnson, Eric D. Jurgenson, and Petr Navratil. Operator evolution for ab initio electric dipole transitions of ^4He . *Phys. Rev.*, C92(1):014320, 2015.
- [127] Thomas Neff, Hans Feldmeier, and Wataru Horiuchi. Short-range correlations in nuclei with similarity renormalization group transformations. *Phys. Rev.*, C92(2):024003, 2015.
- [128] Sigfrido Boffi, Carlotta Giusti, Franco Davide Pacati, and Marco Radici. *Electromagnetic Response of Atomic Nuclei*. Clarendon Press, Oxford, 1996.
- [129] White paper on nuclear astrophysics and low-energy nuclear physics. www.lecmeeting.org, January 2015.
- [130] R. J. Furnstahl and A. Schwenk. How should one formulate, extract, and interpret ‘non-observables’ for nuclei? *J. Phys. G*, 37:064005, 2010.
- [131] Claudio Ciofi degli Atti. In-medium short-range dynamics of nucleons: Recent theoretical and experimental advances. *Phys. Rept.*, 590:1–85, 2015.
- [132] Hartmuth Arenhövel, Winfried Leidemann, and Edward L. Tomusiak. General survey of polarization observables in deuteron electrodisintegration. *Eur. Phys. J.*, A23:147–190, 2005.
- [133] S. Gilad, W. Bertozzi, and Z. L. Zhou. New observables in $^2\text{H}(\text{e}, \text{ep})\text{n}$. *Nucl. Phys.*, A631:276–295, 1998.
- [134] K. S. Egiyan et al. Experimental study of exclusive $\text{H}-2(\text{e}, \text{e-prime p})\text{n}$ reaction mechanisms at high Q^{**2} . *Phys. Rev. Lett.*, 98:262502, 2007.
- [135] C.-J. Yang and Daniel R. Phillips. The longitudinal response function of the deuteron in chiral effective field theory. *Eur. Phys. J. A*, 49:122, 2013.
- [136] H. Arenhövel, W. Leidemann, and E. L. Tomusiak. The Role of the Neutron Electric Form-factor in $D(e, e'N) N$ Including Polarization Observables. *Z. Phys.*, A331:123–138, 1988.
- [137] Willem-Jan Kasdorp. *Deuteron electrodisintegration at large momentum values*. PhD thesis, Utrecht U., 1997.
- [138] Hartmuth Arenhövel, Winfried Leidemann, and Edward L. Tomusiak. Exclusive deuteron electrodisintegration with polarized electrons and a polarized target. *Phys. Rev.*, C46:455–470, 1992.

- [139] Hassan F. Ibrahim. *The $^2H(e, e' p)n$ reaction at high four-momentum transfer.* PhD thesis, Old Dominion U., 2006-12-01.
- [140] Rubin H. Landau. *Quantum Mechanics II.* John Wiley & Sons, New York, 1989.
- [141] C.-J. Yang. *Subtractive Renormalization of the NN interaction in Chiral Effective Theory and the Deuteron Electro-disintegration Calculation.* Ph.d thesis, Ohio University, 2010.
- [142] R. J. Furnstahl and H.-W. Hammer. Are occupation numbers observable? *Phys. Lett. B*, 531:203–208, 2002.
- [143] J. H. Hetherington and L. H. Schick. Exact Multiple-Scattering Analysis of Low-Energy Elastic K-d Scattering with Separable Potentials. *Phys. Rev.*, 137:B935–B948, 1965.
- [144] E. W. Schmid and H. Ziegelmann. *The Quantum Mechanical Three-Body Problem.* Vieweg, Braunschweig, 1974.
- [145] Sergey Bochkhanov. ALGLIB. www.alglib.net.
- [146] Intel. Threading Building Blocks (TBB). www.threadingbuildingblocks.org, September 2015.
- [147] J. Carlson and R. Schiavilla. Structure and dynamics of few nucleon systems. *Rev. Mod. Phys.*, 70:743–842, 1998.
- [148] Sonia Bacca and Saori Pastore. Electromagnetic reactions on light nuclei. *J. Phys.*, G41(12):123002, 2014.
- [149] S. K. Bogner, R. J. Furnstahl, R. J. Perry, and A. Schwenk. Are low-energy nuclear observables sensitive to high-energy phase shifts? *Phys. Lett.*, B649:488–493, 2007.
- [150] Stefan Christlmeier and Harald W. Griesshammer. Pion-less Effective Field Theory on Low-Energy Deuteron Electro-Disintegration. *Phys. Rev.*, C77:064001, 2008.
- [151] A. Lovato, S. Gandolfi, J. Carlson, Steven C. Pieper, and R. Schiavilla. Electromagnetic and neutral-weak response functions of ^4He and ^{12}C . *Phys. Rev.*, C91(6):062501, 2015.
- [152] J. J. Aubert et al. The ratio of the nucleon structure functions F_2^N for iron and deuterium. *Phys. Lett.*, B123:275–278, 1983.

- [153] P. R. Norton. The EMC effect. *Rept. Prog. Phys.*, 66:1253–1297, 2003.
- [154] H. P. Stapp, T. J. Ypsilantis, and N. Metropolis. Phase shift analysis of 310-MeV proton proton scattering experiments. *Phys. Rev.*, 105:302–310, 1957.
- [155] Sebastian König. *Effective quantum theories with short- and long-range forces*. PhD thesis, Bonn University, 2013.

Appendix A: t -matrix details

A.1 Solving the Lippmann-Schwinger equation

The Lippmann-Schwinger equation (LSE), which is essentially the Schrödinger equation for scattering states is given in operator form by

$$t = V + V G t , \quad (\text{A.1})$$

where t is the t -matrix, V is the potential, and G is the Green's function. In momentum space, Eq. A.1 becomes

$$t_{ll}(E_0=p_0^2/M; p', p) = V_{ll} + \sum_{l''} \frac{2}{\pi} M \int \frac{dp'' p''^2 V_{ll''}(p', p'') t_{l''l}(E_0; p'', p)}{p_0^2 - p'^2 + i\epsilon} . \quad (\text{A.2})$$

Derivation of Eq. A.2 makes use of the completeness relation in Eq. 3.19 and the definition of Green's function in Eq. 3.21. The indices which are the same on both sides of Eq. A.2 and are not summed over are suppressed. For deuteron disintegration calculations, we need only the half on-shell t -matrix. But here we will look at the more general case of evaluating the fully off-shell t -matrix.

For the sake of pedagogy, let us consider that we are evaluating the t -matrix for uncoupled channels. Suppressing the angular momentum indices and putting in the limits of integration, the Eq. A.2 becomes

$$t(E_0; p', p) = V(p', p) + \frac{2}{\pi} M \int_0^\Lambda \frac{dp'' p''^2 V(p', p'') t(E_0; p'', p)}{p_0^2 - p''^2 + i\epsilon} . \quad (\text{A.3})$$

Next we outline the steps involved in solving Eq. A.3 numerically. We follow the approach of Ref. [140].

The integrals are efficiently evaluated numerically using a Gauss-Legendre quadrature. However, the integrand in Eq. A.3 has a pole at $p'' = p_0$, and that needs to be accounted for properly. Let's consider the expression

$$\int_0^\Lambda dp \frac{p^2 f(p)}{p_0^2 - p^2 + i\epsilon} = \int_0^\Lambda dp \frac{p^2 f(p)}{(p_0 + p)(p_0 - p + i\epsilon)} \quad (\text{A.4})$$

$$\equiv \int_0^\Lambda dp \frac{\tilde{f}(p)}{(p_0 - p + i\epsilon)} , \quad (\text{A.5})$$

where we have defined $\tilde{f}(p)$ as

$$\tilde{f}(p) = \frac{p^2 f(p)}{p_0 + p} . \quad (\text{A.6})$$

In principle, we can work without separating the singular and non-singular factors of $p_0^2 - p^2 + i\epsilon$. However, we find better numerical convergence when the pole term is factorized as in Eq. A.4.

Using Sokhotsky's formula

$$\frac{1}{x \pm i\epsilon} = \mathcal{P} \left(\frac{1}{x} \right) \mp i\pi \delta(x) , \quad (\text{A.7})$$

we have

$$\int_0^\Lambda dp \frac{\tilde{f}(p)}{(p_0 - p + i\epsilon)} = \mathcal{P} \int_0^\Lambda dp \frac{\tilde{f}(p)}{p_0 - p} - i\pi \tilde{f}(p_0) . \quad (\text{A.8})$$

Let's first evaluate the principal value integration in the Eq. A.8.

$$\begin{aligned} \mathcal{P} \int_0^\Lambda dp \frac{\tilde{f}(p)}{p_0 - p} &= \mathcal{P} \int_0^\Lambda dp \frac{\tilde{f}(p) - \tilde{f}(p_0) + \tilde{f}(p_0)}{p_0 - p} \\ &= \int_0^\Lambda dp \frac{\tilde{f}(p) - \tilde{f}(p_0)}{p_0 - p} + \tilde{f}(p_0) \mathcal{P} \int_0^\Lambda dp \frac{1}{p_0 - p} . \end{aligned} \quad (\text{A.9})$$

The integrand of the first term on the right side of Eq. A.9 is zero at the pole $p = p_0$ and therefore non-singular. We can therefore drop the principal value for that term

and evaluate it as a normal integral. The second term on the right side of Eq. A.9 can be evaluated analytically.

$$\begin{aligned}
\mathcal{P} \int_0^\Lambda dp \frac{1}{p_0 - p} &= \int_0^{p_0 - \epsilon} dp \frac{1}{p_0 - p} + \int_{p_0 + \epsilon}^\Lambda dp \frac{1}{p_0 - p} \\
&= -\ln(p_0 - p) \Big|_0^{p_0 - \epsilon} + -\ln(p_0 - p) \Big|_{p_0 + \epsilon}^\Lambda \\
&= -\ln \left(\frac{\Lambda - p_0}{p_0} \right). \tag{A.10}
\end{aligned}$$

From Eqs. A.10, A.9, and A.8, we have

$$\int_0^\Lambda dp \frac{\tilde{f}(p)}{p_0 - p + i\epsilon} = \int_0^\Lambda dp \frac{\tilde{f}(p) - \tilde{f}(p_0)}{p_0 - p} - \tilde{f}(p_0) \ln \left(\frac{\Lambda - p_0}{p_0} \right) - i\pi \tilde{f}(p_0). \tag{A.11}$$

Discretizing this on the Gauss-Legendre mesh we have

$$\int_0^\Lambda dp \frac{\tilde{f}(p)}{p_0 - p + i\epsilon} = \sum_{j=1}^N \frac{\tilde{f}(p_j)}{p_0 - p_j} w_j - \tilde{f}(p_0) \left[i\pi + \ln \left(\frac{\Lambda - p_0}{p_0} \right) + \sum_{j=1}^N \frac{w_j}{p_0 - p_j} \right]. \tag{A.12}$$

p_j 's are the momentum mesh points, N is the number of mesh points, and w_j 's are the associated weights.

Comparing Eqs. A.3 and Eq. A.5, the corresponding \tilde{f} function for the LSE is

$$\tilde{f}(p'') = \frac{2}{\pi} M \frac{p''^2 V(p', p'') t(E_0; p'', p)}{(p_0 + p'')} . \tag{A.13}$$

Using the result of Eq. A.12, the LSE from Eq. A.3 on the Gauss-Legendre mesh becomes

$$\begin{aligned}
t(E_0; p', p) &= V(p', p) + \frac{2}{\pi} M \sum_{j=1}^N \frac{k_j^2 V(p', k_j) t(E_0; k_j, p)}{p_0^2 - k_j^2} w_j \\
&\quad - \frac{2}{\pi} M \frac{p_0^2 V(p', p_0) t(E_0; p_0, p)}{2p_0} \left[i\pi + \ln \left(\frac{\Lambda - p_0}{p_0} \right) + \sum_{j=1}^N \frac{w_j}{p_0 - k_j} \right]. \tag{A.14}
\end{aligned}$$

Note that k_j are Gauss-Legendre momentum mesh points and w_j are the corresponding weights.

Let's define an array D such that

$$D_j = \begin{cases} \frac{2}{\pi} M \frac{k_j^2 w_j}{p_0^2 - k_j^2} & \text{for } j = 1, \dots, N \\ -\frac{2}{\pi} M \frac{p_0^2}{2p_0} \left(i\pi + \ln\left(\frac{\Lambda - p_0}{p_0}\right) + \sum_{j=1}^N \frac{w_j}{p_0 - k_j} \right) & \text{for } j = N+1. \end{cases} \quad (\text{A.15})$$

Using this definition of D and with the identification that $k_{j=N+1} = p_0$, Eq. A.14 can be written as

$$t(E_0; p', p) - \sum_{j=1}^{N+1} V(p', k_j) D_j t(E_0; k_j, p) = V(p', p). \quad (\text{A.16})$$

To solve Eq. A.16 in matrix form, we let $p' \rightarrow \{p_i\}$, where $i = 1, \dots, N$ are the Gauss-Legendre mesh points and $i = N+1$ is the on-shell point $p = p_0$ ¹⁵. Eq. A.16 can then be written as a matrix multiplication equation.

$$t(E_0; p'_i, p) - \sum_{j=1}^{N+1} V(p'_i, k_j) D_j t(E_0; k_j, p) = V(p'_i, p) \quad (\text{A.17})$$

$$\sum_{j=1}^{N+1} \underbrace{(\delta_{ij} - V(p_i, k_j) D_j)}_{\equiv F_{ij}} t(E_0, k_j, p) = V(p_i, p) \quad (\text{A.18})$$

$$[F]_{(N+1) \times (N+1)} [t]_{N+1} = [V]_{N+1} \quad (\text{A.19})$$

Note that $[V]$ in Eq. A.19 is an array whose $N+1^{\text{th}}$ element is $V(p_0, p)$ and the first N elements are $V(p_i, p)$, where as mentioned before p_i 's are the Gauss-Legendre mesh points. The same indexing holds for $[t]$.

$[F]$ and $[V]$ in Eq. A.19 are known. Eq. A.19 can be solved using standard matrix equation solving subroutines to get the t -matrix array $[t]$. Recall that $[t] = (t(E_0; p_{j=1, \dots, N}, p), t(E_0; p_0, p))$. Thus, for a given p and E_0 , we have the t -matrix $t(E_0; p_j, p)$ for any point p_j on the Gauss-Legendre mesh, and also have

¹⁵ k_i 's and p_i 's are actually the same set of momentum points. To avoid confusion, we keep the notation separate.

it at the half on-shell point $t(E_0; p_0, p)$. In principle, we can use any standard interpolation routine to get the t -matrix at a point not on the Gauss-Legendre mesh. However, it turns out that we can use the LSE itself for interpolation. Consider a point \tilde{p} not on the momentum mesh. From Eq. A.16, we have

$$t(E_0; \tilde{p}, p) = V(\tilde{p}, p) + \sum_{j=1}^{N+1} V(\tilde{p}, k_j) D_j t(E_0, k_j, p). \quad (\text{A.20})$$

As mentioned before $\{k_j\} = \{p_j\}$, and therefore all the terms on the right side of Eq. A.20 are known allowing us to evaluate $t(E_0; \tilde{p}, p)$. To interpolate the potential, which is stored on a momentum-space grid, we use the two-dimensional cubic spline algorithm from ALGLIB [145].

Coupled channels

The neutron-proton system has both spin $S = 0$ and $S = 1$ channels. The uncoupled channels have $S = 0$, whereas coupled channels have $S = 1$. The angular momentum numbers of the coupled channel pairs differ by 2. For example, some of the coupled channel pairs are $^3S_1 - ^3D_1$, $^3P_2 - ^3F_2$, $^3D_3 - ^3G_3$, so on.

For coupled channels Eq. A.1 becomes

$$\begin{pmatrix} t_{00} & t_{02} \\ t_{20} & t_{22} \end{pmatrix} = \begin{pmatrix} V_{00} & V_{02} \\ V_{20} & V_{22} \end{pmatrix} + \begin{pmatrix} V_{00} & V_{02} \\ V_{20} & V_{22} \end{pmatrix} \begin{pmatrix} G_0 & 0 \\ 0 & G_0 \end{pmatrix} \begin{pmatrix} t_{00} & t_{02} \\ t_{20} & t_{22} \end{pmatrix} \quad (\text{A.21})$$

where the subscripts 00, 02 etc. indicate the coupled channels. Following steps similar to the uncoupled case, the analog of Eq. A.17 is

$$\begin{pmatrix} t_{00}(p'_i, p) & t_{02}(p'_i, p) \\ t_{20}(p'_i, p) & t_{22}(p'_i, p) \end{pmatrix} - \sum_{j=1}^{N+1} \begin{pmatrix} V_{00}(p'_i, k_j) & V_{02}(p'_i, k_j) \\ V_{20}(p'_i, k_j) & V_{22}(p'_i, k_j) \end{pmatrix} \begin{pmatrix} \mathcal{D}(k_j) & 0 \\ 0 & \mathcal{D}(k_j) \end{pmatrix} \begin{pmatrix} t_{00}(k_j, p) & t_{02}(k_j, p) \\ t_{20}(k_j, p) & t_{22}(k_j, p) \end{pmatrix} = \begin{pmatrix} V_{00}(p'_i, p) & V_{02}(p'_i, p) \\ V_{20}(p'_i, p) & V_{22}(p'_i, p) \end{pmatrix}. \quad (\text{A.22})$$

\mathcal{D} is a $(N + 1) \times (N + 1)$ diagonal matrix element with the diagonal matrix elements given by D from Eq. A.15. Each of $V_{0,20,2}(p'_i, k_j)$ are a $(N + 1) \times (N + 1)$ matrix, whereas $t_{0,20,2}(p'_i, p)$ and $V_{0,20,2}(p'_i, p)$ have dimensions of $(N + 1) \times 1$.

Analogous to Eqs. A.18 and A.19, we now have

$$\sum_{j=1}^{N+1} \left[\delta_{ij} \begin{pmatrix} \mathbb{1}_{(N+1) \times (N+1)} & 0 \\ 0 & \mathbb{1}_{(N+1) \times (N+1)} \end{pmatrix} - \begin{pmatrix} V_{00}(p'_i, k_j) D_j & V_{02}(p'_i, k_j) D_j \\ V_{20}(p'_i, k_j) D_j & V_{22}(p'_i, k_j) D_j \end{pmatrix} \right] \\ \begin{pmatrix} t_{00}(k_j, p) & t_{02}(k_j, p) \\ t_{20}(k_j, p) & t_{22}(k_j, p) \end{pmatrix} = \begin{pmatrix} V_{00}(p'_i, p) & V_{02}(p'_i, p) \\ V_{20}(p'_i, p) & V_{22}(p'_i, p) \end{pmatrix}, \quad (\text{A.23})$$

and

$$[F]_{(2N+2) \times (2N+2)} [t]_{(2N+2) \times 2} = [V]_{(2N+2) \times 2}. \quad (\text{A.24})$$

Solving Eq. A.24 for a given E_0 and p yields $t_{0,20,2}(E_0; k_j, p)$ for points k_j on the mesh. Analogous to Eq. A.20, we can again use the LSE to interpolate the t -matrix in coupled channel. Below, we note interpolation for one of the components for the point $p = \tilde{p}$ not on the mesh.

$$t_{02}(E_0; \tilde{p}, p) = V_{02}(\tilde{p}, p) + \sum_{j=1}^{N+1} V_{00}(\tilde{p}, k_j) D_j t_{02}(E_0, k_j, p) + \sum_{j=1}^{N+1} V_{02}(\tilde{p}, k_j) D_j t_{22}(E_0, k_j, p) \quad (\text{A.25})$$

Note that all the quantities on the right side of Eq. A.25 are known allowing us to evaluate $t_{02}(E_0; \tilde{p}, p)$. Similarly, we can write down equations for interpolation of other components of the t -matrix.

A.2 t -matrix checks

We checked the accuracy of our t -matrix by calculating the phase shifts and verifying them against standard values (such as from NN-online). For uncoupled channels, the on-shell part of the t -matrix is related to the phase shift as follows ¹⁶

¹⁶Be aware that the factors of M (nucleon mass) and \hbar might differ based on the conventions and units used.

$$t_l(E_k; k, k) = \frac{e^{i\delta_l} \sin \delta_l}{-M k}. \quad (\text{A.26})$$

Thus, argument of the t -matrix gives the phase shift.

$$\delta_l(k) = \arg(t_l(E_k; k, k)) \quad (\text{A.27})$$

The coupled channel calculation involves an additional parameter called mixing angle denoted by $\bar{\epsilon}$. In the “Stapp” or the “bar” phase shift parametrization [154], the S -matrix is written as

$$S = \begin{pmatrix} \cos 2\bar{\epsilon} e^{2i\bar{\delta}_1} & i \sin 2\bar{\epsilon} e^{i(\bar{\delta}_1 + \bar{\delta}_2)} \\ i \sin 2\bar{\epsilon} e^{i(\bar{\delta}_1 + \bar{\delta}_2)} & \cos 2\bar{\epsilon} e^{2i\bar{\delta}_2} \end{pmatrix}. \quad (\text{A.28})$$

We calculate S in terms t -matrix using (see for instance Eq. (8.70) in [140])

$$S = \begin{pmatrix} 1 - 2ik t_{00}(E_k; k, k) & -2ik t_{02}(E_k; k, k) \\ -2ik t_{20}(E_k; k, k) & 1 - 2ik t_{22}(E_k; k, k) \end{pmatrix}. \quad (\text{A.29})$$

From Eq. A.28, we can work out that the phase shifts and the mixing angles are given as follows.

$$\bar{\delta}_1 = \frac{1}{2} \tan^{-1} \left(\frac{\text{Im}[S[1, 1]]}{\text{Re}[S[1, 1]]} \right) \quad (\text{A.30})$$

$$\bar{\delta}_2 = \frac{1}{2} \tan^{-1} \left(\frac{\text{Im}[S[2, 2]]}{\text{Re}[S[2, 2]]} \right) \quad (\text{A.31})$$

$$\bar{\epsilon} = \frac{1}{2} \sin^{-1} \left(\frac{\text{Im}[S[1, 2]]}{\text{Re}[\sqrt{\det(S)}]} \right) \quad (\text{A.32})$$

The phase shifts and the mixing angles calculated using these formulas match the results on NN-online. This indicates that t -matrix we have is correct.

Checking the imaginary part of the t -matrix

The formulas for phase shifts check the ratio of real and imaginary parts of t -matrix. This is particularly evident in Eq. A.27. But it is also possible to check the

imaginary part of the t -matrix. From Eq. A.26, we have (suppressing the arguments of the t -matrix)

$$t = \frac{\sin \delta}{-M k (\cos \delta - i \sin \delta)} . \quad (\text{A.33})$$

$$\Rightarrow \frac{1}{-M t} = k \cot \delta - i k . \quad (\text{A.34})$$

$$\Rightarrow \text{Im}[1/t] \propto k . \quad (\text{A.35})$$

Thus, the imaginary part of $1/t_l(E_k; k, k)$ when plotted as a function of k should be a straight line. Our t -matrix satisfies this condition. The slope of the line in this case is M , but in general depends on the units chosen.

Symmetric property of t -matrix

The phase shifts, mixing angles, and the behavior of the imaginary part of t -matrix described in Eq. A.35, all check the on-shell part of the t -matrix. To get some confidence about the off-shell part of t -matrix, we can check if it has the right symmetries. The t -matrix is symmetric under the angular momentum and momentum interchange, i.e.,

$$t(E_0; k, k', L, L', J, S, T) = t(E_0; k', k, L', L, J, S, T) . \quad (\text{A.36})$$

Note that the t -matrix is not Hermitian as one would naively expect.

A.3 Using the LSE for the wave function interpolation

Solving Schrödinger's equation we obtain the deuteron wave function on the momentum mesh on which our potential is stored. We can use the LSE to obtain the wave function at any intermediate momentum point. We use the property that near

the bound state pole, the t -matrix factorizes as (see Appendix of Ref. [155] and references therein)

$$\lim_{E \rightarrow -E_B} (E + E_B) t(E; k, k') = \mathcal{B}^*(k) \mathcal{B}(k') , \quad (\text{A.37})$$

where E_B is the bound state energy, and the factor \mathcal{B} is the wave function apart from a factor of propagator

$$\mathcal{B}(q) = \frac{-\pi(k_B^2 + q^2)}{2M} \psi(q) , \quad (\text{A.38})$$

where k_B is the bound state momentum.

Multiplying the LSE equation for the t_{22} channel by $(E + E_B)$ and taking the limit $E \rightarrow -E_B$, we have

$$\begin{aligned} \lim_{E \rightarrow -E_B} (E + E_B) t_{22}(E; k, k') &= \lim_{E \rightarrow -E_B} (E + E_B) V_{22}(k, k') \\ &+ \frac{2}{\pi} M \lim_{E \rightarrow -E_B} \int dp p^2 V_{20}(k, p) \frac{t_{02}(E; p, k')}{k_E^2 - p^2 + i\epsilon} (E + E_B) \\ &+ \frac{2}{\pi} M \lim_{E \rightarrow -E_B} \int dp p^2 V_{22}(k, p) \frac{t_{22}(E; p, k')}{k_E^2 - p^2 + i\epsilon} (E + E_B) . \end{aligned} \quad (\text{A.39})$$

The first term on the right side of Eq. A.39 vanishes as the potential does not have a singular part. Using Eq. A.37, we get

$$\mathcal{B}_2^*(k) = \frac{2}{\pi} M \int dp p^2 \frac{V_{20}(k, p) \mathcal{B}_0^*(p)}{-k_B^2 - p^2} + \frac{2}{\pi} M \int dp p^2 \frac{V_{22}(k, p) \mathcal{B}_2^*(p)}{-k_B^2 - p^2} . \quad (\text{A.40})$$

In deriving Eq. A.40, we have dropped the factor of $\mathcal{B}_2(k')$ which is common on both sides. Substituting Eq. A.38 gives

$$\frac{-\pi}{2M} (k_B^2 + k^2) \psi_2^*(k) = \int dp p^2 V_{20}(k, p) \psi_0^*(p) + \int dp p^2 V_{22}(k, p) \psi_2^*(p) . \quad (\text{A.41})$$

The wave function in our case is real and therefore the complex conjugation can be dropped. Writing the integral in terms of sum, we have

$$\psi_2(k) = \frac{-2M}{\pi(k_B^2 + k^2)} \left[\sum_{j=1}^N w_j p_j^2 V_{20}(k, p_j) \psi_0(p_j) + \sum_{j=1}^N w_j p_j^2 V_{22}(k, p_j) \psi_2(p_j) \right] . \quad (\text{A.42})$$

The wave functions on the mesh— $\psi_0(p_j)$ and $\psi_2(p_j)$ —are already known from solving the Schrödinger equation and therefore Eq. A.42 allows us to obtain $\psi_2(k)$ for any desired momentum k . We also checked that if we choose k in Eq. A.42 to be one of the on mesh points, then we get back the expected answer.

Similarly for the S -state wave function, we have

$$\psi_0(k) = \frac{-2M}{\pi(k_B^2 + k^2)} \left[\sum_{j=1}^N w_j p_j^2 V_{00}(k, p_j) \psi_0(p_j) + \sum_{j=1}^N w_j p_j^2 V_{02}(k, p_j) \psi_2(p_j) \right]. \quad (\text{A.43})$$

A word of caution—the M in Eqs. A.42 and A.43 depends on conventions. In some cases, the mass factor is absorbed in the potential. Same goes for the factor of \hbar 's. Therefore, it is important to check that the units are consistent.

The interpolation techniques for the wave functions and for the t -matrix (Eqs. A.20 and A.25) keep the numerical errors minimal. In our case, the only source of error is from interpolation of the potential.

Appendix B: Evolution details for deuteron disintegration

B.1 Expressions for the evolved matrix elements

Here we document the expressions used in Subsec. 3.2.2. As seen in Eq. 3.29, in order to evaluate the term $\langle \phi | J_0^\lambda | \psi_i^\lambda \rangle$ we split it into four terms: B_1 , B_2 , B_3 , and B_4 . B_4 is obtained from Eq. 3.9 by using the evolved deuteron wave function instead of the unevolved one. The expressions for the terms B_3 , B_2 , and B_1 are as follows:

$$\begin{aligned}
B_3 \equiv \langle \phi | J_0 \tilde{U}^\dagger | \psi_i^\lambda \rangle &= 2 \sqrt{\frac{2}{\pi}} \sum_{T_1=0,1} (G_E^p + (-1)^{T_1} G_E^n) \sum_{L_1=0}^{L_{\max}} (1 + (-1)^{T_1} (-1)^{L_1}) \\
&\times Y_{L_1, m_{J_d} - m_{s_f}}(\theta', \varphi') \sum_{J_1=|L_1-1|}^{L_1+1} \langle L_1 m_{J_d} - m_{s_f} S=1 m_{s_f} | J_1 m_{J_d} \rangle \\
&\times \sum_{\tilde{m}_s=-1}^1 \langle J_1 m_{J_d} | L_1 m_{J_d} - \tilde{m}_s S=1 \tilde{m}_s \rangle \sum_{L_2=0}^{L_{\max}} \langle L_2 m_{J_d} - \tilde{m}_s S=1 \tilde{m}_s | J=1 m_{J_d} \rangle \\
&\times \sum_{L_d=0,2} \int dk_3 \psi_{L_d}^\lambda(k_3) k_3^2 \int d\cos \theta P_{L_1}^{m_{J_d} - \tilde{m}_s}(\cos \theta) P_{L_2}^{m_{J_d} - \tilde{m}_s}(\cos \alpha'(p', \theta, q)) \\
&\times \tilde{U}\left(k_3, \sqrt{p'^2 - p'q \cos \theta + q^2/4}, L_d, L_2, J=1, S=1, T=0\right), \quad (\text{B.1})
\end{aligned}$$

$$\begin{aligned}
B_2 \equiv \langle \phi | \tilde{U} J_0 | \psi_i^\lambda \rangle &= 2 \sqrt{\frac{2}{\pi}} \sum_{T_1=0,1} (G_E^p + (-1)^{T_1} G_E^n) \sum_{L_1=0}^{L_{\max}} (1 + (-1)^{T_1} (-1)^{L_1}) \\
&\times Y_{L_1, m_{J_d} - m_{s_f}}(\theta', \varphi') \sum_{J_1=|L_1-1|}^{L+1} \langle L_1 m_{J_d} - m_{s_f} S=1 m_{s_f} | J_1 m_{J_d} \rangle \\
&\times \sum_{L_2, \tilde{m}_s} \langle J_1 m_{J_d} | L_1 m_{J_d} - \tilde{m}_s S=1 \tilde{m}_s \rangle \sum_{L_d=0,2} \langle L_d m_{J_d} - \tilde{m}_s S=1 \tilde{m}_s | J=1 m_{J_d} \rangle \\
&\times \int dk_2 k_2^2 \tilde{U}(p', k_2, L_1, L_2, J_1, S=1, T_1) \int d\cos \theta P_{L_2}^{m_{J_d} - \tilde{m}_s}(\cos \theta) \\
&\times P_{L_d}^{m_{J_d} - \tilde{m}_s}(\cos \alpha'(k_2, \theta, q)) \psi_{L_d}^\lambda \left(\sqrt{k_2^2 - k_2 q \cos \theta + q^2/4} \right), \quad (\text{B.2})
\end{aligned}$$

$$\begin{aligned}
B_1 \equiv \langle \phi | \tilde{U} J_0 \tilde{U}^\dagger | \psi_i^\lambda \rangle &= \frac{4}{\pi} \sqrt{\frac{2}{\pi}} \sum_{T_1=0,1} (G_E^p + (-1)^{T_1} G_E^n) \sum_{L_1=0}^{L_{\max}} (1 + (-1)^{T_1} (-1)^{L_1}) \\
&\times Y_{L_1, m_{J_d} - m_{s_f}}(\theta', \varphi') \sum_{J_1=|L_1-1|}^{L+1} \langle L_1 m_{J_d} - m_{s_f} S=1 m_{s_f} | J_1 m_{J_d} \rangle \\
&\times \sum_{L_2, \tilde{m}_s} \langle J_1 m_{J_d} | L_2 m_{J_d} - \tilde{m}_s S=1 \tilde{m}_s \rangle \sum_{L_3=0}^{L_{\max}} \langle L_3 m_{J_d} - \tilde{m}_s S=1 \tilde{m}_s | J=1 m_{J_d} \rangle \\
&\times \int dk_2 k_2^2 \tilde{U}(p', k_2, L_1, L_2, J_1, S=1, T_1) \sum_{L_d=0,2} \int dk_4 k_4^2 \psi_{L_d}^\lambda(k_4) \\
&\times \int d\cos \theta P_{L_2}^{m_{J_d} - \tilde{m}_s}(\cos \theta) P_{L_3}^{m_{J_d} - \tilde{m}_s}(\cos \alpha'(k_2, \theta, q)) \\
&\times \tilde{U} \left(k_4, \sqrt{k_2^2 - k_2 q \cos \theta + q^2/4}, L_d, L_3, J=1, S=1, T=0 \right). \quad (\text{B.3})
\end{aligned}$$

In deriving the equations for B_1 , B_2 , and B_3 we have made use of the fact that the matrix elements with J_0 are twice the matrix elements with J_0^- , i.e., $\langle \phi | J_0 \tilde{U}^\dagger | \psi_i^\lambda \rangle = 2 \langle \phi | J_0^- \tilde{U}^\dagger | \psi_i^\lambda \rangle$, and similarly for B_2 and B_1 (cf. Eq. 3.26).

Evaluating Eq. 3.30 involves calculating the individual terms A_1 , A_2 , A_3 , and A_4 . The expressions for A_4 and A_3 can be obtained from expressions for B_2 and B_1 , respectively, by replacing \tilde{U} with \tilde{U}^\dagger . The U -matrices are real. Therefore, \tilde{U}^\dagger is obtained from \tilde{U} by interchanging momentum and angular momentum indices. The

expressions for A_2 and A_1 are

$$\begin{aligned}
A_2 \equiv \langle \phi | \tilde{U}^\dagger \tilde{U} J_0 | \psi_i^\lambda \rangle &= \frac{4}{\pi} \sqrt{\frac{2}{\pi}} \sum_{T_1=0,1} (G_E^p + (-1)^{T_1} G_E^n) \sum_{L_1=0}^{L_{\max}} (1 + (-1)^{T_1} (-1)^{L_1}) \\
&\times Y_{L_1, m_{J_d} - m_{s_f}}(\theta', \varphi') \sum_{J_1=|L_1-1|}^{L+1} \langle L_1 m_{J_d} - m_{s_f} S=1 m_{s_f} | J_1 m_{J_d} \rangle \\
&\times \sum_{L_3, \tilde{m}_s} \langle J_1 m_{J_d} | L_3 m_{J_d} - \tilde{m}_s S=1 \tilde{m}_s \rangle \sum_{L_2=0}^{L_{\max}} \int dk_2 k_2^2 \tilde{U}(k_2, p', L_2, L_1, J_1, S=1, T_1) \\
&\times \sum_{L_d=0,2} \langle L_d m_{J_d} - \tilde{m}_s S=1 \tilde{m}_s | J=1 m_{J_d} \rangle \int dk_3 k_3^2 \tilde{U}(k_2, k_3, L_2, L_3, J_1, S=1, T_1) \\
&\times \int d\cos \theta P_{L_3}^{m_{J_d} - \tilde{m}_s}(\cos \theta) P_{L_d}^{m_{J_d} - \tilde{m}_s}(\cos \alpha'(k_3, \theta, q)) \psi_{L_d}^\lambda \left(\sqrt{k_3^2 - k_3 q \cos \theta + q^2/4} \right)
\end{aligned} \tag{B.4}$$

and

$$\begin{aligned}
A_1 \equiv \langle \phi | \tilde{U}^\dagger \tilde{U} J_0 | \psi_i^\lambda \rangle &= \frac{8}{\pi^2} \sqrt{\frac{2}{\pi}} \sum_{T_1=0,1} (G_E^p + (-1)^{T_1} G_E^n) \sum_{L_1=0}^{L_{\max}} (1 + (-1)^{T_1} (-1)^{L_1}) \\
&\times Y_{L_1, m_{J_d} - m_{s_f}}(\theta', \varphi') \sum_{J_1=|L_1-1|}^{L+1} \langle L_1 m_{J_d} - m_{s_f} S=1 m_{s_f} | J_1 m_{J_d} \rangle \\
&\times \sum_{L_3, \tilde{m}_s} \langle J_1 m_{J_d} | L_3 m_{J_d} - \tilde{m}_s S=1 \tilde{m}_s \rangle \sum_{L_4=0}^{L_{\max}} \langle L_4 m_{J_d} - \tilde{m}_s S=1 \tilde{m}_s | J=1 m_{J_d} \rangle \\
&\times \sum_{L_2=0}^{L_{\max}} \int dk_2 k_2^2 \tilde{U}(k_2, p', L_2, L_1, J_1, S=1, T_1) \int dk_3 k_3^2 \tilde{U}(k_2, k_3, L_2, L_3, J_1, S=1, T_1) \\
&\times \sum_{L_d=0,2} \int dk_5 k_5^2 \psi_{L_d}^\lambda(k_5) \int d\cos \theta P_{L_3}^{m_{J_d} - \tilde{m}_s}(\cos \theta) P_{L_4}^{m_{J_d} - \tilde{m}_s}(\cos \alpha'(k_3, \theta, q)) \\
&\times \tilde{U}\left(k_5, \sqrt{k_3^2 - k_3 q \cos \theta + q^2/4}, L_d, L_4, J=1, S=1, T=0\right).
\end{aligned} \tag{B.5}$$

Evaluating the evolved current while including the final-state interactions involves computing the terms F_1 , F_2 , F_3 , and F_4 , as indicated in Eq. 3.34. F_4 is obtained from Eqs. 3.24 and 3.26 by replacing the deuteron wave function and the t -matrix by their evolved counterparts. The expressions for the terms F_3 , F_2 , and F_1 are then as follows:

$$\begin{aligned}
F_3 \equiv \langle \phi | t_\lambda^\dagger G_0^\dagger J_0 \tilde{U}^\dagger | \psi_i^\lambda \rangle &= \frac{4}{\pi} \sqrt{\frac{2}{\pi}} \frac{M}{\hbar c} \int \frac{dk_2 k_2^2}{(p' + k_2)(p' - k_2 - i\epsilon)} \sum_{T_1=0,1} (G_E^p + (-1)^{T_1} G_E^n) \\
&\times \sum_{L_1=0}^{L_{\max}} (1 + (-1)^{T_1} (-1)^{L_1}) Y_{L_1, m_{J_d} - m_{s_f}}(\theta', \varphi') \sum_{J_1=|L_1-1|}^{L+1} \langle L_1 m_{J_d} - m_{s_f} S=1 m_{s_f} | J_1 m_{J_d} \rangle \\
&\times \sum_{L_2=0}^{L_{\max}} t_\lambda^*(k_2, p', L_2, L_1, J_1, S=1, T_1) \sum_{\tilde{m}_s=-1}^1 \langle J_1 m_{J_d} | L_2 m_{J_d} - \tilde{m}_s S=1 \tilde{m}_s \rangle \\
&\times \sum_{L_3=0}^{L_{\max}} \langle L_3 m_{J_d} - \tilde{m}_s S=1 \tilde{m}_s | J=1 m_{J_d} \rangle \int d\cos\theta P_{L_2}^{m_{J_d} - \tilde{m}_s}(\cos\theta) P_{L_3}^{m_{J_d} - \tilde{m}_s}(\cos\alpha'(k_2, \theta, q)) \\
&\times \int dk_5 k_5^2 \sum_{L_d=0,2} \tilde{U}\left(k_5, \sqrt{k_2^2 - k_2 q \cos\theta + q^2/4}, L_d, L_3, J=1, S=1, T=0\right) \psi_{L_d}^\lambda(k_5), \\
\end{aligned} \tag{B.6}$$

$$\begin{aligned}
F_2 \equiv \langle \phi | t_\lambda^\dagger G_0^\dagger \tilde{U} J_0 | \psi_i^\lambda \rangle &= \frac{4}{\pi} \sqrt{\frac{2}{\pi}} \frac{M}{\hbar c} \int \frac{dk_2 k_2^2}{(p' + k_2)(p' - k_2 - i\epsilon)} \sum_{T_1=0,1} (G_E^p + (-1)^{T_1} G_E^n) \\
&\times \sum_{L_1=0}^{L_{\max}} (1 + (-1)^{T_1} (-1)^{L_1}) Y_{L_1, m_{J_d} - m_{s_f}}(\theta', \varphi') \sum_{J_1=|L_1-1|}^{L+1} \langle L_1 m_{J_d} - m_{s_f} S=1 m_{s_f} | J_1 m_{J_d} \rangle \\
&\times \sum_{L_2=0}^{L_{\max}} t_\lambda^*(k_2, p', L_2, L_1, J_1, S=1, T_1) \sum_{L_3=0}^{L_{\max}} \int dk_4 k_4^2 \tilde{U}(k_2, k_4, L_2, L_3, J_1, S=1, T_1) \\
&\times \sum_{\tilde{m}_s=-1}^1 \langle J_1 m_{J_d} | L_3 m_{J_d} - \tilde{m}_s S=1 \tilde{m}_s \rangle \sum_{L_d=0,2} \langle L_d m_{J_d} - \tilde{m}_s S=1 \tilde{m}_s | J=1 m_{J_d} \rangle \\
&\times \int d\cos\theta P_{L_3}^{m_{J_d} - \tilde{m}_s}(\cos\theta) P_{L_d}^{m_{J_d} - \tilde{m}_s}(\cos\alpha'(k_4, \theta, q)) \psi_{L_d}^\lambda\left(\sqrt{k_4^2 - k_4 q \cos\theta + q^2/4}\right), \\
\end{aligned} \tag{B.7}$$

$$\begin{aligned}
F_1 \equiv \langle \phi | t_\lambda^\dagger G_0^\dagger \tilde{U} J_0 \tilde{U}^\dagger | \psi_i^\lambda \rangle &= \frac{8}{\pi^2} \sqrt{\frac{2}{\pi}} \frac{M}{\hbar c} \int \frac{dk_2 k_2^2}{(p' + k_2)(p' - k_2 - i\epsilon)} \sum_{T_1=0,1} (G_E^p + (-1)^{T_1} G_E^n) \\
&\times \sum_{L_1=0}^{L_{\max}} (1 + (-1)^{T_1} (-1)^{L_1}) Y_{L_1, m_{J_d} - m_{s_f}}(\theta', \varphi') \sum_{J_1=|L_1-1|}^{L_1+1} \langle L_1 m_{J_d} - m_{s_f} S=1 m_{s_f} | J_1 m_{J_d} \rangle \\
&\times \sum_{L_2=0}^{L_{\max}} t_\lambda^*(k_2, p', L_2, L_1, J_1, S=1, T_1) \sum_{L_3=0}^{L_{\max}} \sum_{\tilde{m}_s=-1}^1 \langle J_1 m_{J_d} | L_3 m_{J_d} - \tilde{m}_s S=1 \tilde{m}_s \rangle \\
&\times \sum_{L_4=0}^{L_{\max}} \langle L_4 m_{J_d} - \tilde{m}_s S=1 \tilde{m}_s | J=1 m_{J_d} \rangle \int dk_4 k_4^2 \tilde{U}(k_2, k_4, L_2, L_3, J_1, S=1, T_1) \\
&\times \int d\cos \theta P_{L_3}^{m_{J_d} - \tilde{m}_s}(\cos \theta) P_{L_4}^{m_{J_d} - \tilde{m}_s}(\cos \alpha'(k_4, \theta, q)) \int dk_6 k_6^2 \sum_{L_d=0,2} \psi_{L_d}^\lambda(k_6) \\
&\times \tilde{U}\left(k_6, \sqrt{k_4^2 - k_4 q \cos \theta + q^2/4}, L_d, L_4, J=1, S=1, T=0\right). \quad (\text{B.8})
\end{aligned}$$

B.2 Evolution of the final state

The interacting final neutron-proton state $|\psi_f\rangle$ as defined in Eq. 3.7 is the formal solution of the Lippmann–Schwinger (LS) equation for the scattering wave function,

$$\begin{aligned}
|\psi_f\rangle &= |\phi\rangle + G_0(E') V |\psi_f\rangle \\
&= |\phi\rangle + G_0(E') t(E') |\phi\rangle. \quad (\text{B.9})
\end{aligned}$$

The t -matrix, in turn, is defined by the LS equation

$$t(E') = V + V G_0(E') t(E'). \quad (\text{B.10})$$

The substitution $E' \rightarrow E' + i\epsilon$ and the limit $\epsilon \rightarrow 0$ are implied to select outgoing boundary conditions. We want to show now that the SRG-evolved final state can be obtained directly by using the solution t^λ of Eq. B.10 with $V \rightarrow V_\lambda$ in the second line of Eq. B.9, which is the same as Eq. 3.7 in Subsec. 3.2.1, i.e.,

$$U_\lambda |\psi_f\rangle = |\psi_f^\lambda\rangle, \quad (\text{B.11})$$

where

$$|\psi_f^\lambda\rangle = |\phi\rangle + G_0(E') t_\lambda(E') |\phi\rangle. \quad (\text{B.12})$$

In this section, we suppress all spin and isospin degrees of freedom, and only denote the (arbitrary) energy parameter as E' for consistency with Subsec. 3.2.1.

First, it is important to recall that by definition the free Hamiltonian H_0 does not evolve, so that for $H = H_0 + V$ we have

$$H_\lambda = U_\lambda H U_\lambda^\dagger \equiv H_0 + V_\lambda . \quad (\text{B.13})$$

In other words, the evolved potential V_λ is defined such that it absorbs the evolution of the initial free Hamiltonian (kinetic energy) as well.

In order to prove Eq. B.11, it is convenient to consider the evolved and unevolved full Green's functions $G_\lambda(E')$ and $G(E')$, defined via

$$G_\lambda(z)^{-1} = z - H_\lambda = G_0^{-1}(z)^{-1} - V_\lambda , \quad (\text{B.14a})$$

$$G(z)^{-1} = z - H = G_0^{-1}(z)^{-1} - V . \quad (\text{B.14b})$$

Here, $G_0^{-1}(z)^{-1} = z - H_0$ is the free Green's function (which does not change under the SRG evolution because H_0 does not), and z is an arbitrary complex energy parameter that is set to $E' + i\epsilon$ to recover the physically relevant case. The Green's functions can be expressed in terms of the t -matrix as

$$G(z) = G_0(z) + G_0(z) t(z) G_0(z) , \quad (\text{B.15})$$

and analogously for the evolved version. Furthermore, the Green's functions can be written in their spectral representations

$$G_\lambda(z)^{-1} \simeq \int d^3k \frac{|\psi_f^\lambda(k)\rangle\langle\psi_f^\lambda(k)|}{z - k^2/M} + \text{bound states} , \quad (\text{B.16a})$$

$$G(z)^{-1} \simeq \int d^3k \frac{|\psi_f(k)\rangle\langle\psi_f(k)|}{z - k^2/M} + \text{bound states} . \quad (\text{B.16b})$$

Here, $|\psi_f^{(\lambda)}(k)\rangle$ denotes the (evolved) continuum states with momentum k , and we have $|\psi_f^{(\lambda)}\rangle = |\psi_f^{(\lambda)}(\sqrt{ME'})\rangle$

From Eqs. B.13 and B.14 it now follows that

$$\begin{aligned} G_\lambda(z)^{-1} &= z - H_\lambda = z - U_\lambda H U_\lambda^\dagger \\ &= U_\lambda(z - H)U_\lambda^\dagger = U_\lambda G(z)^{-1} U_\lambda^\dagger. \end{aligned} \quad (\text{B.17})$$

Combining this with Eqs. B.16 and matching residues at $z = E' + i\epsilon$, we find that indeed $|\psi_f^\lambda\rangle = U_\lambda|\psi_f\rangle$, as stated in Eq. B.11.

B.3 Evolution of the current

Here we document the equations used to obtain the results in Subsec. 3.2.5. The evolved current J_0^λ is given by

$$J_0^\lambda = \underbrace{\tilde{U} J_0 \tilde{U}^\dagger}_{J_1} + \underbrace{\tilde{U} J_0}_{J_2} + \underbrace{J_0 \tilde{U}^\dagger}_{J_3} + J_0. \quad (\text{B.18})$$

$$\begin{aligned} J_3 \equiv \langle k_1 J_1 m_{J_d} L_1 S=1 T_1 | J_0^-(q) \tilde{U}^\dagger | k_2 J=1 m_{J_d} L_2 S=1 T=0 \rangle &= \frac{2}{\pi} \frac{\pi^2}{2} (G_E^p + (-1)^{T_1} G_E^m) \\ &\times \sum_{L_p} \int_{|k_1-q/2|}^{k_1+q/2} dp p^2 \sum_{\tilde{m}_s=-1}^1 \langle J_1 m_{J_d} | L_1 m_{J_d} - \tilde{m}_s S=1 \tilde{m}_s \rangle \frac{2}{k_1 p q} \\ &\times P_{L_1}^{m_{J_d}-\tilde{m}_s} \left(\frac{k_1^2 - p^2 + q^2/4}{k_1 q} \right) P_{L_1}^{m_{J_d}-\tilde{m}_s} \left(\frac{k_1^2 - p^2 - q^2/4}{pq} \right) \\ &\times \langle L_p m_{J_d} - \tilde{m}_s S=1 \tilde{m}_s | J=1 m_{J_d} \rangle \tilde{U}^\dagger(p_1, k_2, L_p, L_2, J=1, S=1, T=0). \end{aligned} \quad (\text{B.19})$$

Evaluation of J_2 requires writing the current J_0 such that the integration over the bra state can be done. We get the same expression as in Eq. 3.49, but on a different domain.

$$\begin{aligned}
\langle k_1 J_1 m_{J_d} L_1 S=1 T_1 | J_0^- | k_2 J=1 m_{J_d} L_2 S=1 T=0 \rangle &= \frac{\pi^2}{2} (G_E^p + (-1)^{T_1} G_E^n) \\
\times \sum_{\tilde{m}_s=-1}^1 \langle J_1 m_{J_d} | L_1 m_{J_d} - \tilde{m}_s S=1 \tilde{m}_s \rangle P_{L_1}^{m_{J_d}-\tilde{m}_s} \left(\frac{k_1^2 - k_2^2 + q^2/4}{k_1 q} \right) \frac{2}{k_1 k_2 q} \\
\times P_{L_2}^{m_{J_d}-\tilde{m}_s} \left(\frac{k_1^2 - k_2^2 - q^2/4}{k_2 q} \right) \langle L_2 m_{J_d} - \tilde{m}_s S=1 \tilde{m}_s | J=1 m_{J_d} \rangle \\
&\quad \cdots \text{for } k_1 \in (|k_2 - q/2|, k_2 + q/2) \\
&\quad = 0 \text{ otherwise}
\end{aligned} \tag{B.20}$$

Equation B.20 is gotten from the following expression for the current:

$$\begin{aligned}
\langle k_1 J_1 m_{J_d} L_1 S=1 T_1 | J_0^- | k_2 J=1 m_{J_d} L_2 S=1 T=0 \rangle &= \frac{\pi^2}{2} (G_E^p + (-1)^{T_1} G_E^n) \\
&\quad \times \sum_{\tilde{m}_s=-1}^1 \int d\cos \theta \langle J_1 m_{J_d} | L_1 m_{J_d} - \tilde{m}_s S=1 \tilde{m}_s \rangle P_{L_2}^{m_{J_d}-\tilde{m}_s}(\cos \theta)
\end{aligned} \tag{B.21}$$

$$\begin{aligned}
&\quad \times P_{L_1}^{m_{J_d}-\tilde{m}_s}(\cos \alpha''(k_1, \theta, q)) \frac{\delta(k_1 - \sqrt{k_2^2 + k_2 q \cos \theta + q^2/4})}{k_1^2} \\
&\quad \times \langle L_2 m_{J_d} - \tilde{m}_s S=1 \tilde{m}_s | J=1 m_{J_d} \rangle.
\end{aligned} \tag{B.22}$$

$$\tag{B.23}$$

$$\tag{B.24}$$

Note that Eq. B.24 differs from Eq. 3.22 in terms of the arguments of the δ function and the Legendre polynomials.

Using Eq. B.20, we can derive the expression for J_2 .

$$\begin{aligned}
J_2 \equiv \langle k_1 J_1 m_{J_d} L_1 S=1 T_1 | \tilde{U} J_0^-(q) | k_2 J=1 m_{J_d} L_2 S=1 T=0 \rangle &= \frac{2\pi^2}{\pi 2} (G_E^p + (-1)^{T_1} G_E^n) \\
\times \sum_{L_p} \int_{|k_2-q/2|}^{k_2+q/2} dp p^2 \sum_{\tilde{m}_s=-1}^1 \langle J_1 m_{J_d} | L_p m_{J_d} - \tilde{m}_s S=1 \tilde{m}_s \rangle \frac{2}{k_2 p q} \\
\times P_{L_p}^{m_{J_d}-\tilde{m}_s} \left(\frac{p^2 - k_2^2 + q^2/4}{pq} \right) P_{L_2}^{m_{J_d}-\tilde{m}_s} \left(\frac{p^2 - k_2^2 - q^2/4}{k_2 q} \right) \\
\times \langle L_2 m_{J_d} - \tilde{m}_s S=1 \tilde{m}_s | J=1 m_{J_d} \rangle \tilde{U}(k_1, p, L_1, L_p, J=1, S=1, T=0).
\end{aligned} \tag{B.25}$$

Finally, the expression for J_1 is

$$\begin{aligned}
J_1 \equiv & \langle k_1 J_1 m_{J_d} L_1 S=1 T_1 | \tilde{U} J_0^-(q) \tilde{U}^\dagger | k_2 J=1 m_{J_d} L_2 S=1 T=0 \rangle = \left(\frac{2}{\pi}\right)^2 \frac{\pi^2}{2} \\
& \times (G_E^p + (-1)^{T_1} G_E^n) \sum_{L_{p_1}, L_{p_2}, \tilde{m}_s} \int dp_1 \int_{p_2=|p_1-q/2|}^{p_1+q/2} dp_2 p_1^2 p_2^2 \frac{2}{p_1 p_2 q} \\
& \times \tilde{U}(k_1, p_1, L_1, L_{p_1}, J_1, S=1, T_1) \tilde{U}^\dagger(p_2, k_2, L_{p_2}, L_2, J=1, S=1, T=0) \\
& \times \langle J_1 m_{J_d} | L_{p_1} m_{J_d} - \tilde{m}_s S=1 \tilde{m}_s \rangle \langle L_{p_2} m_{J_d} - \tilde{m}_s S=1 \tilde{m}_s | J=1 m_{J_d} \rangle \\
& \times P_{L_{p_1}}^{m_{J_d} - \tilde{m}_s} \left(\frac{p_1^2 - p_2^2 + q^2/4}{p_1 q} \right) P_{L_{p_2}}^{m_{J_d} - \tilde{m}_s} \left(\frac{p_1^2 - p_2^2 - q^2/4}{p_2 q} \right) \quad (\text{B.26})
\end{aligned}$$